COMPOSITION – PROCESSING – MICROSTRUCTURE – PROPERTY RELATIONSHIPS OF THE ZINC-MAGNESIUM SYSTEM FOR ABSORBABLE BIOMEDICAL IMPLANT APPLICATIONS

By

David Hernández Escobar

A DISSERTATION

Submitted to
Michigan State University
in partial fulfillment of the requirements
for the degree of

Materials Science and Engineering − Doctor of Philosophy

2021

ABSTRACT

COMPOSITION – PROCESSING – MICROSTRUCTURE – PROPERTY RELATIONSHIPS OF THE ZINC-MAGNESIUM SYSTEM FOR ABSORBABLE BIOMEDICAL IMPLANT APPLICATIONS

By

David Hernández Escobar

Absorbable metals have the potential to serve as the next generation of temporary medical implants by safely dissolving in the human body upon vascular tissue healing and bone regeneration. Their incorporation in the market could greatly reduce the need and risks associated with additional surgeries and other complications often related to permanent devices. Despite the extensive research on magnesium (Mg) and iron (Fe) based alloys over the last two decades, they have not exhibited an optimal combination of mechanical properties, biocompatibility, and controlled degradation rate for absorbable implant applications. Zinc (Zn) and Zn-based alloys have recently emerged as an alternative, as they have demonstrated an attractive combination of *in vivo* biocompatibility and degradation behavior. However, their mechanical properties are generally insufficient for load-bearing implant applications.

In this dissertation, Zn-xMg (x = 3, 10, 30 wt.%) hybrid samples were synthesized for the first time using high-pressure torsion (HPT) to mechanically bond pure Zn and Mg disks. These samples were characterized to investigate their processing-microstructure-property relationships. The effects of HPT on the microstructural and hardness evolution were systematically studied in all the materials, with special emphasis on the regions of highest plastic deformation. The effects of post-deformation annealing (PDA) on the Zn-3Mg hybrid were also investigated. Also, an as-homogenized Zn-3Mg (wt.%) alloy was HPT-processed and subjected to PDA, and the microstructure and hardness evolution was compared with that of the Zn-3Mg hybrid. In addition, four different biodegradable coatings (based on zinc phosphate (ZnP), collagen (Col), and Ag-

doped bioactive glass nanoparticles (AgBGN)) were synthesized by chemical conversion, spin-coating, or a combination of both, on the as-homogenized Zn-3Mg alloy substrates. The effects of the coatings on the *in vitro* degradation behavior, cytocompatibility, and antibacterial activity were evaluated.

A significant microstructural refinement was obtained after HPT processing for 30 turns, reaching equiaxed grains of ~ 200 nm in both the Zn-3Mg hybrid and alloy. Unlike in the alloy, HPT induced the nucleation of Mg_2Zn_{11} and $MgZn_2$ intermetallic compounds, as well as the formation of supersaturated solid solutions in the hybrid, both of which led to maximum hardness values in the range of ~ 220-230 HV. PDA resulted in both an increased hardness (up to ~ 250 HV) and strain rate sensitivity. A plastic deformation model is proposed to explain the strain-hardening behavior of the hybrid after PDA, which suggested an enhanced strength-ductility relationship. This was consistent with the strain rate sensitivity results from nanoindentation.

In vitro degradation of ZnP coated samples for 21 days immersion showed a controlled weight loss over time associated with a decreased corrosion rate, while maintaining a physiological pH range of 7.5-7.6. The uncoated, ZnP coated, and Col-AgBGN coated sample extracts led to higher cell viability over 6 days culture, which generally increased with extract concentration. In addition, the Col-AgBGN coated samples led to ~ 31 % bacterial viability, compared to the ~ 65-75 % of the other samples, hence, indicating a strong antibacterial effect.

Overall, the insights gained from this dissertation enabled a better understanding of the composition-processing-microstructure-property relationships of the Zn-Mg system and served as a roadmap for the design of hybrid materials with enhanced mechanical properties. Moreover, the synthesis of biodegradable coatings has potential to tailor the Zn-Mg materials for specific biomedical implant applications.

A mi familia:
Por siempre haber creído en mí, este doctorado va por vosotros.

ACKNOWLEDGMENTS

First of all, I would like to express my sincere gratitude to my advisor, Prof. Carl Boehlert, for giving me the opportunity to perform this work, for his continuous support and invaluable guidance during my Ph.D. studies at Michigan State University (MSU). I am truly grateful for his patience, motivation, willingness to discuss about the research at any time, and the opportunity to showcase my research at several technical conferences. He also supported me to conduct key research for my dissertation at the Center of Nanophase Materials Science (CNMS), at Oak Ridge National Laboratory (ORNL). Beyond the academics, Prof. Boehlert has taught me how to be a good mentor, and to become a better person overall. He has always been there for anything I needed, making me feel somewhat closer to home, and I will be forever grateful for that.

I would also like to thank my committee members, Prof. Martin Crimp, Dr. Xanthippi Chatzistavrou, and Prof. Xinran Xiao, for their insightful comments, and valuable suggestions that helped me build a solid dissertation project. Dr. Chatzistavrou connected me with Prof. Kurt Hankenson from the Department of Orthopaedic Surgery at University of Michigan (UofM), and to Dr. Neal Hammer from the Department of Microbiology and Molecular Genetics at MSU. The research collaborations with Dr. Chatzistavrou, Prof. Hankenson, and Dr. Hammer were essential to carry out the *in vitro* experiments presented in this dissertation.

This work would not have been possible without the collaboration of Dr. Megumi Kawasaki at Oregon State University, who was responsible for HPT processing the materials studied in this dissertation. I would also like to thank Dr. Hakan Yilmazer at Yildiz Technical University, who supplied the as-cast alloy used in this work. I would like to thank Dr. Raymond Unocic, Dr.

Jonathan Poplawsky, Mr. James Burns, and Ms. Dorothy Coffey for their invaluable assistance with the sample preparation and operation of the TEM and APT equipment during my stay at the CNMS.

I would like to thank Ms. Parker Acevedo and Dr. Yadav Wagley, from Prof. Hankenson´s group, for teaching me the best practices of cell culture manipulation, which enabled me to perform the in vitro assays independently. I also would like to thank Dr. Per Askeland and Dr. Ed Drown for their help operating the SEM and the nanoindenter at MSU´s Composite Materials and Structures Center. I would like to thank Dr. Melinda Frame for her assistance with the CLSM at MSU's Center of Advanced Microscopy. I am also thankful to our collaborators at Central Michigan University, Dr. Waseem Haider and Dr. Zia Ur Rahman, for their help performing the electrochemical testing.

I would like to also thank Prof. Thomas Bieler and Dr. Philip Eisenlohr for their feedback during the Metals Group's meetings, as well as that from former and current graduate students, namely Dr. Aritra Chakraborty, Dr. Satyapriya Gupta, Dr. Vahid Khademi, Mr. Harish Chakravarty, Dr. Di Kang, Dr. Songyang Han, Dr. Mingmin Wang, Ms. Chelsea Edge, Dr. Aida Amroussia, Ms. Geeta Kumari, Ms. JoAnn Ballor, Mr. Harsha Phukan, Ms. Eureka Pai, Mr. Yang Su, Mr. Zhuowen Zhao, Mr. Jiawei Lu, Ms. Uche Okeke, and Mr. Zackery Thune. I would also like to thank Dr. Ajith Chakkedath, who enabled me to actively participate in his research activities in the summer of 2015, when I was a junior undergraduate exchange student at Technical University of Madrid.

I would like to acknowledge that the funding for this research was provided by the National Science Foundation Division of Materials Research (Grant No. DMR1607942) through the Metals and Metallic Nanostructures program. A portion of this research was conducted at ORNL's

CNMS, a U.S. Department of Energy Office of Science User Facility, under CNMS2018-218 user project proposal.

I would like to thank Dr. Katy Colbry and Dr. Matt Helm for giving me the opportunity to take on different leadership roles at the graduate level in the College of Engineering. I feel very grateful for all the great people I have met and the friends I have made during this journey, including Mr. Juan Pablo Rojas, Mr. Mario Calderón, Mr. Raúl Vega, Dr. Kanchan Chavan, Dr. Sabyasachi Das, Mr. Alex Mirabal, Mr. Chauncey Splichal, Dr. Mary Ensch, Ms. Lexi Rogien, Dr. Maddie Shellgren, and Dr. Makena Neal.

Finally, my deepest gratitude goes to my family. I would like to thank my parents and sister, whose love, unconditional support, and encouragement are always with me in whichever challenge I pursue. My grandparents, who are waiting for me at the other side of the planet, have always been, and will be, a tremendous source of inspiration and motivation during my life. Last, but definitely not least, thanks to my loving and wonderful life partner, Natalia Pajares, without whose day-to-day emotional support, I would not have survived this Ph. D.

TABLE OF CONTENTS

LIST OF TABLES

LIST OF FIGURES

KEY TO SYMBOLS AND ABBREVIATIONS

AgBGN	Silver-doped bioglass nanoparticles
Ag	Silver
APT	Atom probe tomography
ARB	Accumulative roll bonding
b	Burger's vector
BF	Bright field
BG	Bioglass
BSE	Backscattered electron
CAM	Center for advanced microscopy
CCK-8	Cell counting kit-8
CFU	Colony forming unit
CI	Confidence index
CLSM	Confocal laser scanning microscopy
CNMS	Center for nanophase materials sciences
Col	Collagen
CSR	Constant strain rate
DDRX	Discontinuous dynamic recrystallization
DI	Deionized
DMEM	Dulbecco's modified Eagle medium
EBSD	Electron-backscattered diffraction
ECAP	Equal channel angular pressing

E_{corr}	Corrosion potential
EDS	Energy dispersive spectroscopy
EEC	Electrical equivalent circuit
ε_f	Elongation-to-failure
EIS	Electrochemical impedance spectroscopy
FEG	Field emission gun
FFT	Fast Fourier transform
FIB	Focused-ion beam
gf	Gram force
GIXRD	Grazing incidence x-ray diffraction
GS_{ave}	Average grain size
H	Nanoindentation hardness
HAADF	High angle annular dark field
HABs	High-angle grain boundaries
HCP	Hexagonal closed-packed
h_{max}	Maximum displacement at peak load
HMDS	Hexamethyldisilazane
hMSC	Human marrow stromal cells
HPT	High-pressure torsion
HRTEM	High resolution transmission electron microscopy
HV	Vickers hardness
I_{corr}	Corrosion current
ICP	Inductively couple plasma

ICSD	Inorganic crystal structure database
IFFT	Inverse fast Fourier transform
KAM	Kernel average misorientation
m	Strain rate sensitivity
Mg	Magnesium
MRSA	*Methicillin-resistant Staphylococcus aureus*
MSU	Michigan State University
OCP	Open circuit potential
OD	Optical density
OM	Optical microscopy
ORNL	Oak Ridge national laboratory
PBS	Phosphate buffered saline
PDA	Post-deformation annealing
PDF	Powder diffraction files
PDP	Potentiodynamic polarization
RDI	Recommended daily intake
ROI	Region of interest
RT	Room temperature
S	Unloading stiffness
SAD	Selected area diffraction
SBF	Simulated body fluid
SCE	Saturated calomel electrode
SE	Secondary electron

SEM	Scanning electron microscopy
SPD	Severe plastic deformation
STEM	Scanning transmission electron microscopy
TEM	Transmission electron microscopy
T_h	Homologous temperature
TSB	Tryptic soy broth
UFG	Ultrafine-grained
UTS	Ultimate tensile strength
UV	Ultraviolet
V*	Activation volume
XRD	X-ray diffraction
YS	Yield strength
ZA	Zone axis
Z	Atomic number
Zn	Zinc
ZnP	Zinc phosphate

1. INTRODUCTION

1.1. Motivation

Over the last two decades, the field of biomedical implants has attracted considerable attention due to its potential to improve human life (both quality and longevity) by replacing damaged hard and soft tissues, such as bone, cartilage, blood vessels, or even entire organs [1]. Metallic implants have been widely used as orthopedic and vascular devices, as well as tissue engineering scaffolds, due to their high strength and fracture toughness compared with polymers and ceramic materials. Traditional metallic biomaterials with high corrosion resistance, such as stainless steel, titanium alloys, cobalt-chromium alloys, and tantalum, are typically considered for permanent implant applications [2].

However, in many cases, the function of the implant is temporary and, thereby, not needed after full recovery. Moreover, the permanent presence of the implant in the body upon healing can develop multiple complications. For instance, the release of metal ions from the implant device over time can lead to the accumulation of trace metals in the surrounding tissues, which can, in turn, trigger a chronic inflammatory response. In such circumstances, a second surgery may be necessary for implant extraction and/or replacement, resulting in additional injury, expense, and discomfort, as well as an extra risk of infection [2,3]. In addition, implant failure can occur in bone fixation devices due to the stress-shielding effect, which refers to the fact that implants carry most of the mechanical load, impeding load transfer to the bone tissue, which is necessary to stimulate new bone formation [4,5]. This occurs when the stiffness of the implant material is substantially higher than the bones to be replaced, which is often the case of the metals typically used for permanent applications.

Absorbable metals offer the opportunity to design temporary implant devices able to overcome the above-mentioned limitations related to the existing corrosion-resistant metals used for permanent implant applications. Absorbable metal implants are expected to maintain the mechanical integrity during tissue healing and then, corrode gradually and safely over time, while progressively transferring the mechanical load to the healed tissue [6,7]. Therefore, absorbable metal implants must be designed to have a balance between strength and corrosion resistance in a physiological environment, while maintaining their biocompatibility during the degradation time.

In the last decade, iron (Fe) and magnesium (Mg), both pure and alloyed, have been extensively studied as potential absorbable metals for biomedical applications [8,9]. However, the large number of research studies with these material systems has noted several major limitations in terms of their suitability for clinical applications. On the one hand, Fe and Fe-based alloys generally exhibit corrosion rates substantially below the clinical needs, which unnecessarily prolongs the exposure time of the organism to the implant after the healing and recovery period [10]. In addition, the corrosion products of Fe tend to be stable in the physiological environment, resulting in long-term retention causing metabolic complications, rather than promoting cells to integrate around the degrading implant [11]. On the other hand, Mg and Mg alloys typically exhibit insufficient mechanical strength, as well as excessive corrosion rates in physiological environments. The latter issue is particularly detrimental, as it leads to the formation of hydrogen gas pockets near the implant, compromising its structural integrity during the healing period [12]. Therefore, recognizing the substantial research efforts and knowledge gained over the years on Fe and Mg alloys for implant applications, the biomedical field is still in need of metallic materials able to satisfy the demanding set of requirements of absorbable medical implant applications.

In 2013, zinc (Zn) emerged as an alternative material to overcome the challenges of Fe and Mg for absorbable medical implant applications, mainly due to its moderate corrosion rate in simulated body fluid [13]. The following are some aspects that make Zn and Zn-based alloys especially attractive for use in temporary clinical applications:

- Similar to Fe and Mg, Zn is an essential trace element in the human body, critical for a significant number of metabolic activities and cellular functionalities, including cell growth, proliferation, and differentiation. Thus, the Zn ions released from the implant during degradation are expected to integrate into the normal metabolic activity of the host without causing toxic side effects [2,14].
- The standard electrode potential of Zn is -0.76 V, which is between that of Mg (-2.37 V) and Fe (-0.44 V). This indicates that Zn exhibits moderate corrosion rates (faster than the slowly degrading Fe and its alloys, but slower than the rapidly degrading Mg), and this is caused by the corrosion products forming passive layers of moderate stability [13,15]
- In general, Zn and Zn alloys are easier to cast and process compared to Mg and Fe alloys due to their low melting points, low chemical reactivity, and good machinability [13,16].

The feasibility of producing Zn and Zn-alloys with desirable corrosion rates and biocompatibility has been demonstrated in numerous research studies, both *in vitro* and *in vivo,* as summarized in section 2.1.1. Nevertheless, limitations of pure as-cast Zn include its low strength (i.e., UTS < 20 MPa) and elongation-to-failure ($\varepsilon f < 0.5\%$) [17]. The mechanical properties of Zn have been improved considerably over the last several years by alloying and thermomechanical processing, as reported in recent reviews [18,19]. However, there are still a number of Zn-based alloys with interesting combinations of corrosion behavior and biocompatibility but insufficient mechanical properties for load-bearing applications. This motivated the investigation of high-pressure torsion

(HPT) in this dissertation, which is a severe plastic deformation processing method capable of obtaining ultrafine-grained microstructures with mechanical properties not generally achievable from conventional deformation processes [20]. Moreover, ultrafine-grained materials have shown potential to overcome the typical strength-ductility tradeoff [21] through the application of post-deformation annealing (PDA) [22]. Despite the numerous SPD-processed metals and alloys investigated over the last several years, few studies have focused on enhancing the mechanical properties of biocompatible materials for biomedical applications [23]. In addition, recent works have demonstrated that HPT can be used to synthesize metal hybrids, from mechanical bonding of dissimilar bulk materials, with heterogenous microstructures leading to high strength and enhanced plasticity [24,25].

Therefore, the overarching goal of this dissertation was to investigate the feasibility of HPT processing to produce Zn-Mg hybrids (with various compositions), which may be attractive for biomedical implant applications, and to examine the effect of HPT and PDA on their microstructural and hardness evolution. In addition, different biocompatible coatings (based on zinc phosphate (ZnP), collagen (Col), and Ag-doped bioactive glass (AgBGN)) were synthesized on a Zn-3Mg alloy substrate with the objective to tune the corrosion properties, cell viability, and antibacterial activity. These coatings are anticipated to be applicable to the Zn-Mg HPT hybrids as well. The insights gained during this work are expected to guide future researchers towards a further exploration of the Zn-Mg HPT hybrid system for absorbable implant applications.

1.2. Work performed and dissertation structure

In this dissertation, a series of Zn-xMg hybrids (x = 3, 10, 30 wt.%) were synthesized by HPT, for the first time, from mechanical bonding of Zn/Mg/Zn disks with various thicknesses to match the targeted compositions. The hybrid samples were HPT-processed at room temperature (RT) for up to 30 turns at 1 rpm, with 6 GPa applied pressure. The effect of HPT on the microstructural and hardness evolution was studied in the three hybrid compositions, with particular attention to the regions of highest accumulated plastic strain near the sample periphery. The effect of Mg concentration on the HPT-processed microstructures and hardness was evaluated. The effect of PDA (200 ºC, 1h) on the microstructure and hardness of the Zn-3Mg hybrid after 30 turns was also investigated. A cast-then-homogenized Zn-3Mg (wt.%) alloy was also processed by HPT for 30 turns and subjected to PDA, and the microstructure and hardness evolution was compared with those of the hybrid with an equivalent nominal composition and processing history.

In addition, four different biocompatible coatings (i.e., ZnP, ZnP-Col, Col, Col-AgBGN) were synthesized in the cast-then-homogenized Zn-3Mg (wt.%) alloy using either a chemical conversion method, a spin-coating technique, or a combination of both. The *in vitro* degradation, cytocompatibility, and antibacterial behavior of the different coated substrates were assessed and compared to that of the uncoated sample. A flowchart outlining the materials and characterization techniques used in this dissertation is provided in Figure 1.

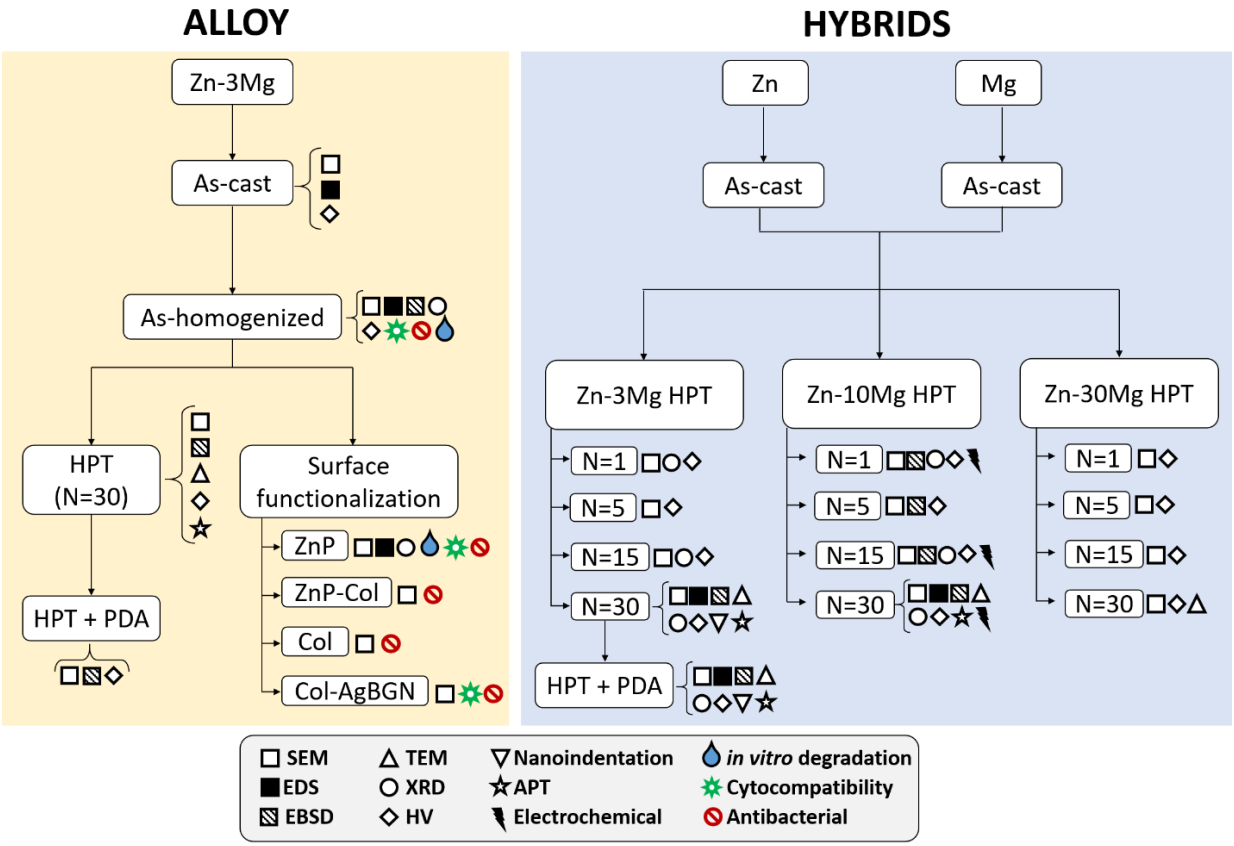

Figure 1: Flowchart of the materials studied and the characterization techniques used in this dissertation. All compositions are in (wt.%). The following acronyms were used: HPT: high-pressure torsion; N: number of HPT turns; PDA: post-deformation annealing; SEM: scanning electron microscopy; EDS: energy-dispersive X-ray spectroscopy; EBSD: electron backscattered diffraction; TEM: transmission electron microscopy; XRD: X-ray diffraction; HV: Vickers hardness; APT: atom probe tomography; ZnP: zinc phosphate; Col: collagen; AgBGN: Ag-doped bioactive glass nanoparticles.

In Chapter 2, a background on absorbable Zn-based alloys for biomedical applications is presented, including their biocompatibility from *in vitro* and *in vivo* studies, their common alloying systems and microstructures, as well as mechanical properties. The research gaps and novel opportunities for the development of absorbable Zn-based alloys are also presented. A review of the current understanding of the HPT processing of hybrid metals, including their major microstructural and mechanical properties, is also provided.

In Chapter 3, the materials and experimental procedures used are described. The experimental setup used for the synthesis of the HPT hybrids and the processing parameters are presented. The details of the sample preparation for microstructural characterization and micro-mechanical testing, as well as the parameters used for the analysis of the results, are provided. The protocols developed for the synthesis of the different biodegradable coatings, and the details for the *in vitro* characterization performed are also provided.

In Chapter 4, the results from the microstructural characterization, micro-mechanical testing, and *in vitro* studies are provided. The grain size, orientation, and texture were characterized using SEM and EBSD. The compositions were measured using EDS, XRD, TEM, and APT. TEM was also used to investigate the ultrafine-grained structure and the distribution and morphology of the nanosized intermetallic phases. The Vickers hardness (HV) and distributions were measured in all the samples, whereas nanoindentation load-displacement tests were performed on the Zn-3Mg hybrid after HPT and HPT+PDA. The hardness (H) and strain rate sensitivity (m) were measured from nanoindentation. The surface morphology for all the coated samples was analyzed by SEM. The *in vitro* degradation behavior of the ZnP coated and uncoated samples were evaluated from immersion testing, and the corrosion rates were estimated from weight loss measurements. The cell viability of the uncoated, ZnP, and Col-AgBGN samples was evaluated from indirect contact proliferation assays with sample extracts. The antibacterial viability was assessed in the uncoated and all coated samples by their capability to resist bacteria colonization. The characteristics of bacteria attached to the sample surfaces were investigated by SEM, and live/dead staining was combined with confocal laser scanning microscopy (CLSM) to analyze bacteria viability.

In Chapter 5, a discussion of the effects of HPT and PDA on the microstructure and the hardness evolution of the studied materials is presented. The differences between the microstructure, composition, texture of each material are discussed in relation to their processing history and the resulting hardness evolution. The effects of HPT and PDA on the microstructural and hardness evolution of the Zn-3Mg alloy and the Zn-3Mg hybrid are also discussed. In addition, hardness was plotted as a function of accumulated strain to investigate the strain hardening capability during HPT, and this is the first time that such work has been reported for HPT hybrids. Based on the H-m relationship obtained from nanoindentation after HPT + PDA, a plastic deformation model leading to the suggested enhanced strength-ductility was proposed to explain the roles of the different domains observed in the heterogeneous microstructure. From the *in vitro* work, the uniform degradation behavior of the ZnP sample is discussed in relation to its enhanced corrosion resistance. The increased cell viability of the tested samples, in particular, that of the Col-AgBGN sample, is discussed in relation to their ionic release. Lastly, the characteristics of bacteria attached to the sample surfaces are related to their live/dead ratios and discussed together with the viability of planktonic bacteria.

In Chapter 6, the conclusions are presented, and potential future work is suggested. It is expected that the microstructural and micro-mechanical characterization of the Zn-Mg HPT hybrid system, as well as the *in vitro* studies performed in this research, will serve future researchers to continue gaining insights and making progress in this area.

2. BACKGROUND AND LITERATURE REVIEW

2.1. Zinc-based absorbable alloys for biomedical applications

This section summarizes the current state-of-the-art pertaining to absorbable Zn-based alloys, as well as the future challenges and opportunities facing Zn-based alloys with respect to satisfying the demanding clinical benchmark for absorbable medical applications. An overview of their biocompatibility, both *in vitro* and *in vivo*, as well as their microstructures and mechanical properties, are presented.

2.1.1. Biocompatibility of absorbable Zn-based alloys

Zn plays a fundamental role in multiple functions in the human body, including cell division, cell growth, and wound healing [26]. Moreover, Zn deficiency has been linked to the impairment of physical growth and development in infants and young adults, a greater risk of infection, a loss of cognitive function, memory, and behavioral problems, as well as learning disability [27,28]. For mature adults, the recommended daily intake (RDI) of Zn is 8-20 mg/day, which is lower than that for Mg (240-420 mg/day) and similar to that for Fe (8-18 mg/day) [29]. An excess of Zn above the recommended daily intake (RDI) may cause toxicity and detrimentally affect different organs, such as the brain, heart, and liver, or systems like the respiratory, epidermal, skeletal, and immune systems [18]. Zn is mainly found in animal proteins, nuts, whole grains, legumes, and yeast, and it is released from food as free ions that are absorbed in the small intestine [30]. Zn is mainly present in the human body as Zn^{2+}, and its optimal concentration in eukaryotic cells is about 10 ng/L. Apoptosis (i.e., cell death) can be triggered when Zn levels fall below 0.06 ng/L, whereas toxic effects can be induced when Zn levels rise above 60 ng/L [31]. Despite the toxicity concern, Zn is relatively harmless compared to other metal ions, and healthy individuals are at a higher risk

of suffering from Zn deficiency than from Zn intoxication [14], since only high Zn overdoses (i.e., 10 times greater than the RDI dose) generally lead to acute toxicity [32]. In fact, Zn supplements are often prescribed by physicians to meet the minimum RDI dose and prevent consequences associated with Zn deficiency [33]. In light of the development of absorbable Zn-based implants, the release of Zn^{2+} ions during degradation must be considered as an extra source of Zn, and maintained within the physiological levels mentioned above to ensure adequate tissue regeneration.

After implantation of Zn-based materials, Zn^{2+} is released to the bloodstream, coming into contact with different types of cells, whose interactions influence cell adhesion, viability, proliferation, differentiation, and gene expression [34]. The cytocompatibility of Zn and Zn-based alloys have been studied, both *in vitro* and *in vivo*, as they are being targeted for future applications as bone implants and vascular implants.

In an *in vitro* cytotoxicity evaluation of absorbable Zn-3Mg (wt%), Murni et al. [35] reported that the alloy extract at a concentration of 0.75 mg/mL (0.49 ppm Zn and 10.75 ppm Mg) exhibited adjustable cytotoxic effects on human osteoblast cells. In a comparative study of Zn exposure to three vascular cell types, Shearier et al. [36] determined the LD_{50} values (i.e., lethal dose that causes the death to 50% of the cells or animals in a study) of 50 μM for human dermal fibroblast (3.5 ppm), 70 μM for human aortic smooth muscle cells (4.5 ppm), and 265 μM for human endothelial cells (17.5 ppm). This demonstrated a dose-dependent effect of Zn on cell spreading and migration, suggesting that both adhesion and cell mobility may be hindered by free Zn^{2+} above a certain threshold. Similar concentration-related effects in different cellular environments have been reported in other works. For example, Krones et al. [37] reported that a Zn^{2+} concentration of 5.4 μM significantly increased cell viability and proliferation of pig pulmonary artery

endothelial cells, whereas 153.8 μM inhibited both cellular responses. Similarly, Ma et al. [38] showed that concentrations of Zn^{2+} below 80 μM promoted cell viability, proliferation, adhesion, and migration of human coronary artery endothelial cells, whereas higher Zn^{2+} concentrations led to opposite cellular responses. Interestingly, Zhu et al. [39] investigated the biological responses of human bone marrow mesenchymal cells (hMSC) to Zn and found that Zn exposure significantly enhanced hMSC growth, osteogenic differentiation, extracellular matrix production, and mineral deposition. The outcome of the latter work is particularly important since hMSC was the cell line used for the *in vitro* cell work in this dissertation. In addition to the beneficial effects of Zn^{2+} for different cell lines at specific concentrations, the antibacterial potential or Zn^{2+} has been also identified in several Zn alloys against pathogens related to implant sepsis failure, such as *E. coli*, *P. aeruginosa*, and *S. aureus*. The ability of Zn^{2+} to bind with bacterial DNA and to damage the bacterial membrane, assist Zn-based alloys in fighting bacteria colonization and biofilm formation [40,41].

Animal studies have shown the outstanding *in vivo* biocompatibility of Zn-based implants, both in bone tissues and vascular tissues, as observed in Figure 2 (a-c) and (d-f), respectively. The following works show examples of bone tissue implants. Xiao et al. [42] performed implantations of pure Zn and Zn-0.05Mg (wt%) in a rabbit femoral shaft and showed a uniform degradation rate with no inflammatory response for up to 6 months (Figure 2 (a)). New bone tissue formation was observed at the bone/implant interface, and strong antibacterial activity was found against *E. coli* and *S. aureus* [42]. After inspection of the *in vivo* degradation behavior of Zn pins implanted in rat femur condyle for 1 month, Su et al. [43] reported that the corrosion products formed a segmental layer, not uniformly distributed over the implant surface (Figure 2 (b)). This was related to the mixed static/circulation conditions of the bone tissue environment. Upon implantation of

Zn-1X (wt%) (X = Mg, Ca and Sr) pins in a mouse femoral shaft for up to 2 months (Figure 2 (c)), Li et al. [44] showed that the pins induced osteogenesis (i.e., new bone formation and remodeling) and no inflammation was observed around the surgical site [44].

In order to assist the *in vivo* evaluation of absorbable vascular devices, Pierson et al. [11] proposed a simplified approach consisting of inserting a wire through the blood vessel, thereby simulating the service conditions of a stent. Bowen et al. [45] examined the degradability of pure Zn wire in the abdominal aorta of rats and showed that the wire remained intact for 4 months before the corrosion rate accelerated. The corrosion products, which consisted of Zn oxide interspersed in Zn carbonate (Figure 2 (d)), did not provoke restenosis (i.e., narrowing of the vascular vessel) [45]. Furthermore, a correlation between the *in vivo* corrosion of a pure Zn stent implanted in rabbit abdominal aorta and the artery healing process was reported by Yang et al. [46] for a 12 month implantation study (Figure 2 (e)). A uniform corrosion layer between the Zn stent surface and the vascular lumen tissue after 1 month implantation in abdominal rabbit aorta was observed by Su et al. [43] (Figure 2 (f)). No additional connective tissue was found at the material-host interface, indicating excellent biocompatibility of the Zn stent.

Overall, *in vitro* and *in vivo* studies of Zn and Zn-based alloys have demonstrated a promising physiological response, which may able to overshadow the detrimental side effects associated with permanent implants (i.e., stress shielding, trace metal accumulation in the surrounding tissue, and the need of a second surgery for implant removal/replacement). Therefore, Zn and Zn-based alloys exhibit potential to be used as the next generation of absorbable biomedical implants for both bone and vascular applications. However, some inconsistencies between *in vitro* and *in vivo* degradation mechanisms and biocompatibility of Zn, as well as the effect of different microenvironments, have yet to be completely understood [36].

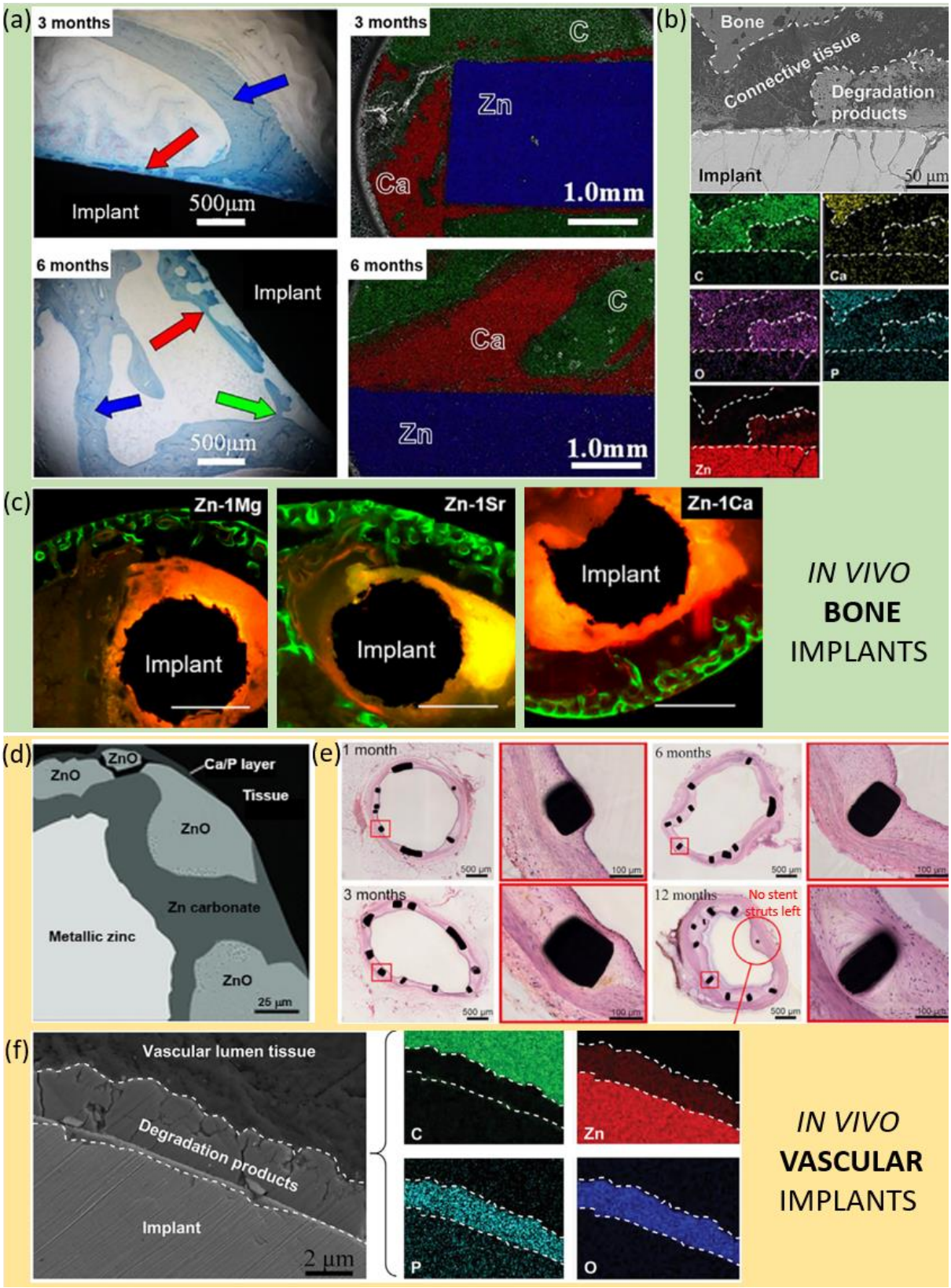

Figure 2: Examples of *in vivo* Zn-based bone implants (green background) and vascular implants (yellow background) reported in the literature.

Figure 2 (cont'd)
(a) histological section and elemental distributions of Zn implanted in a rabbit femoral shaft for 3 and 6 months (blue arrows indicate original cortical bone, red arrows indicate newly formed bone and green arrow indicate the interface between original and newly formed bone), (b) cross-sectional BSE view and corresponding elemental mapping of a Zn pin after 1 month implantation in a rat femur condyle, (c) histological section of a mouse femoral shaft from Zn-1Mg, Zn-1Sr and the sham control group after 2 months implantation under fluorescent microscopy (green fluorescence indicates new bone formation, scale bar: 500 um, (d) cross-sectional BSE view of a Zn wire after implantation in an abdominal aorta of a rat for 4.5 months, (e) histological sections of abdominal aorta after 1, 3, 6, and 12 months implantation of Zn stents, (f) cross-sectional BSE view and corresponding elemental mapping of Zn stent after 1 month implantation in a rabbit abdominal aorta. Adapted from [42–46].

2.1.2. Microstructures of absorbable zinc-based alloys

Most commercial Zn-based alloys belong to two categories based on the Zn-Al system: ZA (Zn-Al) and Zamak (Zn-Al-Mg-Cu) alloys [47]. Despite the wide selection of alloys having good mechanical and corrosion properties, the alloys targeted for biomedical application must be designed with non-toxic elements. Consequently, ZA and Zamak alloy series cannot be used as they contain large amounts of Al, which is considered potentially toxic by the FDA [48], as it has been reported to be harmful to osteoblasts and neurons [49], and also associated with dementia [50] and Alzheimer disease [51]. Acceptable alloying elements used for developing biomedical Zn-based alloys include nutrient elements present in the bone matrix (e.g., Mg, Ca, and Sr) and other essential elements in different human physiological activities (e.g., Cu and Mn). A summary of the microstructures reported from Zn-based alloys targeted for medical purposes is given below, in relation to the region of interest in their corresponding equilibrium phase diagrams, see Figure 3.

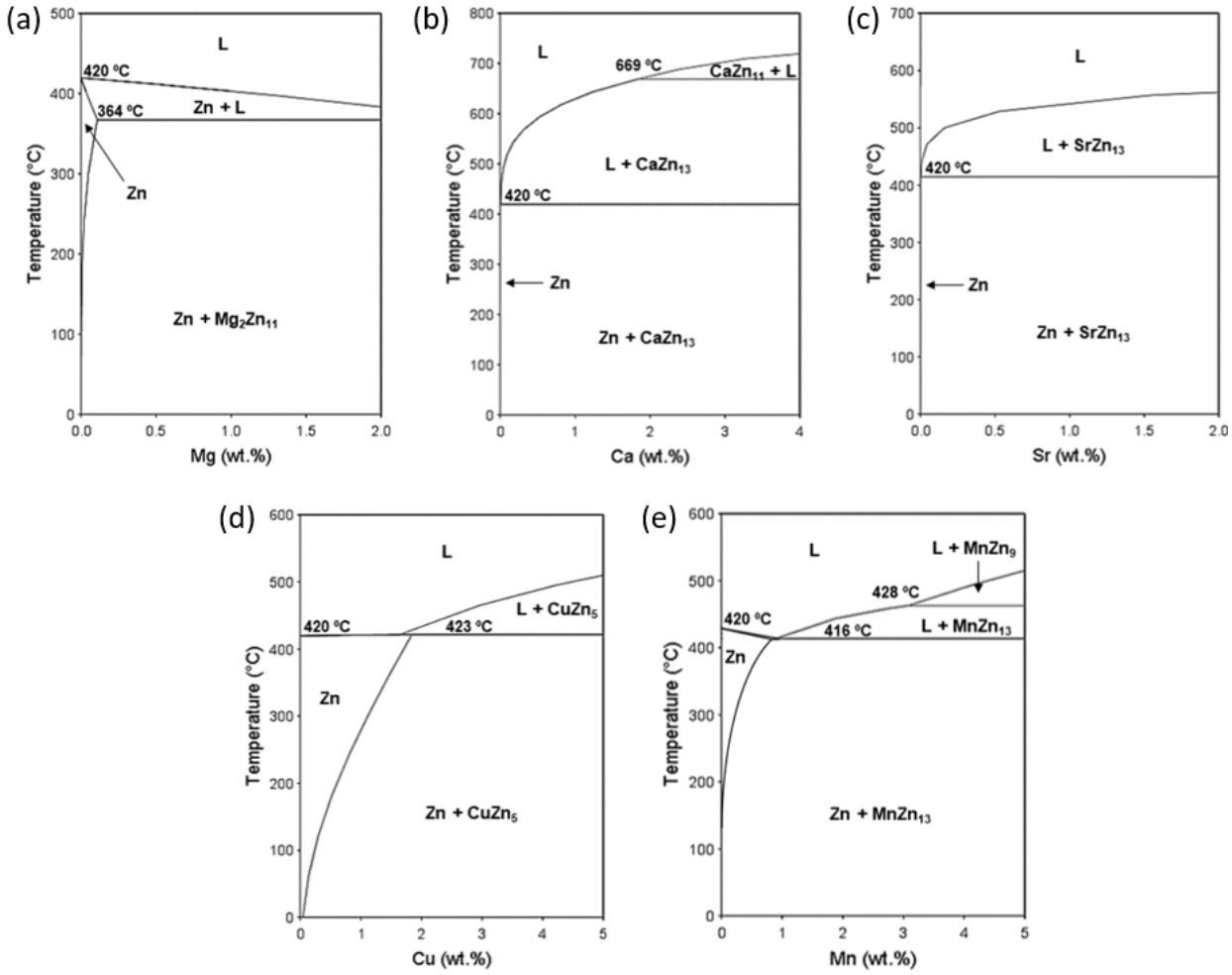

Figure 3: Equilibrium binary phase diagrams showing regions of interest for the development of Zn-based absorbable alloys: (a) Zn-Mg, (b) Zn-Ca, (c) Zn-Sr, (d) Zn-Cu, and (e) Zn-Mn. Adapted from [18,52]

According to the portion of Zn-Mg phase diagram shown in Figure 3 (a), the maximum solubility of Mg in Zn is about 0.1 (wt. %) at 364 °C, and it becomes nearly negligible at RT. Consequently, minimal additions of Mg to Zn lead to the formation of the Mg_2Zn_{11} intermetallic compound. Mostaed et al. [53] synthesized Zn-xMg alloys (x = 0.15, 0.5, 1 and 3 wt. %) by casting at 500 ºC, and annealing at 350 ºC followed by water quenching for microstructural homogenization. The resulting alloys were extruded to obtain mini-tubes with similar dimensions to real vascular stents. As expected from the Zn-Mg phase diagram, the microstructures of hypoeutectic Zn-0.15Mg, Zn-0.5Mg, and Zn-1Mg alloys consisted of Zn grains embedded in a eutectic matrix of Zn and

Mg_2Zn_{11}, whereas the eutectic Zn-3Mg alloy exhibited a fully-eutectic microstructure with alternate Zn and Mg_2Zn_{11} lamellae. Increasing the Mg content in the former Zn-Mg alloys led to a decrease in grain size [53], which was consistent with the trend reported by Jin et al. [54] from extruded and drawn Zn-Mg alloys containing 0.08, 0.005, and 0.002 (wt. %) Mg. Further additions of Ca and Sr to the Zn-Mg system led to finer grain sizes and more homogenous microstructures containing additional precipitates phases, namely $CaZn_{13}$ and $SrZn_{13}$ [17,55].

As observed in the portion of the Zn-Ca and Zn-Sr phase diagrams presented in Figure 3 (b) and (c), respectively, neither Ca nor Sr are soluble Zn, such that small additions of Ca to Zn and Sr to Zn lead to the formation of $CaZn_{13}$ and $SrZn_{13}$ intermetallic phases, respectively. The Zn-1Ca and Zn-1Sr (wt. %) alloys were studied by Li et al. [44], who reported that the as-cast microstructures consisted of Zn dendrites in a eutectic matrix of Zn and $CaZn_{13}$ for the Zn-Ca alloy, and Zn and $SrZn_{13}$ for the Zn-Sr alloy. Further additions of Sr to the Zn-1Ca alloy and subsequent extrusion and rolling produced a more homogenous and fine-grained microstructure [17].

Based on the portion of the Zn-Cu phase diagram shown in Figure 3 (d), Cu has a maximum solubility of about 2 (wt. %) in Zn at 423 ºC, and at that composition-temperature combination, an eutectic reaction forms a mixture of the Zn and $CuZn_5$ phases. Binary Zn-xCu (x = 1, 2, 3, and 4 wt. %) alloys were investigated by Tang et al. [56] and Niu et al. [16] for absorbable cardiovascular applications. The as-cast microstructures consisted of dendritic $CuZn_5$ phase embedded in a primary Zn matrix, with an increasing dendritic volume fraction at higher Cu concentrations. Small additions of Mg to the Zn-Cu system resulted in a more homogeneous and fine-grained microstructure containing $CuZn_5$ and Mg_2Zn_{11} phases [57].

Lastly, according to the portion of the Zn-Mn phase diagram presented in Figure 3 (e), Mn has a maximum solubility of 0.8 (wt. %) in Zn at 416 ºC, and a solid solution of the Zn and $MnZn_{13}$ intermetallic phases forms at that temperature due to an eutectic reaction. Sun et al. [58] obtained Zn-xMn binary alloys (x = 0.2, 0.4, and 0.6 wt. %) and reported that the Zn-0.2Mn alloy showed only Zn-rich phases, whereas the $MnZn_{13}$ intermetallic phase was identified in the Zn-0.4Mn and Zn-0.6Mn alloys. Sotoudeh Bagha et al. [59] fabricated biocompatible Zn-xMn (x = 4, and 24 wt. %) alloys via powder metallurgy and reported microstructures consisting of nano-sized crystallites with $MnZn_{13}$ and $MnZn_3$ second phases.

2.1.3. Mechanical properties of absorbable Zn-based alloys

Naturally, there is not an ideal combination of mechanical properties (i.e., YS, UTS, εf, hardness, etc.) that can satisfy the demands of all absorbable implant devices. Thus, the desired set of mechanical properties is application-specific and can differ significantly among different applications. For example, the desired mechanical requirements of absorbable metal stents proposed by Bowen et al. [45] were: YS > 200 MPa, UTS > 300 MPa, and εf > 18%. The inherently poor mechanical properties of as-cast Zn (i.e., UTS < 20 MPa, εf < 0.5% [17]) are well below the mechanical benchmark for vascular stents, and presumably also for other load-bearing biomedical applications. Therefore, the mechanical properties of pure Zn have been improved by two main routes: alloying and thermomechanical processing.

Alloying is typically the preferred choice to enhance the mechanical properties through solid solution strengthening and precipitation hardening. Nevertheless, the effect of thermomechanical processing on the mechanical properties of Zn-based alloys has also been extensively explored in the literature. Traditional wrought processes like rolling, extrusion, and drawing, as well as

advanced metal forming techniques such as hydrostatic extrusion and equal-channel angular pressing, have been studied. The mechanical properties of absorbable Zn-based alloys subjected to different thermomechanical processes were tabulated in a recent review article [18]. The plots in Figure 4 (a) and (b) aim to provide a visual representation of the effects of alloying and the processing method, respectively, on the resulting mechanical properties of Zn-based alloys.

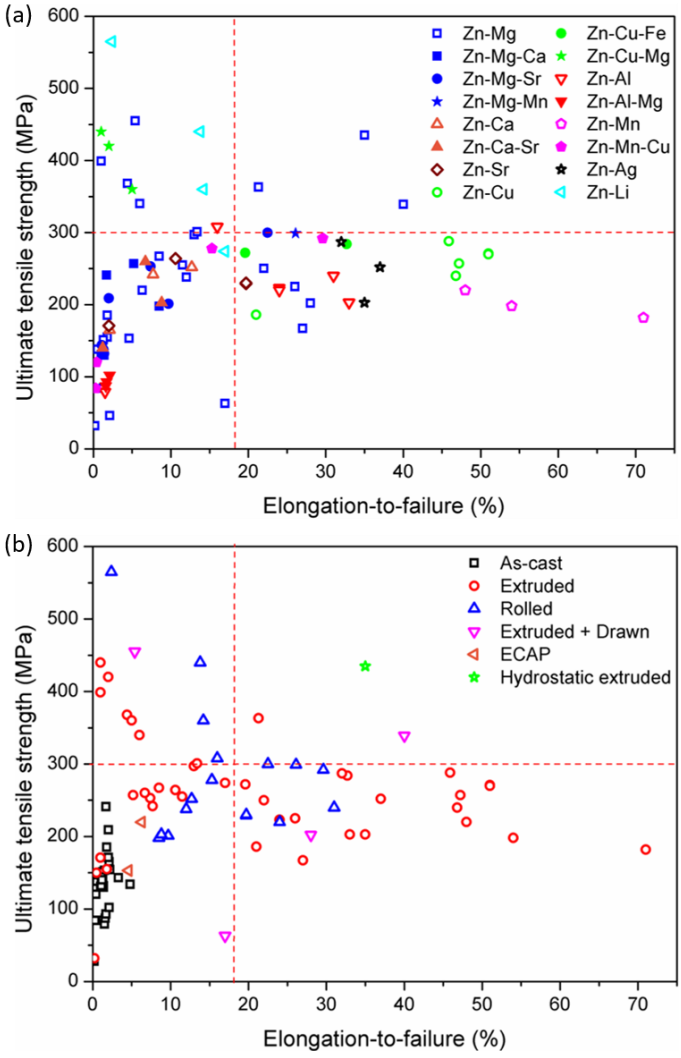

Figure 4: Plot of UTS vs. ε_f from absorbable Zn-based alloys (a) as a function of the alloying elements and (b) as a function of the processing method. All plotted values correspond to the references given in Table 2 of [18]. Red dashed lines indicate the mechanical benchmark values for absorbable vascular devices (i.e., UTS = 300 MPa, ε_f =18%), such that the top-right quadrant of the plot contains alloys fulfilling both criteria. Note that open symbols in (a) represent binary systems, and filled symbols of the same color represent associated ternary systems. Note also that symbols of different colors in (b) refer to different processing techniques. [18]

Alloying with Mg was reported to have the greatest impact on enhancing the UTS, whereas Mn and Cu alloying led to the highest ε_f values for the absorbable Zn-based alloys studied [18]. As observed in Figure 4 (a), only three Zn-Mg alloys (containing between 0.1-1.2 wt.% Mg) exceeded the mechanical benchmark established for vascular implant materials [45], suggesting that Zn-Mg binary alloys are, to date, the best candidates from the mechanical standpoint. Regarding the influence of the number of alloying elements, the addition of any new element to a Zn-X binary alloy, given the same processing conditions, generally increased the UTS but decreased the ε_f. Similarly, increasing the alloy content also led to an increased UTS at the expense of ε_f [18].

Overall, thermomechanical processing (i.e., extrusion, rolling, drawing) led to a better combination of mechanical properties (i.e., higher UTS and ε_f) as compared to their as-cast counterparts. For instance, the UTS and ε_f of as-cast Zn-1Sr [44] were simultaneously enhanced from 171 MPa and 2%, to 264 MPa and 10.6% by hot- extrusion, and to 230 MPa and 19.7% by hot-rolling [18]. As observed in Figure 4 (b), the three Zn-Mg alloys fulfilling the mechanical benchmark were processed by extrusion, extrusion + drawing, and hydrostatic extrusion. Therefore, extrusion-based techniques were deemed as the most effective deformation processes to increase the mechanical properties of Zn-based alloys [18].

Ultimately, it should be emphasized that temporary medical devices, such as stents, wires, pins, plates, or screws, may differ significantly in terms of their morphology, mechanical constraints, and desired degradation rates. Consequently, it is essential to identify the mechanical requirements on a case-by-case basis and account for the progressive deterioration of the mechanical properties as the implantation time advances to prevent catastrophic failure of the implant during service.

2.1.4. Research gaps and novel strategies for the design of absorbable Zn-based alloys

Future absorbable Zn-based implants may not only overcome the serious concerns associated with permanent implants (i.e., stress shielding, trace metal accumulation on surrounding tissues, the need for a second surgery for implant replacement/removal), but also outperform the absorbable metals currently used for temporary applications (i.e., Mg and Fe alloys) [18]. Although a large number of *in vitro* and *in vivo* works have shown potential for Zn-based alloys, further research is needed before they can be considered for absorbable medical implant devices.

To date, the majority of research works have focused on conventional processing techniques, such as extrusion or rolling, in which considerable knowledge has been established over the years. However, as noted from Figure 4, the best combination of UTS and ε_f was achieved by hydrostatic extrusion, which belongs to the family of severe plastic deformation (SPD) techniques. SPD processing offers the opportunity to overcome the so-called "paradox of strength and ductility" [21] by producing materials with ultrafine-grained microstructures that have been associated with a simultaneous enhancement of the UTS and ε_f [20,21,60,61]. Nevertheless, few studies have reported SPD-processed materials suitable for absorbable medical applications; hence, this is an avenue to be explored. In this dissertation, Zn-xMg (x = 3, 10, 30 wt. %) materials were investigated for the first time after processing by HPT, which is considered the most promising SPD technique in terms of grain refinement. The hypothesis is that the microstructural refinement during HPT can significantly improve the strength of the different Zn-Mg compositions evaluated.

Bowen et al. [45] sparked the interest in Zn-based alloys for temporary implant applications in 2013 after their article "Zinc exhibits ideal physiological corrosion behavior for bioabsorbable stents". Ever since, multiple studies have consistently demonstrated the promising potential of Zn

and Zn-based alloys for bone and vascular implant applications for a wide variety of animal models, as summarized in section 2.1.1. However, most *in vitro* works identified a concentration-dependent effect of Zn^{2+} on cell behavior (i.e., adhesion, viability, proliferation, and differentiation), above which the Zn or Zn-based materials were cytotoxic. This contradicting phenomenon between *in vivo* and *in vitro* may result from radically different Zn^{2+} concentrations between both types of tests. Based on the current studies, it is suggested that the static conditions of *in vitro* tests facilitate the accumulation of Zn^{2+} at the cell culture, whereas the *in vivo* dynamic conditions (i.e., continuous blood flow) allows for a distribution of Zn^{2+} through the bloodstream, leading to a significantly lower Zn^{2+} concentration at the implantation site.

In addition, as mentioned earlier, the RDI of Zn is relatively low compared to that of Mg, such that rapid degradation of the Zn-based implant could lead to systemic toxicity. Thus, controlling the burst release of Zn^{2+} could be key to minimize the risk of Zn toxicity, and one way to do this is by designing coatings able to tune the degradation rate. Therefore, in this dissertation, a zinc phosphate (ZnP) coating was developed on a Zn-3Mg (wt. %) substrate with the goal of reducing the corrosion rate; hence, decreasing the Zn^{2+} release rate and enhancing the *in vitro* biocompatibility. Additional coatings containing collagen (Col) were synthesized for promoting cell adhesion, and the latter was combined with ZnP giving a ZnP-Col coating with the idea to obtain the dual effect of both individual coatings. Lastly, a coating based on Ag-doped bioactive glass nanoparticles (AgBGN) was obtained with the aim of improving the biocompatibility and antibacterial properties simultaneously.

2.2. Processing of metal hybrids by high-pressure torsion

This section highlights the potential of SPD processing techniques before focusing on the HPT method. The use of HPT principles to synthesize different types of metal hybrids is then presented, followed by a summary of their microstructural characteristics and mechanical properties.

The application of SPD methods is today a well-established strategy for the fabrication of bulk ultrafine-grained (UFG) materials having grain sizes within the nanometer (10-100 nm) and sub-micrometer (100-1000 nm) ranges [62]. SPD processes encompass a series of metal forming techniques, in which large plastic strains are applied through high hydrostatic pressure, usually at RT, leading to accumulated strains > 4-6 [20]. Some of the major advantages of SPD methods are their ability to produce significant grain refinement without changing the overall dimensions of the sample. The resulting UFG microstructures, characterized by large volume fractions of high-angle grain boundaries (HABs), are ultimately responsible for the unique physical, mechanical and functional properties of SPD-processed materials, and are difficult to obtain from traditional deformation methods [63].

The scope of traditional thermomechanical processes, such as rolling, extrusion, forging, swaging, and drawing, is often limited by the strength-ductility tradeoff typically observed in engineering materials, which may be strong or ductile, but rarely both at once [61]. Unlike these deformation processes, SPD-processed materials with high fractions of HABs are considered interface-controlled materials [20] and have demonstrated superior mechanical properties (i.e., UTS, ε_f, fatigue, hardness, superplasticity) [64–67] and functional properties (i.e., electrical conductivity, magnetic resistance, hydrogen storage, superconductivity) [68–72] in a wide range of UFG metals and alloys.

2.2.1. High-pressure torsion: principles, equations, and hybrid systems

High-pressure torsion (HPT) [73] is one of the most established SPD processes, together with equal-channel angular pressing (ECAP) [74] and accumulative roll bonding (ARB) [75]. The foundations of HPT granted Bridgman the Nobel prize in 1946 [73], and it is considered the most efficient SPD technique in terms of grain refinement. During HPT, a disk-like shaped specimen (typically 10 mm diameter and 1 mm thickness) is subjected to a large hydrostatic pressure (usually 6 GPa) and severe torsional straining simultaneously, as shown schematically in Figure 5 (a). In this unconstrained HPT setup, the lack of lateral constraints prevents a uniform applied pressure, thereby leading to a continuous decrease in sample thickness during processing, as observed in Figure 5 (c).

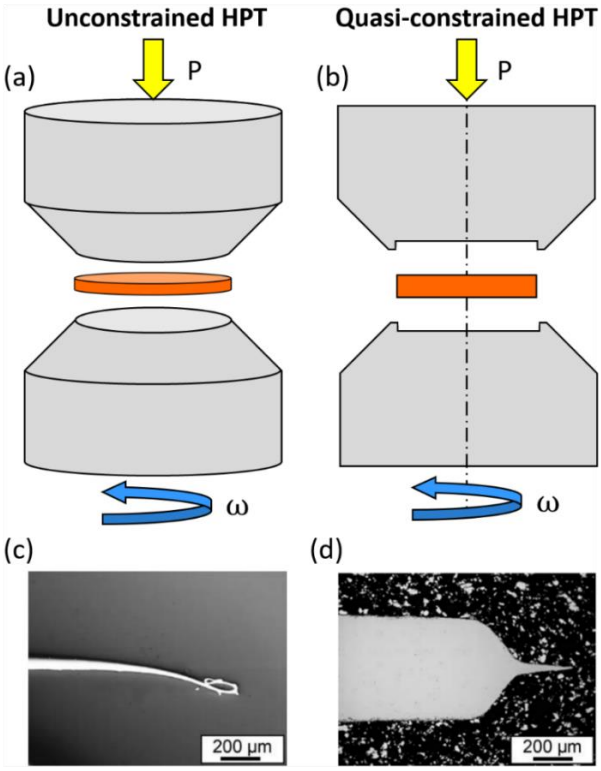

Figure 5: Schematic set up of (a) unconstrained HPT and (b) quasi-constrained HPT, where P indicates the applied pressure and ω indicates the rotational speed. The appearance of the peripheral cross-section of samples produced by (c) unconstrained HPT applied to pure Cu for 5 turns and (d) quasi-constrained HPT applied to pure Fe for 5 turns. Adapted from [76].

In contrast, a constrained version of HPT would theoretically lead to pure torsion deformation under hydrostatic pressure without altering the sample geometry. However, such an idealized constrained setup assumes a frictionless condition at the sample, which is practically impossible to achieve in real conditions [77]. Thus, quasi-constrained HPT, such as that sketched in Figure 5 (b), which includes a cylindrical cavity in each anvil that is slightly shallower than the sample, is the most frequently used setup. As a result, a small amount of material flows out of this cavity, as shown in Figure 5 (d), ensuring a uniform sample thickness over the majority of the sample diameter under a nearly ideal hydrostatic pressure during torsion [76].

The concurrent action of compressive and shear stresses introduces a significant amount of point and line defects within the specimen, which enhances atomic diffusion even at RT [78]. As shown in Equation 1, the shear strain (γ) in the disk specimen during HPT can be expressed in terms of the number of rotations (N), the distance from the center of the disk (r), and the disk thickness (h) [79]. The equivalent Von Mises strain (ε_{eq}) can be then calculated using Equation 2 for $\gamma < 0.8$, and Equation 3 for $\gamma \geq 0.8$ [80,81]:

$$\gamma = \frac{2\pi Nr}{h} \qquad \text{Equation 1}$$

$$\varepsilon_{eq} = \frac{\gamma}{\sqrt{3}} = \frac{2\pi Nr}{h\sqrt{3}} \quad (\text{for } \gamma < 0.8) \qquad \text{Equation 2}$$

$$\varepsilon_{eq} = \left(\frac{2}{\sqrt{3}}\right) \ln\left[\sqrt{\left(1 + \frac{\gamma^2}{4}\right)} + \frac{\gamma}{2}\right] \quad (\text{for } \gamma \geq 0.8) \qquad \text{Equation 3}$$

Despite the significant grain size refinement achieved by HPT, often to the nanoscale range (1-100 nm), the resulting strengthening increase is limited by a steady-state regime reached at strain

values of about 8-10 [82]. Thereby, the saturation of grain size refinement, which results in an increase of strength and hardness during HPT, has been demonstrated in multiple metals and alloys with homogenous microstructures before HPT processing [83–85]. Consequently, in an attempt to delay the saturation regime and promote additional strengthening mechanisms, HPT principles have been used to promote solid-state reactions between dissimilar metals through direct mechanical bonding at RT. The feasibility of this approach to synthesize HPT metal hybrids has been investigated in numerous metal systems, including Al-Cu [86–88], Al-Mg [25,89–95], Al-Fe [25], Al-Ti [25], Cu-Ta [96], Fe-V [97,98], and V-Zr [99]. These HPT hybrids are defined as metal-based composites, comprised of at least two elements, whose final properties are determined by their unique UFG microstructures achieved through mechanical bonding of dissimilar bulk metals by HPT processing.

Despite the promising mechanical properties reported from the above-mentioned HPT hybrid systems, none of them are appropriate for absorbable biomedical implant applications due to their toxicity. Therefore, the same experimental approach was used to explore the Zn-Mg HPT hybrid system in this dissertation, with the goal of improving the mechanical properties beyond those reported from current absorbable Zn-based alloys, which were summarized in section 2.1.3.

2.2.2. Synthesis of HPT metal hybrids: origin, limitations, and latest trends

This section describes the origin of the mechanical bonding of dissimilar bulk metals via HPT, the different sample formats used to obtain HPT hybrids, current limitations associated with the HPT processing, and the latest trends for synthesizing metal hybrids using HPT.

The idea of mechanically bonding different metals via HPT originated from the experimental setup used in ARB, which is a popular SPD technique that was introduced at the beginning of section 2.2.1. In ARB, a single multilayered metal sheet can be produced from individual metal sheets stacked on top of each other, which are rolled, cut in half, restacked, and rolled again for multiple cycles. One disadvantage of the ARB process is that it requires continuous supervision during processing to ensure good material bonding (i.e., surface brushing and decontamination between rolling cycles). Thus, despite its feasibility to produce UFG multilayered metal hybrids, the inherent microstructural and mechanical anisotropy between the rolling and transverse planes of ARB sheets [100] motivated the research of alternative SPD processes capable of overcoming the latter issues. The accumulated plastic strain during HPT is generally higher than that for ARB [101], thereby resulting in a more efficient production of metallic hybrids at RT.

Unlike that for conventional HPT processing of pure metals and alloys, where a single disk is used (Figure 6 (a)), the fabrication of HPT hybrids offers a wide variety of sample formats, like those sketched in Figure 6 (b-d), for obtaining tailored microstructures and mechanical properties. The feasibility to produce mechanical bonding between dissimilar bulk metals through HPT at RT was first demonstrated by two independent research groups in 2011: Sun et al. [102] (through the combination of Cu/Zr, Cu/Ni, and Cu/Ag half disks) and Miyazaki et al. [103] (through the combination of Ag/Ni and Nb/Zr half disks). Both groups used the experimental setup illustrated

in Figure 6 (c). The combination of four alternate quarter disks of Al-6061 alloy and Cu, as seen in Figure 6 (b), was reported by Bouaziz et al. [104], where 1 turn under 2.5 GPa resulted in the joining of the two materials into a single bulk disk with an average grain size (GS_{ave}) ranging between 100-200 nm. Solid-state reactions at RT were reported from HPT hybrids for the first time by Oh-ishi et al. [86] from mechanical bonding of two alternate Al and Cu half disks (Figure 6 (c)) after 1, 10, and 100 turns with 6 GPa. The previous work [86] led to the formation of nanoscale Al-Cu intermetallic phases, namely Al_2Cu, AlCu, and Al_4Cu_9, as well as the dissolution of Al in the Cu matrix due to the enhanced atomic diffusion. The former studies demonstrated that HPT was not only capable of successfully achieving mechanical bonding between different metals and alloys into compact samples, but also imposing significant microstructural changes. However, given the complexity associated with the arrangement of the quarter-disks and half-disks in the HPT anvils before processing, alternative less-complex sample formats were investigated.

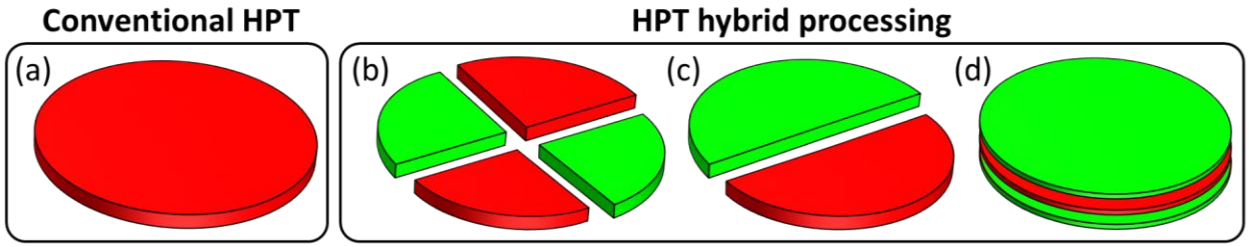

Figure 6: Sample formats used in (a) conventional HPT and (b-d) HPT hybrid processing: (b) quarter-disk, (c) half-disk and (d) stack-disk.

A more straightforward approach to producing HPT hybrids was introduced by Ahn et al. [95] in 2015, which consisted of stacking different metal disks without any surface adhesion or brushing treatment prior to HPT processing. This sample format was developed for three metallic disks stacked in an A/B/A sequence, where the top and bottom material (A) was different from that in the center (B), as sketched in Figure 6 (d). The first HPT hybrid system that was processed using

this format was the Al-Mg, and was subjected to 6 GPa for 5, 10, and 20 turns. Similar to the Al-Cu HPT hybrid system mentioned earlier, the resulting Al-Mg HPT hybrids exhibited a nanosize-grained structure containing nanoscale Al-Mg intermetallic compounds, namely Al_3Mg_2 and $Al_{12}Mg_7$ [95]. After this study demonstrated the combined potential of HPT and the multilayered approach to producing bulk hybrid samples containing UFG microstructures with a relatively simple experimental setup, several other metal systems have been explored. The HPT hybrid systems investigated to date using this sample format were the ones mentioned earlier, namely Al-Cu [86–88], Al-Mg [25,89–95], Al-Fe [25], Al-Ti [25], Cu-Ta [96], Fe-V [97,98], and V-Zr [99]. The stacking approach in Figure 6 (d) is now routinely used to produce metallic hybrids due to their versatility and adaptability for use by almost all metal systems without the need for a binder. The ease of controlling the final composition, by adjusting the thickness and/or the number of the disks in the stacking sequence, makes HPT an attractive approach for synthesizing this type of metal hybrids.

Nevertheless, one of the main disadvantages of the HPT-processed samples is their limited dimensions, which typically are 10 mm in diameter and 1 mm in thickness. Large applied pressures are required to prevent sliding between the sample and the anvils during torsional straining. Thereby, increasing the sample dimensions increases the forces required. After investigating the effect of the applied pressures, between 1 and 9 GPa, on HPT processing, Zhilyaev et al. [105] concluded that 6 GPa was reasonable to provide uniform grain sizes and hardness values across the HPT-processed sample, and thus, 6 GPa is now used in most studies. Moreover, two conditions must be met simultaneously in order to obtain HPT samples with uniform UFG microstructures. First, the saturation strain (i.e., strain value above which the grain size remains constant) must be achieved. Second, a certain thickness (t) to diameter (d) ratio, t/d, must be obtained to achieve both

axial and radial microstructural homogeneity. This ratio depends on the sample composition, and thus, cannot be universally applied to all materials [76].

In order to overcome the reputation of HPT as a merely academic curiosity, significant efforts over the last years have focused on upgrading the HPT machinery for producing larger samples. The torque required to enable torsional straining of the sample under fully plastic flow is proportional to d^3, where d is the sample diameter, such that more powerful motors are required for samples with larger dimensions. Consequently, the anvil diameters must be increased accordingly to withstand higher torques [77]. To date, the largest HPT-processed samples (60 mm diameter and 12 mm thickness) were produced using a machine with 10,000 kN maximum loading capacity and 130 kN·m maximum torque [106]. The feasibility of scaling up the dimensions of A/B/A type HPT hybrids was investigated recently in the Al-Mg system [94], and it was concluded that the microstructures and hardness of the upscaled samples (25 mm diameter and 2 mm thickness) were similar to those of the conventional samples (10 mm diameter and 1 mm thickness) after 10 and 20 turns. Other researchers have focused on adapting the HPT principles into novel techniques that enable continuous processing, which is key for industrial applications, while maintaining the exceptional grain refinement. Such efforts have resulted in the development of novel SPD techniques like high-pressure sliding [107], high-pressure compressive shearing [108], and continuous high-pressure torsion [109].

In addition to the sample formats described earlier to process HPT hybrids from mechanical bonding of bulk materials, other works have used HPT to consolidate materials in the form of powders [110] and machining chips [111]. In both cases, the material is filled into the cavity formed between the HPT anvils to produce compact samples. These setups enable a wide variety of compositions in powder form and the recycling of chips.

2.2.3. Microstructural evolutions of HPT-processed metal hybrids

This section presents the major microstructural transformations reported from different HPT hybrid systems, including grain refinement, the *in situ* formation of intermetallic phases and supersaturated solid solutions (SSSS), and the effect of PDA on the microstructure.

Processing of Al-Cu, Al-Mg, Al-Ti, and Al-Fe HPT hybrids at RT, using the stacking format sketched in Figure 6 (d), led to a good mechanical bonding of the metal disks into a compact sample after 1 single turn. Increasing torsional straining resulted in the interruption of the original multilayered structure, leading to an increased phase fragmentation and grain refinement for higher number of turns. In addition, for some metal systems, like Al-Cu and Al-Mg, the compositional mixing during HPT induced the *in situ* nucleation of intermetallic phases in the microstructure. However, other metal systems, like Al-Ti and Al-Fe, did not exhibit any phase transformation during HPT.

Al-Cu HPT hybrids have been synthesized at RT under 6 GPa, at 1 rpm, for 10, 20, 40, and 60 turns [87]. The microstructure analysis after HPT demonstrated an ultrafine-layered structure with a GS_{ave} ~ 80 nm after 20 turns, and an equiaxed microstructure with a GS_{ave} ~ 30 nm in the peripheral regions of the disk after 60 turns. However, relatively large Al-rich and Cu-rich phases were still present within the central regions of the disk after 60 turns, as observed in Figure 7 (a). Three different intermetallic compounds, namely Al_2Cu, AlCu, and Al_4Cu_9, were identified after 20 turns, as observed in Figure 7 (b), which gradually increased in volume fraction after 40 and 60 turns.

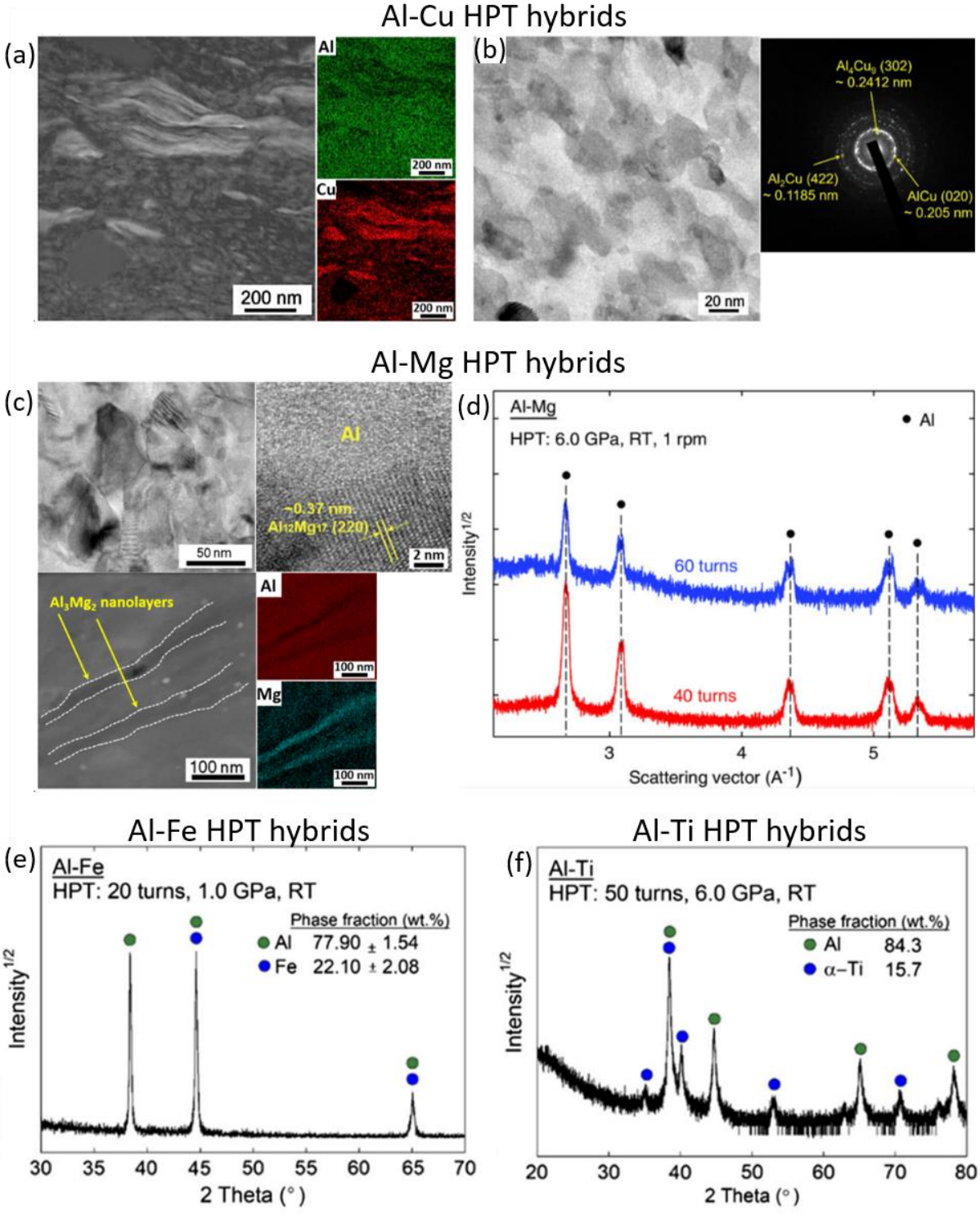

Figure 7: Microstructures of Al-Cu, Al-Mg, Al-Fe, and Al-Ti HPT hybrids. Al-Cu system after HPT for 60 turns: (a) SEM image with EDS elemental maps of Al and Cu, (b) TEM micrograph and corresponding SAD pattern; Al-Mg system after HPT for 10 turns: (c) TEM micrographs and corresponding EDS elemental maps of Al and Mg, (d) XRD patterns after 40 and 60 turns; XRD patters of the (e) Al-Fe system after 20 turns, and (f) Al-Ti system after 50 turns. Adapted from [25,87,91,95].

Al-Mg HPT hybrids have been processed at RT under 6 GPa, at 1 rpm, for 1, 5, 10, 20, 40, and 60 turns [91,95]. Microstructural analysis revealed a significant grain refinement after 5, 10, and 20 turns, with a GS_{ave} ~ 190 nm, ~ 90 nm, and ~ 60 nm, respectively. The disk after 10 turns exhibited two intermetallic compounds close to the peripheral regions: Al_3Mg_2 in the form of ~ 30 nm nanolayers and $Al_{12}Mg_{17}$ in the Al-rich matrix, which was in a SSSS state (see Figure 7 (c)). Further HPT processing for 40 and 60 turns resulted in a slight decrease of the GS_{ave} to ~ 40 nm and ~ 30 nm, respectively, and the dissolution of both Al_3Mg_2 and $Al_{12}Mg_{17}$ in the Al-rich matrix (see Figure 7 (d)). This was associated with an increased Mg concentration in the Al-rich matrix after 40 and 60 turns, which occurred due to enhanced diffusion of Mg in the intermetallic compounds.

The extreme grain refinement achieved in the Al-Cu and Al-Mg HPT hybrid systems, along with the nucleation of different intermetallic compounds, had a strong effect on their mechanical performance, as will be detailed in section 2.2.4. However, as mentioned earlier, the Al-Fe and Al-Ti HPT hybrids did not exhibit *in situ* formation of any intermetallic compound during HPT. This can be observed in the XRD patterns of the Al-Fe and Al-Ti HPT hybrids after 20 and 50 turns, respectively, which are depicted in Figure 7 (e) and (f). Consequently, hardness measurements in the Al-Fe and Al-Ti hybrid systems reached values consistent with the saturated hardness exhibited when both pure Fe and Ti were processed separately by HPT [25,112].

The previous works demonstrated that HPT processing of metal hybrids has the potential to drive the material far from equilibrium, allowing solubility levels and phase transformations not predicted by phase diagrams nor expected in equilibrium systems. Experimental observations revealed that severe sliding dramatically changes the material adjacent to the sliding interface, which is both structurally and chemically different from the bulk material [113]. Based on this, it

is hypothesized that the severe sliding between fragmented phases during the processing of HPT hybrids is responsible for the introduction of metastable phases, including intermetallic compounds and supersaturated phases, which are not typically observed in their homogenous equilibrium counterparts.

The major contributing factor to the formation of intermetallic compounds during mechanical bonding of dissimilar metals is the enhanced atomic diffusion achieved during HPT processing, which is due to a significant increase of point defects [114]. Different mechanisms involving enhanced atomic mobility have been proposed to explain the shear-induced chemical mixing in heterogeneous microstructures, similar to those observed in HPT hybrids [115,116]. For instance, an ECAP-processed Cu-Pb alloy demonstrated increased atomic mobility through the introduction of additional free volume in the form of non-equilibrium interfaces, vacancy clusters, nanovoids, and micropores [117]. An estimation of the diffusion coefficients of the Al-Cu HPT hybrids revealed that they were about 10^{12}-10^{22} times larger than those of lattice diffusion in the Al-Cu alloy system. Thus, this was suggested to be a critical factor for the *in situ* nucleation of Al_2Cu, AlCu, and Al_4Cu_9 intermetallic phases in the Al-Cu HPT hybrid system [86].

A recent review on deformation-induced supersaturation during HPT concluded that mechanical mixing was mainly influenced by the level of positive heat of mixing (i.e., energy required to mix two elements) and the deformation behavior [118]. The deformation process, which is in turn influenced by the strength differences between the different phases, was also proposed to affect the chemical mixing. Thus, large differences in strength between individual phases of the hybrid can lead to strong strain localization, thereby impeding mechanical mixing during deformation. Therefore, notable hardness differences between Al and Ti phases, as well as between Al and Fe

phases, may have contributed to the lack of chemical mixing in their respective HPT hybrid systems, hence, inhibiting the nucleation of additional intermetallic phases or SSSS.

The significance of PDA was demonstrated by Valiev et al. [119] to improve both the UTS and ε_f of nanostructured HPT-processed Ti after annealing at 300 ºC for 10 min. According to a later review [22], the main reason why PDA is an effective strategy to improve the overall ductility of a severely deformed material is associated with an ordering of the defect structures within the grain boundaries, resulting in a near-equilibrium state without significant grain growth. In addition, PDA was found to reduce the dislocation density in the grain interiors of the UFG materials, giving an opportunity to increase the dislocation storage capability during plastic deformation, hence, leading to higher ε_f values. The influence of PDA on the microstructural evolution and mechanical behavior of HPT hybrids was originally investigated by Han et al. [90] in the Al-Mg system by subjecting samples processed for 20 turns to 300 ºC for 1 h. The microstructural analysis near the disk edge revealed that the GS_{ave} increased from ~ 60 nm to ~ 380 nm after PDA. The equiaxed microstructure after PDA also contained $Al_{12}Mg_{17}$ and Al_3Mg_2 intermetallics and an Al-7Mg (at. %) solid solution phase. The authors concluded that HPT + PDA promoted the formation of a multicomponent Al-Mg hybrid system, which resulted in a simultaneous increase of the strain rate sensitivity from ~ 0 to 0.1, and thus, enhanced plasticity, while maintaining a reasonable hardness (~ 220 HV). This study [90] motivated the investigation of the effect of PDA on the microstructural and mechanical behavior of the Zn-Mg HPT hybrid system in this dissertation.

2.2.4. Mechanical properties of HPT-processed metal hybrids

The small dimensions of the HPT samples limit the broad-scale evaluation of their mechanical properties beyond microhardness and nanoindentation using standard testing geometries and procedures. Though several works have measured global mechanical properties like UTS, YS, and ε_f from tensile testing of miniature specimens taken from HPT-processed metals and alloys, no such data is yet available for multilayered HPT-processed hybrids in the literature. Considering the microstructural heterogeneity across the HPT hybrids, microhardness and nanoindentation have been deemed versatile techniques for testing the local mechanical properties, enabling the investigation of the plastic behavior in small volumes of the sample. Thus, this section summarizes the knowledge derived from the Vickers microhardness (HV) and nanoindentation studies performed on Al-Cu and Al-Mg HPT hybrid systems.

The hardness evolution of the Al-Cu HPT hybrids after 10, 20, 40, and 60 turns along their sample diameters is presented in Figure 8 (a) [87]. For comparison, the HV values for Al and Cu processed separately by HPT for 10 turns are denoted by dashed lines at ~ 65 HV and ~ 150 HV, respectively. The central regions of the disk after 10 turns at $r < 3$ mm, after 20 turns at $r < 2$ mm, and after 40 turns at $r < 1$ mm, showed similar hardness values, around 130-140 HV. In contrast, the hardness at peripheral regions of the disks after 10, 20-40, and 60 turns reached maximum values of ~ 250, ~ 400, and ~ 500 HV, respectively. This increasing hardness trend was consistent with the presence of Al_2Cu, AlCu, and Al_4Cu_9 intermetallic compounds near the disk edges after 20 turns and their higher volume fractions at increasing numbers of turns [87].

For Al-Mg HPT hybrids processed for 1, 5, 10, 20, 40, and 60 turns, their hardness evolution is plotted in Figure 8 (b) [120]. For reference, the saturation HV values reported for Al-1050 [121]

and ZK60 [122] alloys after HPT for 5 turns are denoted with dashed lines at ~ 65 HV and ~ 110 HV, respectively. At least 10 turns were needed in order to obtain significantly higher hardness than the range defined by the reference Al and Mg alloys, and these were found at $r > 3$ mm. After 20 turns, a saturation hardness value of 330 HV was found close to the disk periphery, $r > 4$ mm, which was relatively uniform after 60 turns. A gradual hardness increase at the central disk region, $r < 2$ mm, to ~ 115 HV and ~ 140 HV was reported with increasing number of turns to 40 and 60, respectively.

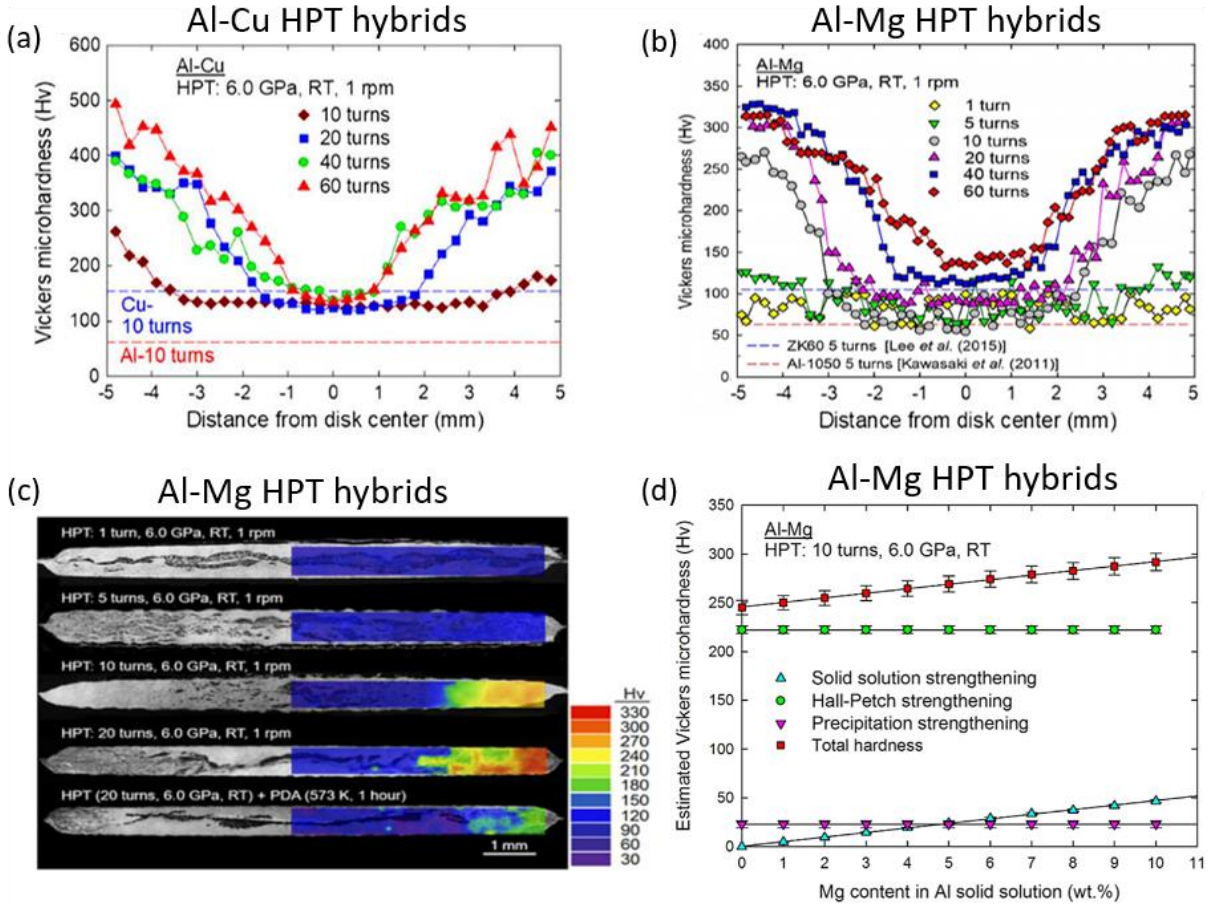

Figure 8: Evolution of the Vickers microhardness (HV) evolution across the diameter of the (a) Al-Cu HPT hybrid system from 10 to 60 turns, and (b) Al-Mg HPT hybrid system from 1 to 60 turns; (c) color-coded HV contour plots of the Al-Mg HPT hybrid system from 1 to 20 turns, and subsequent PDA (300 ºC, 1 h), overlapped on top of their corresponding SEM cross-sections; (d) estimated contributions of different strengthening mechanisms to the overall HV in the Al-Mg HPT hybrid after 10 turns as a function of the Mg content in Al solid solution. Adapted from [25,87,91,95].

The two-dimensional hardness distributions in the Al-Mg HPT hybrids after 1, 5, 10, 20 turns, and 20 turns + PDA (300 ºC, 1 h) are displayed in the form of color-coded contour maps in Figure 8 (c) [90]. Consistent with the hardness evolution presented in Figure 8 (b), the hardness increased notably in the peripheral regions, at r > 3 mm, after 10 and 20 turns, whereas the rest of the sample maintained a significantly lower hardness. PDA after 20 turns resulted in a hardness decrease, from ~ 60 to ~ 30 HV in the central regions, at r < 3 mm, and from ~ 330 to ~ 220 HV at the disk periphery, at r > 4 mm. This softening was attributed to both the increase of the GS_{ave} from ~ 60 nm to ~ 380 nm and the dissolution of the $Al_{12}Mg_{17}$ intermetallic as a result of the PDA treatment.

To investigate the reason for the extraordinary hardness increase at the periphery of the Al-Mg HPT hybrid after 10 turns, Ahn et al. [95] developed a model to estimate the contribution of different strengthening mechanisms as a function of the Mg content in Al solid solution, as shown in Figure 8 (d). The total hardness increase was assessed through the combination of (1) Hall-Petch strengthening, associated with the significant grain refinement, (2) precipitation strengthening, associated with the nucleation of Al_3Mg_2 and $Al_{12}Mg_{17}$ intermetallic compounds, and (3) solid-solution strengthening, due to the accelerated diffusivity of Mg into Al-rich phases. The model was fed with microstructure-dependent parameters (i.e., grain sizes, phase fractions, etc.) measured experimentally from TEM and XRD, and constant parameters (i.e., Burger's vector, activation energies, etc.) obtained from Al-Mg alloys in the literature. The model indicated that the contribution of Hall-Petch strengthening and precipitation hardening to the total hardness was independent of the Mg content, and that grain refinement was by far the most contributing factor. The authors reported that the hardness model was consistent with the experimental HV values measured. For example, for a 5 (wt. %) Mg in Al, the model predicted ~ 269 ± 8 HV, which is in good agreement with the experimental value at the periphery after 10 turns, as observed in Figure

8 (b). Besides the strengthening mechanisms considered above, the authors [95] recognized that other mechanisms (the load transfer effect and the coefficient of thermal expansion mismatch) important for metal matrix composites might have also played a role, but not significantly.

As mentioned earlier, the plastic deformation at the nanoscale has been assessed in HPT hybrids through nanoindentation experiments. Due to the generally heterogenous microstructures of HPT hybrids, plastic instability has manifested through relative deviations between load-displacement nanoindentation curves within the same local area. This phenomenon can be observed in Figure 9 (a), in a series of load-displacement curves obtained under an applied load of 50 mN and an equivalent strain rate ($\dot{\varepsilon}$) of $2.5 \cdot 10^{-4}$ s^{-1} from the disk edges of the Al-Cu HPT hybrids after 20 and 60 turns [91]. Increasing the number of turns from 20 to 60 resulted in a significant decrease of plastic instability, as the broadening between different load-displacement curves was greatly reduced. This was attributed to an enhanced microstructural uniformity at increased torsional straining, which also led to a higher *H* as a result of the increased content of intermetallic phases and extreme grain size refinement, as observed by the lower displacement values after 60 turns. The load-displacement curves obtained at different $\dot{\varepsilon}$ were then used to obtain the *m* values, which are plotted in Figure 9 (b) in comparison with those of commercially pure Cu and Al HPT-processed separately for 10 turns. It was found that both the *H* and *m* values increased in the Al-Cu hybrids with increasing number of turns, and that they were generally higher than those of Al and Cu HPT-processed separately. The almost threefold increase in *m* from 20 to 60 turns was associated with the transformation from a layered nanostructure after 20 turns into an equiaxed nanostructure after 60 turns, which was expected to enhance grain boundary sliding activity, hence, providing potential for achieving enhanced plasticity.

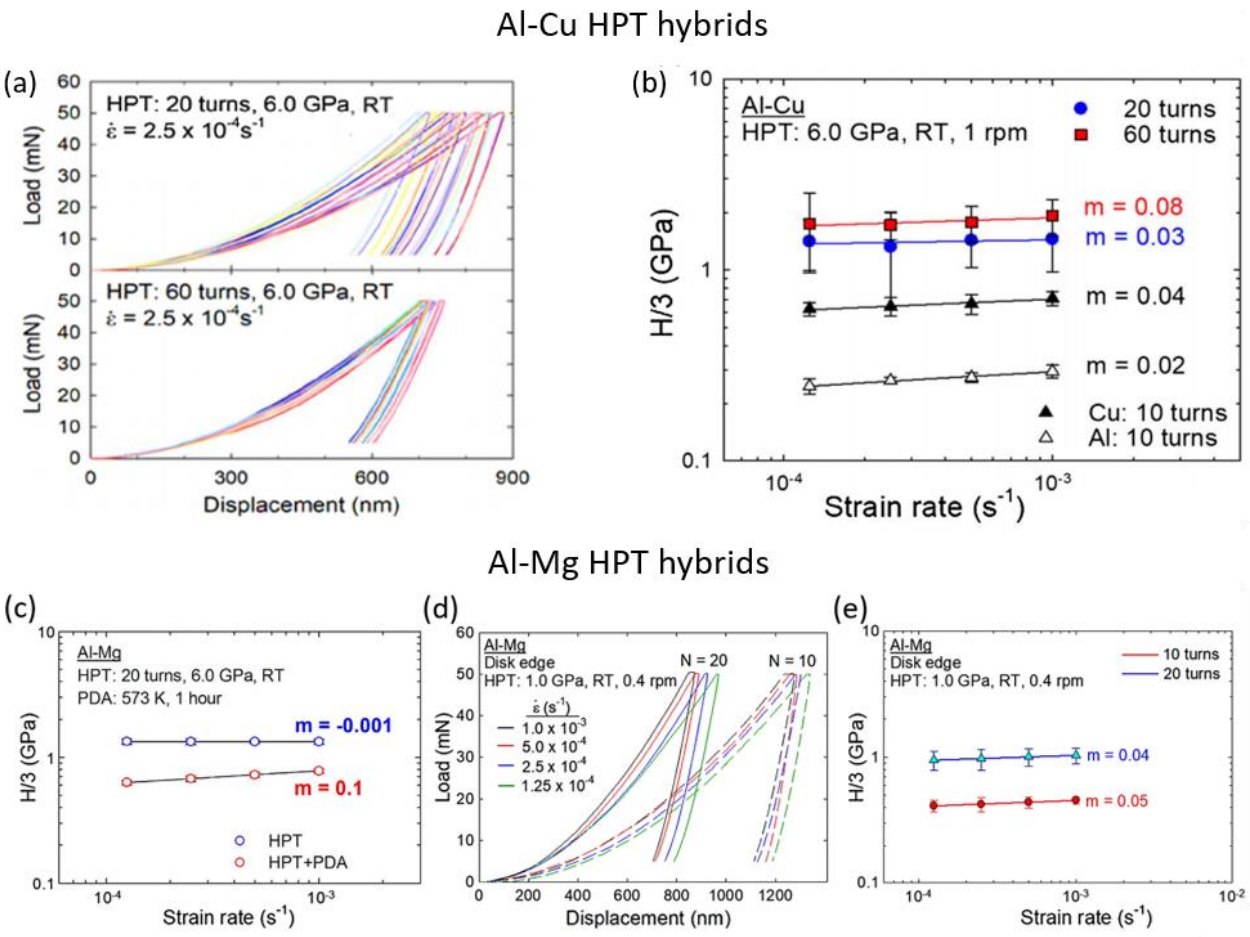

Figure 9: Evolution of the nanoindentation behavior of Al-Cu HPT hybrids after 20 and 60 turns: (a) load-displacement curves from the edge of the samples, and (b) logarithmic plot of H/3 vs. $\dot{\varepsilon}$ showing the corresponding m values, which are compared to those of pure Cu and Al after HPT for 10 turns; Evolution of the nanoindentation behavior of Al-Mg HPT hybrids: (c) logarithmic plot of H/3 vs. $\dot{\varepsilon}$ showing the corresponding m values after 20 turns, and 20 turns + PDA, (d) load-displacement curves from the edge of the samples after 10 and 20 turns, and (e) corresponding logarithmic plot of H/3 vs. $\dot{\varepsilon}$ showing the m values obtained at the disk edge (r ~ 10 mm) of scaled-up hybrids. Adapted from [90–92,94].

Unlike in the Al-Cu HPT hybrid system, no strain rate dependency was observed in the Al-Mg HPT hybrids processed for 20 turns [92], as observed in Figure 9 (c). However, the microstructural changes reported earlier from the Al-Mg system during PDA resulted in decreasing displacements at higher $\dot{\varepsilon}$ values, thereby showing a strain rate dependency of the mechanical behavior. For all the strain rates tested, the hybrids after HPT led to higher H values than those after PDA, which

was consistent with the hardness levels in the color-contour maps in Figure 8 (c). The m increase after PDA indicated that the PDA treatment was effective in improving the plasticity of the Al-Mg HPT hybrid system at RT without compromising the hardness significantly, thus, suggesting an enhanced strength-ductility combination.

The effect of scaling up the dimensions of the conventional HPT samples (i.e., 10 mm diameter, 1 mm thickness) on the nanoindentation behavior was investigated near the edge of Al-Mg hybrids having 25 mm diameter after HPT processing for 10 and 20 turns [94]. The hardness increase from 10 to 20 turns was evident from the decrease in the final displacement values of the load-displacement curves, which are plotted in Figure 9 (d). Moreover, the H values after 10 and 20 turns increased slightly, but gradually, with increasing $\dot{\varepsilon}$, leading to a positive m value similar in both samples, as observed in Figure 9 (e). By comparing the conventional and scaled-up hybrids after 20 turns, in Figure 9 (c) and (e), respectively, there was a reasonably consistent hardness of ~ 1 GPa in both cases, which might be slightly lower in the scaled-up hybrid due to the lower applied pressure used. The scaled-up hybrid exhibited a higher m value than that of the conventional sample, which might be associated with an enhanced atomic mixing due to a larger sample volume leading to a larger microstructure homogeneity.

The former microhardness and nanoindentation studies served as a reference for the ones carried out in this dissertation in the Zn-Mg HPT hybrids. In addition to reporting the HV values and distributions from microhardness, as well as the H and m values from nanoindentation, the experimental data collected was used to analyze the strain hardening capability and propose a plastic deformation model of the Zn-Mg HPT hybrids accounting with the microstructural observations.

3. EXPERIMENTAL METHODS

3.1. Materials

The following materials were used for the synthesis of the HPT samples studied in this dissertation. Commercially pure Zn (ZN007920-99.90 % purity) and commercially pure Mg (MG007922-99.97 % purity) were purchased from Goodfellow Corporation, Coraopolis, PA, in the as-drawn state. As-cast Zn-3Mg (wt.%) alloy was received from Dr. Hakan Yilmazer from Yildiz Technical University, Turkey. Each of these materials was received in the form of 10 mm diameter rods, which were sliced across their diameters into disks of specific thicknesses prior to HPT processing, as detailed in section 3.3. The pure Zn and pure Mg rods were used for processing the HPT hybrids.

3.2. Homogenization heat treatment of the as-cast Zn-3Mg alloy

In order to obtain a homogeneous microstructure, the as-cast Zn-3Mg (wt.%) alloy was subjected to a homogenization heat treatment before any HPT processing. The as-cast-then-homogenized Zn-3Mg (wt. %) alloy will be referred to as "as-homogenized Zn-3Mg alloy" hereafter. This homogenization heat treatment was performed at 360 ± 2 ºC for 15 h inside a vacuum-sealed (~ 10^{-4} torr) quartz tube followed by water quenching. The temperature, which was monitored with two thermocouples located just underneath the quartz tubes, was maintained within the desired range. The vapor pressure curves of the materials were considered when performing this heat treatment, as this is especially critical when working near the melting temperature, as observed in the Zn-Mg binary phase diagram in Figure 96.

3.3. Processing of Zn-Mg HPT hybrids

For the preparation of the HPT hybrid samples, a series of disks having 10 mm diameter were sliced to specific thicknesses from the pure Zn and pure Mg rods using electro-discharge machining (EDM). Each HPT hybrid sample consisted of a set of three disks stacked on top of each other in the order of Zn/Mg/Zn, such that the top and bottom Zn disks had the same thickness. The final thickness of the Zn and Mg disks were chosen based on the density of each material (ρ_{Zn}=7.14 g/cm^3; ρ_{Mg}=1.74 g/cm^3) to achieve the nominal targeted composition in the hybrids after HPT processing. Regardless of the composition, the thickness of the Zn/Mg/Zn stack before HPT processing was 1.5 mm, which decreased to approximately 1 mm after HPT processing. No adhesive or metal brushing treatment was applied on the separate disk surfaces prior to HPT processing.

Three different Zn-Mg hybrid compositions were investigated in this work: Zn-3Mg, Zn-10Mg, and Zn-30Mg (wt. %). The Zn and Mg disk thicknesses before HPT processing are detailed in sections 3.3.1, 3.3.2, and 3.3.3, respectively, and summarized in Table 1. After HPT processing, these samples will be referred to as “Zn-3Mg HPT hybrid”, “Zn-10Mg HPT hybrid”, and “Zn-30Mg HPT hybrid” hereafter.

All the hybrid samples were processed using a conventional HPT facility (installed in Dr. Megumi Kawasaki’s laboratory at Oregon State University), which is shown in Figure 10, under quasi-constrained conditions in monotonic torsional straining. Sample processing was conducted at room temperature (RT), under an applied pressure of 6 GPa, at a constant rotational speed of 1 rpm, and for a total number of 1, 5, 15, and 30 turns.

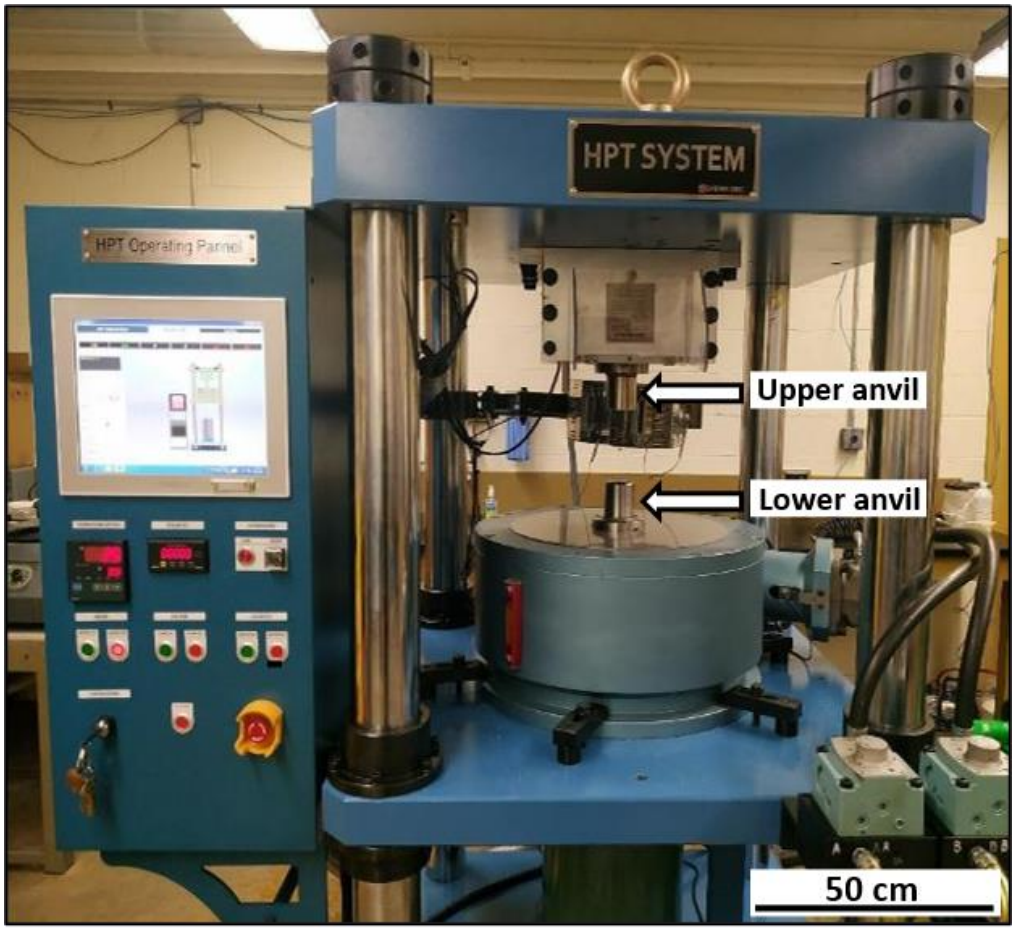

Figure 10: Digital image of the HPT facility used to produce the HPT hybrid, and alloy samples studied. (Courtesy of Dr. Megumi Kawasaki, Oregon State University).

For the preparation of the HPT alloy samples, 1.5 mm thick disks were sliced from the as-homogenized Zn-3Mg alloy bar using a low-speed diamond saw. These disks were then slightly polished to obtain flat surfaces prior to HPT processing. The HPT-processed Zn-3Mg alloy, referred to as "Zn-3Mg HPT alloy" hereafter, was obtained using the same processing parameters mentioned above for the HPT hybrids, with the exception that the Zn-3Mg HPT alloy was only processed for 30 turns. Similar to that of the HPT hybrids, the thickness of the Zn-3Mg alloy sample decreased from 1.5 mm to about 1 mm after HPT processing. A schematic of the experimental set-up used to fabricate the HPT hybrid and HPT alloy samples is provided in Figure 11.

It is worthwhile mentioning that for all the samples, the temperature increase during HPT processing was monitored using a set of thermocouples attached to the anvils close to the sample surfaces. The maximum temperature recorded was always less than 50 ºC. This temperature increase was not expected to have had a significant effect on the microstructural evolution of the HPT-processed materials, in agreement with a recent report [123].

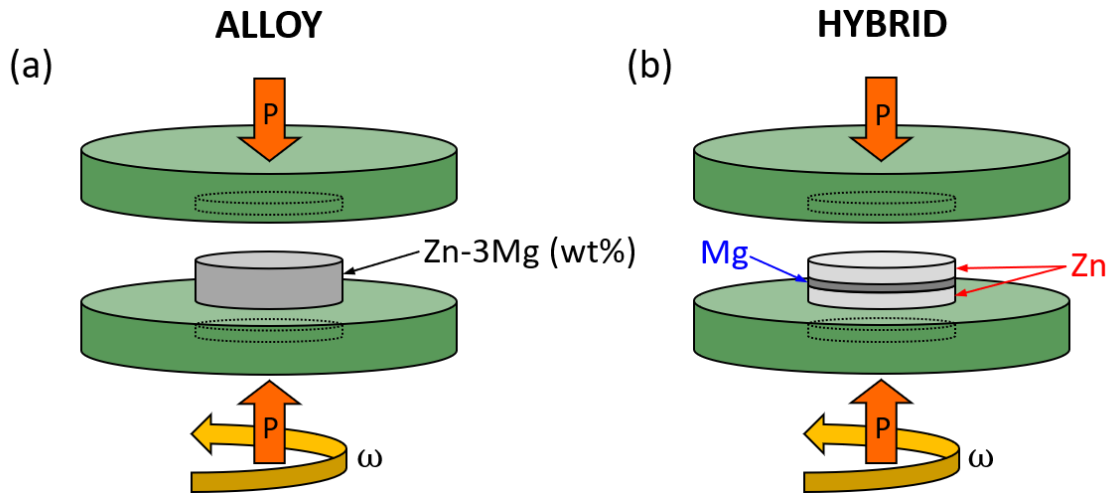

Figure 11: Experimental set-up used for the fabrication of the HPT (a) alloy and (b) hybrid samples. P denotes the applied pressure (whose direction is indicated by orange arrows) and indicates the rotational speed (whose direction is indicated by yellow arrows) [124].

3.3.1. Zn-3Mg (wt.%) hybrid

For the Zn-3Mg (wt.%) hybrid, the thickness of the top and bottom Zn disks was 0.665 mm, whereas the thickness of the central Mg disk was 0.169 mm. Note that uniform disk thicknesses of ~ 200 μm were quite challenging to achieve from EDM cutting, and even more from soft metals like Zn and Mg.

3.3.2. Zn-10Mg (wt.%) hybrid

For the Zn-10Mg (wt.%) hybrid, the thickness of the top and bottom Zn disks, as well as the central Mg disk, was 0.5 mm.

3.3.3. Zn-30Mg (wt.%) hybrid

For the Zn-30Mg (wt.%) hybrid, the thickness of the top and bottom Zn disks was 0.272 mm, whereas the thickness of the central Mg disk was 0.957 mm. As mentioned above for the Zn-3Mg hybrids, obtaining disks with ~ 200 μm thickness from EDM cutting was quite challenging.

3.3.4. Zn-3Mg (wt.%) alloy

The thickness of the as-homogenized Zn-3Mg (wt.%) disk before HPT processing was 1.5 mm, which is the same as the total thickness of the Zn/Mg/Zn stacks for the HPT hybrids mentioned above, regardless of the composition.

Table 1: Summary of thicknesses of the Zn and Mg disks used in the Zn/Mg/Zn stacks for HPT-processing of the hybrid samples with different nominal compositions. For reference, the thickness of the Zn-3Mg alloy sample is also included. All compositions are in (wt.%).

Sample	Thickness (mm)		
	Zn disk	Mg disk	Sample before HPT
Zn-3Mg HPT hybrid	0.665	0.169	1.5
Zn-10Mg HPT hybrid	0.5	0.5	1.5
Zn-30Mg HPT hybrid	0.272	0.957	1.5
Zn-3Mg HPT alloy	N/A	N/A	1.5

3.4. Post-deformation annealing (PDA) treatment

After HPT processing for 30 turns, some hybrid and alloy samples with the same nominal composition, Zn-3Mg (wt.%), were subjected to a post-deformation annealing (PDA) treatment at 200 ± 2 ºC for 1 h in a low vacuum (~ 10^{-2} torr) tube furnace, followed by air cooling. The temperature of the sample during the PDA treatment was monitored using a thermocouple spot welded to the edge of the sample.

3.5. Microstructural characterization

3.5.1. Metallographic sample preparation

HPT-processed samples were sectioned vertically along their diameter, using a low-speed diamond saw, to give two semi-circular disks. Both the cross-section and the horizontal surface of each disk were mounted in a 1-inch diameter puck of conductive thermosetting phenolic resin (Konducto-Met, Agar Scientific). The mounted samples were mechanically ground using SiC abrasive planar papers (MetLab) through 600, 800, and 1200 US grit size (equivalent to 1200, 2400, 4000 FEPA grit size, respectively). The specimens were further polished using polycrystalline diamond paste (MetLab) of 6, 3, and 1 μm particle size, sequentially, using a MD-Nap polishing cloth (Struers). Each of these polishing steps lasted 5 to 10 minutes. For final polishing to mirror finish, a colloidal SiO_2 suspension of 0.04 μm particle size (OP-S NonDry, Struers) was used on a chemically resistant MD-Chem polishing cloth (Struers) for times ranging between 5 and 15 minutes. Ethanol was used as both the lubricant during grinding and polishing, as well as the immersion medium for the 5 min ultrasonic cleaning performed between all the grinding and polishing steps. In addition, samples prepared for grain size measurement were etched for 5 to 10 seconds in a solution containing 6 g picric acid, 5 mL acetic acid, 10 mL distilled water, and 100 mL ethanol. All samples were stored in a vacuum chamber at 0.2-0.3 atm to prevent excessive oxidation.

3.5.2. Scanning electron microscopy

The scanning electron microscope (SEM) is a highly versatile instrument that scans a focused beam of electrons over a sample surface, generating various types of signals resulting from electron-sample interactions, which can reveal information about the surface morphology, elemental composition, and crystalline structure and orientation [125]. The microstructures of the

HPT-processed samples were examined using a TESCAN MIRA-3 (field-emission gun) FEG SEM located in the Engineering Building at Michigan State University.

Imaging was performed using secondary electron (SE) and backscattered electron (BSE) detectors, with an accelerating voltage of 20-25 kV and a working distance between 5-10 mm. It is noted that the spatial resolution in SE mode is about 4 nm, whereas that in BSE mode is about 15 nm [125]. Unless otherwise specified, the SEM images presented for the HPT-processed materials were acquired near the disk periphery (~ 1 mm away from the edge) from the cross-section of the samples, corresponding to the thickness-radial plane in Figure 12. It should be noted that the imaging planes for the SEM and TEM/STEM samples were perpendicular to each other, defining a coordinate system (thickness-radial-shear), which enabled a three-dimensional characterization of the microstructure. The grain size of the Zn-rich matrix was measured, according to ASTM E112-12: Standard Test Methods for Determining Average Grain Size [126], using SEM images taken at the mid-thickness of the horizontal surface of the samples, corresponding to the radial-thickness plane in Figure 12.

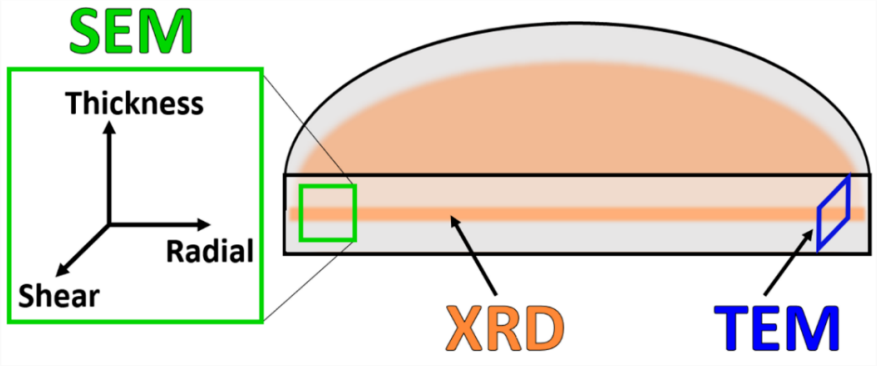

Figure 12: Schematic representation of the planes investigated in the Zn-Mg HPT samples by the different characterization techniques. SEM imaging, HV testing, and Berkovich nanoindentation were performed at the thickness-radial plane. TEM imaging was carried out at the thickness-shear plane. XRD scanning was collected from the shear-radial plane. The mid-thickness region of the samples is highlighted in orange, where the SEM, TEM, XRD, and Berkovich data were collected from [127].

3.5.3. Energy dispersive spectroscopy

The energy dispersive spectroscopy (EDS) technique is used, in combination with a SEM or TEM, for qualitative and semi-quantitative analysis of the elemental composition [125]. The working principle of EDS analysis is based on the detection of characteristic X-rays ejected from the sample atoms upon electron-sample interaction. The direct correlation between the X-ray energy and the atomic number of each element in the periodic table, according to Moseley's Law [128], enables the elemental composition analysis. This way, EDS analysis can offer X-ray counts vs. energy spectra from specific regions of the sample, as well as elemental distribution maps.

It is important to highlight some limitations of quantitative EDS analysis that need to be considered. The typical energy resolution of EDS is about 150 eV. The detection limit of EDS is about 0.1 (wt. %), meaning that it cannot detect trace elements (i.e. concentrations below 0.01 wt. %) [129]. Light elements, typically Z < 6, cannot be detected due to the low energy of the X-rays being absorbed by the specimen. The SEM accelerating voltage plays a critical role in the spatial resolution during EDS analysis, as it influences the size of the interaction volume (i.e., the depth of X-ray excitation in the sample). According to the Castaing's formula [130] shown in Equation 4, the X-ray production depth (Z_m) in a given material can be estimated as a function of the accelerating voltage (E_0) in kV, the minimum emission voltage (E_C) in keV, the atomic mass (A), the atomic number (Z) and the density (ρ) in kg/m^3.

$$Z_m = 0.033(E_0{}^{1.7} - E_C{}^{1.7})\frac{A}{\rho Z} \qquad \text{Equation 4}$$

EDS point analysis and elemental maps were acquired using an EDAX TEAM detector installed on the TESCAN MIRA-3 FEG-SEM mentioned in section 3.5.2, with an accelerating voltage of

6-10 kV, which resulted in an interaction depth ≤ 0.6 μm according to Equation 4. EDS analysis was performed on the Zn-10Mg HPT hybrid sample, on the as-cast Zn-3Mg alloy, on the as-homogenized Zn-3Mg alloy, and on the Zn-3Mg HPT hybrid after HPT and PDA. The EDS results presented in this dissertation are considered to be semi-quantitative and were not used alone to draw any final conclusion.

3.5.4. Electron-backscattered diffraction

Electron-backscattered diffraction (EBSD) analysis is used, in conjunction with a SEM, to reveal crystallographic information about the microstructure of a sample. For the EBSD scans, the samples are tilted to 70º with respect to the horizontal plane towards the fluorescent phosphor screen. This screen, located in the EBSD detector, is responsible for collecting the diffraction patterns characteristic of both the crystal structure and the orientation of the sample. EBSD scans were always acquired near the disk periphery (~ 1 mm away from the edge) of the samples, from the thickness-radial plane in the Zn-3Mg HPT hybrid and Zn-3Mg HPT alloy samples, and from the radial-shear plane in the Zn-10Mg HPT hybrid sample.

EBSD orientation maps of the Zn-3Mg HPT hybrid and alloy samples, with an area of ~ 12 x 12 mm^2, were acquired with an accelerating voltage of 20-25 kV, a working distance of 15-18 mm, and a step size of 0.05 mm with an EDAX TSL OIM Data Collection System 7, attached to the TESCAN MIRA-3 FEG-SEM. Dynamic background subtraction was used to produce Kikuchi patterns with similar intensities. EBSD orientation maps were also acquired for the as-homogenized Zn-3Mg alloy before HPT processing, with the same parameters mentioned above, but with a step size of 0.5 mm for an area of ~ 250 x 250 mm^2. The EBSD datasets were analyzed using EDAX TSL OIM Analysis 6.1 and 7, from which inverse pole figure (IPF) maps, kernel

average misorientation (KAM) maps, phase maps, grain size distribution plots, and misorientation angle plots were obtained. IPF maps were used to generate basal (0001) pole figures for Zn and Mg phases. Clean-up procedures, including neighbor confidence index (CI) correlation and grain dilation, were systematically applied to the as-processed EBSD scans to minimize the number of incorrectly indexed pixels. First, the neighbor CI correlation clean-up step replaced the orientation of erroneous pixels, defined as any pixel with CI < 0.05, with that of the neighboring pixel with the highest CI. Second, the grain dilation clean-up step was used to define the grains as any set of 5-10 neighboring pixels with a CI > 0.1 having a misorientation angle less than 5 º. Only points with CI > 0.1 were considered for statistical measurements. KAM maps, including all the pixels with a CI > 0.1, were generated such that misorientation angles up to 3 º (with respect to the first nearest neighboring pixels) were recorded.

3.5.5. Transmission electron microscopy

The transmission electron microscope (TEM) uses a high-energy electron beam with an accelerating voltage ranging between 100-300 kV. This beam interacts with very thin samples, typically 100-200 nm, producing elastic and inelastic electron scattering used to generate high-resolution images and diffraction patterns. Coherent elastic scattering is responsible for electron diffraction, which is used to analyze the crystal structures at the nanoscale [131].

3.5.5.1. TEM sample preparation

For the preparation of TEM lamellae, different focused-ion beam (FIB) lift-out techniques were used in this dissertation. For the Zn-3Mg HPT hybrid and alloy samples, a HITACHI NB5000 FIB-SEM was used for *in situ* lift-out. This instrument was located at the Center for Nanophase Materials Sciences (CNMS) at Oak Ridge National Laboratory (ORNL). It was accessed as part

of an accepted user proposal, and it was operated by ORNL staff members. TEM lamellae with approximate dimensions of ~ 5 x 15 μm and 50-80 nm thickness were extracted from the thickness-shear plane of the HPT-processed samples near disk periphery (~ 1 mm away from the edge), as sketched in Figure 12. The steps followed for *in situ* lift-out are summarized below and can be visualized in Figure 13:

1. The stage was tilted 52 º such that the incident ion beam was perpendicular to the material surface. The region of interest (ROI) in the sample was protected from ion milling with a Pt layer deposited with an ion beam current of 0.5 nA. The surrounding of the sample was ion milled, with an ion beam current of 10-20 nA, by making side cut wedges (with ± 12º stage tilt) in a "C" shape, leaving a bridge that maintained the sample attached to the rest of the material. This is observed in Figure 13 (a).
2. The sample was attached to the micromanipulator needle from its corner by Pt deposition, and the bridge was cut free, as observed in Figure 13 (b).
3. The sample was transferred with the micromanipulator to the TEM grid. After attaching the sample by Pt deposition from one short edge to the side of the grid, it was cut free from the needle. This is observed in Figure 13 (c-d).
4. The lift-out sample attached to the TEM grid was further thinned until electron transparency was achieved in the SEM at 3 kV. As observed in Figure 13 (e-f), this was done in 2-3 separate windows, instead of in the whole sample, for improved structural stability of the lift-out.

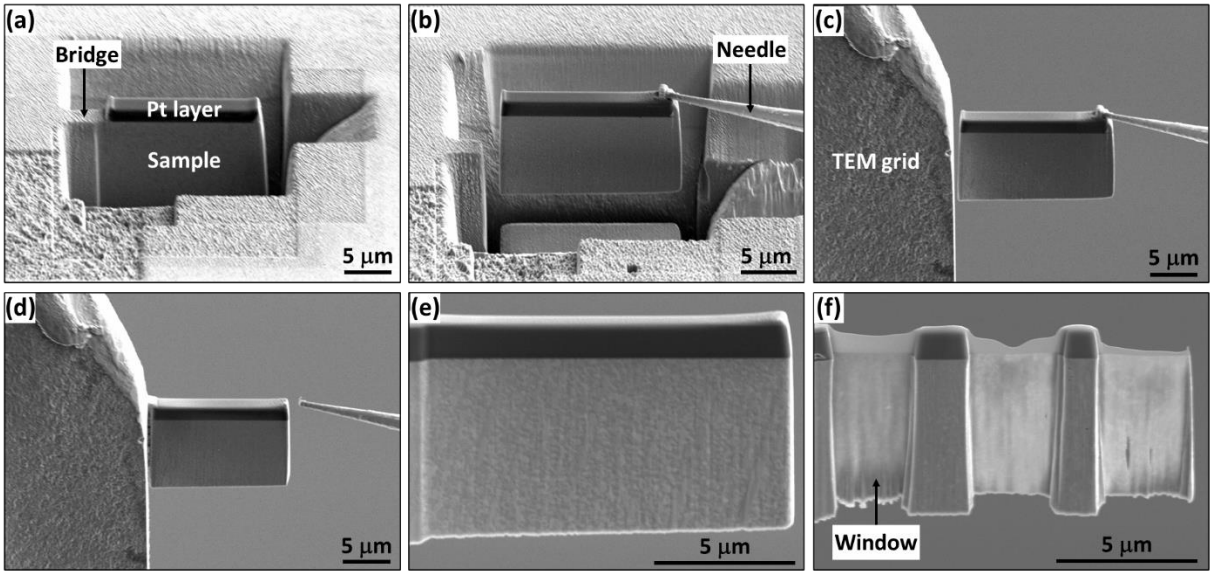

Figure 13: Images acquired in the FIB-SEM during *in situ* lift-out preparation of TEM lamellae showing (a) the sample after FIB cutting the side wedges but still supported by the bridge, (b) the sample after the micromanipulator needle is attached and the bridge is cut free, (c) the sample transferred with the micromanipulator before being attached to the TEM grid, (d) the sample after being attached to the TEM grid and cut free from the micromanipulator needle, (e) the sample at the beginning of the thinning process, (f) the sample after final thinning to electron transparency in different windows.

For the preparation of the TEM lamellae from Zn-10Mg HPT hybrids, a FEI Nova 200 Nanolab SEM-FIB and a EXpressLO Nicola G2 *ex situ* lift-out system were used. These instruments were operated with the assistance of Dr. Lucille A. Giannuzzi as part of a product demonstration at the Michigan Center for Materials Characterization (MC^2) at the University of Michigan. *Ex situ* TEM lamellae had similar dimensions to those mentioned earlier for the *in situ* lift-out procedure and were also extracted from the thickness-shear plane near the periphery of the Zn-10Mg HPT hybrid samples. The *ex situ* lift-out procedure consisted of performing the side cuts, undercuts, and the final thinning to electron transparency in the SEM-FIB, while the sample was still supported from both side tabs, as observed in Figure 14 (a). Then, the final side tabs of material were cut free, and the sample was observed to fall over slightly in the trench. At this point, the sample was removed from the SEM-FIB and placed on the stage equipped with a micromanipulator system, which

consisted of a light optical microscope and a glass rod attached to a hydraulic micromanipulator. *Ex situ* lift-out took place by gently approaching the fine tip of the glass rod (~ 1 μm diameter) to the electron transparent sample freed inside the trench, causing the sample to cling to the glass rod tip via electrostatic interaction [132]. Finally, the lift-out specimen was positioned in a C-coated Cu grid for TEM, as observed in Figure 14 (b).

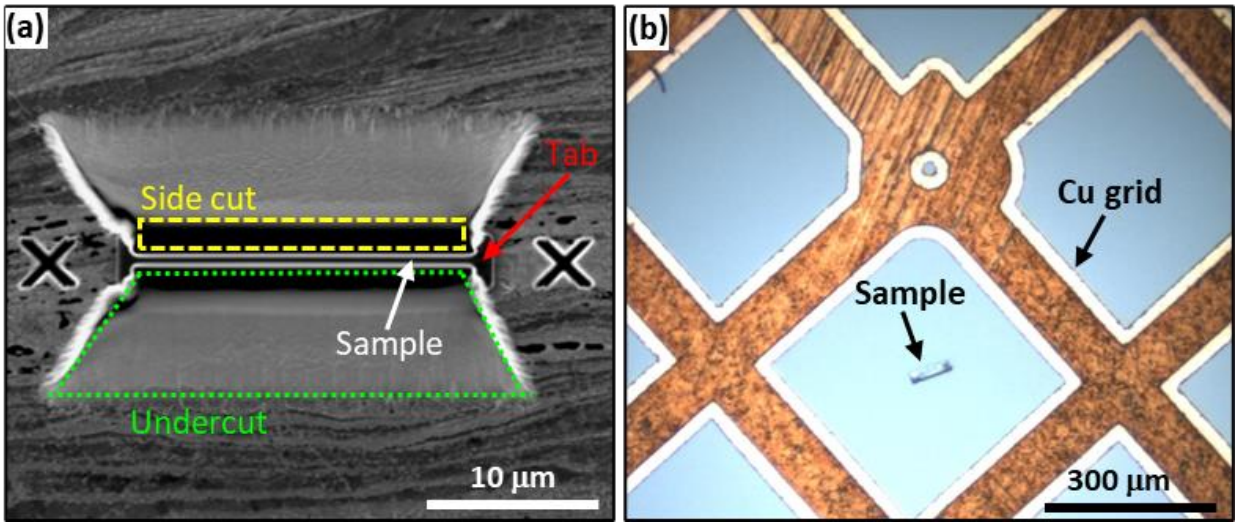

Figure 14: Images acquired during *ex situ* lift-out preparation of TEM lamella samples showing (a) the lamella sample in the SEM-FIB after the side cuts and undercuts but still attached from the side tabs to the bulk; (b) the lamella sample visualized through the optical microscope after being lifted-out and positioned in the C-coated Cu grid using the micromanipulator system.

3.5.5.2. TEM sample observation

The TEM lamellae extracted from the Zn-10Mg HPT hybrids were observed using a JEOL 100CX TEM operated at 120 kV. This TEM was located at the MSU Center for Advanced Microscopy (CAM). Bright-field (BF) images, as well as selected area diffraction (SAD) patterns, were collected upon calibration of the camera length. The radii of the diffraction rings (R) in the SAD patters were measured in reciprocal space units (nm^{-1}) using ImageJ (NIH, USA), and their values,

together with that of the camera constant (λL) calculated during calibration, were introduced in Equation 5 below to compute the corresponding interplanar spacings (d_{hkl}).

$$\lambda L = R\, d_{hkl} \qquad \text{Equation 5}$$

Note that Equation 5 is derived from Bragg´s Law, which is provided in Equation 6 in section 3.5.6, assuming that the angle between the diffracted and the direct beam is very small, which is the case in TEM [131]. The computed d_{hkl} values were compared against tabulated crystal structure data from the Inorganic Crystal Structure Database (ICSD) with the following material files: Zn (421014), Mg (77908), Mg_2Zn_{11} (104898), and $MgZn_2$ (104897). The identified phases and their corresponding diffraction planes were labeled accordingly in the SAD patterns collected.

The TEM lamellae extracted from the Zn-3Mg HPT hybrid and Zn-3Mg HPT alloy were observed using a FEI Titan aberration-corrected TEM/STEM operated at 300 kV. This instrument, located at the CNMS at ORNL, was operated by Dr. Raymond Unocic. All TEM/STEM images were taken in the shear-thickness plane near the periphery of the HPT disks. BF images and SAD patterns were collected in TEM mode. Phase identification via SAD ring pattern analysis was carried out using the ringGUI package of the CrysTBox (Crystallographic Toolbox) open software [133]. In addition, BF and high-angle annular dark-field (HAADF) images were acquired in STEM mode.

High-resolution TEM (HRTEM) phase-contrast imaging was also performed, and the corresponding Fast Fourier Transform (FFT) diffractograms were obtained and analyzed using the Gatan Digital Micrograph 3 software. The image processing procedure followed for the identification of the crystal structures from HRTEM images is explained below and illustrated in Figure 15:

1. A ROI was selected in the HRTEM image of interest, as shown in red in Figure 15 (a).
2. FFT calculation was performed on the selected ROI, and the corresponding diffractogram was displayed, in reciprocal space, as observed in Figure 15 (b).
3. Pattern mask filtering corresponding to the structural periodicity of diffractogram was applied on the original FFT, as observed in Figure 15 (c). This step was crucial to reduce noise signal and obtain a high-quality atomic resolution image.
4. Inverse FFT (IFFT) calculation was applied to the masked FFT, transforming to real space, as observed in Figure 15 (d). By comparing Figure 15 (a) and (d), it is evident that the reconstruction of the filtered diffractogram transformed to a processed image with enhanced image quality, as observed in the higher magnification insets of Figure 15 (d).
5. The interplanar angles were measured from the FFT images, and the interplanar spacings were measured from the IFFT images, as illustrated in Figure 15 (e) and (f), respectively.

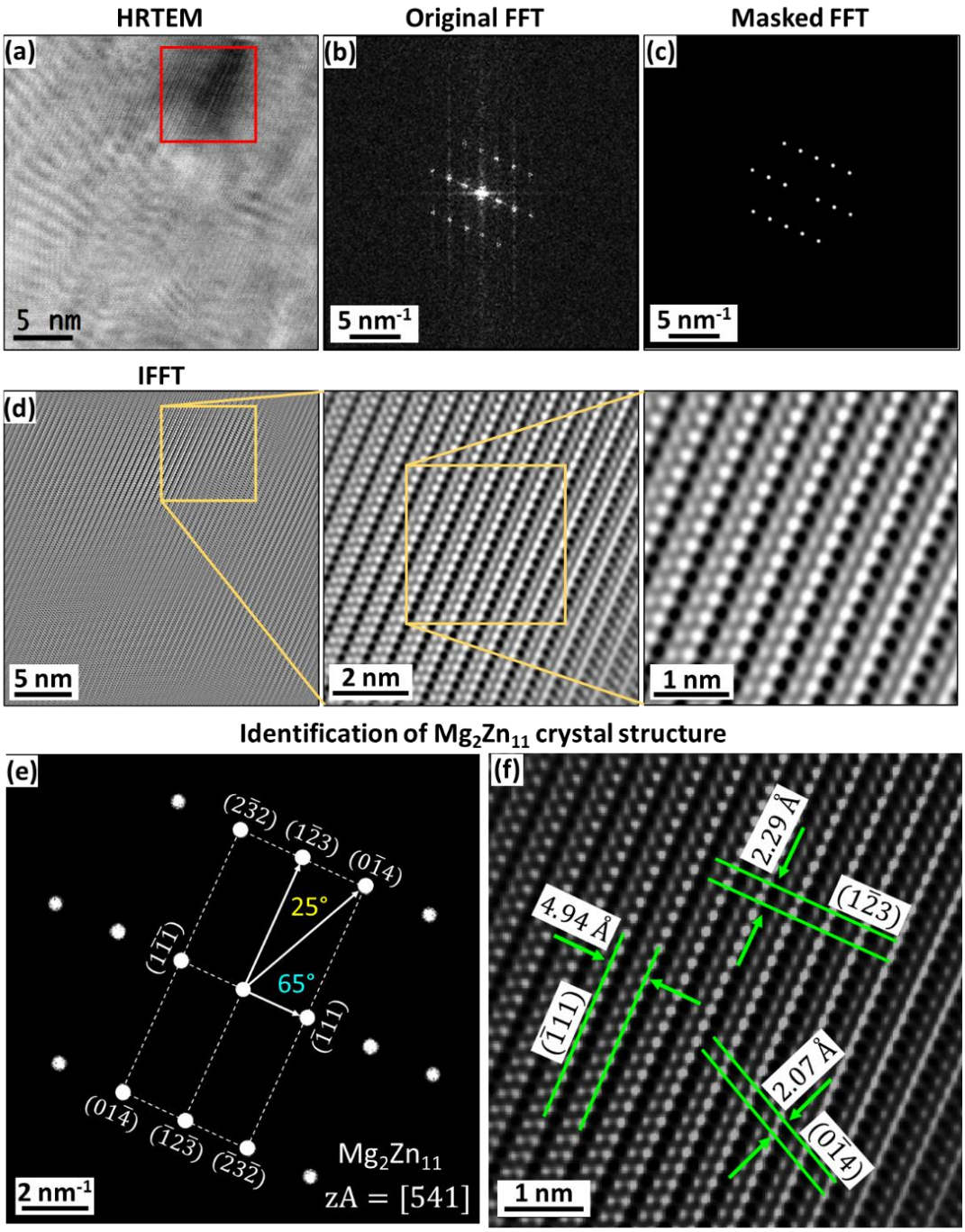

Figure 15: FFT analysis procedure for the identification of crystal structures from HRTEM images. (a) Selected ROI (marked in red) in the HRTEM image, (b) diffractogram, in reciprocal space, obtained after performing FFT calculation on the selected ROI, (c) diffractogram after applying pattern mask filtering on the original FFT to reduce the noise signal an improve quality of the resulting image after processing, (d) image, in real space, after performing IFFT calculation on the masked FFT. Note the atomic resolution achieved in the higher magnification insets after FFT analysis. (e) measurement of the interplanar angles and identification of the zone axis (zA) of Mg_2Zn_{11} in the FFT diffractogram, (f) measurement of the interplanar distances corresponding to the diffractogram in (e) in the IFFT image.

3.5.6. X-ray diffraction

X-ray diffraction (XRD) is an analytical technique that utilizes a monochromatic X-ray beam (typically, a Cu-Kα radiation source: λ=1.5406 Å) to interact with a sample, producing reflected X-rays that are captured by a detector. The resulting XRD pattern can be used to elucidate the crystal structure of crystalline/semicrystalline materials, including the nature of present phases and their fractions, texture, and other structural parameters like the average crystallite size, lattice constant, lattice strain, and degree of crystallinity (in semicrystalline materials) [134].

For the analysis of powder and bulk samples, a Bragg-Brentano configuration is typically used, where the incident angle (ω) is always half of the detector angle (2θ), as illustrated in Figure 16 (a). This can be achieved either by (1) fixing the X-ray source while simultaneously rotating the sample at θ °/min and the detector at 2θ °/min; or by (2) fixing the sample while simultaneously rotating the X-ray source at -θ °/min and the detector at θ °/min [134].

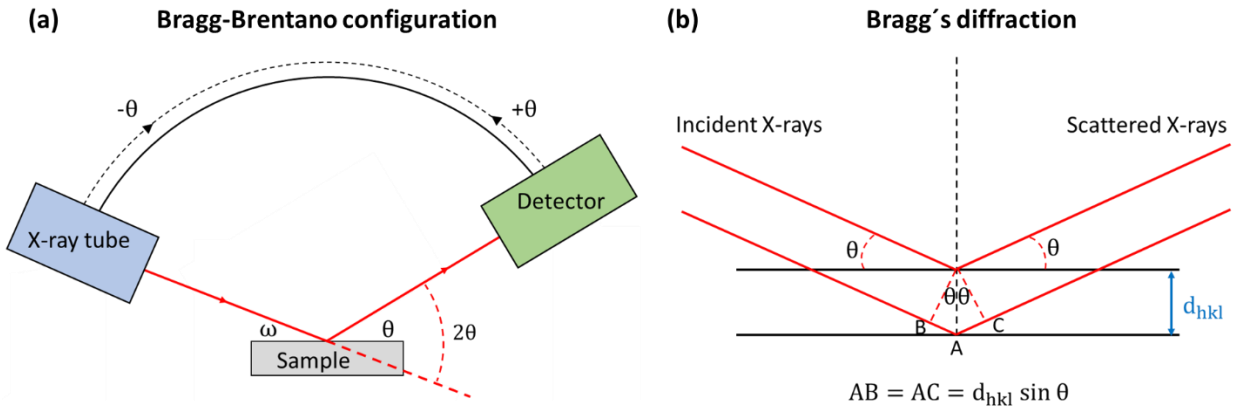

Figure 16: (a) Schematic of the Bragg-Brentano configuration typically used in powder and bulk XRD analysis, where ω indicates the incident angle of the X-ray source and 2θ indicates the detector angle; (b) Sketch of the condition for Bragg´s diffraction, where θ indicates the angle formed between the incident X-rays and the atomic planes with interplanar spacing d_{hkl}. The path length difference between the diffracted X-rays is AB + BC, which leads to the Bragg´s law shown in Equation 6.

According to the Bragg´s scattering condition schematically shown in Figure 16 (b), the diffraction angle θ can be related to the interplanar spacing (d_{hkl}) and the wavelength of the incident X-ray (λ) beam through the Bragg's law presented in Equation 6. Note that only when the X-rays scattered from the lattice planes of the material interfere constructively, their path length difference (AB+AC in Figure 16 (b)) can be related with λ.

$$\lambda = 2d_{hkl} \sin\theta \qquad \text{Equation 6}$$

XRD analysis was performed at the mid-thickness of the shear-radial plane (see Figure 12) using a high-resolution Rigaku Ultima IV XRD system located at MSU to investigate the phase changes with increasing plastic deformation. For the Zn-10Mg HPT hybrid samples, only the areas near the periphery of the disk (~ 2 mm away from the edge) were XRD scanned. This was achieved by removing the central region of the samples with a radius of ~ 2.5 mm prior to XRD scanning, obtaining a donut-like sample. For the Zn-3Mg HPT hybrids, the central region was not removed, meaning that the whole samples were scanned.

All the XRD data in this dissertation was collected with an accelerating voltage of 44 kV and a beam intensity of 44 mA, within the range 20° < 2θ <90° using a Cu-Kα radiation in a Bragg–Brentano configuration. According to the Beer-Lambert law [135], with these settings, the X-ray beam penetrates ~ 0.26 mm into the sample. Therefore, the HPT hybrid samples were slightly polished in the thickness direction prior to XRD analysis to investigate the mid-thickness plane of the samples, as indicated by the region highlighted in orange in Figure 12. All XRD scans were collected with a step size of 0.01 ° and a scanning speed of 3 °/min. The Rigaku PDXL software, along with the ICSD, was used for peak matching to reveal the phases present in all samples. It

should be noted that the same ICSD material files were used consistently for the analysis of the TEM and XRD results: Zn (421014), Mg (77908), Mg_2Zn_{11} (104898), and $MgZn_2$ (104897).

For the Zn-10Mg HPT hybrids, after identification of the phases present, their amounts were quantified by means of Rietveld analysis by following the Rigaku PDXL User Manual version 2.6. The background signal was subtracted, and peaks in the XRD spectra were identified by comparison with ICSD files. After confirming the phases present in the material, the theoretical diffraction pattern was simulated and displayed together with the experimental pattern. The residual intensity plot indicated the relative differences in peak heights between the theoretical and experimental XRD patterns. After a series of iterations that adjusted the relative intensity ratios of each phase as well as the scale factor, the residual intensity was reduced. Once both theoretical and experimental patterns were brought practically coincident, the refinement processed was completed, and the quantitative information of each phase in (wt.%) was provided.

3.5.7. Atom probe tomography

Atom probe tomography (APT) is a characterization technique that offers a unique combination of three-dimensional imaging with a spatial resolution of 0.3 nm, and chemical composition analysis with a sensitivity of 10 ppm [136]. This enables the investigation of local compositions and interfacial mixing at the atomic scale. APT relies on the ionization and subsequent field evaporation of individual atoms from a needle-like specimen surface with an apex radius < 100 nm. Field evaporation occurs by applying a DC voltage bias (typically between 1-10 kV) and a pulsed voltage (conductive samples) or pulsed laser (semiconductive and insulating samples). During field evaporation, the APT needle is cooled down to cryogenic temperatures ranging

between 25-80 K and maintained under ultrahigh vacuum (i.e., < 10^{-9} Torr) to suppress thermal lattice vibrations and improve spatial positioning [136].

In this dissertation, APT was used to analyze the local compositions, including that of the matrix and the intermetallic phases in the Zn-Mg HPT-processed samples, at the same radial positions investigated by TEM (i.e., ~ 1 mm away from the sample edge).

3.5.7.1. APT sample preparation

For the preparation of APT needles from Zn-3Mg HPT hybrid and alloy samples, a FEI Nova 200 FIB-SEM was used for *in situ* lift-out. This instrument, located at the CNMS at ORNL, was accessed as part of an accepted user proposal, and was operated by ORNL staff. Lamellae samples with dimensions of ~ 10 x 5 x 1 μm were extracted from the thickness-shear plane near the periphery of the HPT-processed samples, as indicated in Figure 12. The steps followed for the *in situ* lift out, and preparation of APT needles are both summarized below and illustrated in Figure 17.

1. With the stage tilted to 52º, a protective Pt layer of 10 x 2 x 1 μm was deposited at the ROI, for reducing Ga implantation, using an ion beam with an accelerating voltage of 30 kV and a current of 0.3 nA. The ion beam current was increased to 6.5 nA, and a 17 x 6 x 7 μm regular cross-section pattern was milled at both long sides of the Pt layer to trench for the lift-out.
2. The stage was tilted to 22 º to make the undercuts at both long sides of the Pt layer, using a 17 x 2 x 3 μm rectangle pattern. In the second undercut, the sample was released from

the bottom. One short side of the lift-out was cut free from the bulk sample, leaving it connected by a bridge, similar to that shown in Figure 13 (a).

3. The stage was tilted to 0 º and dropped to bring in the manipulator needle. This needle was attached to one end of the lift-out using a Pt deposit. The sample was cut free from the other end and lifted out, similar to that shown in Figure 13 (b).
4. The lift-out was attached to one tip of a Si microtip array coupon using a Pt deposit, as observed in Figure 17 (a) and (b) from the top and the side, respectively, corresponding to the SEM and FIB angles, respectively. An extra Pt deposit was applied to the back side of the lift-out/tip interface for stability during further milling, and the sample was cut free from the rest of the lift-out, as shown in Figure 17 (c).
5. The first annular mill was done with a circular pattern milling of 4 μm outer diameter and 1.25 μm inner diameter, at 30 kV and 1 nA, as observed in Figure 17 (d). The final annular mill was done with a 1.5 μm outer diameter and 0.2 μm inner diameter and a FIB current of 50 pA, as shown in Figure 17 (e).
6. Finally, the Pt on the tip of the APT needle and any Ga-induced damage was removed, with an ion beam of 2 kV and 1 nA, leaving a sharp APT needle, as shown at high magnification in Figure 17 (f).

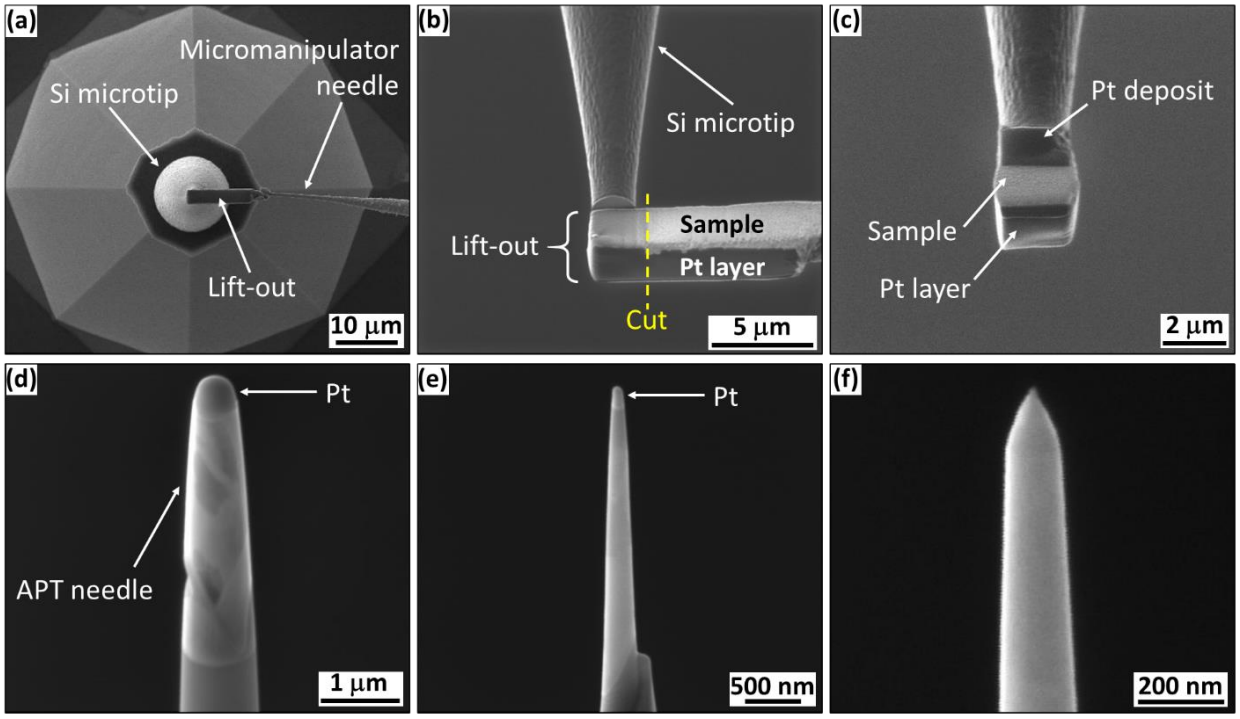

Figure 17: Images acquired in the FIB-SEM during *in situ* lift-out preparation of FIB needles showing (a) the lift-out attached to the micromanipulator needle just before being mounted on the Si microtip, as viewed from the top (i.e., Si microtip is pointing out of the page) and (b) as viewed from the side; (c) the sample after being attached to the Si microtip and cut free from the rest of the lift-out; (d) the APT needle after the first annular mill; (e) the APT needle after the final annular mill and (f) the APT needle after removal of the Pt deposit at the tip.

3.5.7.2. APT sample analysis

The APT needles were characterized using a CAMECA Local Electrode Atom Probe (LEAP) 4000X HR located at the CNMS at ORNL, operated by Dr. Jonathan Poplawsky. APT needles with tip radii of approximately 30-50 nm were analyzed at 30 K, with a laser pulse rate of 200 kHz, a laser pulse energy of 25-50 pJ, and a detection rate of 0.5 %. Typically, 2-10 million ions were collected per needle to ensure statistical significance. APT data was processed and analyzed through the CAMECA Integrated Visualization and Analysis Software (IVAS) version 3.8. Peaks in the APT mass spectra were ranged according to traditional mass ranging methods [136], and the resulting data was investigated in the form of:

- Atom maps: showing the atomic distribution of different elements in the APT needle.
- Isoconcentration surface maps (isosurfaces): showing surfaces containing particular atomic composition thresholds.
- Proximity histograms (proxigrams): showing unidimensional concentration profiles with respect to distance from the interfaces identified in the isosurfaces.

3.6. Micro-mechanical testing

3.6.1. Vickers microhardness

The Vickers microhardness (HV) is determined by measuring the diagonals of a square-shaped indent performed in a material with a four-sided diamond pyramidal indenter [137]. Indentation loads for HV testing can range between 10 and 1000 gram force (gf), and they are applied for a predefined time, known as dwell time, which typically ranges between 5 and 20 s. To obtain reliable HV data, it is crucial that the sample surface is flat and perpendicular to the indenter. In addition, to prevent the effect of the residual plastic zone, the distance between two HV indents, or an indent and the edge of the test material, must be at least 2.5 times the diagonal of the indentation, as indicated in ASTM E384: Standard Test Method for Microindentation Hardness of Materials [137].

All the HV measurements in the HPT-processed samples were performed, with a load of 50 gf and a dwell time of 5 s, at the cross-section (radial-thickness plane), along the sample diameter, using a Clark CM-800AT microhardness tester. For the Zn-10Mg HPT hybrids, the HV values were reported every 200 μm as the average between three individual indents located 50 μm apart from each other. These HV values were plotted against their distance from the center of the sample to investigate the HV variation across the diameter. In addition, for all the Zn-Mg HPT hybrid and

alloy samples, HV values were recorded over the entire cross-section by following a rectilinear grid pattern at a uniform incremental spacing of 150 μm in the horizontal (radial) and vertical (thickness) directions, as shown in Figure 18. This resulted in a 4 x 65 matrix of hardness indents containing a total number of 260 different HV values for each of the investigated samples. The resulting HV datasets were plotted using Origin software, without any averaging or manipulation, in the form of color-coded contour maps to provide a two-dimensional representation of the HV distribution across the diameter and the thickness of the samples.

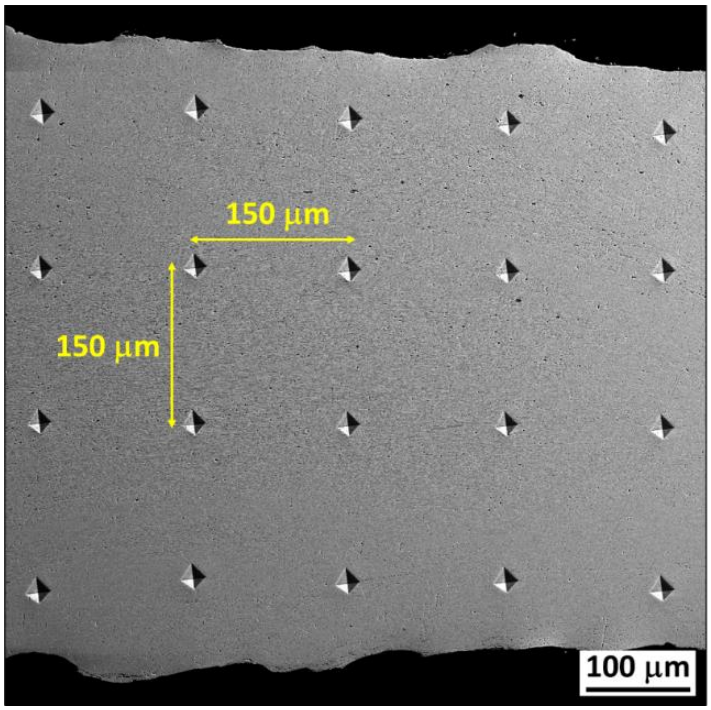

Figure 18: SE-SEM image showing a portion of the rectilinear grid pattern of HV indents performed at the cross-section of the Zn-3Mg HPT alloy after 30 turns. Note the 150 μm separation between neighboring indentations.

The average hardness of the pure Zn, pure Mg, as-cast Zn-3Mg alloy, and homogenized Zn-3Mg alloy was measured, using 100 gf and 10 s dwell time, from at least 10 individual HV indents at different locations across the disk surface (shear-radial plane).

3.6.2. Berkovich nanoindentation

Berkovich nanoindentation is used for the evaluation of the local mechanical properties at the nanoscale. The three-sided pyramidal shape of the Berkovich indenter induces plasticity at very small loads (i.e., in the order of mN), which enables a meaningful measurement of different properties such as hardness, Young's modulus, strain rate sensitivity, and activation volume of local regions of the microstructures [138].

Nanoindentation experiments were performed at constant strain rate (CSR) at the mid-thickness of the cross-section (i.e., radial-thickness plane), near the periphery (~ 1 mm away from sample edge) of the Zn-3Mg HPT hybrid samples after 30 turns, and 30 turns + PDA. An MTS nanoindenter XP equipped with a Berkovich tip having a centerline-to-face angle of 65.3° was used for all the experiments. A nanoindentation method was developed within the nanoindenter software in order to perform CSR experiments, according to the proportional loading protocol described by Lucas and Oliver [138]. Equation 7 indicates the relationship between the indentation strain rate ($\dot{\varepsilon}_i$), the indentation depth (h), the indentation load (P), and the indentation hardness (H).

$$\dot{\varepsilon}_i = \frac{\dot{h}}{h} = \frac{1}{2}\left(\frac{\dot{P}}{P} - \frac{\dot{H}}{H}\right) \approx \frac{\dot{P}}{2P} \qquad \text{Equation 7}$$

The indentation strain rate ($\dot{\varepsilon}_i$) can be directly expressed as a function of the indentation load (P) and the loading rate ($\dot{P}$). In the CSR nanoindentation method developed, $\dot{\varepsilon}_i$ was defined as an input, such that $\dot{P}/P = 2\dot{\varepsilon}_i$ was constant during loading and unloading for each test, according to Equation 7. The nanoindentation method consisted of an initial loading segment at a specific CSR to a prescribed maximum load (P_{max} = 50 mN), which was maintained during a hold segment of 10 s, followed by unloading at the same CSR. The experimental indentation strain rates ($\dot{\varepsilon}_i$ =

0.0125, 0.025, 0.05, 0.1 s^{-1}) were equivalent to uniaxial strain rates (ε = $1.25 \cdot 10^{-4}$, $2.5 \cdot 10^{-4}$, $5.0 \cdot 10^{-4}$, and $1.0 \cdot 10^{-3}$ s^{-1}) as determined from the empirical relationship ($\varepsilon = 0.01\dot{\varepsilon}_i$) described in [139,140]. The value selected for the Poisson ratio was 0.24, according to that of pure Zn [141]. The CSR nanoindentation method was validated for the different strain rates investigated, as shown in Figure 19 (a, b, c, and d) for $\dot{\varepsilon}_i$ = 0.0125, 0.025, 0.05, and 0.1 s^{-1}, respectively. It can be observed that a constant $\dot{P}/P$ value, equivalent to $2\dot{\varepsilon}_i$, is maintained during the loading segment. Once P_{max} is reached, the $\dot{P}/P$ value becomes zero during the load hold segment. Finally, unloading takes place at the same CSR as loading.

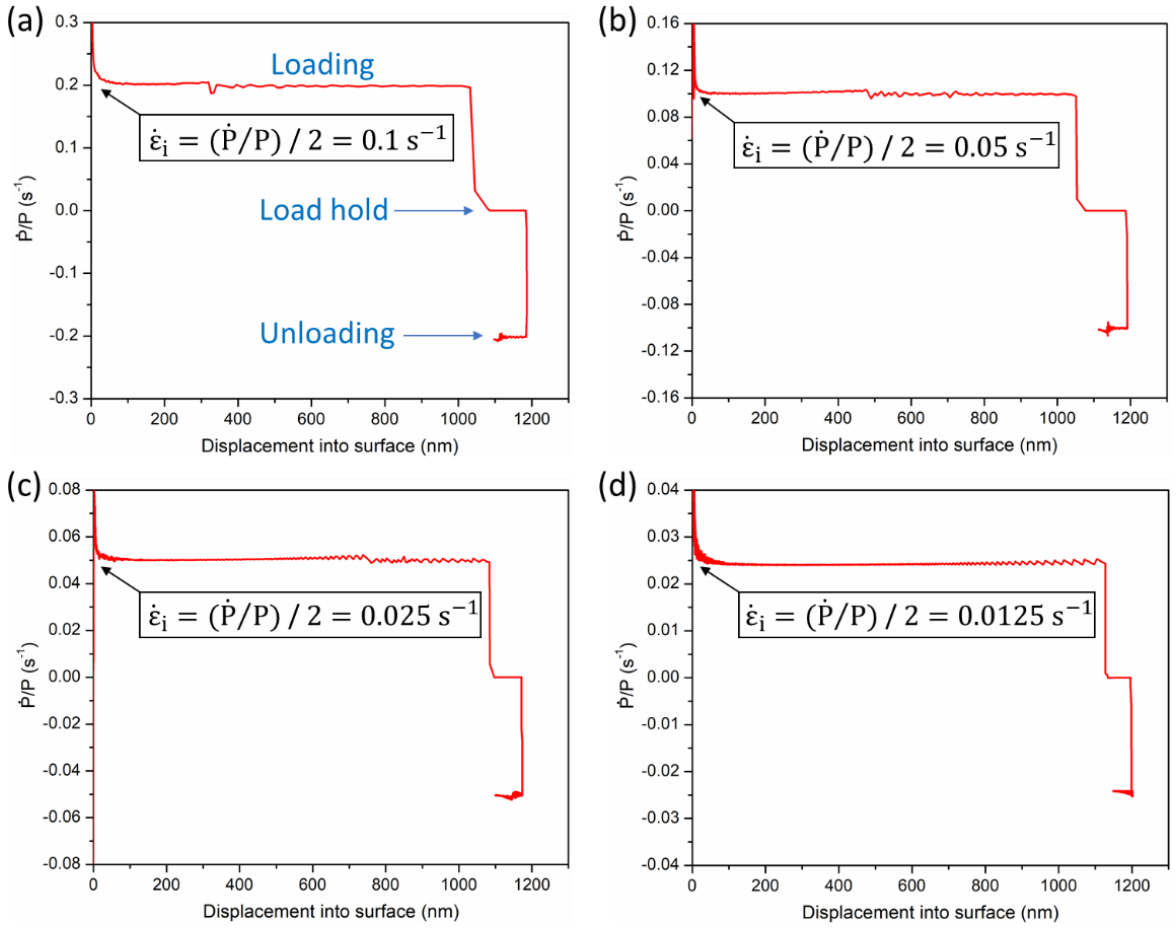

Figure 19: Validation of the CSR nanoindentation method for (a) $\dot{\varepsilon}_i$ = 0.1 s^{-1}, (b) $\dot{\varepsilon}_i$ = 0.05 s^{-1}, (c) 0.025 s^{-1}, and (d) $\dot{\varepsilon}_i$ = 0.0125 s^{-1}. Note that the relation $\dot{P}/P = 2\dot{\varepsilon}_i$ is maintained during the loading and unloading segments, and that $\dot{P}/P = 0$ during the load hold segment, as desired.

A rectilinear array of 12 individual measurements was performed for each of the four CSR examined, with a separation of 30 μm, in both horizontal (radial) and vertical (thickness) directions between neighboring indents, as highlighted in yellow in Figure 20 (a). It was noted that the nanoindenter sometimes failed to detect the surface (when the drift rate of the system exceeded the predefined allowable drift rate of 0.1 nm/s for 50 s) and skipped some measurements, as indicated in white in Figure 20 (a). However, at least 10 individual indents were performed for each of the CSR studied. A detail of a Berkovich indent on the Zn-3Mg HPT hybrid after 30 turns is shown in Figure 20 (b).

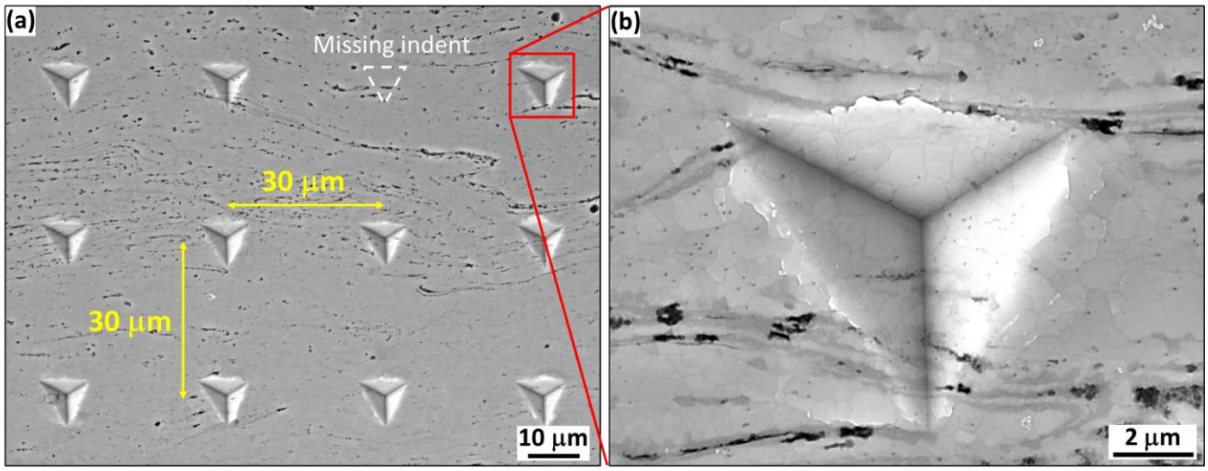

Figure 20: SE-SEM photomicrographs showing (a) a rectilinear array of Berkovich indents, with a separation of 30 μm, performed on the periphery of the Zn-3Mg HPT hybrid after 30 turns. Note that the highlighted "missing indent" was a result of a surface detection error; (b) high-magnification view of an indent illustrating the fine nature of the grains, many of which with sizes below 1 μm.

The nanoindentation data was collected from load on sample vs. displacement into surface curves, which will be referred to as "load-displacement curves" hereafter. The slope of the unloading curve at maximum load, known as the unloading stiffness (S), was calculated with Origin software using a rectilinear fit from the initial unloading portion (from 50 to 30 mN approximately) of the load-displacement curves. Together with S, the area coefficients given by the nanoindenter upon

calibration (C_1 and C_2), and the maximum displacement at peak load (h_{max}) were used to calculate the projected contact area at maximum load (A) using Equation 8, which was in turn obtained from Equation 9 to Equation 11 [142].

$$A = 24.56 \cdot {h_c}^2 + C_1 \cdot {h_c}^1 + C_2 \cdot {h_c}^{1/2} \quad \text{Equation 8}$$

$$h_c = h_{max} - h_s \quad \text{Equation 9}$$

$$h_s = \varepsilon \cdot \frac{P_{max}}{S} \quad \text{Equation 10}$$

$$S = \frac{\partial P}{\partial h} (\text{at } P_{max}) \quad \text{Equation 11}$$

Where h_c is the vertical distance along which contact is made, h_s is the displacement of the surface at the perimeter of the contact [143], and ε is a coefficient equivalent to 0.75 for Berkovich indentation [144]. Note that C_1 and C_2 account for the bluntness of the Berkovich tip, and would be theoretically zero for a perfect tip [145]. After calculating A, the hardness (H) was computed using Equation 12 at the different CSR according to the Oliver-Pharr method [143]. The standard deviation between H values was calculated following the error propagation rules for uncertainty [146].

$$H = \frac{Pmax}{A} \quad \text{Equation 12}$$

The strain rate dependence during plastic deformation was evaluated through the strain rate sensitivity (m), which was determined from H and $\dot{\varepsilon}_i$ values using Equation 13, and considering Tabor´s empirical relationship where the flow stress (σ_f) is equivalent to H/3 for fully plastic deformation at a given CSR [147]. The mechanisms of plastic deformation were estimated through

the activation volume (V^*), which was calculated from m and H values using Equation 14, where k is the Boltzmann's constant and T is the testing temperature [148].

$$m = \left(\frac{\partial \ln \sigma_f}{\partial \ln \dot{\varepsilon}}\right)_{\varepsilon,T} = \left(\frac{\partial \ln(H/3)}{\partial \ln(0.01 \cdot \dot{\varepsilon}_i)}\right)_{\varepsilon,T} \quad \text{Equation 13}$$

$$V^* = \sqrt{3}kT \cdot \left(\frac{\partial \ln \dot{\varepsilon}}{\partial \sigma_f}\right) = \sqrt{3}kT \cdot \left(\frac{\partial \ln(0.01 \cdot \dot{\varepsilon}_i)}{\partial (H/3)}\right) = \frac{3kT\sqrt{3}}{mH} \quad \text{Equation 14}$$

3.7. Electrochemical testing

To investigate the corrosion resistance of Zn-Mg HPT hybrids in a physiological environment, electrochemical testing was carried out in a three-electrode cell coupled with Gamry potentiostat (Ref-3000) and analyzed using the Gamry Echem Analyst software. Electrochemical testing and analysis were performed by Dr. Zia Ur Rahman at Central Michigan University, from Dr. Waseem Haider´s group, as part of a collaborative work project. Before the electrochemical experiments, the Zn-10Mg HPT hybrid samples after 1, 15, and 30 turns were polished to the mid-thickness plane up to 1200 grit size SiC paper. For the three-electrode cell set-up, the Zn-Mg HPT disks, a saturated calomel electrode (SCE), and a graphite rod were used respectively as the working, reference, and counter electrodes. The surface area of the samples was electrically connected with a Cu wire to the potentiostat and sealed with a rubber ring, such that a constant area of 0.5 cm^2 was exposed to the testing electrolyte during all the experiments. Simulated body fluid (SBF) prepared from Kokubo´s recipe: NaCl 8.035 g/L, $NaHCO_3$ 0.355g/L, KCl 0.225 g/L, $K_2HPO_4 \cdot 3H2O$ 0.231 g/L, $MgCl_2 \cdot 6H20$ 0.311 g/L, $CaCl_2$ 0.292 g/L and Na_2SO_4 0.072 g/L, was used as testing electrolyte. The electrochemical interaction of the samples with SBF was

investigated at 37 °C in a 5% CO_2-controlled atmosphere inside a humidified incubator to mimic physiological conditions. All the electrochemical tests described below were carried out in triplicate to ensure reproducibility.

Open circuit potential (OCP) measurements were performed for 10 h to achieve surface stability, when the potential difference between the working and reference electrode, in the absence of any external current, remained relatively stable. After OCP stabilization, potentiodynamic polarization (PDP) was studied at a scan rate of 5 mV/s and a potential range from - 0.5 to 1.5 V vs. SCE. From Tafel linear approximation of the anodic and cathodic branches of the PDP curves, the corrosion potential (E_{corr}), the corrosion current density (I_{corr}), and the anodic and cathodic Tafel constants, βa and βc, respectively, were determined. The corrosion rate (CR) was calculated from the I_{corr} according to ASTM G102-89: Standard Practice for Calculation of Corrosion Rates and Related Information from Electrochemical Measurements [149] using Equation 15:

$$CR = 3.27 \cdot 10^{-3} \frac{I_{corr}\, EW}{\rho} \qquad \text{Equation 15}$$

Where CR is measured in (mm/year) when I_{corr} is given in ($\mu A/cm^2$), EW is the equivalent weight (i.e., 30.6 for a Zn-10Mg (wt.%) alloy), and ρ is the density (i.e., 6.6 g/cm^3 for a Zn-10 Mg (wt.%) alloy). Electrochemical impedance spectroscopy (EIS) was performed in the frequency range from 10 mHz to 100 kHz using a sinusoidal potential perturbation of 10 mV_{rms}. The impedance data was analyzed using Gamry Echem Analyst to obtain the electrical parameters describing the electrode/electrolyte interface, as well as the Nyquist and Bode diagrams. Electrical equivalent circuit (EEC) models simulating the electrochemical reactions that occurred at the disk surfaces were developed by fitting the experimental EIS data.

3.8. Development and characterization of biodegradable coatings

As highlighted in section 2.1.1, local and systemic toxicity of Zn might be a concern for absorbable biomedical implants, as the recommended dietary allowance for Zn is only 15-40 mg/day, which is much lower than that of Mg (300-400 mg/day) [29]. Moreover, cytotoxicity has been reported in different *in vitro* studies, including human bone cell lines [150,151], as well as vascular cell lines [36,44]. Therefore, the study of surface modification techniques able to control the release of Zn^{2+} ions during degradation is important for minimizing the toxicity of Zn-based implants. In this dissertation, different coatings were synthesized onto as-homogenized Zn-3Mg alloy substrates with the goal of controlling the release of Zn^{2+} through a uniform corrosion rate, improving the cell attachment at the surface, and preventing bacteria colonization.

3.8.1. Synthesis of coatings

3.8.1.1. Materials

As-cast Zn-3Mg alloy bars were subjected to the homogenization heat treatment detailed in section 3.2 and cut into disks having dimensions of 10 mm diameter and 1 mm thickness. The disks were ground using SiC abrasive papers up to 1200 US grit size to obtain the samples, also referred to as "Zn-3Mg substrates" hereafter, that were coated as detailed in the next three sections.

For the synthesis of the coatings, the following reagents were used. Zinc nitrate hexahydrate ($Zn(NO_3)_2{\cdot}6H_2O$), phosphoric acid (H_3PO_4), and sodium hydroxide (NaOH) were purchased from Sigma Aldrich (St. Louis, MO). Collagen type I solution (3 mg/ml) PureCol was purchased from Advanced BioMatrix (Carlsbad, CA) and stored at 2-10 ºC to prevent degradation. Phosphate buffered saline (PBS) 10X was purchased from ThermoFisher Scientific (Waltham, MA).

3.8.1.2. Zinc phosphate coating

The idea to develop a zinc phosphate (ZnP) coating arose from the investigation of calcium phosphate (CaP) coatings for orthopedic applications. CaP coatings have been successfully synthesized on Zn-based substrates, exhibiting a composition consisting of carbonated apatite like that of natural bone tissue, leading to enhanced bone-forming ability and tunable degradation rates [152,153]. However, CaP coatings may not be suitable for implants located at, or near to, highly vascularized regions because of their potential adverse effect on vascular calcification [154]. Thus, ZnP coatings, whose feasibility was confirmed on metallic substrates like Ti, Fe, and Mg alloys [155] and recently on pure Zn [156], was proposed to enhance the biocompatibility and reduce the degradation rate of the present Zn-3Mg substrates.

The ZnP coating was prepared following a chemical conversion method at RT, inspired by the work of Su et al. [156] in pure Zn. The following synthesis parameters led to a uniform ZnP coating on the Zn-3Mg substrates. First, a 0.5 M H_3PO_4 solution was prepared by dissolving 7.35 g H_3PO_4 in 150 mL deionized (DI) water. Second, a 1 M NaOH solution was prepared by dissolving 1.6 g in 40 mL DI water. Third, a 0.14 M $Zn(NO_3)_2$ solution was prepared by adding 1.041 g of $Zn(NO_3)_2 \cdot 6H_2O$ in 24.622 mL DI water under magnetic stirring. Note that the zinc nitrate is hydrated, which adds 0.378 mL extra water to the solution, such that the 0.14 M $Zn(NO_3)_2$ solution volume was 25 mL. Fourth, 15 mL of the 0.5 M H_3PO_4 solution were added to the 0.14 M $Zn(NO_3)_2$ solution. The pH was adjusted from 1.37-1.47 to 2.5 by dropwise adding approximately 5 mL of the 1 M NaOH solution, bringing the solution volume to 45 mL. Finally, the total volume of the ZnP solution was adjusted to 50 mL with DI water.

Right before the coating procedure, the Zn-3Mg substrate was slightly polished with 1200 US grit size SiC paper for 20-30 s to remove any oxidation layer. Immediately after, the sample was ultrasonically cleaned for 20-30 s in ethanol (by holding the sample with tweezers), rinsed thoroughly with ethanol, and dried with a compressed air stream for 10-20 s. Then, the sample was immersed for 5 min in a beaker containing 50 mL of the prepared ZnP solution. Finally, the sample was removed from the ZnP solution, rinsed thoroughly with DI water, and dried in air. It was noted that the coating morphology was more uniform when these steps were conducted one right after the other. Therefore, the ZnP coatings were performed one at a time.

3.8.1.3. Collagen coating

After implantation, biomaterials interact with different types of cells immersed in a three-dimensional network known as the extracellular matrix (ECM), which not only provide physical scaffolding, but also trigger cellular responses like proliferation, differentiation, migration, and adhesion [157]. Collagen type I is the major component of the ECM, and thus, plays a fundamental role in the interaction between cells and the host implant. Collagen type I coatings have been developed in Ti alloys [158], Mg alloys [159], and pure Zn [156], promoting enhanced cell attachment. However, these coatings often showed a lack of uniformity across the substrate surface and involved complex synthesis protocols with aggressive chemicals that may denaturalize the collagen protein structure.

In this work, a collagen type I (Col) coating solution was applied onto Zn-3Mg substrates using the spin-coating technique for the first time. This technique enables the production of uniform thin films and potential to scale up [160]. The preparation of the Col solution was performed in sterile conditions inside a laminar flow biosafety cabinet. For that purpose, all the materials involved in

the preparation of the Col solution (i.e., pipette, pipette tips, pH paper strips, and vortex mixer) were sterilized for 15 min under ultraviolet (UV) light inside the biosafety cabinet. Note that the 0.1 M NaOH solution and the distilled water had been previously sterilized by filtering through a 0.22 μm syringe filter, and thus, were not UV sterilized. Similarly, the 10X PBS and PureCol solution (3 mg/mL) were provided in sterile conditions from the respective suppliers.

The PureCol solution was used to prepare a 3-D gel according to the manufacturer's recommendation to obtain 2 mL of Col solution. During this process, all reagents were maintained in ice to prevent the premature polymerization of the collagen. First, 1 part (0.2 mL) of chilled 10X PBS was added to 8 parts (1.6 mL) of PureCol with gentle swirling using the vortex mixer. Second, the pH of the mixture was adjusted to 7.0-7.5, monitoring the pH with paper strips by adding 0.10-0.15 mL of 0.1 M NaOH solution. Third, the final volume of the Col solution was adjusted with distilled water (0.05-0.1 mL) to a total of 10 parts. The resulting Col solution had a concentration of 2.4 mg/mL and was maintained at 2-10 ºC to prevent gelation before spin-coating. This Col solution was also diluted to 1 mg/mL to investigate an alternative collagen concentration.

For spin-coating, the Zn-3Mg substrate sample was secured in the spin-coater (Chemat Technology Spin Coater KW-4A) under vacuum. All the spin-coatings were performed at 3000 rpm for either 20 or 30 s by pipetting 150 μL of the chilled Col solution on the center of the substrate surface. The spin-coated substrate was transferred, using tweezers, to a 12-well plate and incubated for 90-120 min at 37 ºC for gelation. Spin-coated substrates were coded using a ColX_Y nomenclature, where X was the concentration of collagen in mg/mL (i.e., 1 or 2.4) and Y was the spin-coating time in s (i.e., 20 or 30). For instance, Col2.4_30 refers to the spin-coated substrate produced with a collagen solution of 2.4 mg/mL concentration for 30 s.

In addition, a dual coating consisting of ZnP and Col was developed with the goal of modifying the degradation behavior of the Zn-3Mg substrate and improving its biocompatibility simultaneously. First, the ZnP coating was developed by chemical conversion, as detailed in section 3.8.1.2. Then, the ZnP coated substrates were spin-coated with a Col solution of 2.4 mg/ml using 3000 rpm and 20 s. These samples will be referred to as "ZnP-Col" hereinafter.

3.8.1.4. Collagen-based bioactive glass nanoparticle coating

Bioactive glass coatings have been widely applied on biomedical metallic implants to improve their surface biocompatibility and bioactivity with the host tissue and overall biological performance [161]. The investigation of bioactive glass nanoparticles has gained notable interest in the last years due to their potential in medical applications as therapeutical delivery agents [162] and tissue regeneration [163]. Moreover, the composition flexibility of bioactive glasses enables the capability to introduce additional dopants for enhanced functionalities like osseointegration by Sr^{2+}[164], angiogenesis by Cu^{2+}[165], or antibacterial by Ag^{+}[166,167]. Therefore, a coating consisting of Ag-doped bioactive glass nanoparticles (AgBGN) was developed in this work with the aim of enhancing the biocompatibility and antibacterial properties of the Zn-3Mg substrate simultaneously.

The AgBGN used to develop the coatings were previously synthesized by a modified Stöber method with a composition of SiO_2 59.6 – CaO 25.5 – P_2O_5 5.1 – Al_2O_3 7.2 – Ag_2O 2.2 (wt. %) were generously provided by Dr. Xanthippi Chatzistavrou. These AgBGN were surface-functionalized with polyethylene glycol (PEG) to facilitate nanoparticle dispersion in a matrix of 2.4 mg/ml Col solution in order to obtain a more uniform coating. This Col-based AgBGN coating will be referred to as "Col-AgBGN" hereafter and was prepared as follows. First, 20 mg of AgBGN

were dispersed in 20 mL of distilled water under agitation at 500 rpm. Second, 400 μL of a 10 mM PEG solution in H_2O were added into the 1 mg/mL AgBGN solution and mixed at 500 rpm for about 30 min. Third, the AgBGN-PEG mixture was centrifuged, the supernatant was discarded, and 4 mL of distilled water was added to obtain a 5 mg/mL solution of AgBGN-PEG. Fourth, 1 mL of the 5 mg/mL AgBGN-PEG solution was centrifuged for 2 min at 1000 rpm, and the supernatant was replaced by 1 mL of 2.4 mg/mL Col solution. Finally, 130 μL of the resulting Col-AgBGN solution were added onto the center of the Zn-3Mg substrate and spin-coated for 20 s at 3000 rpm.

3.8.2. Microstructural characterization of the coated samples

3.8.2.1. Scanning electron microscopy

A JEOL JSM-7500F SEM coupled with an Oxford EDS system located at the Center of Advanced Microscopy at MSU was used to examine the morphology and to estimate the chemical composition of the coatings, which was further investigated by grazing incidence XRD. EDS elemental maps were acquired at an accelerating voltage of 10 kV and a working distance of 8 mm in the ZnP-coated samples to investigate the elemental distribution. A Zeiss Auriga FIB-SEM was used to mill a portion of the coatings to estimate their thickness.

In order to preserve the structure of the Col-containing samples (i.e., Col, ZnP-Col, and Col-AgBGN) during SEM imaging, they were previously dehydrated and dried in a controlled manner as specified below. It should be noted that failure to conduct these steps would have destroyed the structure of the water-containing samples under vacuum during SEM imaging.

The dehydration procedure consisted of immersing the Col-containing samples in a series of ethanol/distilled water dilutions of 25%, 50%, 75%, and 100% (three times) (vol. %) for 10 min each. The samples were directly transferred from one dilution to the next every 10 min, preventing them from drying in between dehydration steps. Immediately after dehydration, the samples were dried by hexamethyldisilazane (HMDS) evaporation through a series of immersion steps in ethanol/HMDS dilutions of 33%, 50%, 66%, and 100% (two times) (vol. %) for 15 min each. Like in the dehydration process, the samples were transferred from one dilution to the next one every 15 min. When the samples were immersed in the last step of 100% HMDS, the 24-well plate was left capped loosely in the fume hood overnight for HMDS evaporation. It must be emphasized that all steps involving HMDS manipulation were carried out in the fume hood wearing the necessary personal protective equipment, as it is highly toxic. After drying, the samples were sputtered coated with a Pt target for 30 s at 30 mA by using a Denton Desk II sputter coater to prevent surface charging during SEM imaging.

3.8.2.2. Grazing incidence X-ray diffraction

Grazing incidence X-ray diffraction (GIXRD) enables the characterization of thin films and coatings by using small incident angles for the incoming X-ray beam, such that the penetration depth of X-rays is very limited, and thus, diffraction information is highly surface sensitive. Unlike in the Bragg-Brentano configuration shown in Figure 16 (a), in the GIXRD scan, the incident grazing angle is fixed while the detector rotates over a 2θ range. In GIXRD, the critical angle of a material is defined as the incident angle below which the X-ray is fully reflected from the material surface. Therefore, a GIXRD measurement with a grazing incidence angle close to the critical angle would be inherently probing the material surface. Under this condition, the incident X-ray

is nearly parallel to the material surface, and typical grazing incidence angles are between 0.2-2 º [168].

GIXRD was performed in the uncoated and ZnP coated samples (before and after the immersion testing described in section 3.8.3) using the instrument and scanning parameters detailed in section 3.5.6. The critical angle (Θ_c) was calculated in degrees by using Equation 16 [168], from the X-ray refractive index of the material (δ), which was previously obtained using the online tool (https://henke.lbl.gov/optical_constants/getdb2.html)

$$\Theta_c = \sqrt{2\delta} * \frac{180}{\pi} \qquad \text{Equation 16}$$

For the stoichiometric composition of ZnP, $Zn_3(PO_4)_2$, a δ value of $2.16 \cdot 10^{-5}$ was obtained, which resulted in a Θ_c value of 0.377 º. Thus, a minimum Θ_c value of 0.38 º was chosen for all the GIXRD scans.

3.8.3. *In vitro* degradation and corrosion resistance of coated samples

The *in vitro* degradation behavior and corrosion resistance were evaluated by immersion of the samples for 21 days in Dulbecco´s Modified Eagle´s Medium (DMEM) from Sigma Aldrich (St. Louis, MO). Immersion testing was performed inside an incubator at 37 ºC, and half of the DMEM immersion volume was refreshed, after measuring the pH, every other day to mimic physiological conditions. The used immersion medium extracted every two days was collected and stored at 4 ºC. Two conditions of the Zn-3Mg alloy substrates, uncoated and ZnP coated, were studied in triplicate to ensure reproducibility. The rationale for not testing the Col-coated samples was that the Col coating was expected to degrade very rapidly in a physiological environment, and thus, not play a relevant role in the corrosion resistance.

The ratio between the immersion volume and the exposed surface area was 20 mL/cm^2, according to ASTM G31-12a: "Standard Guide for Laboratory Immersion Corrosion Testing of Metals" [169]. Thus, since the total exposed surface area of each sample was ~ 1 cm^2, each sample was initially immersed in 20 mL DMEM, and 10 mL were refreshed every 2 days. During the immersion test, samples were placed inside individual 36 mm diameter plastic containers, such that they stayed isolated from each other for the duration of the test. Containers remained capped during the whole immersion experiment, except during the media replacement, to prevent DMEM degradation.

Three time points (day 6, 12, and 21 of immersion) were used to estimate the corrosion rate. Two time points (day 6 and 21 of immersion) were used to examine the surface characteristics by SEM and compositional changes by EDS. As mentioned earlier, GIXRD was performed before and after the immersion test (day 21). After 6, 12, and 21 days of immersion, triplicate samples for each material condition were taken out of the immersion test, rinsed thoroughly with distilled water, and air-dried at RT completely before being weighted on a precision scale. The corrosion products of the samples were removed by ultrasonic cleaning with a solution of 200 g/L CrO_3 in water, according to ASTM G1-03: "Standard Practice for Preparing, Cleaning, and Evaluating Corrosion Test Specimens" [170]. Then, samples were rinsed with distilled water and weighted to estimate the corrosion rate using Equation 17 [170]:

$$CR = K\frac{w_i - w_f}{A\,t\,\rho} \qquad \text{Equation 17}$$

where CR is the corrosion rate in μm/year, K is a time conversion coefficient equal to $8.76 \cdot 10^7$, w_i and w_f are the initial and final weight of the sample in g, A is the sample area exposed to solution in cm^2, t is the immersion time in h, and ρ is the density of the material in g/cm^3.

3.8.4. Cytocompatibility evaluation of coated samples

The cell viability and proliferation in bulk samples can be investigated by either direct or indirect contact methods. The direct contact method consists of seeding cells at the surface of the sample, while in the indirect, cells are exposed to the degradation products of the sample. In this project, the indirect method was performed by exposing cells to the sample extracts at different concentrations to prevent any potential cross-reaction between the Zn-3Mg alloy substrate and the cell counting assays. Three different samples were evaluated: uncoated, ZnP, and Col-AgBGN. Note that uncoated samples refer to the Zn-3Mg alloy substrate *per se*. The tests were performed in triplicates for statistical analysis. This *in vitro* cell work and data analysis was carried out in collaboration with Dr. Kurt Hankenson´s group from the Department of Orthopedic Surgery at University of Michigan and Dr. Xanthippi Chatzistavrou at MSU.

3.8.4.1. Preparation of sample extracts

UV-sterilized samples (i.e., uncoated, ZnP coated, and Col-AgBGN coated) were immersed for 3 days in cell culture medium inside an incubator at 37 ºC and 5% CO_2 with a surface area to volume ratio of 1.25 cm^2/mL, as recommended by ISO 10993-5: "Biological evaluation of medical devices - Tests for *in vitro* cytotoxicity" [171]. The cell culture medium contained 16.5 % fetal bovine serum (FBS), 1 % Antibiotic/Antimycotic, and 1 % L-glutamine in α-minimum essential medium (α-MEM (-)). All the extracts were collected after 3 days of immersion. Sterile conditions were maintained at all times.

A minimum of 6-fold to a maximum of 10-fold dilution of extracts for indirect *in vitro* cytotoxicity tests has been reported to be close to the real environment in the human body [172]. Even though this recommendation was originally made for Mg-based materials, researchers in Zn-based

materials since 2015 have been using the same approach consistently. Thus, the following three extract dilutions were prepared, from each of the three material conditions, by diluting their corresponding extracts in fresh cell culture medium and stored at 4 ºC before use.

- 10-fold: 10 % extract concentration
- 6-fold: 16.7 % extract concentration
- 4-fold: 25 % extract concentration

3.8.4.2. Preparation of cell culture

Human marrow stromal cells (hMSC) 7043L were purchased from the Center for Gene Therapy, Tulane University. Cells were thawed and propagated at 3000-5000 cells/cm^2 in cell culture medium inside a humidified incubator at 37 ºC and 5% CO_2. Cells were expanded in T75 flasks, with renewal of cell medium every 2-3 days. When the cells reached 80 % confluency (i.e., 80 % of the surface of the flask covered with cells), the medium was aspirated, and the cells were washed with PBS and lifted from the flask bottom by the enzymatic action of trypsin for 2-3 min. Then, an equivalent volume of fresh media was added to stop trypsin activity, and the suspended cells were collected in a 50 mL tube and centrifuged for 5 min at 1200 rpm. The supernatant was discarded, and the cell pellet was resuspended in fresh media for cell counting using a hemocytometer. After calculating the cell density in the cell suspension, cells were plated at specific cell densities either in 12-well or 24-well plates. Cells for these *in vitro* studies were used in passage 4 to 6.

3.8.4.3. Evaluation of cell proliferation

Prior to the indirect contact proliferation assay with the sample extracts dilutions, a preliminary cell proliferation study was performed to monitor the proliferation of hMSC cells at different cell densities, as well as their physical appearance in conventional culture media under optical microscopy.

For the preliminary cell proliferation test, cells at passage 4 were seeded at 10^4, $2 \cdot 10^4$ and $4 \cdot 10^4$ cells/well in a 12-well plate, corresponding to cell densities of $2.5 \cdot 10^3$, $5 \cdot 10^3$ and 10^4 cells/cm^2. Cell proliferation was evaluated at four time points: 2, 4, 7, and 9 days after seeding, refreshing the medium every 2 days. The test was performed in triplicates for statistical analysis. This preliminary experiment aid in the selection of the optimum cell density to work with in the indirect contact test.

Cell proliferation was assessed using a Cell Counting Kit-8 (CCK-8) colorimetric assay (abcam, ab228554), which enables the determination of viable cells upon reduction of a water-soluble tetrazolium (WST-8) salt in the presence of cellular dehydrogenases to give an orange formazan dye. The amount of formazan dye generated by cellular dehydrogenases is directly proportional to the number of live cells. CCK-8 assay was used by adding CCK-8 solution to the cell-containing wells, such that the volume of the CCK-8 solution added was always 10 % of the total volume of the well (i.e., 100 μL CCK-8 solution added to a well with 1 mL). The culture plates containing the CCK-8 solution were incubated at 37 ºC for 3 h. Then, 100 μL aliquots of each well were transferred to a 96-well, and the absorbance, or optical density (OD), was measured at 460 nm.

For the indirect contact proliferation assay, cells at passage 6 were seeded at $5 \cdot 10^3$ cells/well in 24-well plates, corresponding to a cell density of $2.5 \cdot 10^3$ cells/cm^2, in 0.5 mL/well. After allowing

24 h for cell attachment, the cell medium was replaced by the sample extracts. As shown in Figure 21, three different 24-well plates were used, one for each type of sample extract (i.e., uncoated, ZnP and Col-AgBGN), and every plate had its own control. Note that each extract was tested in triplicates for statistical analysis. For each 24-well plate, the wells in rows A, B, and C contained extracts with 10-fold, 6-fold, and 4-fold dilutions, respectively, whereas the wells in row D contained cell medium. All the cellular wells were refreshed every two days with the same media. It should be noted that the wells in column 4 did not contain any cells, such that the OD values measured from these acellular wells after addition of the CCK-8 solution were considered background absorbance and thus, subtracted from those of their respective cellular wells. Cell proliferation was evaluated by CCK-8 measurements at three time points: 2, 4, 6 days after adding the extracts the first time. The student's t-test was used to determine the statistical significance among different extract concentrations, as well as between extracts and the control, with a p-value < 0.05. Cellular health assessment was carried out by optical microscopy at every time point.

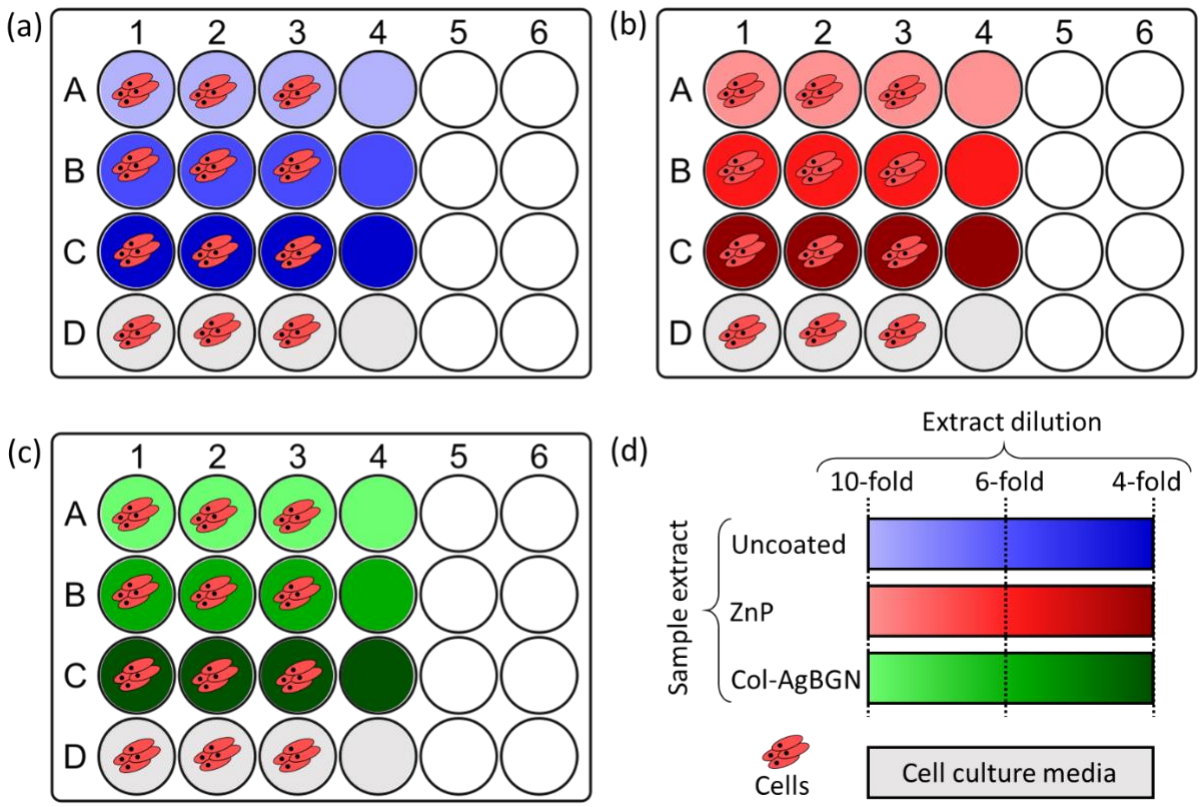

Figure 21: Experimental setup for the indirect contact *in vitro* proliferation assay with sample extracts from (a) uncoated, (b) ZnP coated, and (c) Col-AgBGN coated samples; (d) Key to interpret the different colors and tones in the 24-well plates displayed in (a), (b) and (d).

3.8.5. Antibacterial adhesion and viability assessment of coated samples

The implantation of foreign material in the body is followed by a colonization competition between microorganisms (i.e., bacteria, viruses, etc.) and host cells, a process known as the "race for the surface". In this section, the ability of Zn-3Mg alloy substrates to resist bacteria colonization was evaluated *in vitro*. Samples with four different coatings were examined: ZnP, Col, ZnP-Col, and Col-AgBGN. Uncoated samples, as well as untreated bacteria (i.e., bacteria dispersed in medium), served as controls. The tests were performed in triplicates for statistical analysis.

Methicillin-resistant *Staphylococcus aureus* (MRSA) was the bacterium selected for this experiment, as it is one of the most predominant strains in implant-related infections. The *in vitro*

antibacterial work and data analysis were performed in collaboration with Dr. Xanthippi Chatzistavrou´s group from the Department of Chemical Engineering and Materials Science and Dr. Neal Hammer´s group from the Department of Microbiology and Molecular Genetics at MSU. Manipulation of live bacteria was performed by Natalia Pajares from Dr. Chatzistavrou´s group.

3.8.5.1. Preparation of bacteria culture

Laboratory-derived MRSA USA300 JE2 [173] was streaked in tryptic soy agar and grown at 37 °C overnight. Then, an isolated colony was propagated to stationary phase in 5 mL of tryptic soy broth (TSB) under agitation (~ 230 rpm) at 37 °C overnight. The bacteria culture was centrifuged and washed twice in PBS before their use. Next, 1 mL of bacteria solution in TSB was prepared with a concentration of ~ 10^7 colony forming units (CFU)/mL by adjusting the optical density of the bacteria suspension at 600 nm ($OD_{600\ nm}$) to 0.5 applying Equation 18.

$$C_1 V_1 = C_2 V_2 \qquad \text{Equation 18}$$

C_1 and C_2 correspond to the $OD_{600\ nm}$ of the initial and desired bacteria suspension, respectively. V_1 corresponds to the volume of the initial bacteria suspension required to achieve a final volume (V_2) with the desired bacteria concentration (C_2). In this case, $C_2 = 0.5$ and $V_2 = 1$. After measuring the $OD_{600\ nm}$ of the original bacteria suspension (C_1), the volume of that solution required to achieve the desired bacteria concentration (V_1) was calculated.

3.8.5.2. Assessment of bacteria viability in suspension

The capability of the different samples (i.e., uncoated and coated substrates) to resist MRSA colonization was evaluated by immersing them in 1 mL of the bacteria suspension (OD = 0.5) in TSB prepared as detailed in section 3.8.5.1. UV-sterilized samples were placed in triplicate in a

non-adherent 24-well plate (Nunclon™ Sphera™, ThermoFisher Scientific) to prevent bacterial adhesion to the bottom of the wells. In addition, 1 mL of the bacterial suspension was added to three empty wells for control (i.e., untreated bacteria), as sketched in Figure 22.

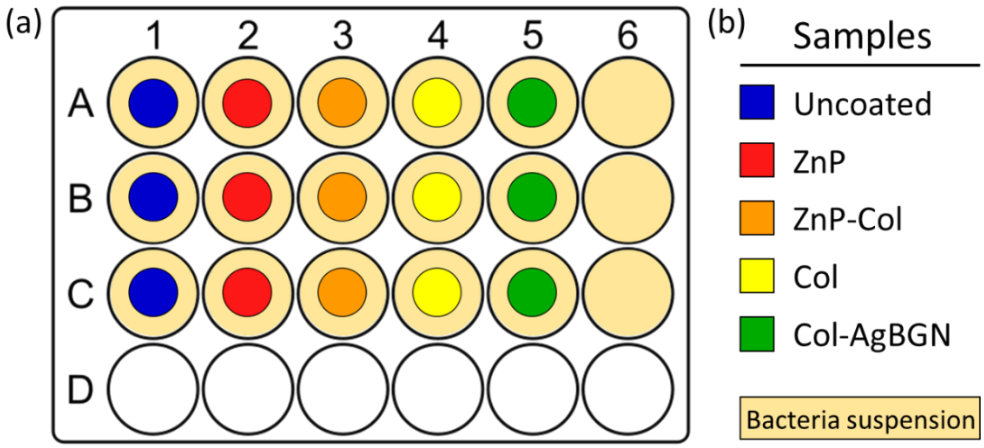

Figure 22: (a) Experimental setup for the assessment of bacteria viability in suspension; (b) key to interpreting the different colors in the 24-well plate shown in (a). The small colored circles in columns 1 to 5 in the 24-well plate represent the different samples, whereas column 6 contains untreated bacteria.

The 24-well plate was incubated at 37 ºC for 7 days. The concentration of bacteria in each of the wells was evaluated after 1, 2, 3, 5, and 7 days by measuring the absorbance of a 10-fold dilution of the culture in a spectrometer at $OD_{600\ nm}$. The concentration of these bacteria suspensions can be correlated to bacteria colonization in the sample surface. For example, a higher concentration of bacteria in suspension would indicate a more impaired attachment to the sample.

3.8.5.3. Evaluation of the viability of bacteria adhered to coated surfaces

The bacteria colonization was also evaluated by analyzing the status of the bacteria adhered to the sample surface. A live/dead BacLight™ Bacterial Viability Kit (L7012, ThermoFisher Scientific) was used for staining the samples according to manufacturer recommendations. Briefly, a solution

of propidium iodide and SYTO 9 stains was prepared such that bacteria with intact cell membranes stain fluorescent green, whereas bacteria with damaged membranes stain fluorescent red.

First, the samples were collected after 7 days of incubation in bacteria suspension, as described in section 3.8.5.2, and washed three times for 10 min each with a filtered 0.85 % NaCl solution in distilled water. Second, 0.15 mL of stain solution was added to each sample to cover its surface and incubated for 25 min at RT in the dark (i.e., by covering the 24-well plate with Al foil). Third, the stain solution was aspirated, and the samples were washed three times for 10 min with a filtered 0.85 % NaCl solution in distilled water, aspirating off after each wash. Manipulation of stained samples here on was performed in the absence of natural light, as much as possible, to prevent stain degradation.

Stained samples were fixed by immersion in a solution containing 2.5 % glutaraldehyde, 2.5 % paraformaldehyde, and 0.1 M cacodylate buffer in distilled water for 2 h at RT to kill bacteria while preserving their morphology. The fixative was aspirated, and the samples were washed once with filtered distilled water before air drying.

Samples were observed using a Nikon C2 confocal laser scanning microscope (CLSM) with a Nikon Eclipse NI-U upright configuration, located at the Center of Advanced Microscopy at MSU, with a 40x magnification Plan Fluor dry objective (numerical aperture = 0.75). The excitation/emission maxima for the stains used are 480/500 nm for SYTO 9 and 490/635 nm for propidium iodide. Therefore, SYTO 9 was excited with a 488 nm diode laser, and the green fluorescence emission was detected using a 500-550 nm bandpass filter. On the other hand, the propidium iodide was excited with a 560 nm diode laser, and the red fluorescence emission was detected using a 575-625 bandpass filter. The configuration of lasers and filters used, together with

the excitation/emission curves of the used stains, can be visualized in the relative intensity vs. wavelength plot displayed in Figure 23.

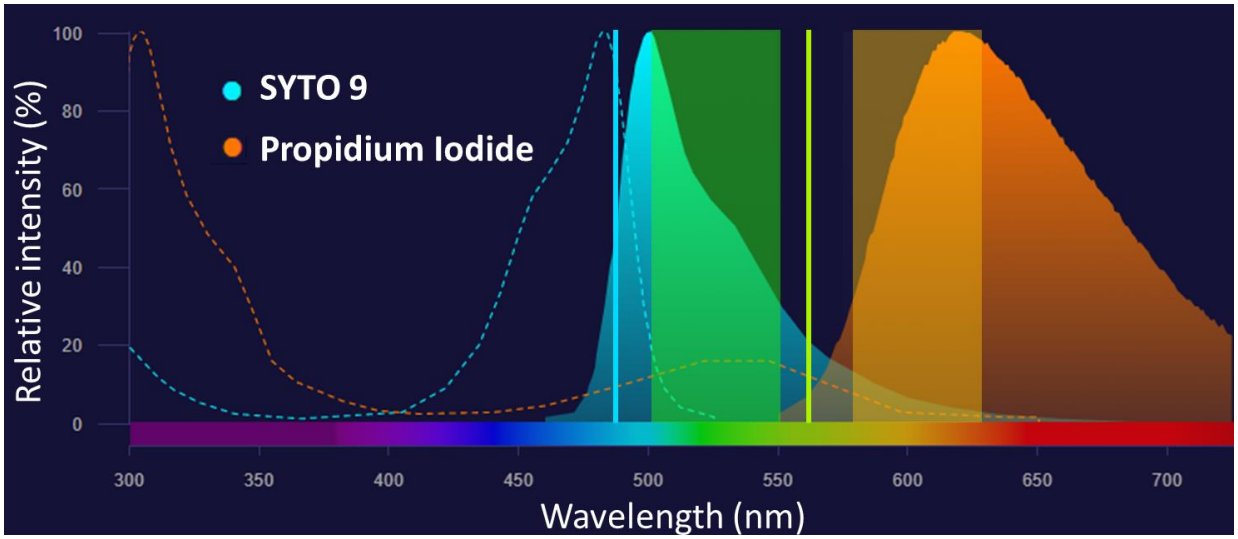

Figure 23: Configuration of lasers and filters used in CLSM for simultaneous imaging of SYTO 9 and propidium iodide stains. The dotted curves represent the excitation plots of the stains. The solid curves represent the emission plots of the stains. Vertical lines indicate the lasers used for excitation of the stains. Semitransparent rectangles indicate the bandpass filters used for detection of fluorescence. The plot was adapted from that obtained from the Thermofisher SpectraViewer software.

CLSM images, of 1024 pixels x 1024 pixels, were acquired using Kalman averaging (for noise reduction) and manipulated with the Nikon NIS-Elements software as follows. Pixel saturation was optimized in both green and red channels by using the look-up table, such that the amount of both undersaturated and oversaturated pixels was minimized before image acquisition. Thereby, the green/red fluorescent images contained the entire dynamic range of intensity values between 0 and 255 (8-bit imaging), and were representative of the live/dead bacteria, respectively. At least three representative ROIs, of 157 μm x 157 μm, were imaged for each sample, with green and red fluorescent signals in separate images, as well as both fluorescent signals combined in the same image.

The numbers of green and red pixels in the CLSM images were obtained using the "Color pixel counter" plugin for ImageJ (NIH, USA) developed by Ben Pichette, using a minimum color intensity between 10-20 (in a 1-255 scale). It should be noted that images with either green or red fluorescence only were used to calculate the number of green or red pixels, respectively, and that images with green and red fluorescence combined were not used for quantification purposes. From the number of green and red pixels counted in each image, the percentages of live and dead bacteria attached to the samples were calculated from Equation 19 and Equation 20, respectively. It should be mentioned that the percentages of live and dead bacteria reported for each sample resulted from averaging the values obtained from at least three different ROIs.

$$\text{Live bacteria } (\%) = \frac{\text{Green pixels}}{\text{Green pixels} + \text{Red pixels}} \cdot 100 \qquad \text{Equation 19}$$

$$\text{Dead bacteria } (\%) = 100 - \text{Live bacteria } (\%) \qquad \text{Equation 20}$$

Each CLSM image contained a total number of $1.05 \cdot 10^6$ pixels in an area of $2.46 \cdot 10^4$ μm^2. The total area occupied by bacteria (i.e., live and dead) in each sample was calculated by adding the number of green pixels and red pixels counted from the same ROI. From there, the bacteria density in the samples was estimated using Equation 21, assuming that a MRSA bacterium has a diameter of 0.5 μm, and thus, an area of ~ 0.2 μm^2. Lastly, the live bacteria density in the samples was estimated from the product of the bacteria density and the live bacteria, as indicated in Equation 22.

$$\text{Bacteria density } = \frac{\frac{\text{Total area occupied by bacteria}}{\text{Area of 1 bacterium}}}{\text{Area of image}} \qquad \text{Equation 21}$$

$$\text{Live bacteria density} = \text{Bacteria density} \cdot \frac{\text{Live bacteria (\%)}}{100} \qquad \text{Equation 22}$$

3.8.5.4. Observation of bacteria adhered to coated surfaces

The distribution and morphology of MRSA adhered to the sample surface were observed after 7 days of incubation, as described in section 3.8.5.2. Samples were collected from the wells and washed twice for 10 min with filtered distilled water. Then, samples were immersed for 2 h in 0.5 mL of a fixative solution containing 2.5% glutaraldehyde, 2.5% formaldehyde, and 0.1 M cacodylate buffer in distilled water to kill bacteria while preserving their morphology. Samples were washed with 0.1 M cacodylate buffer for 15 min to remove the fixative products. Next, dehydration was performed by immersing the samples in a series of ethanol/distilled water dilutions of 25 %, 50 %, 75 %, and 100 % (vol.%) for 5 min each, repeating the last step of 100% ethanol twice. After dehydration, samples were transferred to the critical point dryer (Leica Microsystem model EM CPD300), where ethanol was replaced by CO_2. Finally, the samples were coated with Os for 15 s to obtain a 10 nm conductive layer before observation in SE mode using a JEOL JSM-7500F SEM operated at an accelerating voltage of 5 kV and a working distance of 4-5 mm. Live and dead bacteria in the sample surface were identified based on their morphology in comparison with images from the literature. The density of adhered bacteria observed in the SEM was compared with that estimated from CLSM images as described in 3.8.5.3.

4. RESULTS

4.1. Zn-3Mg alloy

This section presents the microstructures and hardness results obtained from the Zn-3Mg alloy after the following processing procedures: as-cast, as-homogenized, HPT-processed for 30 turns, and HPT-processed for 30 turns and subsequent PDA (200 ºC, 1h). The evolution of the microstructure and hardness after HPT and PDA will be compared to those of the hybrid counterpart with an equivalent nominal composition (i.e., Zn-3Mg hybrid) in sections 5.4 and 5.5.

4.1.1. As-cast Zn-3Mg alloy

4.1.1.1. Microstructures of the as-cast Zn-3Mg alloy

The microstructure of the as-cast Zn-3Mg alloy exhibited a fine lamellar eutectic matrix of Zn and Mg_2Zn_{11}, as shown in the BSE-SEM photomicrographs in Figure 24 (a) and (b). Globular primary or proeutectic Mg_2Zn_{11} was also found across the microstructure, as can be distinguished in the inset of Figure 24 (b). A small amount of porosity was observed in the as-cast microstructure, as shown in Figure 24 (b). The composition of the entire ROI in Figure 24 (c), as well as that of points 1-6, was determined from EDS and is included in Table 2. The Zn and Mg EDS elemental maps from Figure 24 (c) are provided in Figure 24 (d) and (e), respectively. The composition of the dark phase in Figure 24 (c) was ~ 95Zn-5Mg (wt. %), which is reasonably close to that of the Mg_2Zn_{11} phase, whereas the light phase corresponded to Zn (see Table 2).

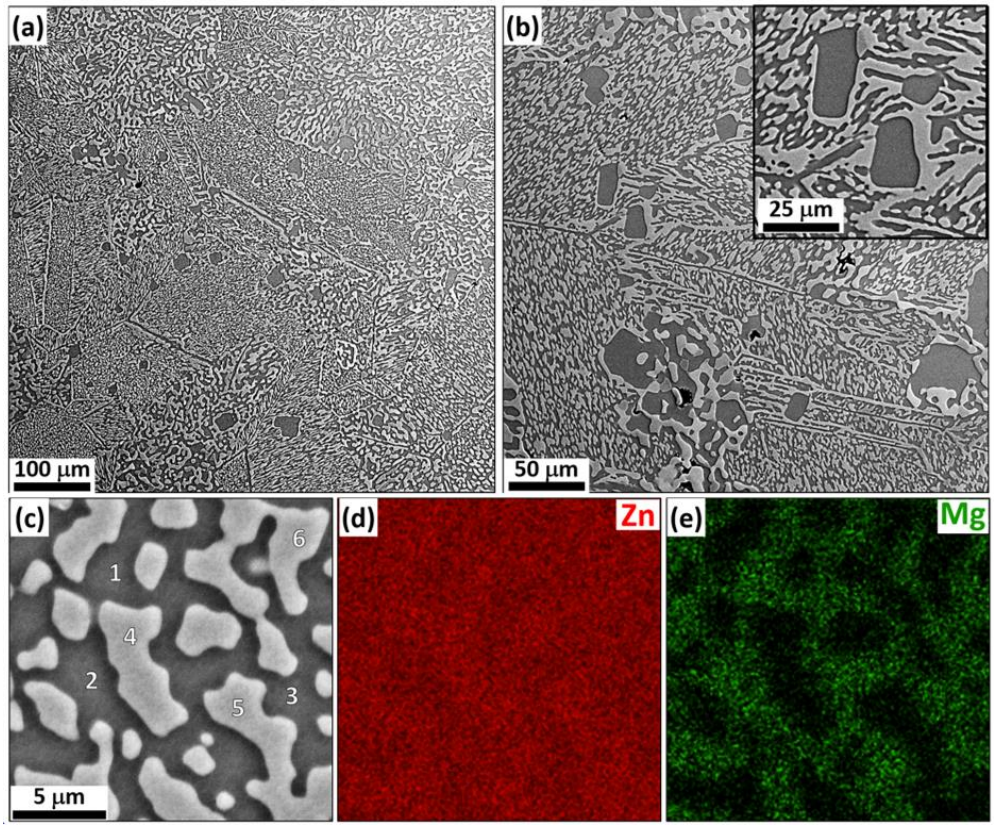

Figure 24: Representative BSE-SEM photomicrographs and EDS elemental maps of the as-cast Zn-3Mg alloy: (a) lower magnification, (b) higher magnification, (c) EDS region where point analysis was performed in locations 1-6, and their chemical compositions are provided in Table 2, (d) Zn EDS map obtained from (c), and (e) Mg EDS map obtained from (c). Adapted from [124].

Table 2: Chemical compositions of the as-cast Zn-3Mg alloy measured by EDS at different locations indicated in Figure 24 (c) with points 1-6. Adapted from [124].

Zn-3Mg alloy	Measurement location	Zn		Mg	
		(wt. %)	(at. %)	(wt. %)	(at. %)
As-cast	Whole area	96.7	91.7	3.3	8.3
	Points 1, 2 and 3	94.7 ± 0.3	86.9 ± 0.7	5.3 ± 0.3	13.1 ± 0.7
	Points 4, 5 and 6	100	100	0	0

4.1.1.2. Hardness of the as-cast Zn-3Mg alloy

A total of 10 individual HV indents were performed at different locations across the surface of the as-cast Zn-3Mg alloy, and the mean ± standard deviation obtained was 139 ± 4 HV.

4.1.2. As-homogenized Zn-3Mg alloy

4.1.2.1. Microstructures of the as-homogenized Zn-3Mg alloy

The homogenization heat treatment performed on the as-cast Zn-3Mg alloy, as described in section 3.2, was effective in dissolving the primary Mg_2Zn_{11} phases and led to a uniform coarser lamellar microstructure, as shown in Figure 25 (a) and (b). The composition of the entire ROI in Figure 25 (c), as well as that of points 1-6, was determined from EDS, and they are included in Table 3.

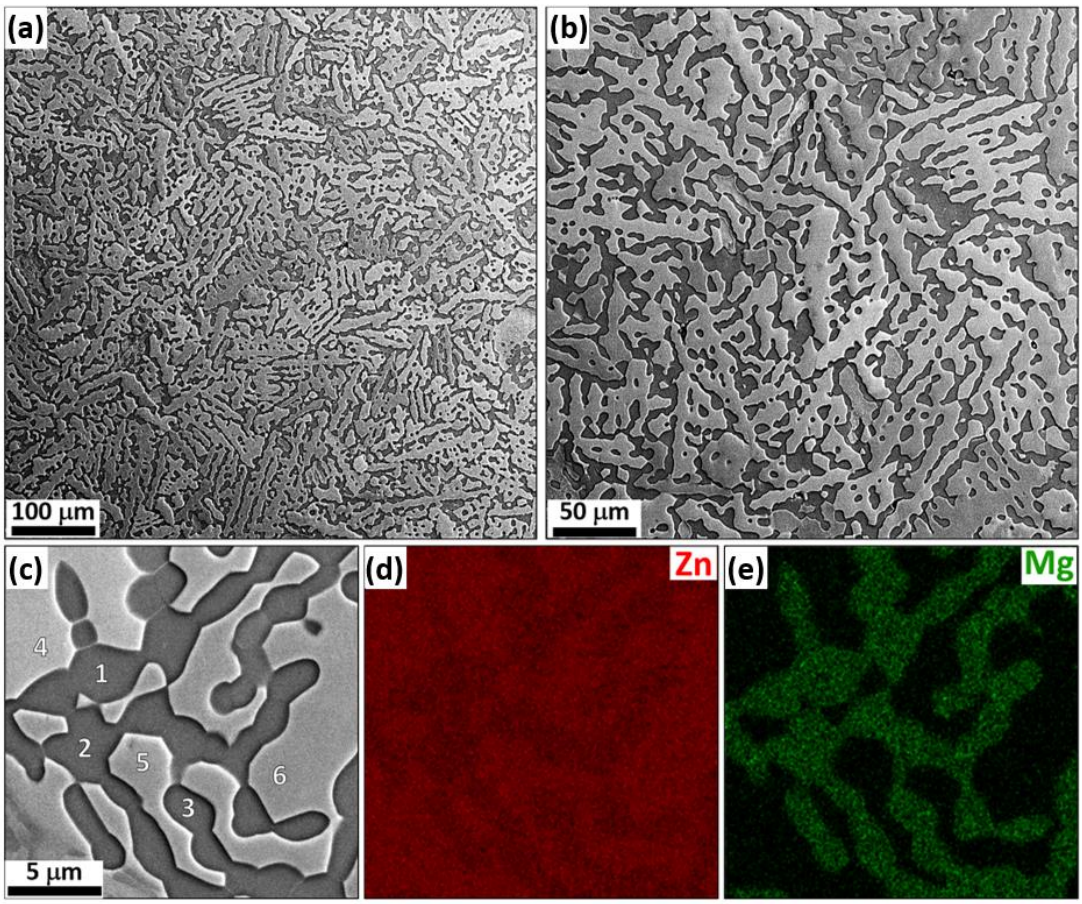

Figure 25: Representative BSE-SEM photomicrographs and EDS elemental maps of the as-homogenized Zn-3Mg alloy: (a) lower magnification, (b) higher magnification, (c) EDS region where point analysis was performed in locations 1-6, and their chemical compositions are provided in Table 3, (d) Zn EDS map obtained from (c), and (e) Mg EDS map obtained from (c). Adapted from [124].

The Zn and Mg EDS elemental maps from Figure 25 (c) are provided in Figure 25 (d) and (e), respectively. The composition of the dark phases in Figure 25 (c) was ~ 94Zn-6Mg (wt. %), consistent with that of the Mg_2Zn_{11} phase, whereas the light phases corresponded to Zn (see Table 3).

Table 3: Chemical compositions of the as-homogenized Zn-3Mg alloy measured by EDS at different locations indicated in Figure 25 (c) with points 1-6. Adapted from [124].

Zn-3Mg alloy	Measurement location	Zn		Mg	
		(wt. %)	(at. %)	(wt. %)	(at. %)
As-homogenized	Whole area	97.2	92.8	2.8	7.2
	Points 1, 2 and 3	94.2 ± 0.1	85.7 ± 0.3	5.8 ± 0.1	14.3 ± 0.3
	Points 4, 5 and 6	100	100	0	0

A series of EBSD maps (i.e., image quality, IPF, phase maps) acquired, as detailed in section 3.5.4, from the as-homogenized Zn-3Mg alloy are displayed in Figure 26. Both Zn and Mg_2Zn_{11} phases were identified, and their IPF and phase maps are shown. From the image quality map in Figure 26 (a), the brighter appearance of the Zn lamellar phase indicated that it exhibited a higher CI than the Mg_2Zn_{11} phase. Despite the relatively low BSE intensity of the Mg_2Zn_{11} phase, it was crystallographically distinguished from Zn due to its cubic lattice structure. Based on the IPF map in Figure 26 (b), the Zn phases in the scanned region did not seem to have a preferred crystal orientation. Due to the relatively low CI value, ~ 0.05-0.08, for the Mg_2Zn_{11} phase, the IPF map in Figure 26 (c) was not used to draw any conclusion about its crystal orientation. Figure 26 (d) and (e) show respectively the locations of the Zn and Mg_2Zn_{11} phases, respectively, in the scanned region. Due to potential interaction volume effects, phase quantification was not performed from EBSD data. The basal pole figure in Figure 27 indicates that the Zn phase did not exhibit basal texture, in agreement with the IPF map in Figure 26 (b), as most of the poles were tilted away from

the {0001} normal. The maximum texture intensity, according to the scale provided in Figure 26 for the Zn phase, was approximately 7.

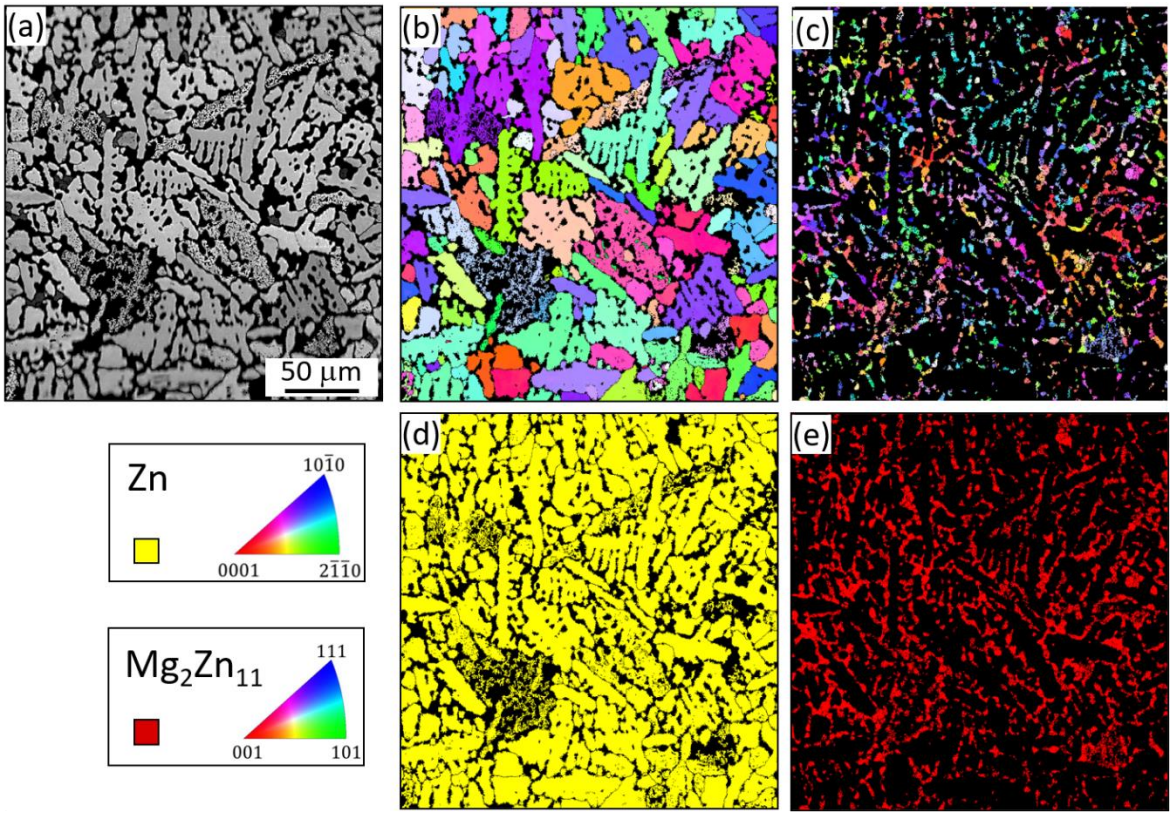

Figure 26: EBSD maps of the as-homogenized Zn-3Mg alloy: (a) image quality map of the scanned area and corresponding (b) Zn IPF map, (c) Mg_2Zn_{11} IPF map, (d) Zn phase map, and (e) Mg_2Zn_{11} phase map. The principal IPF triangles for Zn and Mg_2Zn_{11} phases are provided, with their respective crystal orientations.

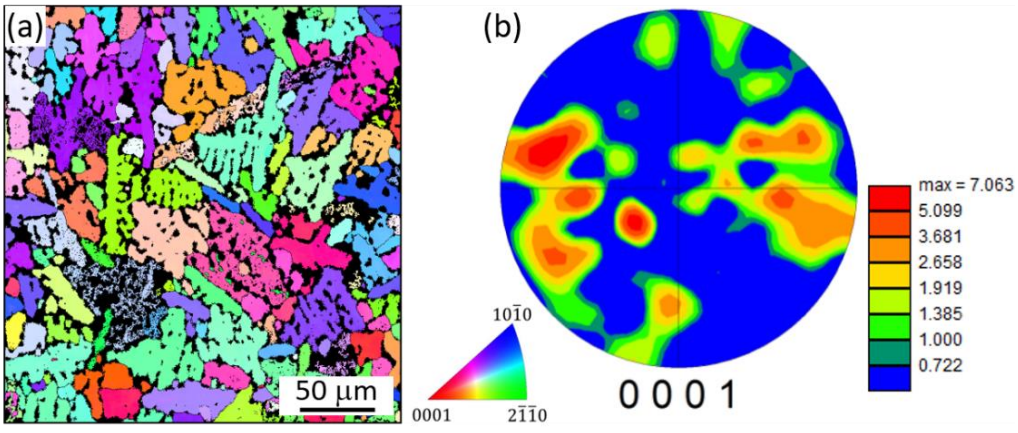

Figure 27: EBSD of as-homogenized Zn-3Mg alloy: (a) Zn IPF map, and (b) corresponding basal (0001) pole figure with color scale displaying the texture intensity.

4.1.2.2. Hardness of the as-homogenized Zn-3Mg alloy

A total of 10 individual HV indents were performed at different locations across the surface of the as-homogenized Zn-3Mg alloy, and the mean ± standard deviation obtained was 109 ± 4 HV.

4.1.3. HPT-processed Zn-3Mg alloy

4.1.3.1. Microstructures of the HPT-processed Zn-3Mg alloy

After subjecting the as-homogenized Zn-3Mg alloy to HPT for 30 turns, i.e., HPT alloy, TEM/STEM imaging was performed near the periphery of the sample at the thickness-shear plane, defined in Figure 12. The microstructure of the HPT alloy consisted of equiaxed grains ranging in diameter from ~ 100-300 nm, as observed in the BF-TEM image in Figure 28 (a). The corresponding SAD pattern is presented in Figure 28 (b), where the left half corresponds to the original pattern, and the right half is the processed pattern after beam-stop removal and rotational averaging about its center to eliminate the influence of diffraction ring artifacts due to non-uniform grain size and/or crystal orientation effects [133]. A magnified view of the rotationally averaged SAD pattern is shown in Figure 28 (c), with its corresponding line radial intensity profile, where the labeled peaks are associated with different Bragg reflections. Peaks having at least 10% maximum intensity were matched to Zn (#421014) and Mg_2Zn_{11} (#104898) phases tabulated in the ICSD. It was noted that the four strongest peaks were associated with more than one reflection and that the most intense peak corresponded to the highest intensity peak in both Zn and Mg_2Zn_{11} theoretical spectra. It should be mentioned that no other Zn-Mg phase was found to be a good fit for the diffraction rings in the SAD pattern.

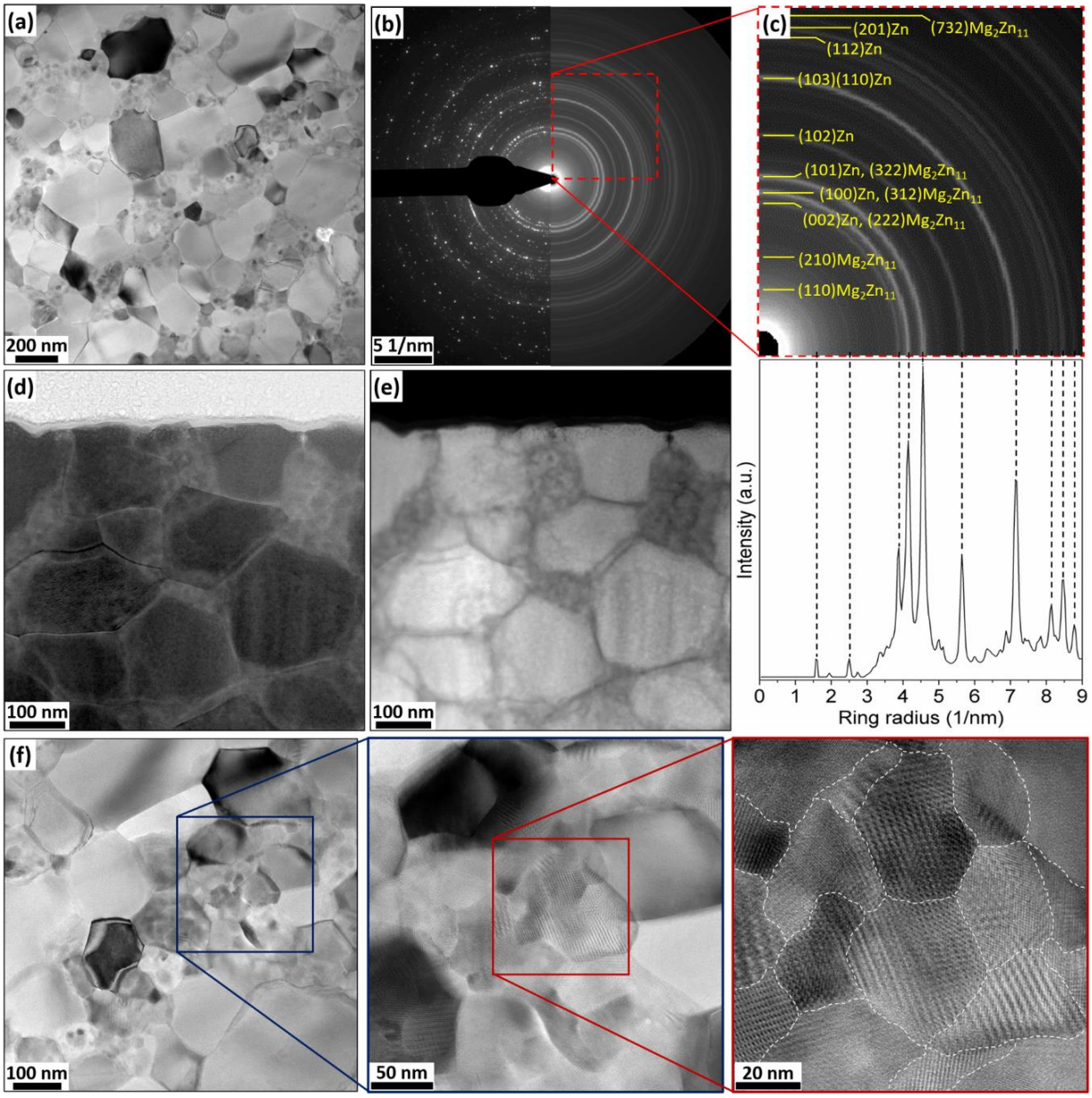

Figure 28: Representative TEM/STEM images of the Zn-3Mg alloy near the periphery of the cross-section after HPT for 30 turns: (a) BF-TEM and (b) corresponding SAD pattern: original (left), processed (right), (c) portion of the SAD pattern where identified phases were labeled, (d) BF-STEM and (e) corresponding HAADF-STEM, (f) HRTEM sequential imaging, where nanocrystalline domains are denoted by white dashed lines. [124]

The contrast differences in the BF and its corresponding HAADF-STEM images, in Figure 28 (d) and (e), respectively, indicate a heterogeneous distribution of Zn and Mg_2Zn_{11} phases. Because the contrast level in HAADF mode is directly proportional to the atomic number, the bright areas

corresponded to Zn (Z=30), whereas the dark regions corresponded to Mg_2Zn_{11} (Z~27.2). Detailed inspection of the microstructure revealed nanocrystalline domains between coarser grains, as indicated by white dashed lines in the highest magnification HRTEM images in Figure 28 (f). Moiré fringe patterns could be distinguished inside some of these nanocrystalline domains due to a superposition of lattice reflections. Although FFT analysis provided evidence for Zn and Mg_2Zn_{11} phases, consistent with the SAD pattern, the orientation relationships between the overlapping lattices could not be identified from the measurements of the Moiré fringes spacings and the diffraction vectors.

Atomic characterization of a small volume near the periphery of the Zn-3Mg alloy after HPT was performed by APT. Figure 29 presents the reconstruction of an APT needle, including the Zn and Mg atom maps, as well as an isosurface and its corresponding proximity histogram. The Zn atoms were distributed across the whole APT needle, as observed in Figure 29 (a), whereas Mg atoms were mainly located at the bottom of the APT needle, as observed in Figure 29 (b). The 3D region highlighted in Figure 29 (c) represents an isoconcentration surface with 10 (at. %) Mg. The black arrow indicates the direction of the corresponding proximity histogram plotted in Figure 29 (d), which shows the evolution of the atomic concentration of Zn and Mg as a function of the distance from the isosurface.

The region highlighted in yellow indicates approximately the transition region between the different compositions at either side of the isosurface. This transition region has an approximate thickness of 5 nm and can be interpreted as a phase boundary, as it represents a spatial interface between two regions of uniform composition. Analysis of Figure 29 (d) revealed that the composition evolved from 99.8Zn-0.2Mg (at. %) at one side of the isosurface to 83.5Zn-16.5Mg (at. %) at the other side of the isosurface. It should be noted that 99.8Zn-0.2Mg (at. %) corresponds

to a solid solution of Mg in Zn, whereas 83.5Zn-16.5Mg (at. %) corresponds to the Mg_2Zn_{11} intermetallic phase.

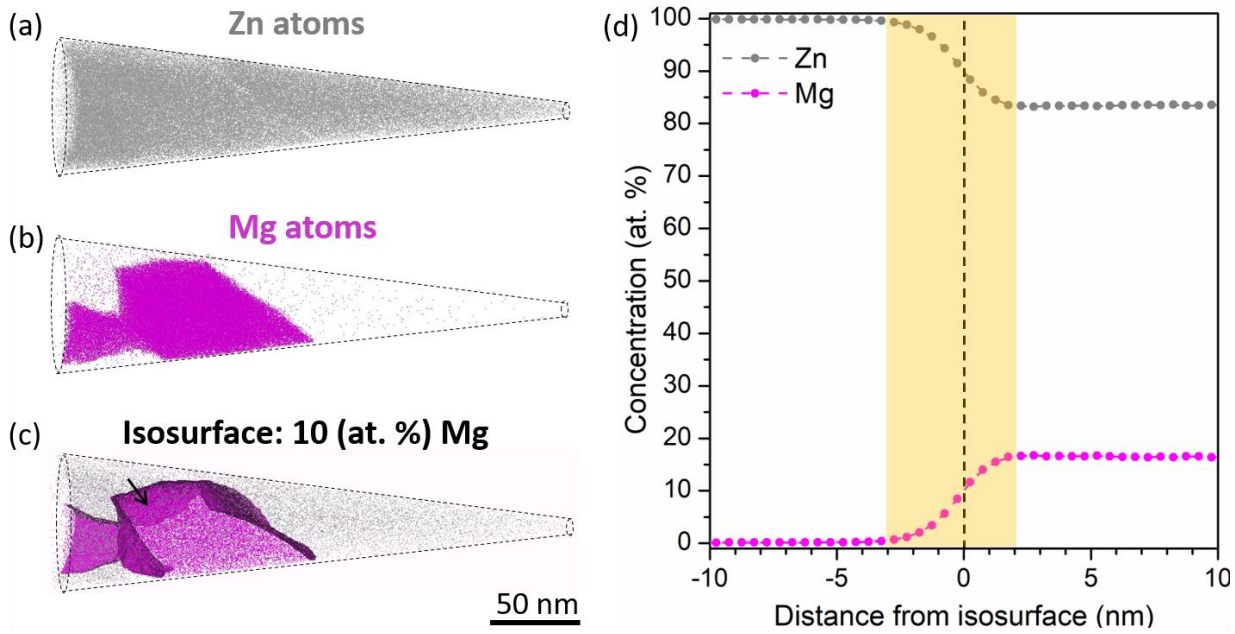

Figure 29: APT reconstruction of a needle extracted near the periphery of the Zn-3Mg alloy after HPT for 30 turns: (a) atom map of Zn, (b) atom map of Mg, (c) 3D isosurface with a concentration of 10Mg (at. %), (d) proximity histogram along the black arrow in the isosurface highlighted in (c). The average composition across the isosurface evolved from 99.8Zn-0.2Mg to 83.5Zn-16.5Mg (at. %). The transition region between the two compositions is highlighted in yellow in (d).

The microstructure of the Zn-3Mg alloy after HPT for 30 turns near the sample periphery was also inspected by SEM, in a plane perpendicular to that of the TEM/STEM images above, and representative BSE-SEM photomicrographs at different magnifications are presented in Figure 30. The grains appeared to be reasonably equiaxed across the microstructure, as observed in Figure 30 (a), with grain diameters ranging between ~ 200-400 nm. Darker areas between neighboring brighter grains could be distinguished at higher magnifications, as observed in Figure 30 (b), consistent with the HAADF-STEM observations above, associated with Mg_2Zn_{11} phases. Nanoscale precipitates were identified in the grain interiors of some Zn-rich grains, as can be distinguished in the inset of Figure 30 (b).

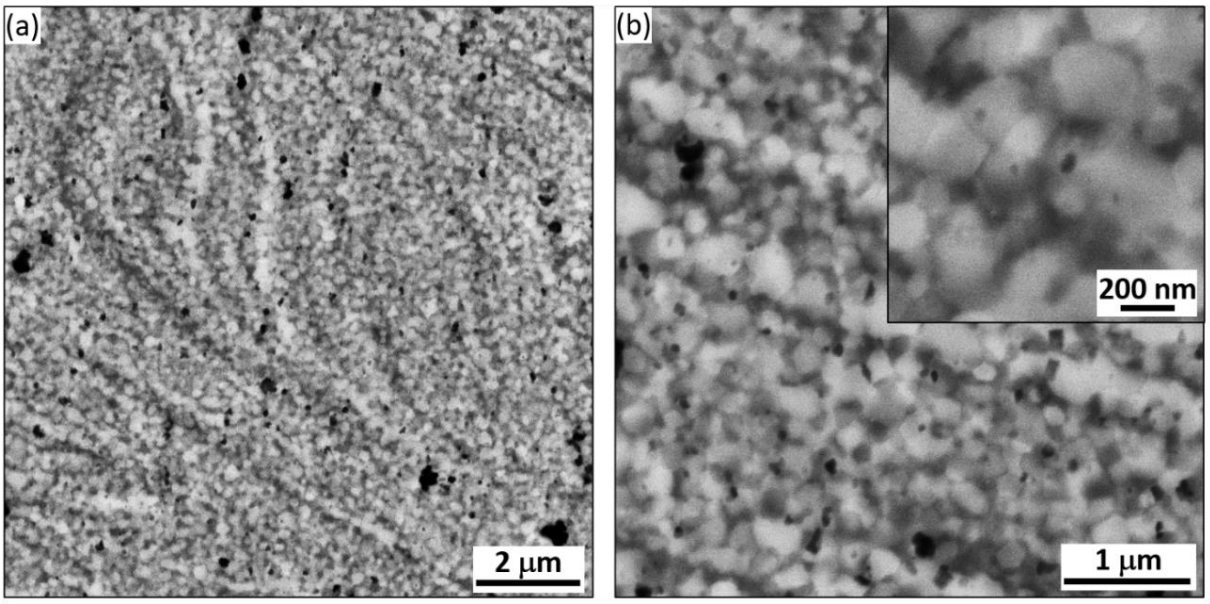

Figure 30: Representative BSE-SEM photomicrographs near the periphery at the cross-section of the as-homogenized Zn-3Mg alloy after HPT for 30 turns: (a) lower magnification, (b) higher magnification. Adapted from [124].

EBSD was performed near the periphery of the Zn-3Mg alloy after HPT for 30 turns, and the image quality, IPF, and phase maps corresponding to the Zn and Mg_2Zn_{11} phases identified are provided in Figure 31. Consistent with the SEM and TEM/STEM images presented earlier, severe grain refinement in the nanoscale regime was achieved in the as-homogenized alloy after 30 turns HPT. Similar to the EBSD analysis of the as-homogenized condition, both Zn and Mg_2Zn_{11} phases were identified, and the latter phase, which corresponded to the darker areas in Figure 31 (a), typically exhibited lower CI values. The IPF map of the Zn phase in Figure 31 (b) indicated that a large fraction of the nanosized grains in the microstructure were relatively well aligned with the basal plane {0001} normal. It should be noted that despite the small sizes of the Mg_2Zn_{11} phases identified, each consisted of at least 10 neighboring pixels with a CI > 0.1 and misorientation angles < 5º.

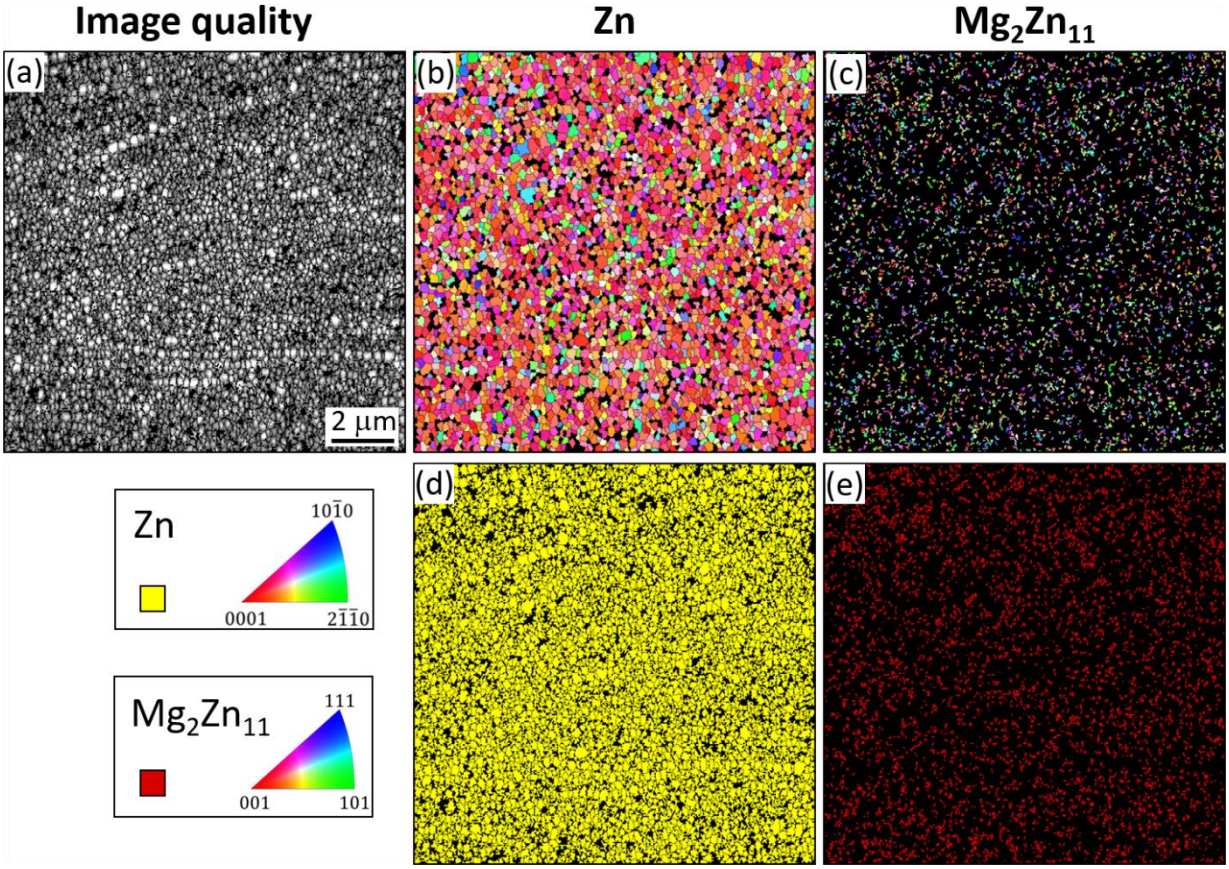

Figure 31: EBSD maps of the as-homogenized Zn-3Mg alloy after HPT processing for 30 turns near the sample periphery: (a) image quality map of the scanned area and corresponding (b) Zn IPF map, (c) Mg_2Zn_{11} IPF map, (d) Zn phase map, and (e) Mg_2Zn_{11} phase map. The principal IPF triangles for Zn and Mg_2Zn_{11} phases, with their respective crystal orientations, are provided.

Similar to the as-cast condition, the IPF map of the Mg_2Zn_{11} phase in Figure 31 (c) was not used to derive any conclusion due to the relatively low CI values (i.e., ~ 0.05-0.08) and the small number of pixels in the Mg_2Zn_{11} phases present. The basal pole figure corresponding to the Zn phase, shown in Figure 32 (b), indicated that a clear basal texture developed in the microstructure after HPT for 30 turns, as most of the poles are approximately parallel to the basal plane normal direction. The maximum texture intensity of the Zn phase for this sample was approximately 5 (see scale in Figure 32).

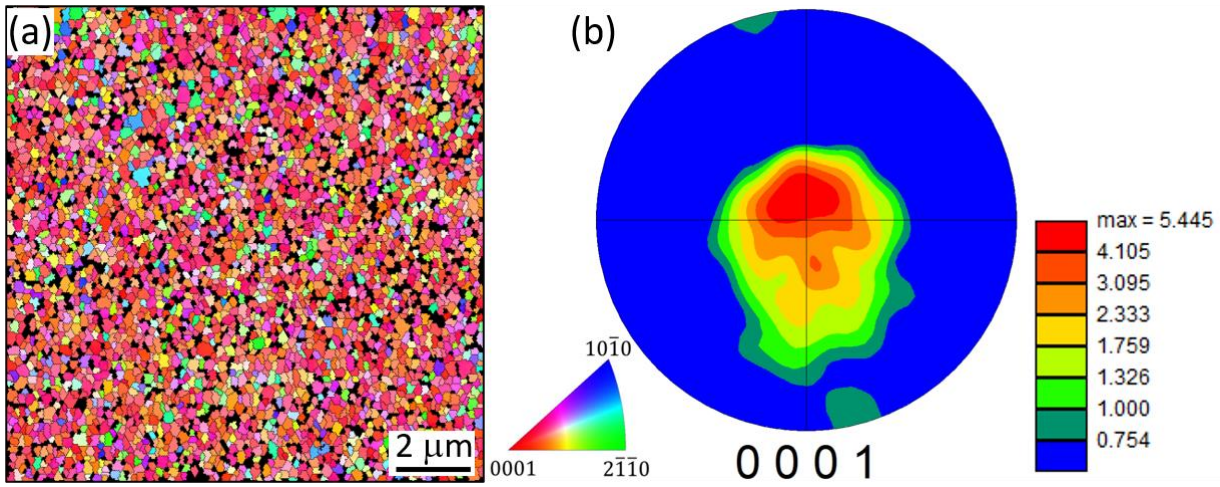

Figure 32: EBSD of the Zn-3Mg alloy after HPT processing for 30 turns: (a) Zn IPF map, and (b) corresponding basal (0001) pole figure with color scale displaying the texture intensity.

The grain size (GS) and misorientation angle distributions of the Zn phase obtained through EBSD analysis of the Zn-3Mg alloy after HPT processing for 30 turns are presented in Figure 33 (a) and (b), respectively. The distribution of GS, in Figure 33 (a), showed a unimodal right-skewed distribution, with a GS_{ave} of ~ 210 ± 60 nm. Thus, it could be inferred that most of the grains had slightly smaller sizes than the latter value, about ~ 170-180 nm, as indicated by the position of the mode in the GS distribution. Few grains had sizes between 300-450 nm, but these represented less than 1% of the total scanned area.

As shown in Figure 33 (b), the fractions of misorientation angles increased rapidly from 2º to 40 º, and then decreased gradually from 40º to 93.5º. The most frequently occurring misorientation angles were in the range of ~ 30-50º. HABs, defined as those > 15º misorientation, represented ~ 97 % of the total number of identified boundaries in the microstructure.

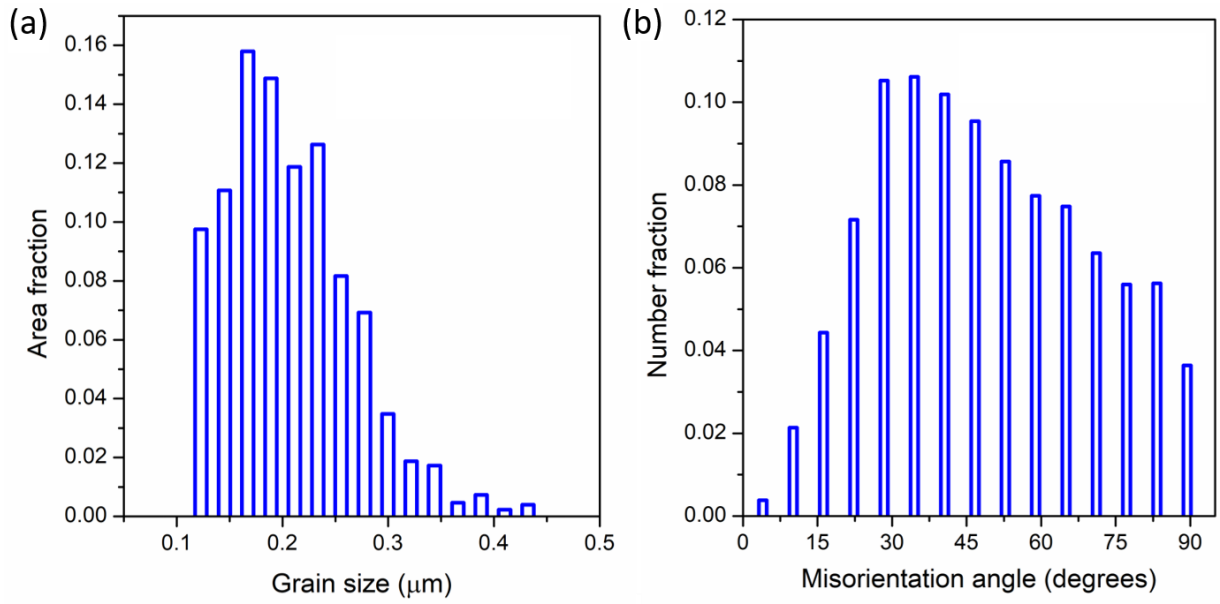

Figure 33: Distributions of (a) grain size and (b) misorientation angle obtained from EBSD analysis of the Zn phase identified near the periphery of the Zn-3Mg alloy after HPT processing for 30 turns.

4.1.3.2. Hardness of the HPT-processed Zn-3Mg alloy

The distribution of HV values recorded at the cross-section over the radius of the Zn-3Mg alloy sample after HPT for 30 turns is presented as a color-coded contour map in Figure 34 (a). The mean ± standard deviations of the HV values measured across the sample are also provided in Figure 34 (b). The average hardness across the sample radius was 139 HV, and the maximum hardness recorded was 150HV. The hardness of the sample appeared to be relatively uniform at r > 1 mm, with values in the range of ~ 135-140 HV. A slight decrease in the hardness was observed for r < 1 mm, where the values ranged between ~ 120-135 HV. The HV measurements recorded at the same distance from the center but at different distances from the mid-thickness, typically differed by ~ 5-10 HV. However, larger standard deviations of ~ ±15 HV were observed near the sample center at r < 1 mm.

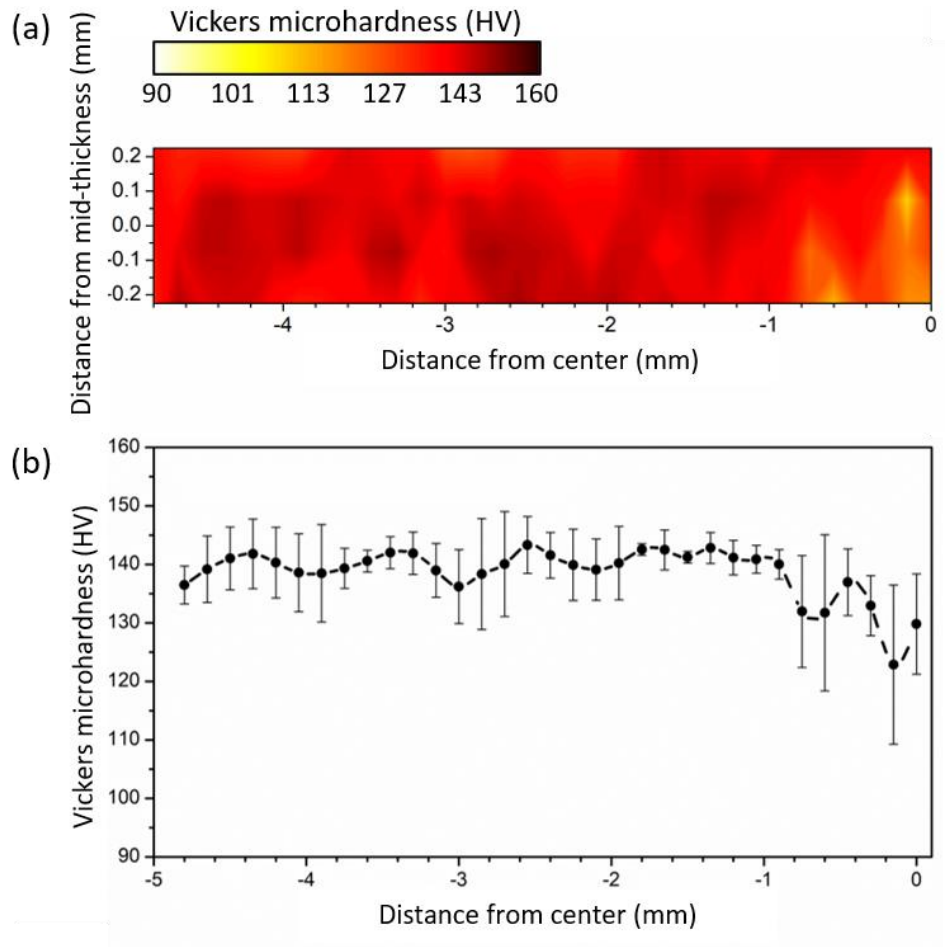

Figure 34: HV values measured at the cross-section over the radius of the Zn-3Mg alloy sample after HPT for 30 turns: (a) color-coded contour map constructed from a 4x32 matrix of HV values, to be interpreted with the color key scale provided, and (b) corresponding plot with the HV values. Each point in the plot represents the average HV values among four different measurements at the same distance from the center, and the error bar represents their standard deviation.

4.1.4. HPT-processed + PDA Zn-3Mg alloy

4.1.4.1. Microstructures of the HPT- processed + PDA Zn-3Mg alloy

The microstructure of the HPT-processed Zn-3Mg alloy after subsequent PDA near the periphery of the sample was examined by SEM, and representative BSE-SEM photomicrographs at different magnifications are provided in Figure 35. The microstructure exhibited grains of two clear contrast levels, with sizes in the range of ~ 600-800 nm, which appeared to be free of precipitates in the

grain interiors, as shown in Figure 35 (b). The brighter areas were associated with Zn, whereas the darker areas were associated with Mg_2Zn_{11}, based on their BSE intensity. The area fractions of the Zn and Mg_2Zn_{11} phases were determined using the threshold tool in ImageJ as 0.59 and 0.41, respectively.

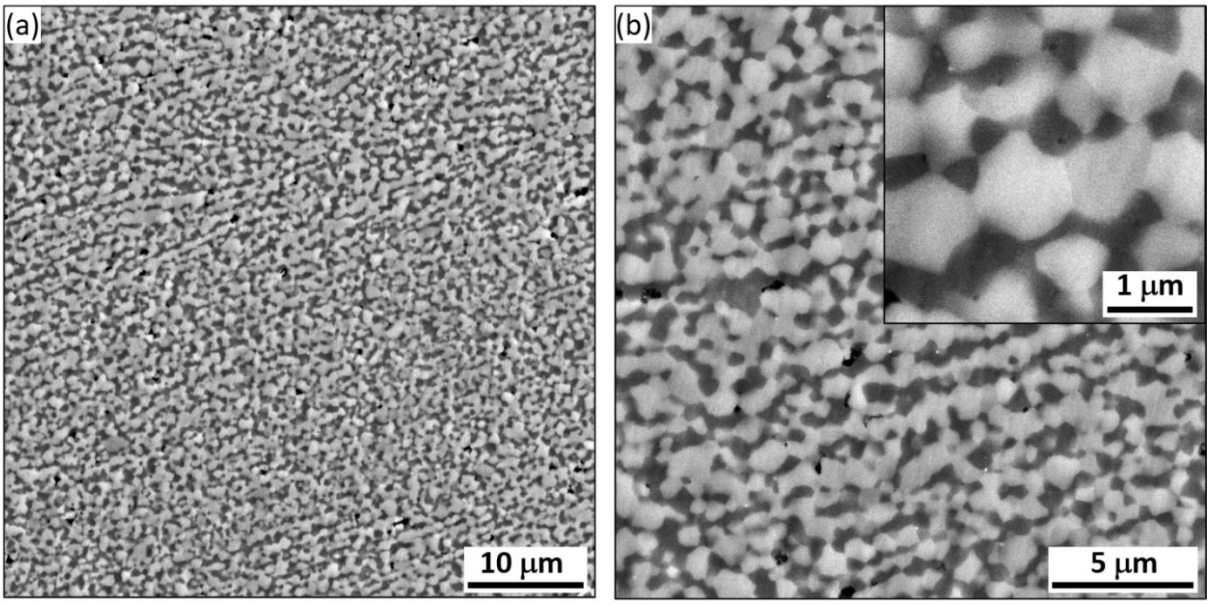

Figure 35: Representative BSE-SEM photomicrographs near the periphery at the cross-section of the as-homogenized Zn-3Mg alloy after HPT for 30 turns + PDA (200 ºC, 1h): (a) lower magnification, (b) higher magnification.

EBSD was performed near the periphery of the Zn-3Mg alloy after HPT for 30 turns + PDA, and the image quality, IPF, and phase maps corresponding to the Zn and Mg_2Zn_{11} phases identified are provided in Figure 36. A relatively equiaxed microstructure was apparent from the image quality map in Figure 36 (a). Some regions with low CI values (i.e., black areas) were distributed across the scanned area, and thus, they were not indexed successfully. From Figure 36 (b) and (d), it is apparent that all the grains in the microstructure were attributed to the Zn phase. The colors of the Zn grains in the IPF orientation map in Figure 36 (b) indicate that most of the grain surfaces lie in the basal planes. The distributions of grain sizes and misorientation angles in the Zn phase are

evaluated in the next paragraph. The Mg_2Zn_{11} phase was identified in the form of small clusters containing ~ 4-6 pixels with CI > 0.1, which were scattered across the microstructure. As mentioned earlier for the sample after HPT, the crystal orientation information from the Mg_2Zn_{11} phases was not analyzed further due to their small phase fractions.

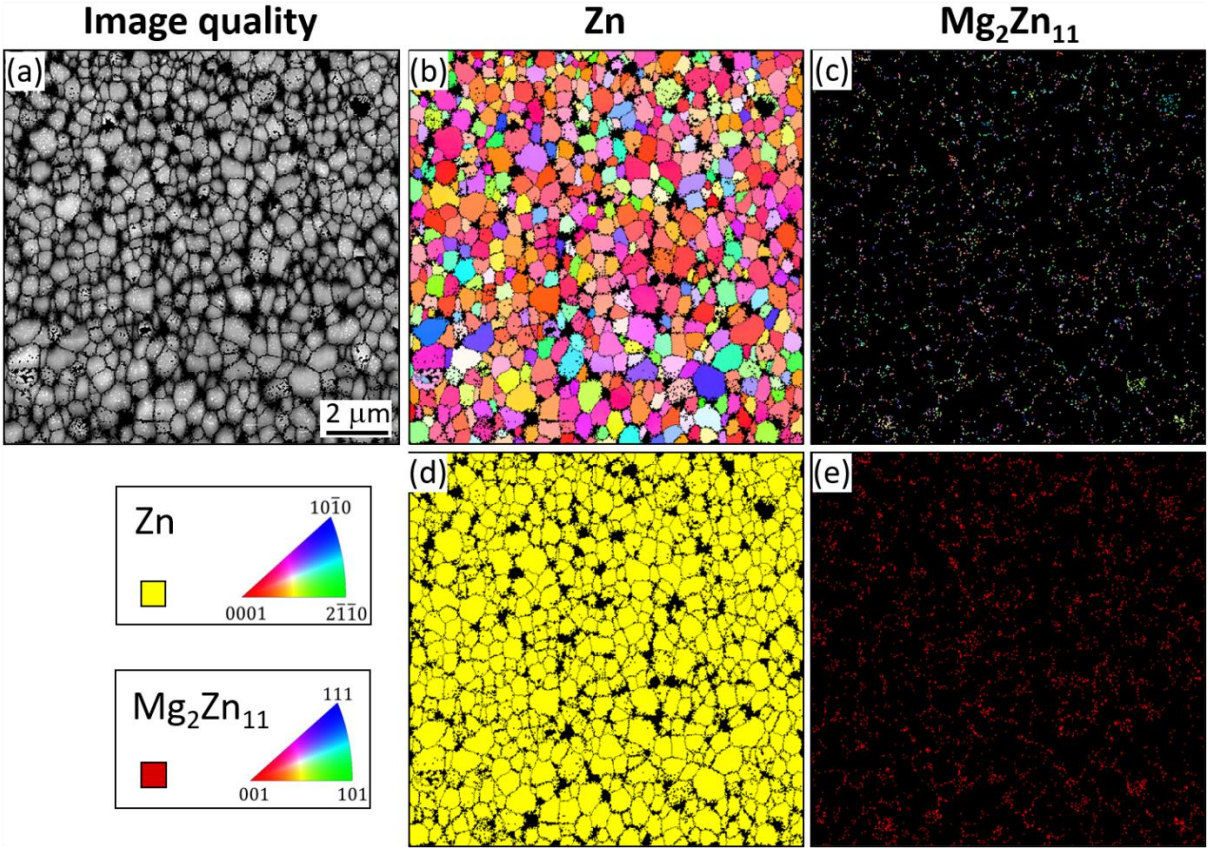

Figure 36: EBSD maps of the Zn-3Mg alloy after HPT processing for 30 turns + PDA (200 ºC, 1h) near the sample periphery: (a) image quality map of the scanned area and corresponding (b) Zn IPF map, (c) Mg_2Zn_{11} IPF map, (d) Zn phase map, and (e) Mg_2Zn_{11} phase map. The principal IPF triangles for Zn and Mg_2Zn_{11} phases, with their respective crystal orientations, are provided.

The basal pole figure corresponding to the Zn phase of the Zn-3Mg alloy after HPT for 30 turns and subsequent PDA, shown in Figure 37 (b), indicated a moderate basal texture in the microstructure, even though a fraction of the poles were tilted away from the {0001} normal. The maximum texture intensity for the Zn phase recorded was approximately 5 (see Figure 37).

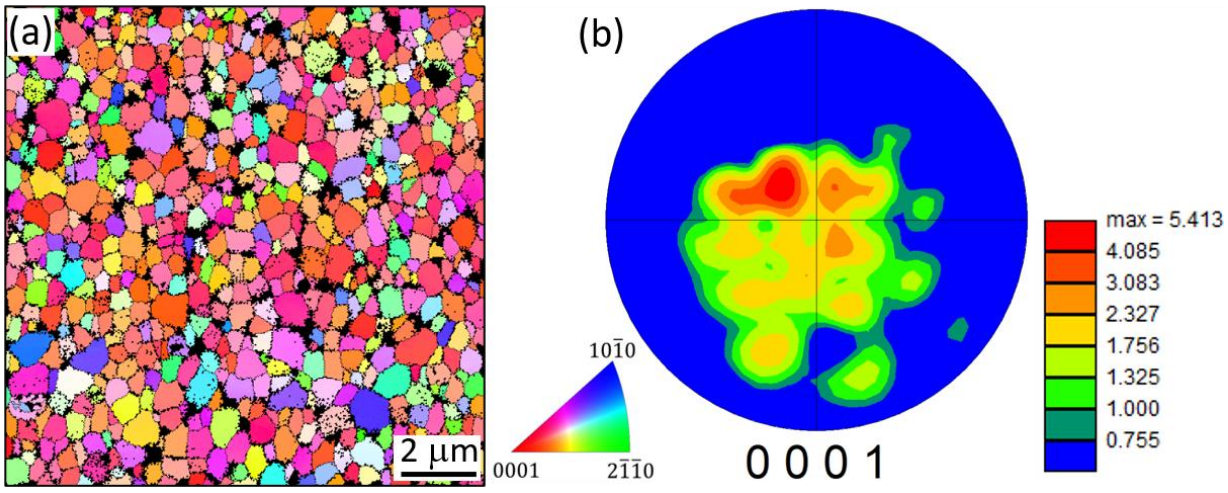

Figure 37: EBSD of Zn-3Mg alloy after HPT processing for 30 turns + PDA: (a) Zn IPF map, and (b) corresponding basal (0001) pole figure with color scale displaying the texture intensity.

The distributions of GS and misorientation angles in the Zn phase from EBSD analysis of the Zn-3Mg alloy after HPT for 30 turns + PDA are provided in Figure 38 (a) and (b), respectively. The GS followed a unimodal normal distribution, as observed in Figure 38 (a), with a GS_{ave} of ~ 680 ± 120 nm. Grains as small as ~ 300 nm and as large as ~ 1.2 mm were present in the microstructure, but the majority of grains had sizes in the range of ~ 500-900 nm.

From Figure 38 (b), it is observed that the fractions of misorientation angles increased gradually from 2º to 40º and then, remained fairly stable from 40º to 80º. The most frequently occurring misorientation angles were in the range of ~ 30-80º. The amount of HABs was ~ 98 % of the total number of identified boundaries in the microstructure.

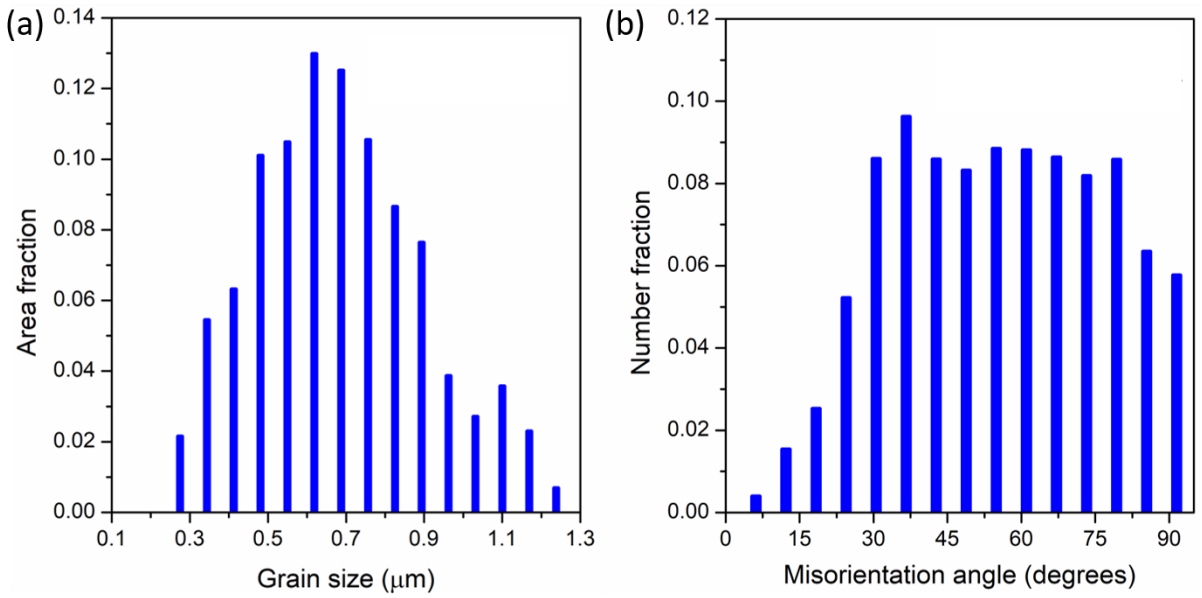

Figure 38: Distributions of (a) grain size and (b) misorientation angle obtained from EBSD analysis of the Zn phase identified near the periphery of the Zn-3Mg alloy after HPT processing for 30 turns + PDA (200 ºC, 1h).

4.1.4.2. Hardness of the HPT- processed + PDA Zn-3Mg alloy

The HV values measured at the cross-section of the Zn-3Mg alloy after HPT for 30 turns and PDA are plotted as a function of the distance from the center and the distance from the mid-thickness of the sample in Figure 39 (a). The mean ± standard deviation of the HV values is also provided in Figure 39 (b). The average hardness across the sample radius was 136 HV, and the maximum hardness recorded was 153 HV. The hardness was lowest near the central region of the sample, at $r < 0.5$ mm, with values ranging at ~ 110-120 HV, and increased progressively with increasing distance from the center up to $r \sim 4$ mm, reaching ~ 150 HV. A slight decrease in hardness was observed from $r \sim 4$ mm to the edge of the sample, with values in the range of ~ 145 HV. It was noted that the standard deviations were particularly larger at $r < 1.5$ mm, where the hardness measurements recorded at a different distance from the mid-thickness varied by up to ± 15 HV.

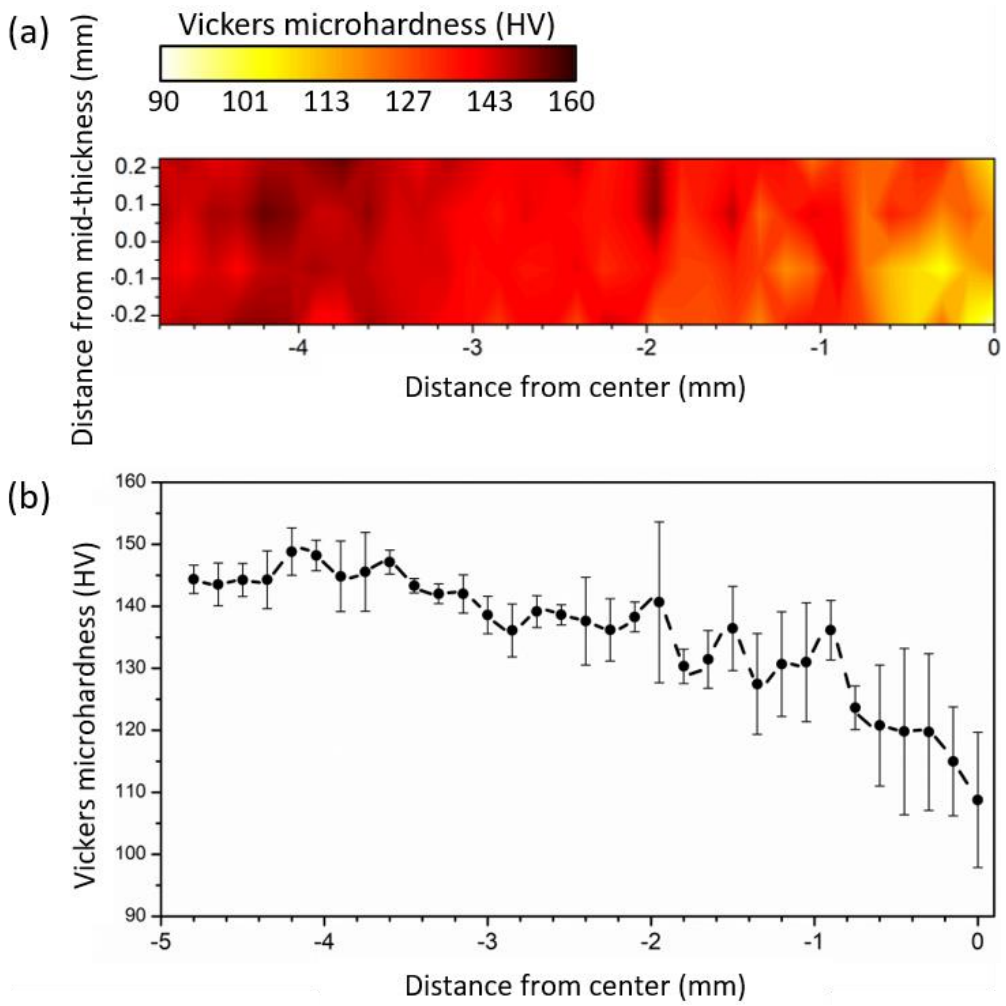

Figure 39: HV values measured at the cross-section over the radius of the Zn-3Mg alloy sample after HPT for 30 turns + PDA: (a) color-coded contour map constructed from a 4x32 matrix of HV values, to be interpreted with the color key scale provided, and (b) corresponding plot with the HV values. Each point in the plot represents the average HV values among four different measurements at the same distance from the center, and the error bar represents their standard deviation.

4.2. Zn-10Mg hybrids

This section presents the microstructures, hardness results, and electrochemical properties of the Zn-10Mg hybrids after HPT for 1, 5, 15, and 30 turns. It should be noted that this hybrid composition was the first one to be studied since it consisted of Zn/Mg/Zn stacked disks of equal thickness, and thus, it served as a baseline for the other two hybrid compositions (i.e., Zn-3Mg and Zn-30Mg presented in sections 4.3 and 4.4, respectively). The microstructures were characterized using SEM, EDS, EBSD, TEM, XRD, and APT. The hardness was examined with HV. Special attention was given to the regions of highest plastic deformation located at the periphery of the samples. The electrochemical properties of this material were characterized to assess the corrosion resistance, as this is important for the biodegradability characteristics.

4.2.1. HPT-processed Zn-10Mg hybrids

4.2.1.1. Microstructures of the HPT-processed Zn-10Mg hybrids

A series of low magnification SE-SEM images acquired from the cross-sections of the Zn-10Mg HPT hybrids after 1, 5, 15, and 30 turns are presented in Figure 40. It should be noted that in all SEM images, the lighter regions correspond to the Zn-rich phases ($Z_{Zn} = 30$), whereas the darker regions correspond to Mg-rich phases ($Z_{Mg} = 12$). After 1 turn, a continuous multi-layered structure was observed along the diameter of the sample, without any proof of voids or segregation, where the Zn/Mg/Zn disk sequence was still distinguishable. This showed an adequate mechanical bonding of the three original Zn and Mg disks through HPT into a compact sample after 1 turn. After 5 turns, the intermediate Mg-rich layer was no longer uniform across the disk diameter, but it was instead fragmented into thinner layers with heterogeneous thicknesses. In addition, it was observed that the fragmentation of different phases into thinner layers, known as necking in the

HPT literature, occurred more notably towards the disk periphery (i.e., at increasing distance from the disk center). After 15 turns, thin Mg-rich phases oriented along the shear direction were identified in the Zn matrix at the central region of the sample at r < 2 mm. However, Mg-rich phases were mainly present closer to the periphery after 15 turns, with a reasonable radial symmetry at both sides of the sample. By contrast, after 30 turns, the outer regions of the samples exhibited significantly finer Mg-rich layers, barely visible in Figure 40, having sub-micron thicknesses.

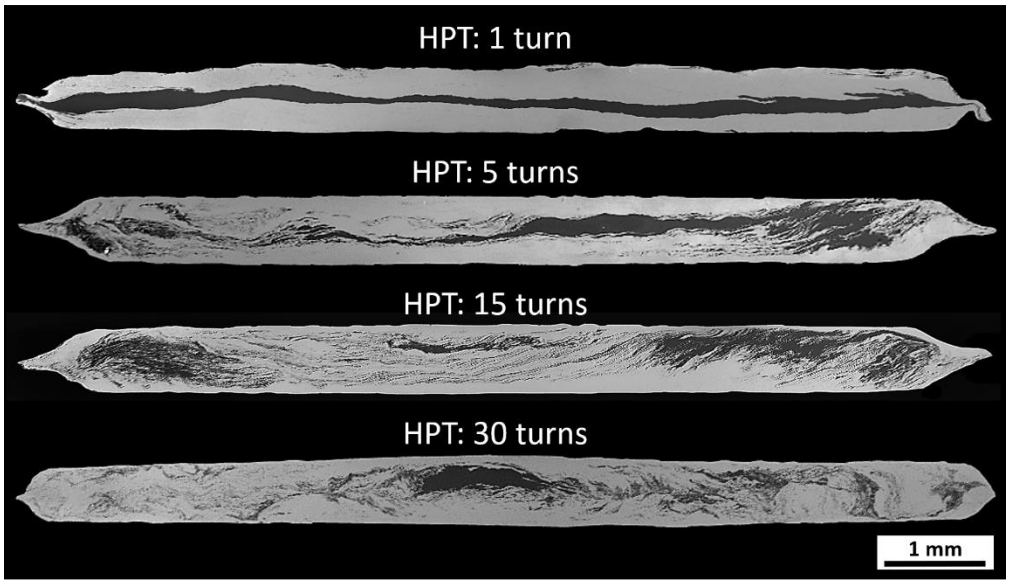

Figure 40: SE-SEM images corresponding to the cross-sections of the Zn-10Mg hybrids after HPT for 1, 5, 15, and 30 turns, processed with an applied pressure of 6 GPa and a rotational speed of 1 rpm. [174]

Higher magnification SE-SEM images representative of the regions near the periphery, at r ~ 4 mm, of the Zn-10Mg HPT hybrids after 15 and 30 turns are presented in Figure 41. On the one hand, Figure 41 (a) and (b) correspond to the cross-sections of the hybrids after 15 and 30 turns, respectively, with the same sample orientation as those in Figure 40 (i.e., compression axis is vertical). On the other hand, Figure 41 (c) and (d) represent the horizontal surface of the samples at the mid-thickness plane. Zn-rich and Mg-rich layers, with thicknesses of ~ 20-40 μm, were

consistently aligned with the shear direction at the disk periphery after 15 turns, as shown in Figure 41 (a). After 30 turns, the thickness of these layers decreased significantly, < 5 μm, after 30 turns, and became more randomly oriented within the microstructure, as shown in Figure 41 (b). Note the difference in scale bar magnitude between Figure 41 (a) and (b). The grain sizes near the sample periphery after 15 tuns ranged between ~ 500 nm and ~ 3.0 μm, as observed in Figure 41 (c), with a GS_{ave} of 815 ± 150 nm. After 30 turns, the grain sizes decreased significantly, as observed in Figure 41 (d), and the grain size distribution was found to be narrower, with a GS_{ave} of 590 ± 60 nm. It should be noted that the GS_{ave} values presented were estimated by the general linear intercept method from at least 15 individual measurements, in accordance with ASTM E112-12.

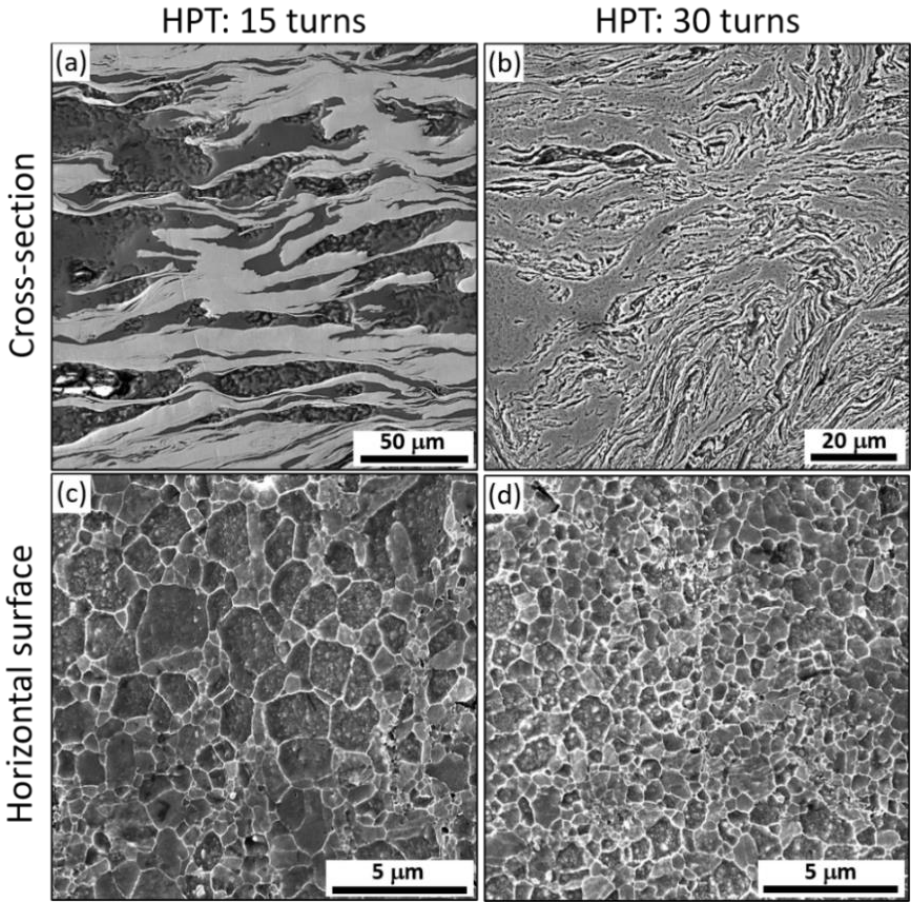

Figure 41: Representative SE-SEM micrographs acquired near the periphery of the Zn-10Mg hybrids after HPT for 15 and 30 turns, at the cross-sections (a) after 15 turns, (b) after 30 turns; and at the mid-thickness plane of the horizontal surface (c) after 15 turns, (d) after 30 turns. [174]

Two BSE-SEM micrographs from the same region of the cross-section of the Zn-10Mg HPT hybrid after 30 turns near the sample periphery at r ~ 4 mm, are observed in Figure 42. A representative area of the ultrafine multilayered structure is presented in Figure 42 (a), where the highlighted region in red is magnified in Figure 42 (b). The black areas in Figure 42 (b) were identified to be Mg by EDS analysis, and the average chemical composition of the light grey phase, estimated at points A, B, C, and D, was ~ 92Zn - 8Mg (wt.%). The results of the EDS analysis are summarized in Table 4, including the theoretical composition of the Mg_2Zn_{11} intermetallic compound as a reference.

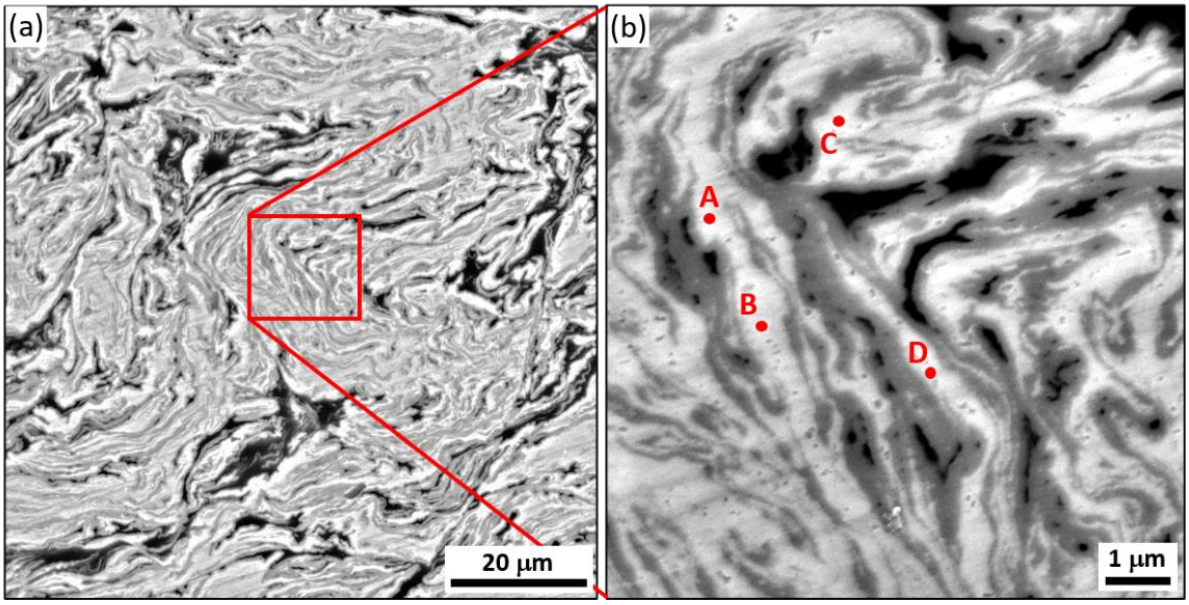

Figure 42: Representative BSE-SEM micrographs obtained near the periphery at the cross-section of the Zn-10Mg hybrid after HPT for 30 turns (a) lower magnification, (b) higher magnification region highlighted in (a), where EDS analysis was performed at points A, B, C and D (EDS results are provided in Table 4.

Table 4: EDS analysis of points A, B, C, and D highlighted in red in Figure *42* (b). The chemical composition of the Mg_2Zn_{11} intermetallic compound is also provided for reference.

	Mg (wt.%)	Zn (wt.%)
Point A	8	92
Point B	7	93
Point C	8	92
Point D	9	91
Mg_2Zn_{11}	6	94

A series of EBSD orientation maps collected at the horizontal surface near the periphery, r ~ 4 mm, of the Zn-rich regions of the Zn-10Mg HPT hybrid samples, with their corresponding misorientation angle distribution plots and basal (0001) pole figures, are presented in Figure 43. After 1 turn, as shown in Figure 43 (a), the microstructure exhibited a heterogeneous distribution of grain sizes, with a GS_{ave} of ~ 43 ± 27 μm, and a high fraction (0.48) of low-angle grain boundaries. As indicated by the (0001) pole figure, a slightly tilted basal texture developed after 1 turn, as the <0001> crystal directions tended to form parallel to the compression axis.

After 5 turns, a more equiaxed microstructure was observed, as shown in Figure 43 (b), with a GS_{ave} of ~ 19 ± 8 μm. This grain refinement was accompanied by an increase in the volume fraction of high-angle grain boundaries (HABs), from 0.52 after 1 turn to 0.78 after 5 turns. Moreover, the associated increase of shear strain after 5 turns gave rise to a better alignment of the c-axes with the disk normal, as observed by a stronger basal texture.

After 15 turns, as shown in Figure 43 (c), an equiaxed fine-grained microstructure was obtained, with a GS_{ave} of ~ 4±1 μm. A large number of grains were tilted away from the c-axis, which resulted in a significant decrease of the (0001) pole figure I_{max} value, from ~25 after 5 turns to ~ 13 after 15 turns, accompanied by an increase in the volume fraction of HABs from 0.78 to 0.83.

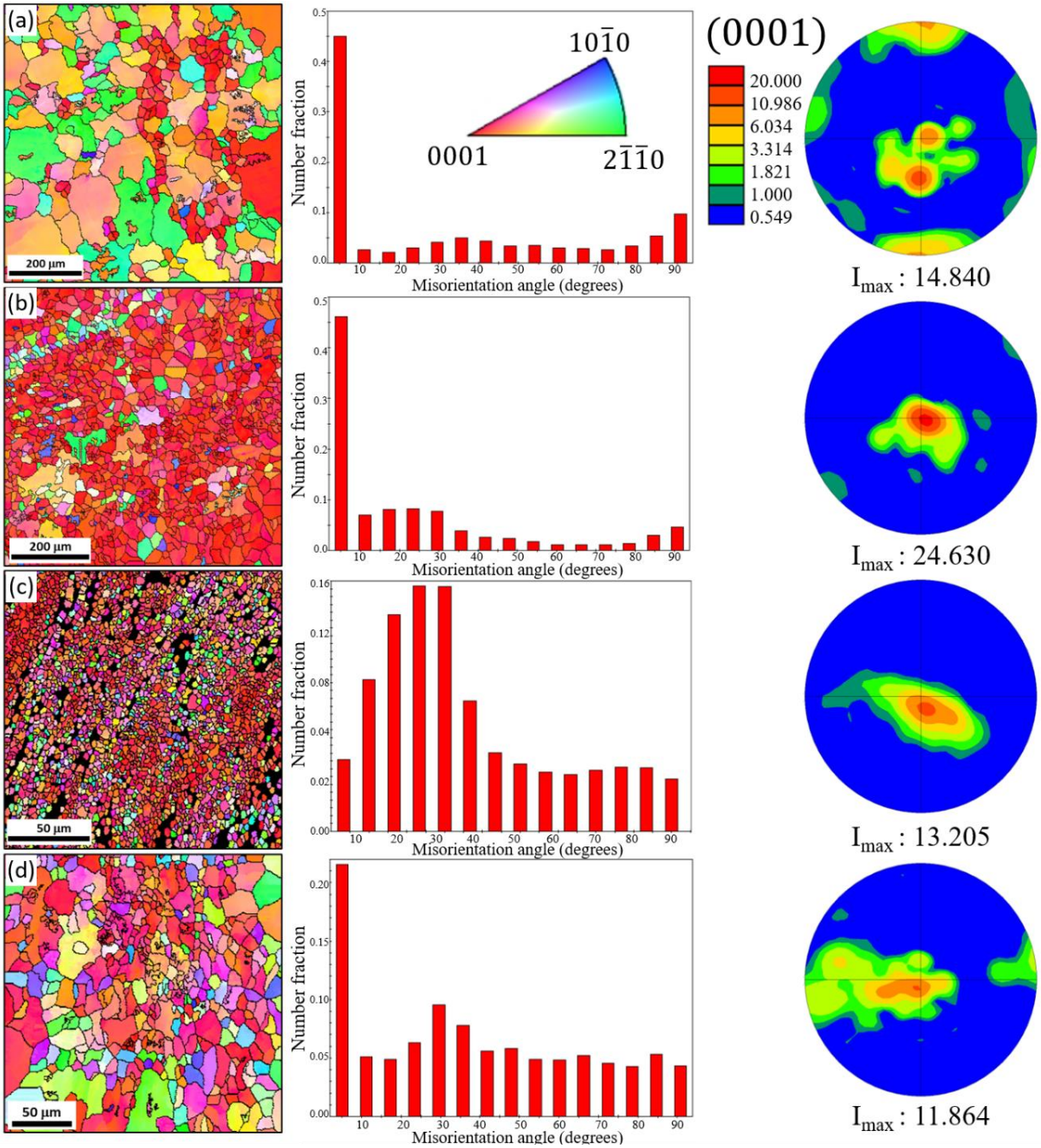

Figure 43: EBSD IPF orientation maps, misorientation angle distribution plots, and basal (0001) pole figures of the Zn matrix collected at the horizontal surface near the periphery of the Zn-10Mg hybrids after HPT for (a) 1 turn, (b) 5 turns, (c) 15 turns, and (d) 30 turns. Imax indicates the maximum intensity values obtained from the respective pole figures. Adapted from [174].

After 30 turns, as shown in Figure 43 (d), the GS_{ave} was ~ 10 ± 7 μm, and a wider distribution of grain sizes was observed compared to after 15 turns. The volume fraction of HABs decreased, from 0.83 after 15 turns to 0.73 after 30 turns, which was similar to that after 5 turns. In addition,

the basal texture weakened, as indicated by a decrease in the I_{max} value of the (0001) pole figure, from 13.2 after 15 turns to 11.9 after 30 turns.

TEM and XRD were used to investigate the phase composition at the regions of highest plastic deformation, which correspond to the periphery of the sample processed for 30 turns. Figure 44 shows a representative BF-TEM image, and its corresponding SAD pattern, of a lift-out extracted from the thickness-shear plane near the periphery, r ~ 4.5 mm, of the Zn-10Mg HPT hybrid after 30 turns. Note that only the transmitted electron beam contributed to the formation of the BF-TEM image in Figure 44 (a), and that the dark areas correspond to strongly diffraction regions of the sample. Nanosized layers, with an approximate thickness of 400-500 nm, as well as nanosized grains with sizes of 200-300 nm, were observed in the severely deformed multilayered microstructure at the sample periphery after 30 turns.

The SAD pattern presented in Figure 44 (b), which corresponds to the entire area shown in Figure 44 (a), shows a clear ring pattern evidencing the polycrystalline nature of the microstructure. The four diffraction rings with a smaller radius, associated with larger interplanar spacings, were identified and labeled according to the following PDF cards of the ICSD: Mg (77908), Zn (421014), Mg_2Zn_{11} (104898), and $MgZn_2$ (104897). The identification of the Mg_2Zn_{11} and $MgZn_2$ intermetallic compounds indicated that a phase transformation in the Zn-10Mg HPT hybrids had occurred after 30 turns.

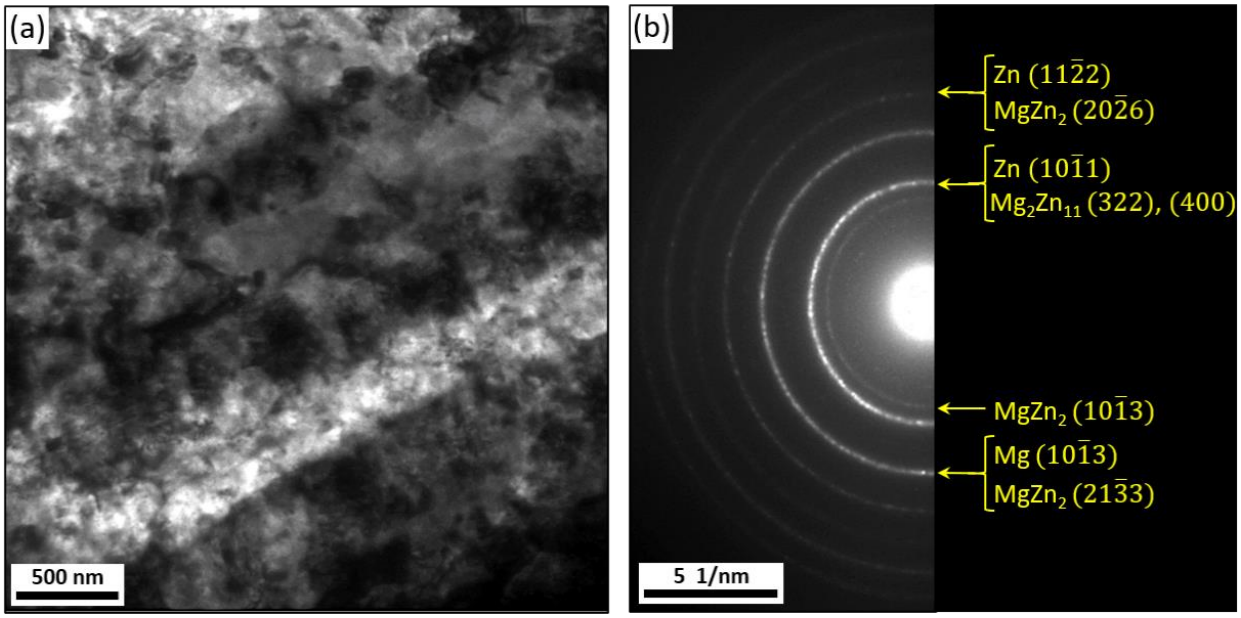

Figure 44: TEM analysis at the thickness-shear plane near the periphery of the Zn-10Mg hybrid after HPT for 30 turns: (a) BF-TEM image and (b) corresponding SAD pattern, where the right half indicates the diffraction rings associated with the phases (Zn, Mg_2Zn_{11}, and $MgZn_2$) identified. [174].

A series of XRD patterns collected from the mid-thickness of the shear-radial plane near the periphery of the Zn-10Mg HPT hybrids after 1, 15, and 30 turns are presented in Figure 45. Conventional background subtraction and peak intensity normalization were performed to facilitate comparison between different XRD scans. It should also be noted that the square root of the intensity is represented in the y axis, in arbitrary units (a.u.), for ease of resolving the lower intensity peaks from the background. Diffraction peaks associated with four different phases were identified and labeled accordingly by using the same PDF cards mentioned in the previous paragraph for the analysis of the SAD pattern. As observed in Figure 45, only diffraction peaks corresponding to Zn and Mg phases were identified after 1 turn, whereas additional peaks associated with Mg_2Zn_{11} and $MgZn_2$ intermetallic compounds were identified after 15 and 30 turns.

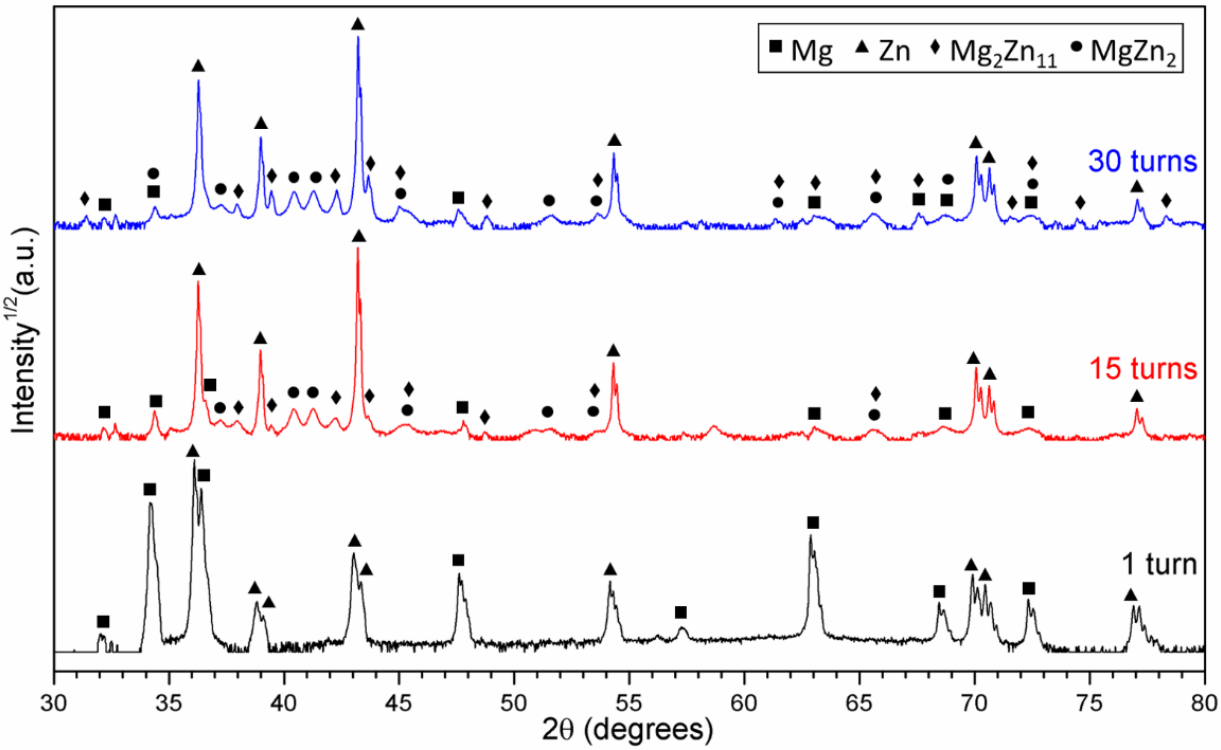

Figure 45: XRD patterns obtained from the periphery at the mid-thickness plane of the Zn-10Mg hybrids after HPT for 1, 15, and 30 turns. The diffraction peaks corresponding to the four phases identified (Zn, Mg, Mg_2Zn_{11}, and $MgZn_2$) are labeled with different symbols. [174].

Despite the similarities between the XRD scans collected from the samples after 15 and 30 turns, a detailed analysis of the peaks associated with the intermetallic phases revealed that they generally exhibited larger intensities after 30 turns. In order to investigate potential variations of the relative peak intensities between different samples, which would be associated with variations in the phase amounts, a quantitative phase analysis was carried out via Rietveld refinement.

The quantification of the phase fractions obtained from the Rietveld refinement are summarized in Table 5. The mass fractions of Zn, and Mg phases changed significantly from 1 to 15 turns, from ~ 0.19 to ~ 0.58, and from ~ 0.81 to ~ 0.28, respectively. However, the mass fractions of Zn and $MgZn_2$ did not change dramatically from 15 to 30 turns, evolving only from ~ 0.58 to ~ 0.62, and from ~ 0.13 to ~ 0.16, respectively. In contrast, the mass fraction of the Mg phase at the

disk periphery decreased by half from 15 to 30 turns, from ~ 0.28 to ~ 0.14, respectively. Conversely, the mass fraction of the Mg_2Zn_{11} phase increased by a factor of four from 15 to 30 turns, from ~ 0.02 to ~ 0.08, respectively.

Table 5: Chemical composition at the periphery of the Zn-10Mg hybrids after HPT from 1, 15, and 30 turns, obtained from Rietveld refinement of the XRD data in Figure 45.

HPT turns	Zn (wt.%)	Mg (wt.%)	Mg_2Zn_{11} (wt.%)	$MgZn_2$ (wt.%)
1	18.6 ± 0.5	81.4 ± 0.5	0	0
15	57.6 ± 0.4	28.0 ± 0.3	1.6 ± 0.2	12.8 ± 0.4
30	62.4 ± 0.4	13.8 ± 0.4	7.5 ± 0.2	16.3 ± 0.3

APT analysis was performed to investigate the atomic composition of a small volume at the periphery of the Zn-10Mg hybrid after 30 turns, and the results are presented in Figure 46. The atom maps for Zn and Mg are provided in Figure 46 (a) and (b), respectively, which evidence an apparent change in atomic concentration for both elements across a diagonal interface in the APT needle extracted. To visualize the morphology and size of this interface, a Zn isoconcentration surface at 30 (at.%) was drawn, and it is highlighted in Figure 46 (c). The black arrow across the isosurface indicates the direction in which the proximity histogram was plotted in Figure 46 (d). The proxigram shows a clear change in atomic composition at either side of the isosurface (indicated by a vertical dashed line), over a 8 nm distance approximately, as highlighted in yellow. The chemical composition evolved from 99.5Mg-0.4Zn (at.%) to 41.5Mg-58.4Zn (at. %). It should be noted that 99.5Mg-0.4Zn (at.%) corresponds to a solid solution of Zn in Mg, whereas 41.5Mg-58.4Zn (at. %) is reasonably close to the Mg_2Zn_3 intermetallic phase, which was not identified via XRD or TEM.

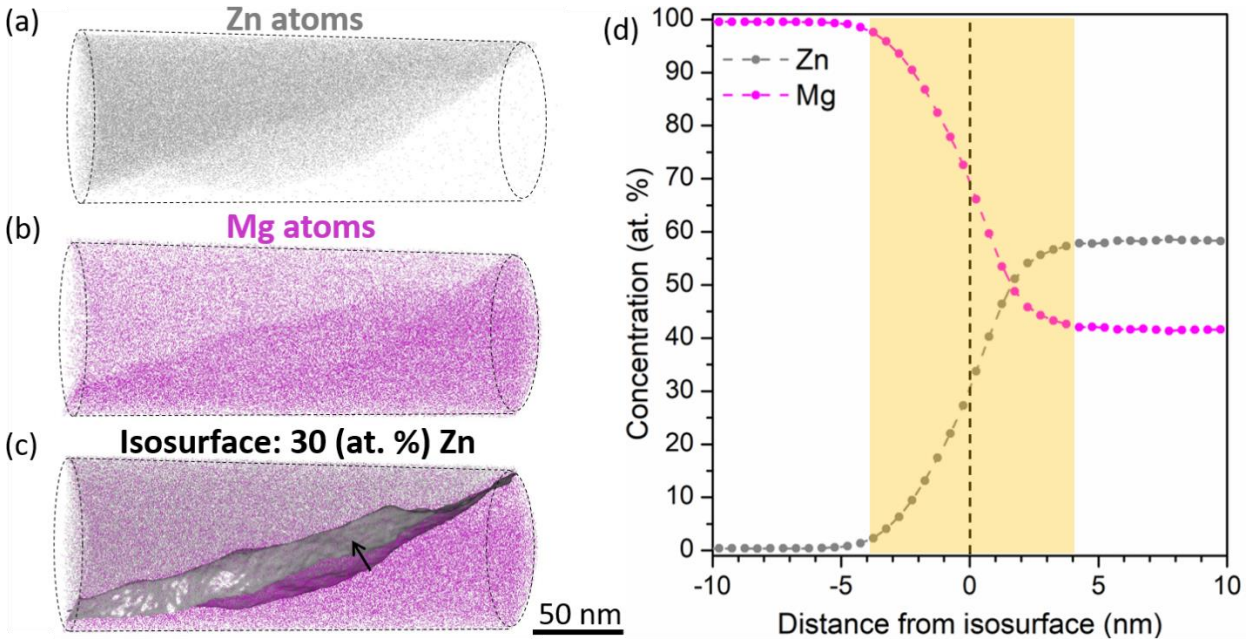

Figure 46: APT reconstruction of a needle extracted near the periphery of the Zn-10Mg hybrid after HPT for 30 turns: (a) atom map of Zn, (b) atom map of Mg, (c) 3D isosurface with a concentration of 30Zn (at. %), (d) proximity histogram along the black arrow in the isosurface highlighted in (c). The average composition across the isosurface evolved from 99.5Mg-0.4Zn to 41.5Mg-58.4Zn (at. %). The transition region between the two compositions is highlighted in yellow in (d).

4.2.1.2. Hardness of the HPT-processed Zn-10Mg hybrids

The HV hardness evolution along the diameter of the cross-section in the Zn-10Mg HPT hybrids is presented in Figure 47. It should be noted that the HV values were measured at the mid-thickness plane of the sample, away from the top and bottom surfaces. The HV values were plotted with respect to the distance from the center of the sample in Figure 47 (a), and with respect to the equivalent Von Mises strain of the region where they were collected in Figure 47 (b). As observed in Figure 47 (a), the HV values were relatively uniform at ~ 35-40 HV across the diameter after 1 turn, consistent with the HV values measured for pure Zn (36 HV) and pure Mg (35 HV) denoted by dashed lines for reference. After 5 turns, the HV values increased within the range of ~ 50-70 HV, reaching a maximum of 82 HV at one of the edges of the sample. After 15 turns, there was

not only an overall significant increase of the HV values, particularly near the disk edge, but also a very wide distribution across the disk diameter, ranging from ~ 70-175 HV, with a maximum value of ~ 200 HV at both edges of the sample. Similarly, after 30 turns, the HV values were generally higher than those after 15 turns, remaining very scattered across the disk in a wide range from ~ 70-200 HV, and reaching maximum values of ~ 250 HV at both edges of the sample. In general, there was a trend of increasing hardness with increasing number of HPT turns.

The Von Mises strain values corresponding to the HV values plotted in Figure 47 (b) were calculated from Equation 3. The maximum strain values after 1, 5, 15, and 30 turns were ~ 20, 100, 300, and 600, respectively, at the periphery of the samples, where the maximum HV values were measured in all cases. Note that the x-axis is plotted in logarithmic scale and that the aggregate HV values increase following an exponential-type trend with increasing strain.

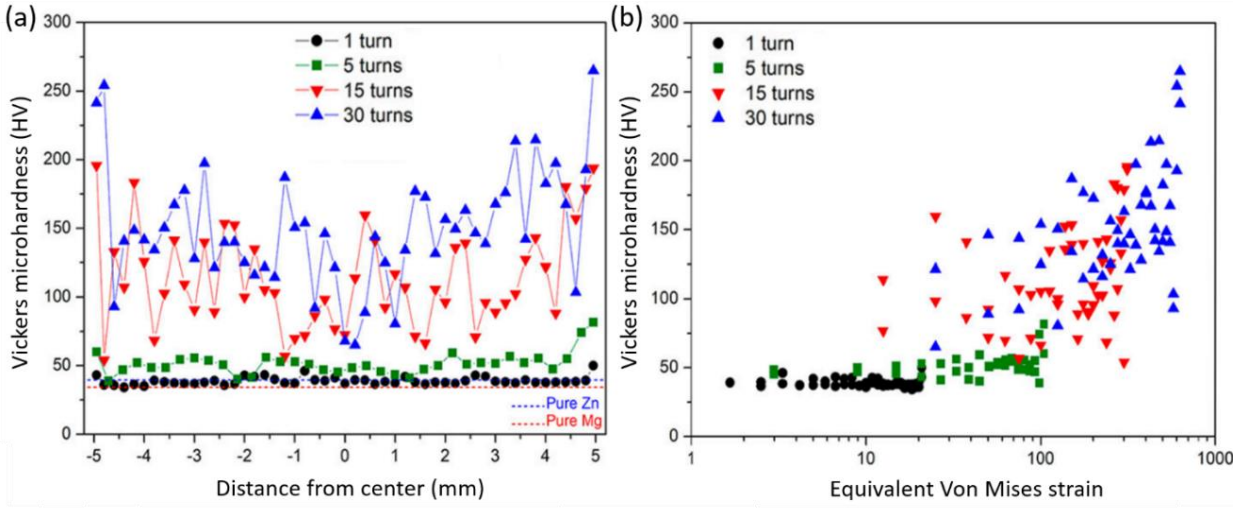

Figure 47: HV measurements along the diameter of the cross-section in the Zn-10Mg hybrids after HPT for 1, 5, 15, and 30 turns with respect to (a) the distance from the center of the sample and (b) the equivalent Von Mises strain at the location where the HV values were performed. Each data point corresponds to the average of four individual HV indents at the mid-thickness of the sample, away from the sample surfaces. [174].

A two-dimensional distribution of the hardness across the HPT-processed samples can be observed in Figure 48, where a 4x65 matrix of HV values (i.e., a total of 260 HV values) was acquired from a rectilinear grid pattern of equispaced HV indents in each sample. It should be mentioned that the color-contour maps provided do not represent the entire cross-section of the sample, as the distance between the center of the indents and the edge of the sample was kept at least 3 times the value of the indentation diagonal to prevent the material from flowing sideways. After 1 turn, the hardness was relatively homogenous along the cross-section, in agreement in Figure 47, with values ranging between 35-40 HV.

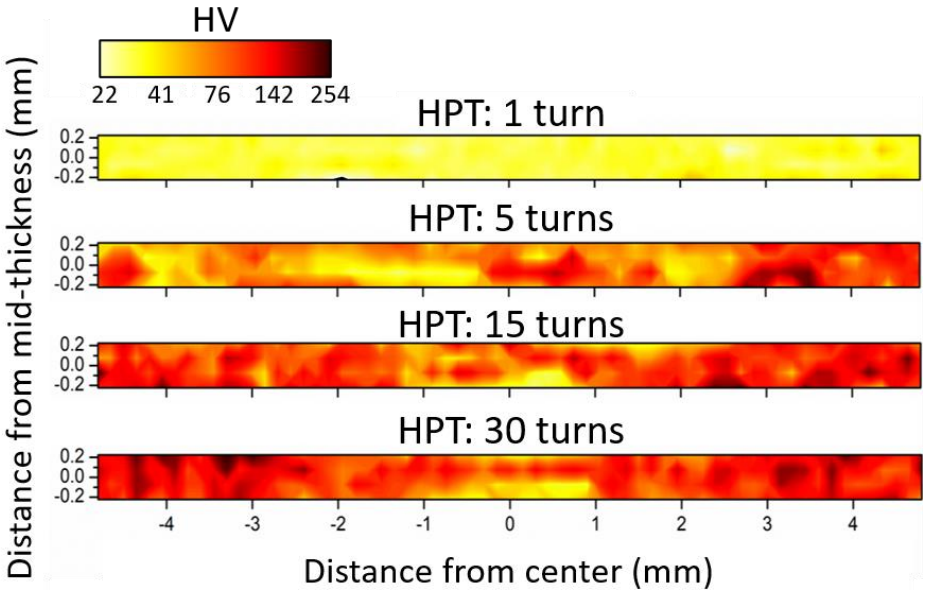

Figure 48: Color-coded HV contour maps corresponding to the cross-sections of the Zn-3Mg hybrids after HPT for 1, 5, 15, 30 turns presented in Figure 40. Each map corresponds to a 4x65 matrix of HV values recorded in a rectilinear grid pattern.

After 5 turns, notable differences in hardness were observed at different locations of the cross-section, with regions reaching maximum values ~ 100 HV near the periphery, whereas other regions displayed hardness values of ~ 60-70 HV. Unlike expected, the lowest HV values measured were not at the sample center, suggesting that the sample may have slipped during HPT processing leading to asymmetrical plastic deformation with respect to the sample center.

After 15 turns, the hardness distribution was reasonably symmetrical, with most of the hardness values ranging between ~ 70-150 HV. As expected, the highest values were recorded near the periphery and the lowest at the sample center. Similarly, after 30 turns, the hardness distribution seemed fairly symmetrical, with average values between ~ 180-200 HV at r ~ 4 mm, and average values of 60-80 HV at r < 1 mm. It was also noted that the HV values recorded at the same distance from the center and different mid-thickness values were not uniform, and this was true for the samples processed for 5, 15, and 30 turns.

4.2.1.3. Electrochemical properties of the HPT-processed Zn-10Mg hybrids

The OCP, PDP, Nyquist, and Bode plots obtained from electrochemical testing of the Zn-10Mg HPT hybrids after 1, 15, and 30 turns in SBF are presented in Figure 49. From the OCP curves in Figure 49 (a) collected for 10 hours, it is observed that right after immersion in SBF, the samples after 1 turn exhibited a potential of -1.014 V vs. SCE, whereas those samples after 15 and 30 turns exhibited more negative potentials, -1.527 and -1.381 V vs. SCE, respectively. After the first hour of immersion, the potential of the samples after 1 turn decreased gradually towards more negative values, reaching a stable potential at -1.116 V vs. SCE, with minimal variations for the rest of the OCP test. On the contrary, the potential of the samples after 15 and 30 turns shifted towards more positive potentials after the first hour of immersion, reaching stable potentials at -1.360 and -1.249 V vs. SCE, respectively, during the next two hours for the rest of the OCP test.

The PDP curves obtained after OCP stabilization are shown in Figure 49 (b), and their corresponding Ecorr and Icorr values, as well as the estimated corrosion rates, are provided in Table 6. It was observed that the Ecorr of the samples after 1 turn was slightly more noble in SBF than that after 15 and 30 turns. The samples after 1 turn exhibited the lowest I_{corr} and the highest

E_{corr} values, whereas those after 15 turns exhibited the highest I_{corr} and the lowest E_{corr} values. Conversely, the samples after 30 turns presented intermediate I_{corr} and E_{corr} values.

The charge transfer and mass transfer reactions associated with the electrochemical responses were evaluated by EIS through the analysis of the Nyquist and Bode plots in Figure 49 (c) and (d), respectively. The EEC models developed from fitting the experimental EIS data for simulating the electrochemical reactions in the samples and the evolution of the oxide film developed during immersion in SBF are shown in Figure 50.

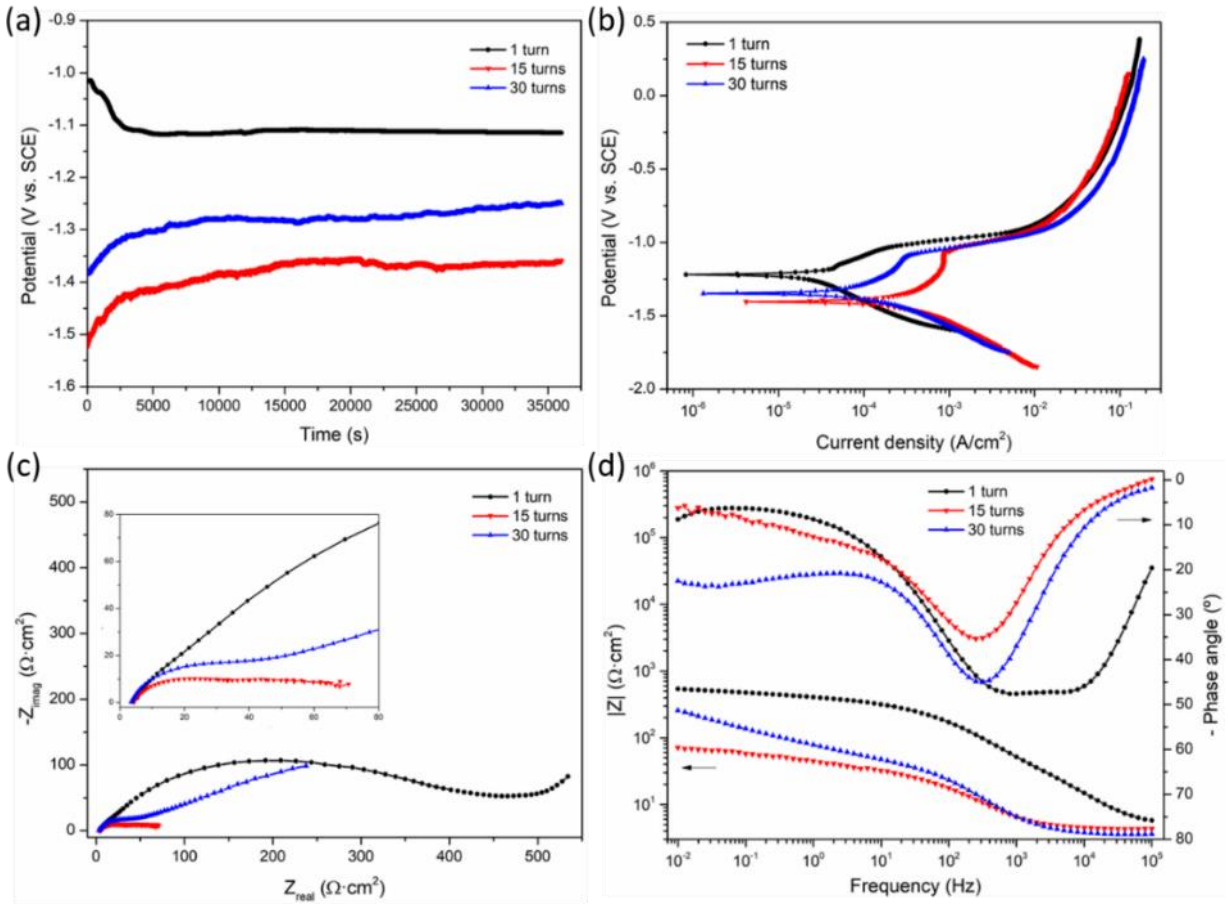

Figure 49: Electrochemical behavior at the mid-thickness plane of the horizontal surface of the Zn-10Mg hybrids after HPT for 1, 15, and 30 turns in SBF: (a) OCP curves, (b) PDP curves, (c) Nyquist plots, and (d) Bode-module and Bode-phase plots. [174].

Table 6: Electrochemical data obtained from the PDP curves in Figure 49 (b).

HPT turns	E_{corr} (V)	I_{corr} (μA/cm2)	β_a (mV/decade)	β_c (mV/decade)	Corrosion rate (mm/y)
1	-1.230	21.28	216.1	-234.3	0.32
15	-1.370	142.90	175.0	-137.0	2.16
30	-1.350	41.87	177.4	-104.5	0.63

The elements used for EEC modeling were: solution resistance (R_s), film resistance (R_f), charge transfer resistance (R_{ct}), constant phase element of the film (Y_f), and constant phase element of the double layer (Y_{dl}). Note that a Warburg element (W) was added to the EEC model to represent the diffusion behavior after 1 and 30 turns. The kinetic parameters obtained from fitting and optimization of the EIS data are provided in Table 7.

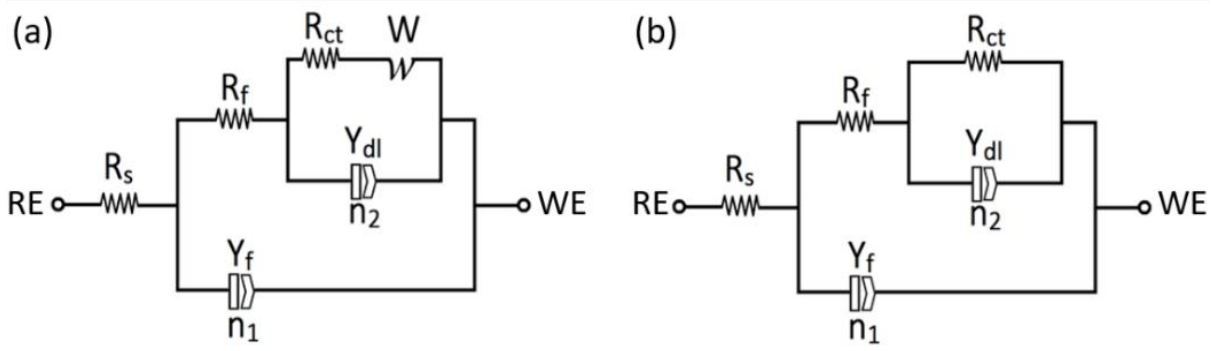

Figure 50: EEC models selected to fit the EIS data obtained from the Zn-10Mg HPT hybrids in SBF after (a) 1 turn and 30 turns and (c) 15 turns. R_s is the solution resistance, R_f is the film resistance, R_{ct} is the charge transfer resistance, Y_f is the constant phase element of the film, Y_{dl} is the constant phase element of the double layer, and W is the Warburg element. RE and WE indicate the reference and working electrodes, respectively. [174].

Table 7: Kinetic parameters obtained from the EIS plots for fitting the EEC models in Figure 50. Adapted from [174].

HPT turns	Rs (Ω cm^2)	Yf		Rf (Ω-cm^2)
		(μS.s^n/cm^2)	n_1	
1	3.92	48.6	0.67	0.62
15	3.93	210.5	0.79	0.0027
30	4.42	920.0	0.45	73.19

HPT turns	Ydl		Rct (Ω-cm^2)	W (S.s$^{0.5}$/cm^2)	Goodness of Fit
	(μS.s^n/cm^2)	n_2			
1	543.6	0.15	592.40	0.034	6.12×10^{-4}
15	7507.0	0.21	354.00	N/A	1.79×10^{-4}
30	8570.0	0.58	371.00	0.015	4.13×10^{-4}

4.3. Zn-3Mg hybrids

This section presents the microstructural characterization and hardness evolution of the Zn-3Mg hybrids after HPT for 1, 5, 15, and 30 turns. The microstructures were characterized using SEM, EDS, EBSD, TEM, XRD, and APT. The hardness was investigated with both HV and nanoindentation. It should be mentioned that this composition represents about the minimum Mg concentration that can be achieved in an HPT hybrid with a Zn/Mg/Zn stack configuration, since the thickness of the central Mg disk in the Zn-3Mg hybrid configuration is ~ 170 μm, which is significantly thinner than that of the external Zn disks (~ 665 μm).

Similar to the Zn-10Mg hybrids investigated in section 4.2, special emphasis is given to the region of highest plastic deformation, corresponding to the periphery of the sample after 30 turns. In addition, the microstructure and hardness were examined in the Zn-3Mg hybrid after 30 turns, followed by PDA (200 ºC, 1h), and the corresponding results are also presented in this section.

4.3.1. HPT-processed Zn-3Mg hybrids

4.3.1.1. Microstructures of the HPT-processed Zn-3Mg hybrids

A series of low-magnification SE-SEM images taken from the cross-sections of the Zn-3Mg HPT hybrids after 1, 5, 15, and 30 turns are shown in Figure 51. The Zn and Mg disks were mechanically bonded into a compact sample after 1 turn, without evidence of voids or major cracks, and the intermediate Mg disk was still observed across the diameter of the sample. After 5 tuns, the Mg layer was fragmented closer to the disk periphery, r > 3 mm, where larger plastic deformation occurred, whereas that Mg-rich region close to the disk center remained unmixed. After 15 and 30 turns, the central region of the disk, r < 2 mm, exhibited finer Mg-rich phases, which were

distributed preferentially aligned with the shear direction. The peripheral areas of the sample became more uniform with increasing number of turns, and there was no macroscopic evidence of Mg-rich phases after 30 turns at r > 3 mm.

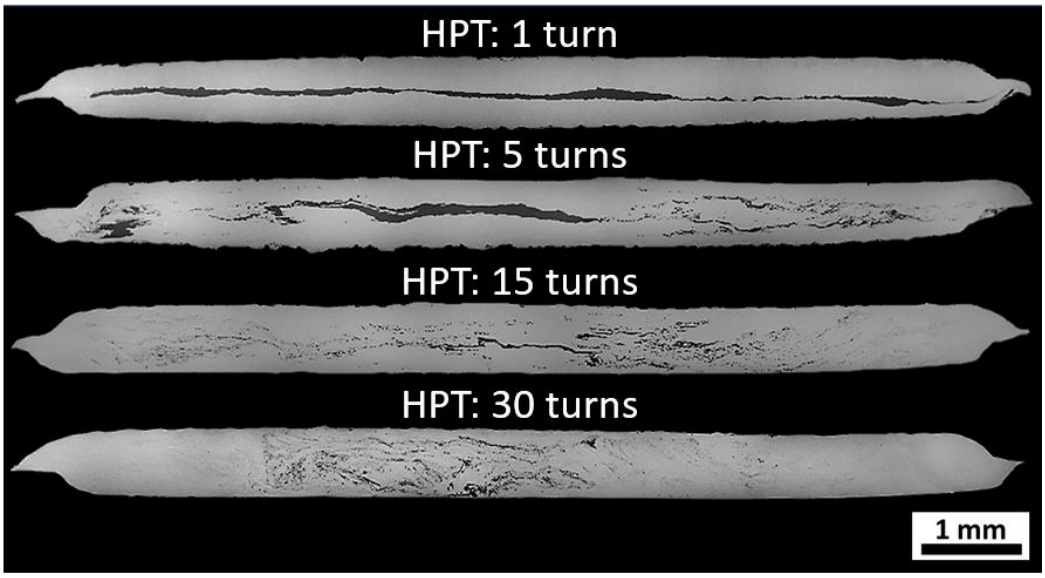

Figure 51: SE-SEM images corresponding to the cross-sections of the Zn-3Mg hybrids after HPT for 1, 5, 15, and 30 turns, processed with an applied pressure of 6 GPa and a rotational speed of 1 rpm. Adapted from [127].

The mixing between Zn and Mg phases at the peripheral region of the Zn-3Mg HPT hybrid after 30 turns was investigated by EDS. The elemental maps, EDS spectrum, and average chemical composition of the area inspected are provided in Figure 52. A uniform elemental distribution of Zn and Mg was identified in the scanned region, as observed in Figure 52 (b) and (c), respectively. Moreover, as indicated in the table next to the EDS spectrum in Figure 52 (d), the average chemical composition was ~ 96.9Zn-3.1Mg (wt.%), in good agreement with the targeted composition for the hybrid. It is important to highlight that this EDS analysis was performed with an accelerating voltage of 25 kV in order to obtain the chemical composition from a relatively large interaction volume of the sample, representative of the bulk composition. For reference, the interaction depth

of a 25 kV electron beam in Zn is ~ 2.7 μm, as calculated from the Castaing´s formula provided in Equation 4.

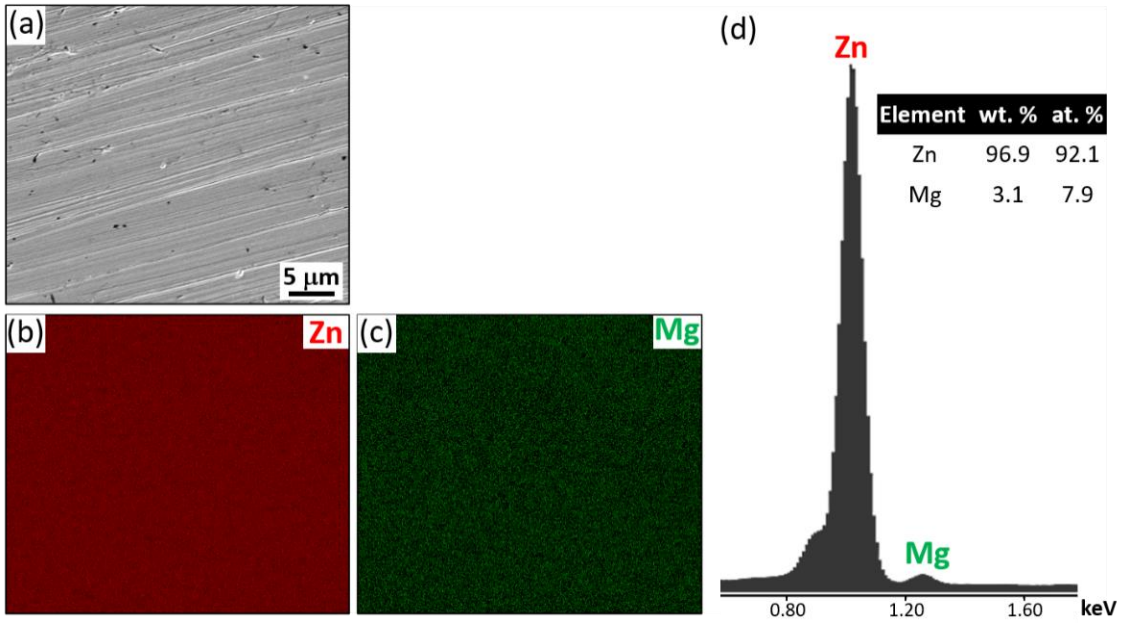

Figure 52: EDS analysis neat the periphery at the cross-section of the Zn-3Mg hybrid after HPT for 30 turns: (a) SE-SEM photomicrograph of the scanned region, (b) Zn map, (c) Mg map, and (d) EDS spectrum with the corresponding chemical compositions. Adapted from [124].

BSE-SEM was used to examine the microstructures at the periphery of the cross-sections after 30 turns, and images at different magnifications are provided in Figure 53 (a-c). It should be noted that the photomicrographs were acquired in the same orientation as those in Figure 51, such that the horizontal and vertical directions correspond to the radial and thickness directions defined in Figure 12, respectively. A fairly equiaxed microstructure with a GS_{ave} of ~ 100-200 nm was observed after HPT for 30 turns. Vortex-like Mg-rich regions were identified, and they are highlighted with yellow arrows in Figure 53 (a) and (b). These microstructural features, often referred to as swirls, are a result of local turbulences, which are characteristic of HPT processing [177,178]. In addition, nanosized precipitates, highlighted with green arrows in Figure 53 (c), ranging from ~ 20-100 nm, were evenly distributed within the microstructure.

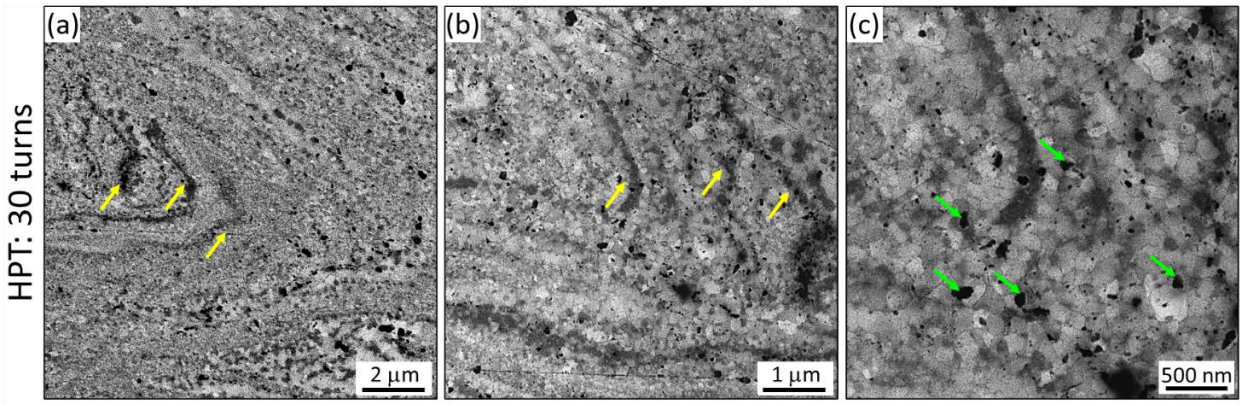

Figure 53: Representative BSE-SEM photomicrographs acquired near the periphery at the cross-section of the Zn-3Mg hybrid after HPT for 30 turns: (a) lower magnification, where yellow arrows indicate Mg-rich swirls, (b) higher magnification of the same region in (a), and (c) higher magnification of the same region in (b), where the green arrows indicate Mg-rich nanoprecipitates in the Zn matrix. The horizontal and vertical directions correspond to the radial and thickness directions, respectively, as defined in Figure 12. Adapted from [127].

The microstructure at the peripheral region of the Zn-3Mg HPT hybrid after 30 turns was further analyzed with TEM/STEM, and representative BF-TEM, BF-STEM, and corresponding HAADF-STEM images are provided in Figure 54 (a), (b), and (c), respectively. It should be noted that the TEM/STEM imaging plane was normal to that of the SEM images in Figure 53, such that the horizontal and vertical directions correspond to the shear and thickness directions defined in Figure 12, respectively.

A reasonably equiaxed microstructure with a GS_{ave} of ~ 100-200 nm was found, as observed in Figure 54 (a), consistent with the GS_{ave} value measured from SEM. Multiple nanoscale precipitates with irregular shapes, ranging from ~ 20-150 nm, were distributed in the Zn-rich matrix, as observed in Figure 54 (b) and (c), in agreement with those identified by SEM in Figure 53 (c). Moreover, the darker appearance of these nanoscale precipitates in the HAADF image indicated that they are richer in Mg than the Zn matrix, since the contrast in HAADF mode is proportional to the atomic number, and Zn (Z=30) has a higher atomic number than Mg (Z=12).

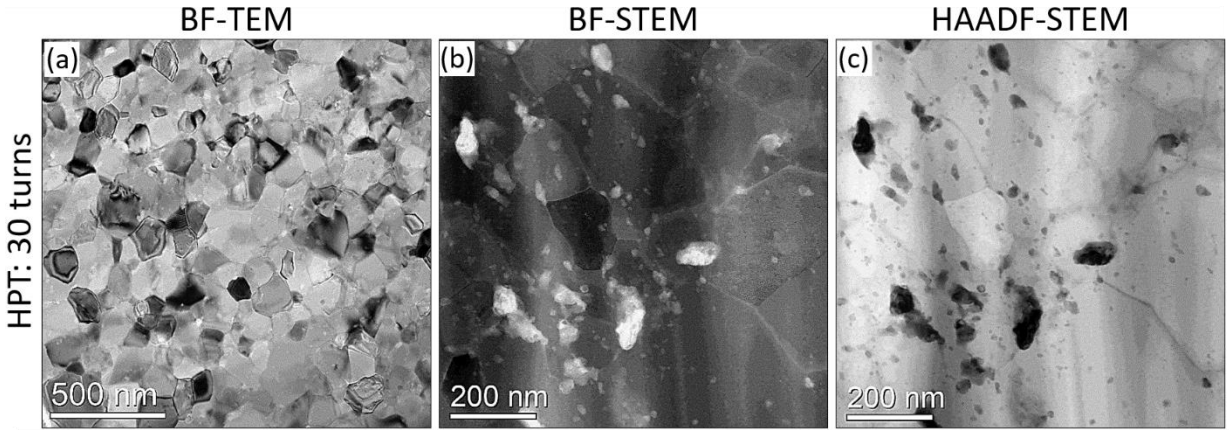

Figure 54: Representative TEM/STEM images acquired near the periphery at the cross-section of the Zn-3Mg hybrid after HPT for 30 turns: (a) BF-TEM, (b) BF-STEM, and (c) corresponding HAADF-STEM. The horizontal and vertical directions correspond to the shear and thickness directions, respectively, as defined in Figure 12. Adapted from [127].

The phases present in the Zn-3Mg HPT hybrids after 1, 15, and 30 turns were investigated by XRD at the mid-thickness plane of the sample surface, and the resulting scans are shown in Figure 55. It should be mentioned that these XRD profiles were obtained from the whole samples, and not just from the sample periphery as those shown for the Zn-10Mg HPT hybrids in section 4.2.1.1. It is also important to note that the intensities of the XRD profiles in Figure 55 were normalized to assist in their comparison, and that the y-axis represents the square root of the intensity to better resolve low-intensity diffraction peaks. Similar to the XRD results of the Zn-10Mg HPT hybrids, four different phases were identified and labeled accordingly: Zn, Mg, Mg_2Zn_{11}, and $MgZn_2$.

After 1 turn, the sample consisted only of Zn and Mg, and the Mg peaks typically exhibited lower intensities than the Zn peaks, which was consistent with the bulk composition of the sample measured by EDS. After 15 and 30 turns, peaks corresponding to Mg_2Zn_{11} and $MgZn_2$ intermetallic compounds were also identified. Furthermore, it was evident from both their peak intensities and the presence of new peaks corresponding to these intermetallic phases that their phase fractions increased with increasing plastic deformation from 15 to 30 turns, yet the fractions

of intermetallic phases were not quantified. It was also noted that the Mg peaks tended to either decrease their intensity or disappear with increasing plastic deformation, and the potential reason for that will be discussed later.

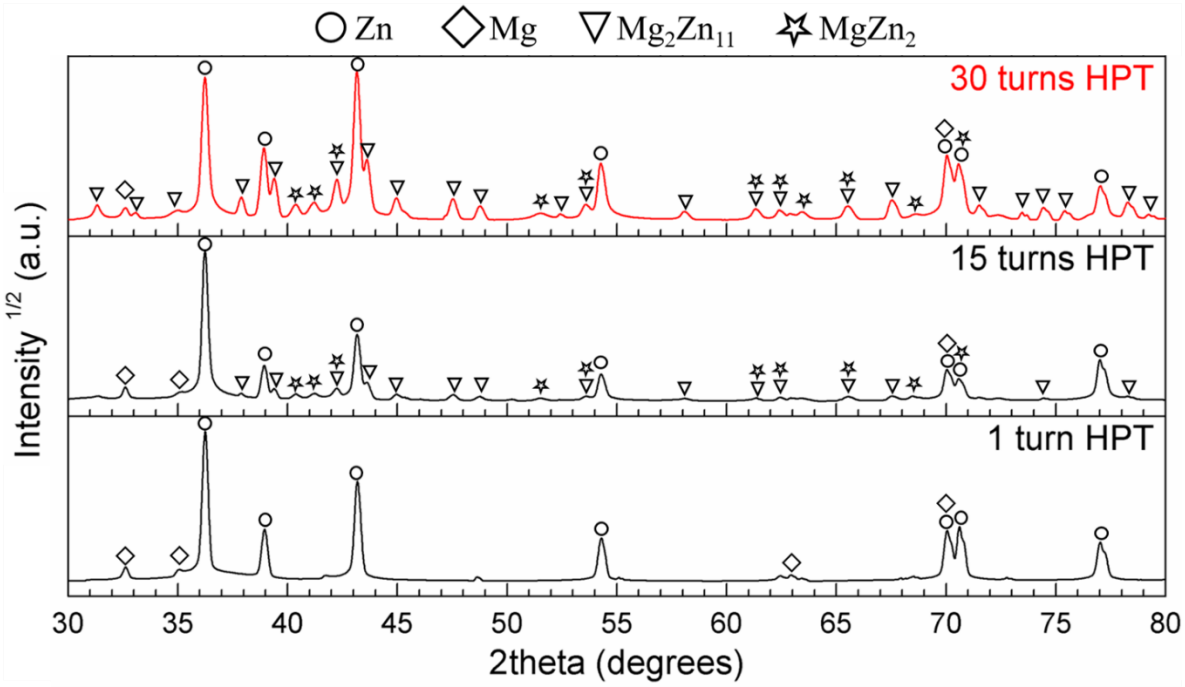

Figure 55: XRD patterns obtained at the mid-thickness plane of the Zn-3Mg HPT hybrids after 1, 15, and 30 turns. The diffraction peaks corresponding to the four phases identified (Zn, Mg, Mg_2Zn_{11}, and $MgZn_2$) are labeled with different symbols. Adapted from [127].

The atomic composition of a small volume near the periphery of the Zn-3Mg HPT hybrid after 30 turns was analyzed by APT, and the results are provided in Figure 56. The atom map for Zn, in Figure 56 (a), shows that Zn atoms were present across the sample, although at a larger concentration at the bottom of the APT needle. On the contrary, the atom map for Mg, in Figure 56 (b), shows that Mg atoms were only present in specific regions of the sample. In order to investigate the change in composition from the Mg-rich regions to the Mg-depleted regions, a Zn isosurface at 90 (at. %) was generated, and it is highlighted in Figure 56 (c). The black arrows

across the isoconcentration surfaces identified indicate the direction of the proximity histogram plotted in Figure 56 (d).

It should be noted that each data point in Figure 56 (d) represents the average atomic concentration of either Zn or Mg at a specific distance from the isosurfaces. The proxigram shows an evident change in composition across the isoconcentration surface (indicated by a vertical dashed line) from 82.7Zn-17Mg (at. %) to 99.2Zn-0.3Mg (at. %) over a distance of ~ 4 nm (highlighted in yellow), which represents the phase boundary. The composition of 82.7Zn-17Mg (at. %) is reasonably close to that of Mg_2Zn_{11}, and 99.2Zn-0.3Mg (at. %) corresponds to a solid solution of Mg in Zn.

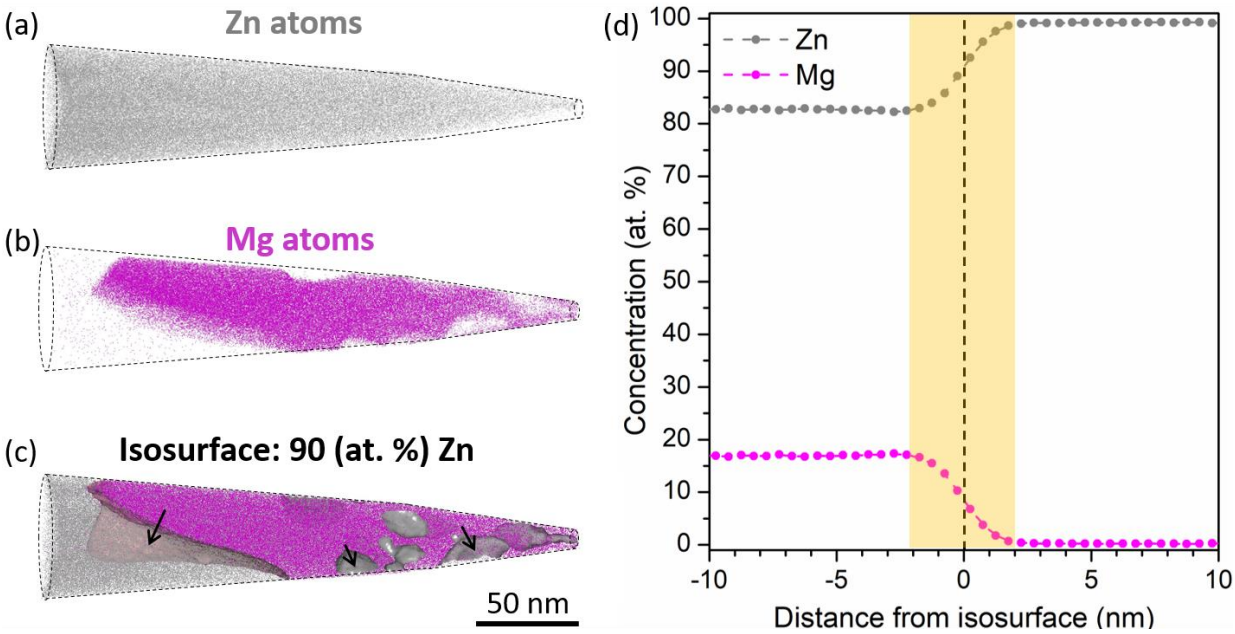

Figure 56: APT reconstruction of a needle extracted near the periphery of the Zn-3Mg hybrid after HPT for 30 turns: (a) atom map of Zn, (b) atom map of Mg, (c) 3D isosurfaces with a concentration of 90Zn (at. %), (d) proximity histogram along the black arrows in the isosurfaces highlighted in (c). The average composition across the isosurface evolved from 82.7Zn-17Mg to 99.2Zn-0.3Mg (at. %). The transition region between the two compositions is highlighted in yellow in (d).

The crystal orientations, distribution of grain sizes, and misorientation angles near the periphery at the thickness-radial plane of the Zn-3Mg HPT hybrid after 30 turns were investigated by EBSD. Figure 57 shows the image quality map of the scanned area in (a), with the IPF maps corresponding to the Zn, Mg, and Mg_2Zn_{11} phases identified in (b), (c), and (d), respectively. Phase maps corresponding to the Zn, Mg, and Mg_2Zn_{11} phases are provided in (e), (f), and (g), respectively. As observed in Figure 57 (a), the microstructure exhibited extreme grain refinement, with similar grain sizes well below 500 nm. Turbulent regions similar to those highlighted with yellow arrows in Figure 53 were identified and corresponded to lower CI value regions, indicated by darker areas in Figure 57 (a).

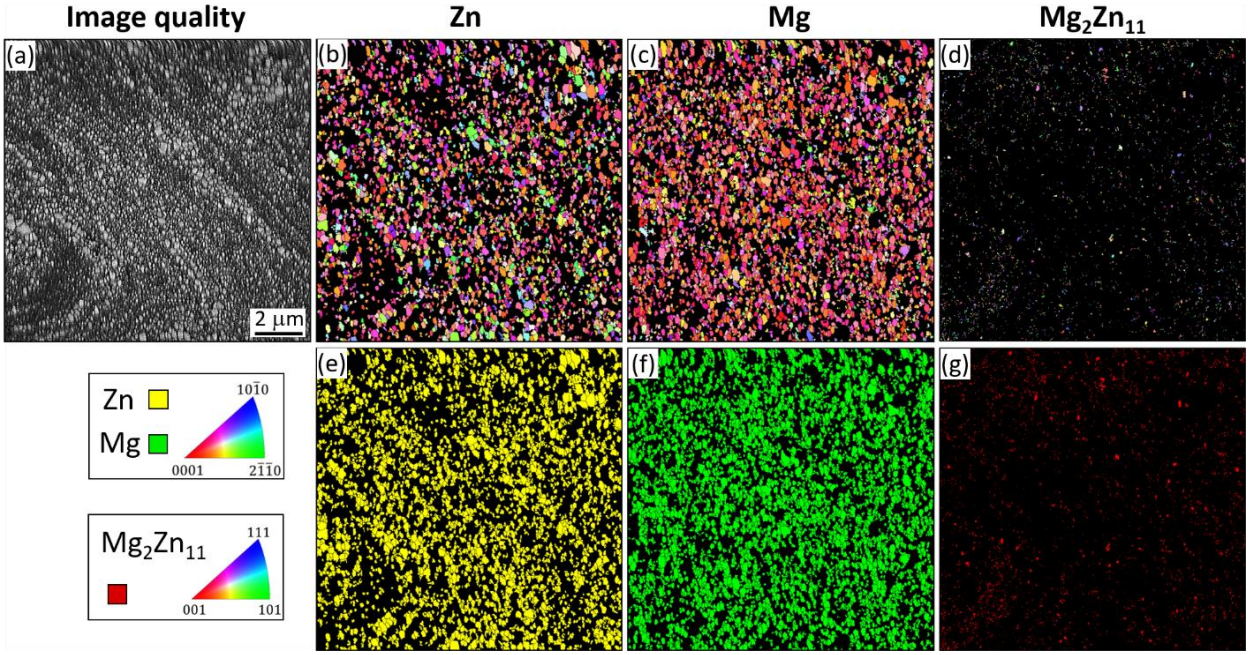

Figure 57: EBSD maps of the Zn-3Mg hybrid after HPT processing for 30 turns near the sample periphery: (a) image quality map of the scanned area and corresponding (b) Zn IPF map, (c) Mg IPF map, (d) Mg_2Zn_{11} IPF map, (e) Zn phase map, (f) Mg phase map, and (g) Mg_2Zn_{11} phase map. The principal IPF triangles for Zn, Mg, and Mg_2Zn_{11} phases, with their respective crystal orientations, are provided.

A larger fraction of grains than expected were associated with the Mg phase, and the potential reason for this will be discussed later. The grain colors in the Zn and Mg IPF maps indicated that the majority of the grain surface normal were closely aligned with <0001>, suggesting a basal texture. The basal pole figures provided in Figure 58 confirmed a strong basal texture for both Zn and Mg phases, although it was noted that most of the poles were slightly misoriented with respect to <0001>.

It should be mentioned that the identification of Mg_2Zn_{11} by EBSD is shown as a proof-of-concept in support of the XRD and APT results presented earlier; however, the EBSD data retrieved from this phase was not used to derive any further conclusion due to the low fraction and generally lower CI values, as compared to the Zn and Mg phases.

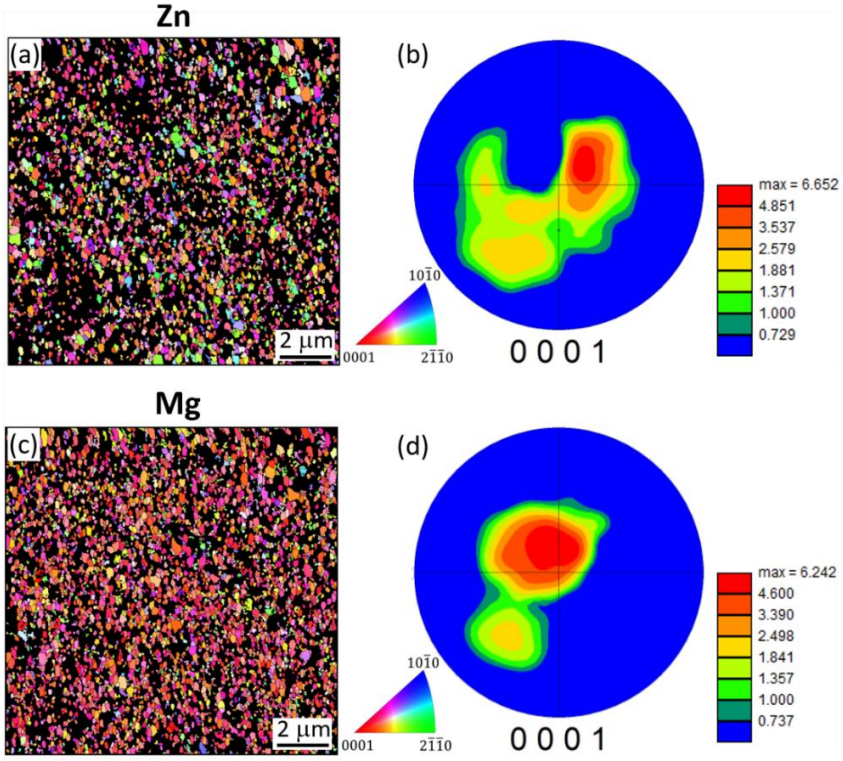

Figure 58: EBSD analysis of the Zn-3Mg hybrid after HPT for 30 turns: (a) Zn IPF map, and (b) corresponding basal (0001) pole figure, (c) Mg IPF map, and (b) corresponding basal (0001) pole figure. The IPF triangles are provided next to the IPF maps, and the color scales indicating the texture intensities are provided next to the pole figures.

The distributions of GS and misorientation angles are plotted in Figure 59 (a) and (b), respectively, for the Zn and Mg phases together. These distributions were obtained from the EBSD results presented in Figure 57. From Figure 59 (a), a GS_{ave} of ~ 180 ± 70 nm was obtained, and the data followed a right-skewed unimodal distribution, indicating that a large fraction of the grains identified were finer than the average value, with sizes of ~ 130-150 nm, as denoted by the position of the mode. The grain sizes in the microstructure ranged from ~ 80-400 nm; however, those with sizes above 250 nm, which were responsible for the positive skewness of the GS distribution, represented less than 15 % of the total scanned area.

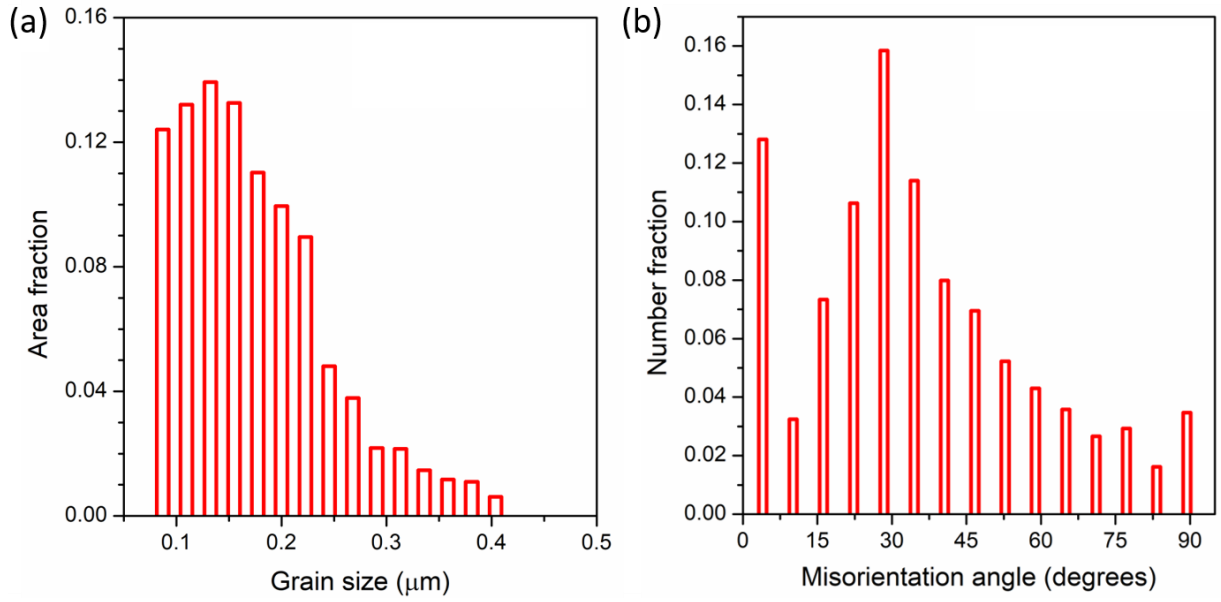

Figure 59: Distributions of (a) grain size and (b) misorientation angle obtained from the Zn and Mg phases together by EBSD analysis near the periphery of the Zn-3Mg hybrid after HPT processing for 30 turns.

From Figure 59 (b), the amount of HABs (above 15º misorientation) was ~ 84 % of the total number of boundaries identified in the microstructure. The fractions of boundaries increased from 10-30º and decreased from 30º to 80º. A slight increase in the fraction of boundaries was observed at ~ 90º.

4.3.1.2. Mechanical properties of the HPT-processed Zn-3Mg hybrids

4.3.1.2.1. Microhardness

The distribution of HV values was examined over the cross-section of the Zn-3Mg HPT hybrids after 1, 5, 15, and 30 turns. In each sample, a rectilinear grid pattern of 4x65 hardness indents (i.e., a total of 260 HV values) was obtained, and they are plotted in Figure 60 in the form of color-coded maps with respect to the distance from the center and the distance from the mid-thickness at which they were measured.

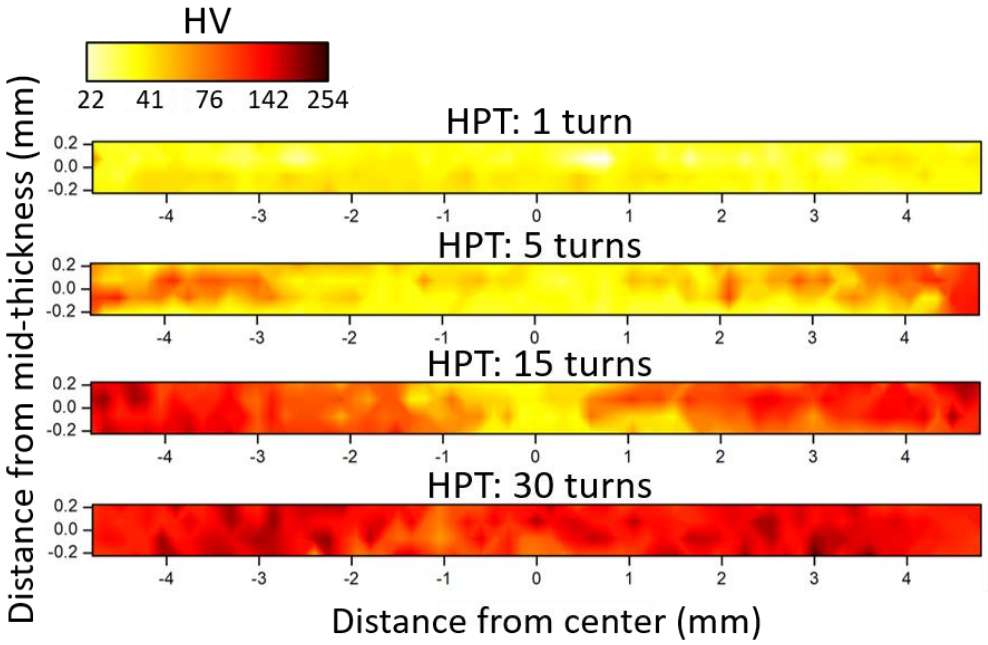

Figure 60: Color-coded HV contour maps corresponding to the cross-sections of the Zn-3Mg hybrids after HPT for 1, 5, 15, 30 turns presented in Figure 51. Each map consists of a 4x65 matrix of HV measurements recorded in a rectilinear grid pattern. Adapted from [127].

The mean values of each of the four different HV measurements collected at the same distance from the sample center, but a different distance from the mid-thickness, are provided in Figure 61. After 1 turn, a uniform hardness distribution was observed across the sample, with an average of ~ 39 HV, which is consistent with the HV values measured for pure Zn (36 HV) and pure Mg (35

HV). After 5 turns, higher hardness values were measured near the periphery of the sample after 5 turns, with an average of ~ 68 HV at r > 3 mm, and an average of ~ 45 HV at r < 3 mm.

After 15 turns, the hardness distribution was reasonably symmetrical with respect to the center of the sample and increased gradually with increasing distance from the center. Like after 5 turns, the central region after 15 turns maintained lower hardness, with average values in the range of ~ 40-60 HV at r < 1 mm. However, the average hardness was ~140-160 at r > 4 mm, and reached maximum values near 200 HV.

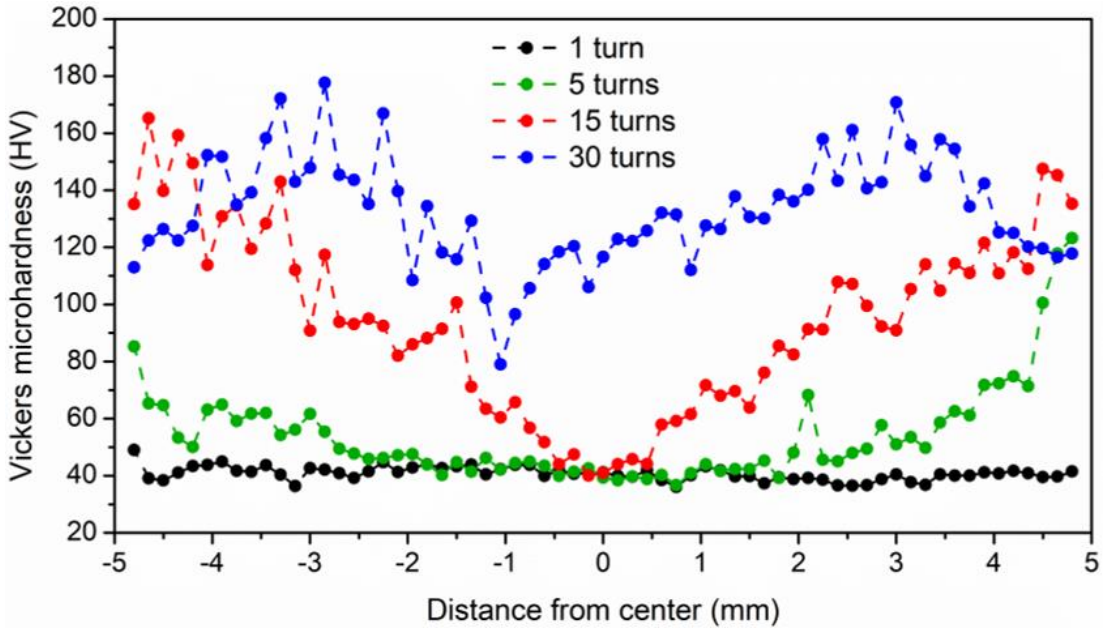

Figure 61: Evolution of the average HV values across the diameter of the Zn-3Mg hybrids after HPT for 1, 5, 15, and 30 turns. This plot is generated with the same HV values shown in Figure 60. Each data point corresponds to the average of four different HV measurements collected at the same distance from the sample center but at different distances from the mid-thickness.

Processing for 30 turns led not only to an overall increase of the hardness, with an average of ~ 133 HV across the entire sample, but also to a more uniform hardness distribution. Unlike after 15 turns, the central region of the sample at r < 1 mm did not exhibit a significant drop in hardness, with average values of ~ 120-130 HV. Maximum hardness values within the range of ~ 200-230

HV were recorded at r > 3 mm. It was interesting to note that after 30 turns, the hardness decreased for r > 3.5 mm consistently at both sides of the sample, and this was not observed after 15 turns. Overall, a symmetric gradient-type distribution of the microhardness with respect to the sample center was found after HPT from 1 to 30 turns, with gradually increasing HV values from the center to the periphery.

4.3.1.2.2. Nanoindentation

The plastic behavior near the periphery of the Zn-3Mg hybrid after HPT for 30 turns was investigated with Berkovich nanoindentation at four different CSR values, as described in section 3.6.2. Representative load-displacement curves recorded at $\dot{\varepsilon} = 1.25 \cdot 10^{-4}$, $2.5 \cdot 10^{-4}$, $5.0 \cdot 10^{-4}$, and $1.0 \cdot 10^{-3}$ s^{-1} are provided in Figure 62 (a). The nanoindentation hardness (H) values corresponding to the load-displacement curves were calculated using Equation 12 in section 3.6.2, and they are plotted in Figure 62 (b) as a function of $\dot{\varepsilon}$ to obtain the strain rate sensitivity (m). The plotted H values (mean ± standard deviation) are also tabulated in Table 8.

From Figure 62 (a), it was noted that the sample exhibited some broadening between different load-displacement curves obtained from neighboring regions, thereby indicating a range of local mechanical responses at the nanoscale. These deviations in the load-displacement curves were found consistently for all CSR values tested, and they reflected a regime of plastic instability during nanoindentation. Detailed inspection of the load-displacement curves revealed that the mean displacement at peak load decreased with increasing $\dot{\varepsilon}$, which led to increasing H values for increasing $\dot{\varepsilon}$.

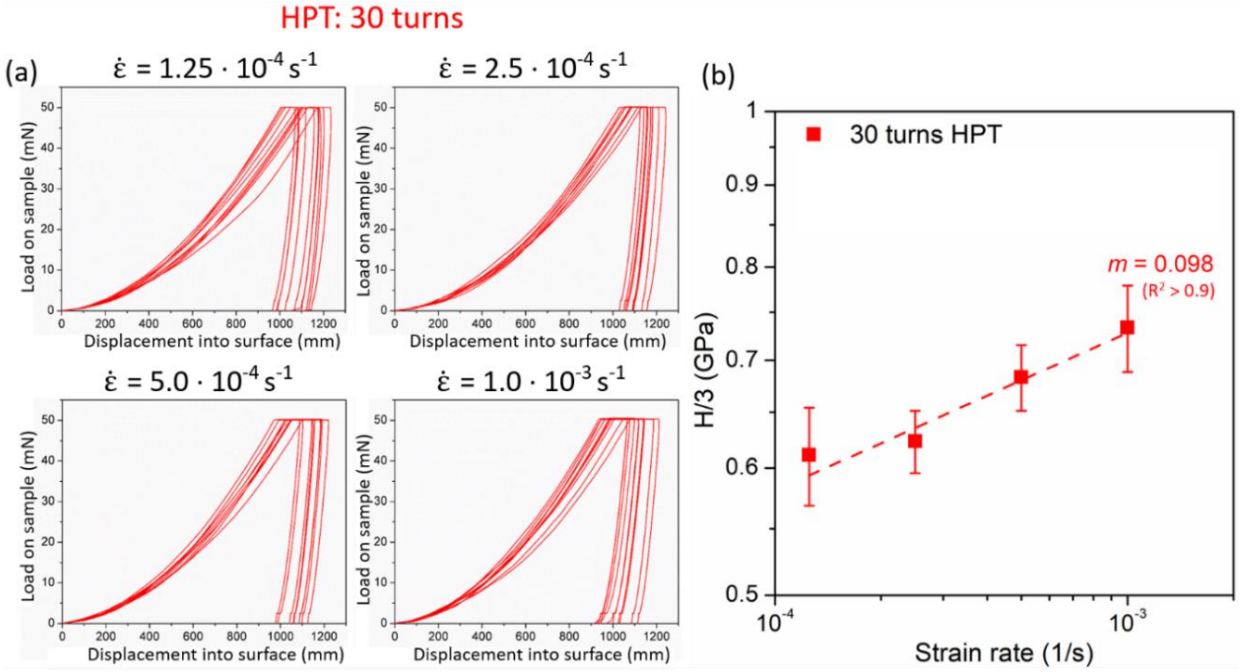

Figure 62: Berkovich nanoindentation near the periphery at the cross-section of the Zn-3Mg hybrid after HPT for 30 turns: (a) representative load-displacement at constant strain rates of $\dot{\varepsilon}$ = 1.25·10-4, 2.5·10-4, 5.0·10-4, and 1.0·10-3 s-1, (b) strain rate sensitivity, m, obtained from the hardness values, H, at different strain rates. R^2 in (b) refers to the adjusted R-squared value of the linear regression. Adapted from [127].

Table 8: Nanoindentation hardness, H, at the periphery of the Zn-3Mg HPT hybrids after 30 turns, obtained from the load-displacement curves at CSR in Figure 62 (a). These H values were plotted against $\dot{\varepsilon}$ in Figure 62 (b) to find the strain rate sensitivity, m. Adapted from [127].

$\dot{\varepsilon}$ (s^{-1})	H (GPa)
$1.25 \cdot 10^{-4}$	1.834 ± 0.129
$2.50 \cdot 10^{-4}$	1.870 ± 0.083
$5.00 \cdot 10^{-4}$	2.050 ± 0.096
$1.00 \cdot 10^{-3}$	2.201 ± 0.136

The strain rate dependence during plastic deformation was investigated by determining the m value, as defined by Equation 13 in section 3.6.2, from the slope of the linear fitting in a logarithmic plot of H/3 vs. $\dot{\varepsilon}$ shown in Figure 62 (b). The error bars represent the standard deviations of the H

values, which are a consequence of the plastic instability evident in their corresponding load-displacement curves. The m value obtained was 0.098 and resulted from a linear regression with a $R^2 > 0.9$, which indicates a good fitting of the experimental data.

The plastic volume involved during nanoindentation was estimated from the activation volume (V^*), using Equation 14 in section 3.6.2, from the slope of the linear fitting in a plot of logarithmic strain rate vs. linear H/3. The V^* obtained was ~ $2.25b^3$ (with a $R^2 > 0.9$), where $b = 2.67 \cdot 10^{-10}$ m is the Burgers vector for Zn [141].

4.3.2. HPT-processed + PDA Zn-3Mg hybrid

4.3.2.1. Microstructures of the HPT-processed + PDA Zn-3Mg hybrid

The cross-sectional image of the Zn-3Mg hybrid after HPT for 30 turns + PDA, in Figure 63, showed no macroscopic evidence of different phases. It should be noted that the Mg-rich phases present in the central region of the sample after 30 turns were no longer distinguishable after further PDA.

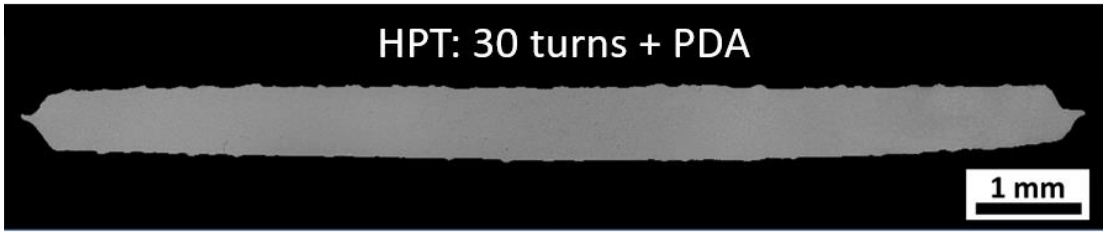

Figure 63: SE-SEM image corresponding to the cross-section of the Zn-3Mg hybrid after HPT for 30 turns followed by PDA (200 ºC, 1h). HPT processing was performed with an applied pressure of 6 GPa and a rotational speed of 1 rpm. Adapted from [127].

The Zn and Mg EDS maps in Figure 64 (b) and (c), respectively, suggested a relatively uniform composition near the periphery of the sample. The average chemical composition of the scanned area, provided in the table next to the EDS spectrum in Figure 64 (d), was ~ 96.3Zn-3.7Mg (wt.%),

indicating that the targeted composition of the hybrid was reasonably maintained after PDA. Like that of the Zn-3Mg hybrid after HPT for 30 turns presented earlier, this EDS analysis was also performed with an accelerating voltage of 25 kV to obtain the chemical composition from a relatively large interaction volume of the sample, representative of the bulk composition.

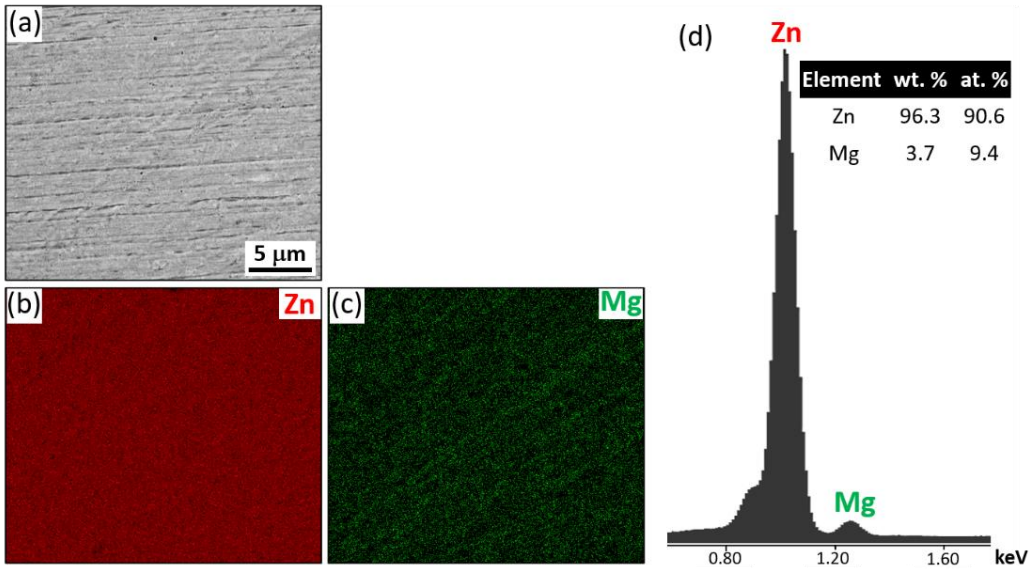

Figure 64: EDS analysis neat the periphery at the cross-section of the Zn-3Mg hybrid after HPT for 30 turns + PDA (200 ºC, 1h): (a) SE-SEM image of the scanned region, (b) Zn map, (c) Mg map, and (d) EDS spectrum with the corresponding chemical compositions. Adapted from [124].

The microstructures near the sample periphery were inspected at higher magnification by BSE-SEM, and representative photomicrographs are provided at different magnifications in Figure 65. The grain size ranged from ~200-1000 nm, and regions of different Z intensities, related to different phases, were reasonably aligned with the radial direction. The lighter areas were associated with the Zn matrix, whereas the darker areas were associated with Mg-rich regions. Nanoscale precipitates were also found scattered across the microstructure. It was noted that the Mg-rich phases, highlighted with blue dashed circles in Figure 65 (c), contained denser nanoscale precipitates, as they exhibited lighter contrast than the Mg-rich regions. These regions were further examined by TEM/STEM.

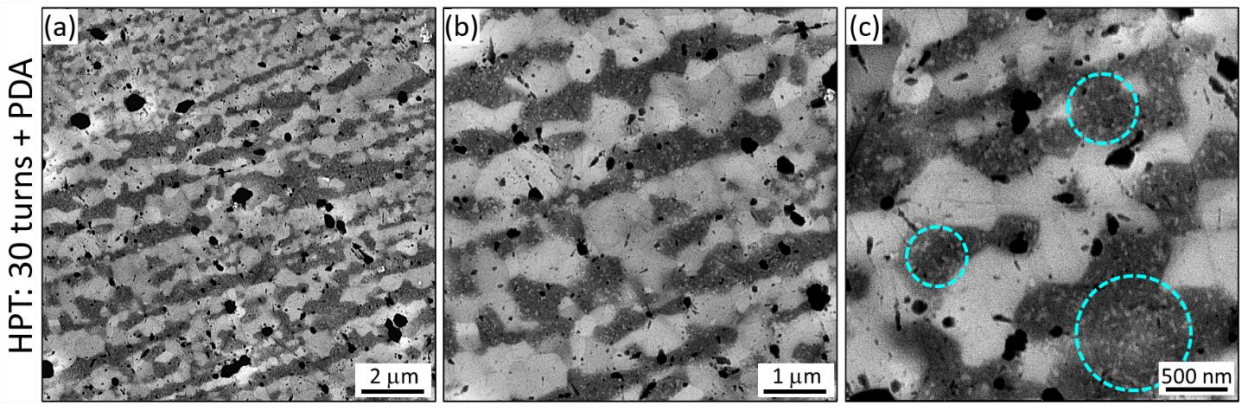

Figure 65: Representative BSE-SEM photomicrographs near the periphery at the cross-section of the Zn-3Mg hybrid after HPT for 30 turns + PDA (200 ºC, 1h): (a) lower magnification, (b) higher magnification, and (c) higher magnification), where the blue dashed circles indicate Mg-rich grains with denser nanoscale precipitates. The horizontal and vertical directions correspond to the radial and thickness directions, respectively, as defined in Figure 12. Adapted from [127].

Detailed analysis of the peripheral region was performed by TEM/STEM, and representative BF-TEM, BF-STEM, and corresponding HAADF-STEM images are provided in Figure 66 (a), (b), and (c), respectively. It should be noted that the TEM/STEM imaging plane was normal to that of the SEM images in Figure 65, such that the horizontal and vertical directions correspond to the shear and thickness directions defined in Figure 12, respectively. A heterogeneous microstructure was evident from the BF-TEM image in Figure 66 (a), where nanosized grains of ~ 100-200 nm were present within a matrix of significantly larger grains ranging from ~ 600-900 nm. The BF and corresponding HAADF STEM images provided in Figure 66 (b) and (c), respectively, showed that the nanoscale precipitates clustered preferentially inside Mg-rich grains, in good agreement with the SEM observations in Figure 65 (c). It was also interesting to find that the precipitate-containing Mg-rich grains were generally finer than those of the relatively precipitate-free Zn matrix, and a hypothesis to rationalize this phenomenon is discussed in section 5.3.2.

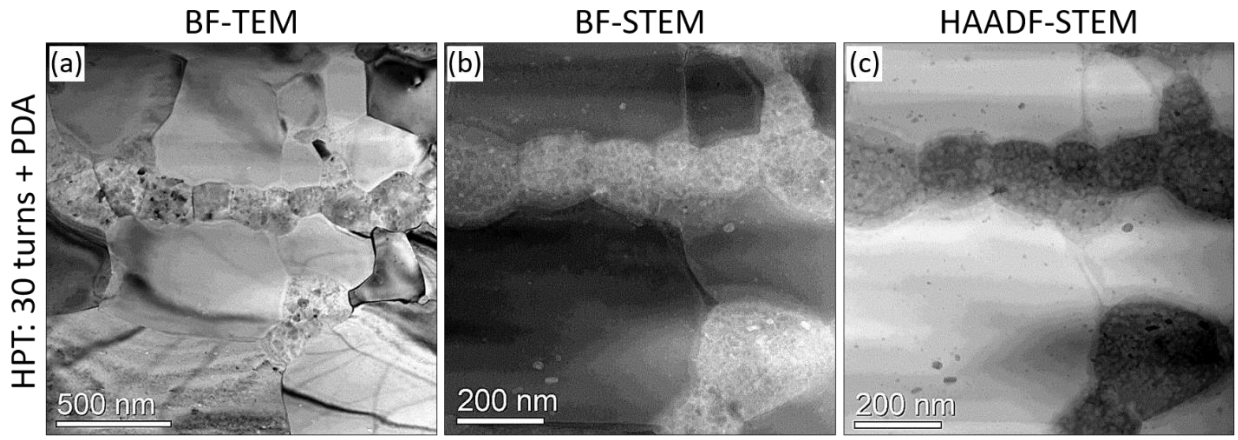

Figure 66: Representative TEM/STEM images acquired near the periphery at the cross-section of the Zn-3Mg hybrid after HPT for 30 turns + PDA (200 ºC, 1h): (a) BF-TEM, (b) BF-STEM and (c) corresponding HAADF-STEM. The horizontal and vertical directions correspond to the shear and thickness directions, respectively, as defined in Figure 12. Adapted from [127].

XRD analysis was used to identify the phases present in the Zn-3Mg HPT hybrid after PDA, and the corresponding XRD spectrum obtained from the mid-thickness plane of the sample surface is provided in Figure 67.

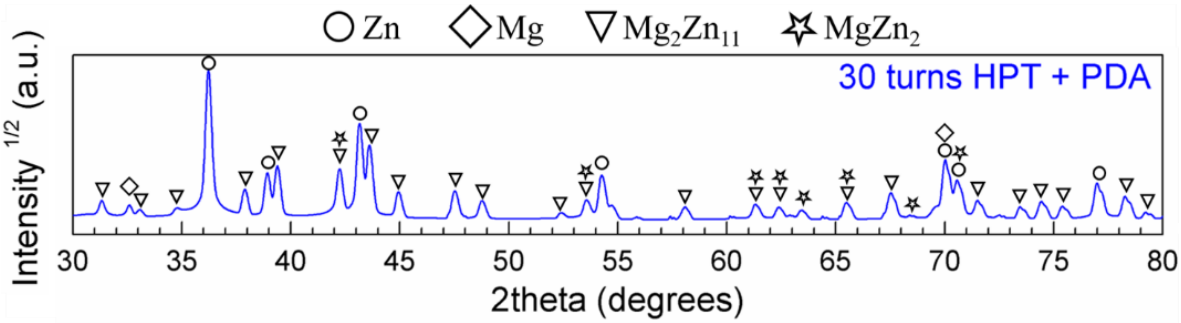

Figure 67: XRD patterns obtained at the mid-thickness plane of the Zn-3Mg hybrid after HPT for 30 turns + PDA (200 ºC, 1h). The diffraction peaks corresponding to the four phases identified (Zn, Mg, Mg_2Zn_{11}, and $MgZn_2$) are labeled with different symbols. Adapted from [127].

It should be mentioned that, like those of Zn-3Mg after HPT presented in 4.3.1.1, the XRD profile was obtained from the whole sample, and not just from the periphery. The sample consisted of four different phases: Zn, Mg, Mg_2Zn_{11}, and MgZn1, and their diffraction peaks were labeled accordingly in Figure 67.

As pointed out earlier, both the BSE-SEM and HAADF-STEM images in Figure 65 (c) and Figure 66 (c), respectively, showed nanoprecipitates in the Mg-rich grains after PDA. These regions were imaged by HRTEM, and FFT analysis was performed, as detailed in section 3.5.5.2, to investigate the phases present. Two different ROIs are highlighted in the HRTEM images in Figure 68 (a) and (c), and their corresponding FFT diffractograms are shown in Figure 68 (b) and (d), respectively. Reflections corresponding to Mg, Mg_2Zn_{11}, and $MgZn_2$ phases were identified and labeled consistently, as well as their associated zone axes (ZA).

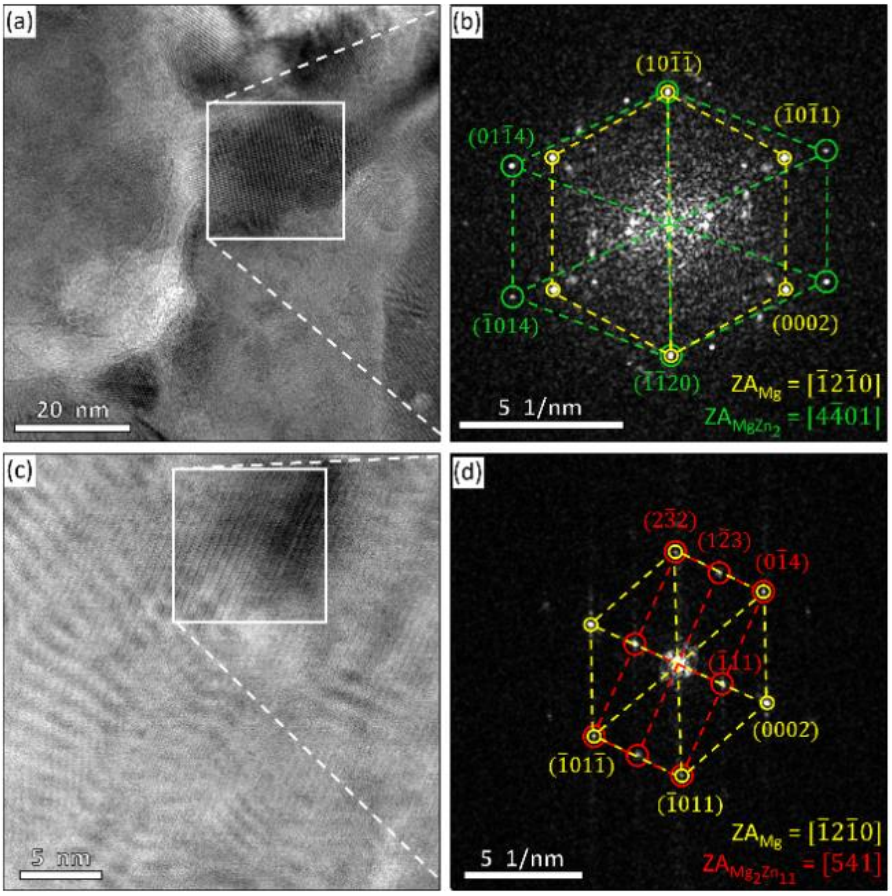

Figure 68: HRTEM analysis of fine Mg-rich grains identified at the periphery of the Zn-3Mg hybrid after HPT for 30 turns + PDA: (a) HRTEM image showing the ROI highlighted in white where FFT analysis was performed, and (b) corresponding FFT diffractogram where Mg and $MgZn_2$ were identified; (c) another HRTEM image showing a ROI highlighted in white where FFT analysis was performed, and (d) corresponding FFT diffractogram where Mg and Mg_2Zn_{11} were identified. The reflection planes of the phases identified are provided, together with their corresponding zone axes (ZA). Adapted from [127].

APT analysis was performed to investigate the atomic composition of a small volume of the sample near the peripheral region of the Zn-3Mg hybrid after PDA, and the results are presented in Figure 69. The atom maps for Zn and Mg, in Figure 69 (a) and (b), respectively, indicate that both elements were present across the APT needle. However, some Mg-depleted regions were found at the bottom and near the apex of the sample. An isoconcentration surface at 85 (at. %) Zn was generated, and it is highlighted in Figure 69 (c).

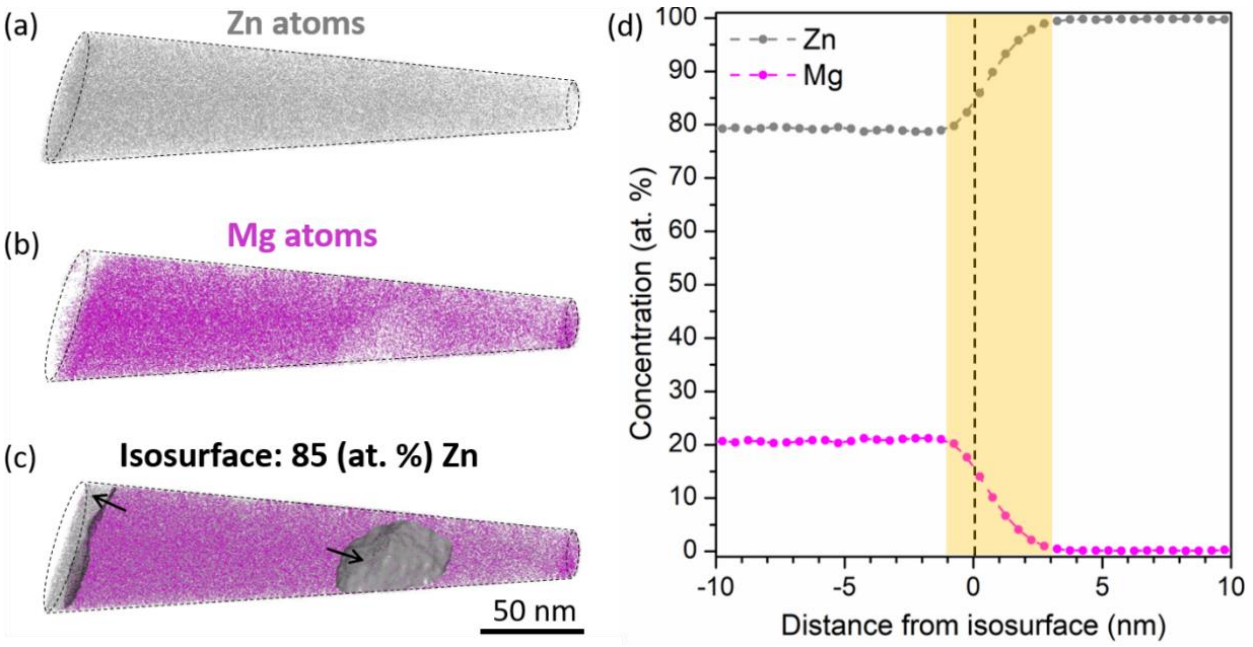

Figure 69: APT reconstruction of a needle extracted near the periphery of the Zn-3Mg alloy after HPT for 30 turns + PDA: (a) atom map of Zn, (b) atom map of Mg, (c) 3D isosurfaces with a concentration of 85Zn (at. %), (d) proximity histogram along the black arrows in the isosurface highlighted in (c). The average composition across the isosurface evolved from 79.0Zn-20.7Mg to 99.7Zn-0.2Mg (at. %). The transition region between the two compositions is highlighted in yellow in (d).

The black arrows across the isosurfaces identified indicate the direction in which the atomic concentration was evaluated, which is displayed in the proximity histogram in Figure 69 (d). A change in composition from 79.0Zn-20.7Mg (at. %) to 99.7Zn-0.2Mg (at. %) across the isoconcentration surfaces (denoted by a vertical dashed line) was found over a distance of ~ 4 nm

(highlighted in yellow). It should be noted that 99.7Zn-0.2Mg (at.%) corresponds to a solid solution of Mg in Zn, whereas 79.0Zn-20.7Mg (at. %) is associated with a supersaturated solid solution, as it is far beyond the equilibrium solubility limit of Mg in Zn.

EBSD analysis was performed to examine the crystal orientations, as well as the distributions of GS and misorientation angles near the periphery of the Zn-3Mg HPT hybrid after PDA. Figure 70 shows the image quality map of the scanned area in (a), with the corresponding IPF maps of the Zn, Mg, and Mg_2Zn_{11} phases identified in (b), (c), and (d), respectively. Phase maps of the Zn, Mg, and Mg_2Zn_{11} phases are provided in (e), (f), and (g), respectively.

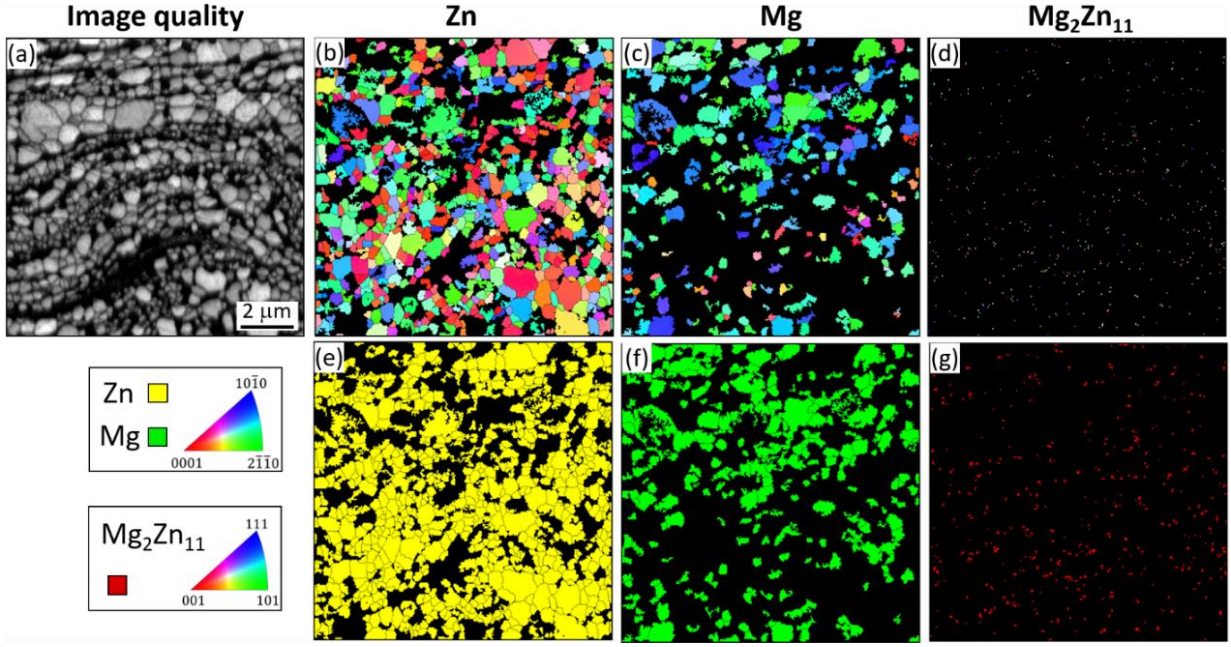

Figure 70: EBSD maps of the Zn-3Mg hybrid after HPT processing for 30 turns + PDA (200ºC, 1h) near the sample periphery: (a) image quality map of the scanned area and corresponding (b) Zn IPF map, (c) Mg IPF map, (d) Mg_2Zn_{11} IPF map, (e) Zn phase map, (f) Mg phase map, and (g) Mg_2Zn_{11} phase map. The principal IPF triangles for Zn, Mg, and Mg_2Zn_{11} phases, with their respective crystal orientations, are provided.

A heterogeneous microstructure consisting of grains with a wide range of sizes was apparent from Figure 70. Some regions with very low CI were not successfully indexed, which correspond to the

black areas in Figure 70. The grains in the microstructure were associated with either the Zn or the Mg phase. Although the Mg_2Zn_{11} phase was identified, its marginal amount made it impractical to be further analyzed by EBSD.

The IPF orientation maps of the Zn and Mg phases, together with their corresponding basal pole figures, are presented in Figure 71. In the IPF map of the Zn phase in Figure 71 (a), most of the grains exhibited colors close to that in the vertices of the principal IPF triangle. Consistently, in the basal pole figure in Figure 71 (b), some poles were aligned with <0001>, whereas other poles were tilted away from the basal plane normal towards $<2\bar{1}\bar{1}0>$ and $<10\bar{1}0>$.

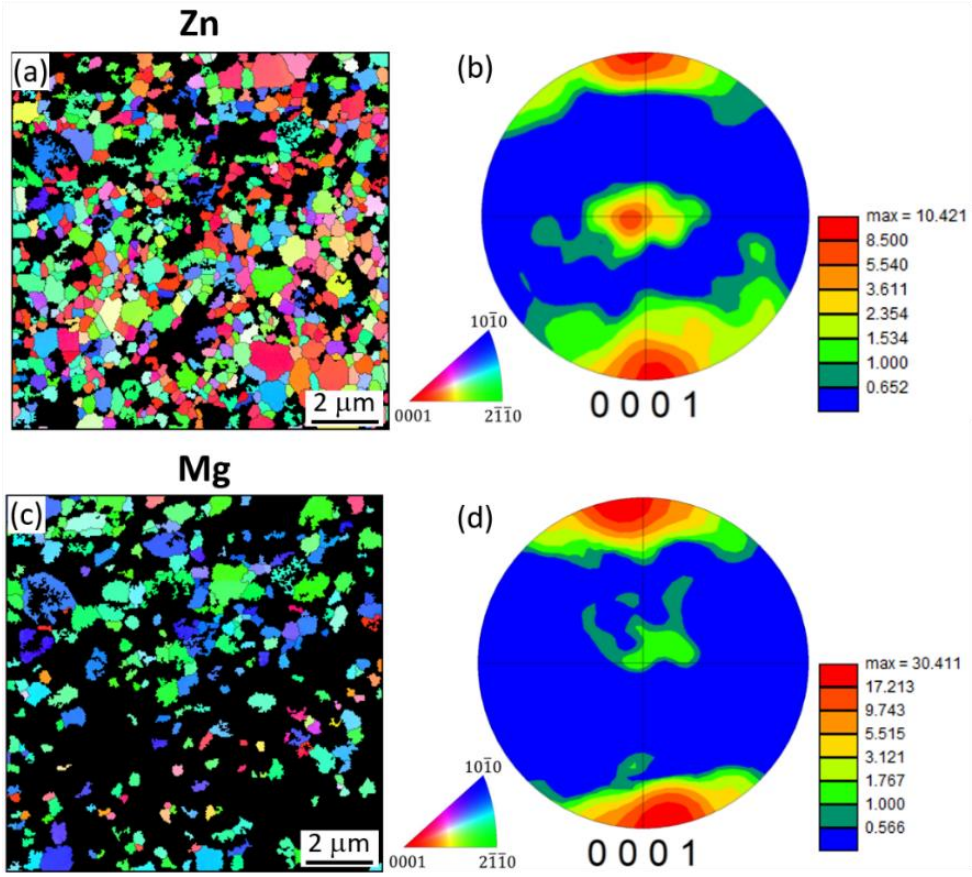

Figure 71: EBSD analysis of the Zn-3Mg hybrid after HPT for 30 turns + PDA (200 ºC, 1h): (a) Zn IPF map, and (b) corresponding basal (0001) pole figure, (c) Mg IPF map, and (b) corresponding basal (0001) pole figure. The IPF triangles are provided next to the IPF maps, and the color scales indicating the texture intensities are provided next to the pole figures.

For the Mg phase, most of the poles were tilted towards <$2\bar{1}\bar{1}0$> and <$10\bar{1}0$>, as evident from the green and blue colors of the Mg grains in the IPF orientation map in Figure 71 (c), and the red spots at the top and bottom of the basal pole figure in Figure 71 (d).

The distributions of GS and misorientation angles obtained from EBSD analysis are plotted in Figure 72 (a) and (b), respectively, for the Zn and Mg phases together. From Figure 72 (a), the grain sizes in the microstructure ranged from ~ 0.2 to 1.2 μm, with a GS_{ave} of ~ 500 ± 150 nm. It was noted that the GS data followed a right-skewed distribution, indicating that most of the grains identified in the microstructure were finer than the average value, with sizes ranging between ~ 350-400 nm, as denoted by the position of the mode in the GS distribution. Approximately 20 % of the scanned area was occupied by grains larger than 700 nm, which are significantly larger than the majority of grains with sizes of ~ 350-400 nm, thereby suggesting the possibility of a bimodal grain size distribution, which would be consistent with the TEM observations in Figure 66.

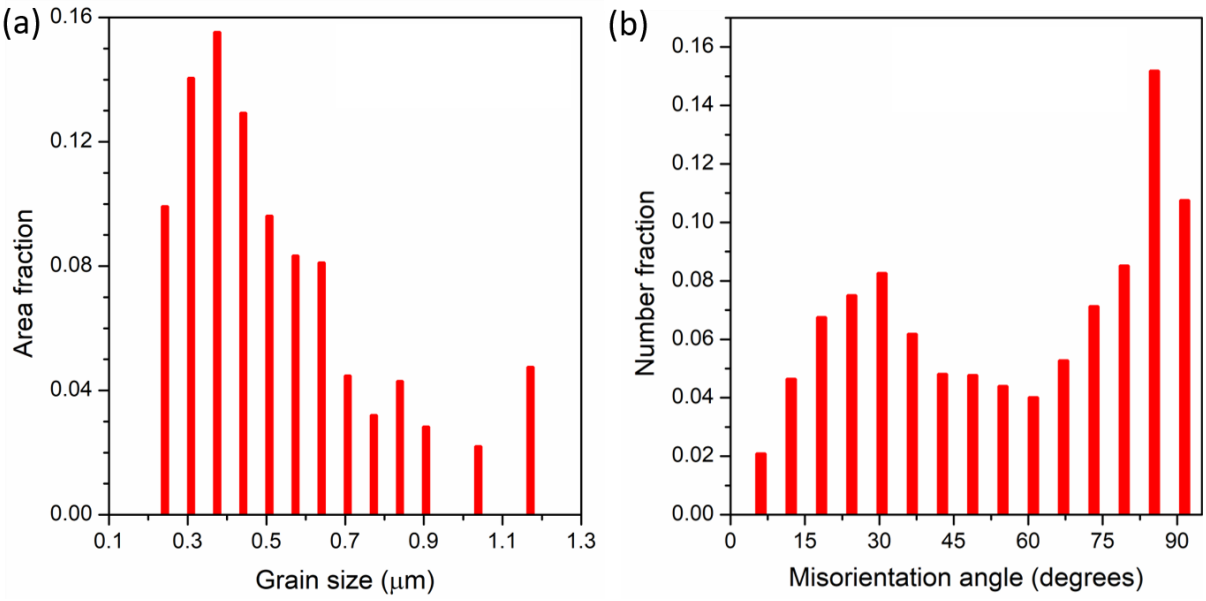

Figure 72: Distributions of (a) grain size and (b) misorientation angle obtained from the Zn and Mg phases together by EBSD analysis near the periphery of the Zn-3Mg hybrid after HPT processing for 30 turns + PDA (200ºC, 1h).

From Figure 72 (b), the amount of HABs (above 15º misorientation) was ~ 93 % of the total number of boundaries identified in the microstructure. The fractions of boundaries increased from 10-30º, then decreased from 30-60º, and finally increased from 60-80º. The range with the largest fraction of misorientation angles was 80-93.5º, with a peak at 80º, which potential presence will be discussed later.

4.3.2.2. Mechanical properties of the HPT-processed + PDA Zn-3Mg hybrid

4.3.2.2.1. Microhardness

The hardness distribution at the cross-section of the Zn-3Mg HPT hybrid after PDA was investigated through a series of 4x65 HV indents performed in a rectilinear grid pattern. This means that a total of 65 measurement locations at different distances from the center were examined, and 4 indents at each of those locations were performed at different distances from the mid-thickness. Thus, a total of 260 HV values were recorded and used to generate the color-contour map in Figure 73. In addition, the mean HV values from indents at the same distance from the center were plotted in Figure 74.

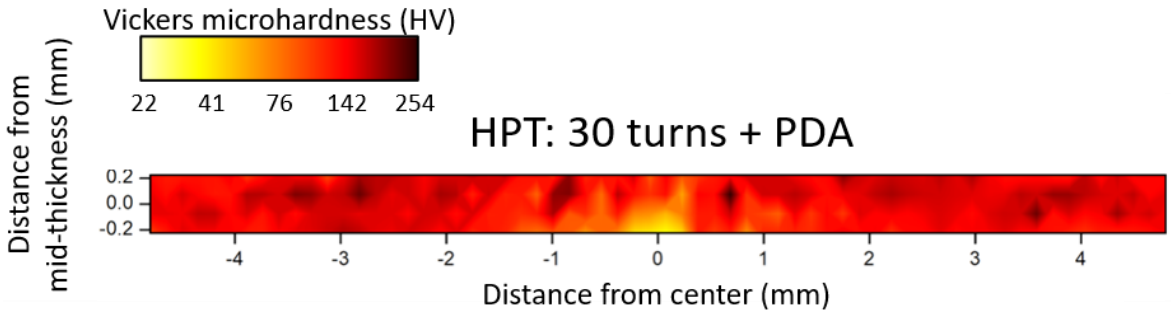

Figure 73: Color-coded HV contour map corresponding to the cross-section of the Zn-3Mg hybrids after HPT for 30 turns + PDA (200 ºC, 1h) presented in Figure 63. The map corresponds to a 4x65 matrix of HV values recorded in a rectilinear grid pattern. Adapted from [127].

It was interesting to find that the sample after PDA did not exhibit a general softening, as it would be expected after an annealing treatment. Instead, the microhardness was maintained reasonably well compared to before PDA, with an average ~ 139 HV across the whole sample. The region at r < 0.5 mm showed a decrease in hardness, with average values in the range of ~ 80-100 HV. It was noted from Figure 74 that the average hardness at both edges of the sample followed different trends. Whereas the average hardness decreased from ~ 160 to 140 HV at the left edge, it was maintained reasonably constant at ~ 150 HV at the right edge. However, it should be emphasized that Figure 74 represents average values, and that standard deviations were as large as ± 20 HV were found at some of the indentation locations. Despite these differences, maximum hardness values within the range of 210–250 HV were found at r > 3 mm at both peripheral regions of the sample.

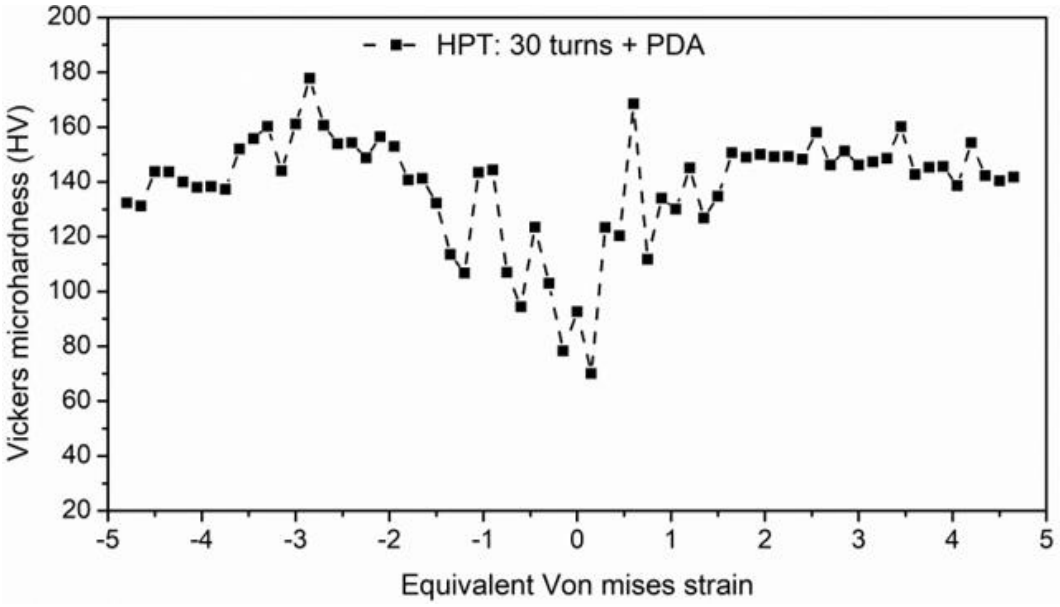

Figure 74: Evolution of the average HV values across the diameter of the Zn-3Mg hybrids after HPT for 30 turns + PDA (200 ºC, 1h). This plot is generated with the same HV values shown in Figure 73. Each data point corresponds to the average of four different HV measurements collected at the same distance from the sample center, but different distances from the mid-thickness.

4.3.2.2.2. Nanoindentation

The plastic deformation behavior was analyzed with Berkovich nanoindentation near the periphery of the Zn-3Mg HPT hybrid after PDA at four different CSR values, as described in section 3.6.2. Representative load-displacement curves obtained at $\dot{\varepsilon} = 1.25 \cdot 10^{-4}$, $2.5 \cdot 10^{-4}$, $5.0 \cdot 10^{-4}$, and $1.0 \cdot 10^{-3}$ s^{-1} are provided in Figure 75 (a). From these curves, the corresponding H values at different CSR were calculated using Equation 12 in section 3.6.2, and they are plotted in Figure 75 (b) as a function of $\dot{\varepsilon}$ to obtain m. The H values (mean ± standard deviation) are also tabulated in Table 9.

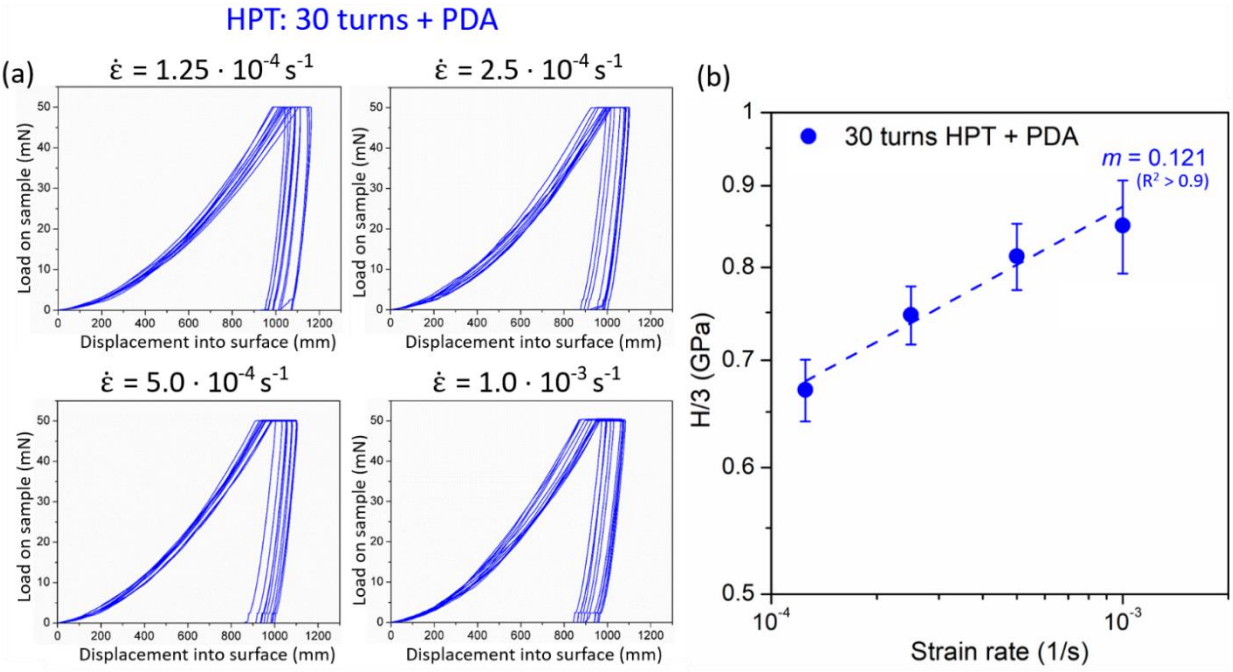

Figure 75: Berkovich nanoindentation near the periphery at the cross-section of the Zn-3Mg hybrid after HPT for 30 turns + PDA (200 ºC, 1h): (a) representative load-displacement at constant strain rates of $\dot{\varepsilon}$ = 1.25·10-4, 2.5·10-4, 5.0·10-4, and 1.0·10-3 s-1, (b) strain rate sensitivity, m, obtained from the hardness values, H, at different strain rates. R^2 in (b) refers to the adjusted R-squared value of the linear regression. Adapted from [127].

The sample after PDA exhibited the same trends mentioned earlier in section 4.3.1.2.2 for the sample after HPT. Namely, some broadening was evident from different load-displacement curves

in Figure 75 (a) obtained with the same $\dot{\varepsilon}$ and loading conditions from nearby locations, which indicated a range of local mechanical responses. This phenomenon was found for all the CSR values tested and resulted from plastic instability during nanoindentation in a heterogenous microstructure like that presented earlier. The mean displacement at peak load was found to decrease for increasing $\dot{\varepsilon}$, leading to increasing H values for increasing $\dot{\varepsilon}$.

Table 9: Nanoindentation hardness, H, at the periphery of the Zn-3Mg HPT hybrids after 30 turns + PDA, obtained from the load-displacement curves at CSR in Figure 75 (a). These H values were plotted against $\dot{\varepsilon}$ in Figure 75 (b) to find the strain rate sensitivity, m. Adapted from [127].

$\dot{\varepsilon}$ (s^{-1})	H (GPa)
$1.25 \cdot 10^{-4}$	2.012 ± 0.089
$2.50 \cdot 10^{-4}$	2.242 ± 0.094
$5.00 \cdot 10^{-4}$	2.440 ± 0.116
$1.00 \cdot 10^{-3}$	2.550 ± 0.170

The value of m was calculated, to investigate the strain rate effect during plastic deformation, using Equation 13 provided in section 3.6.2, from the slope of the linear fitting in a logarithmic plot of H/3 vs. $\dot{\varepsilon}$, as shown in Figure 75 (b). The m value obtained was 0.121 and resulted from a linear regression with a $R^2 > 0.9$, indicating a good fitting of the experimental data.

The value of V*, which can be associated with the plastic volume involved during nanoindentation, was estimated from Equation 14 in section 3.6.2, as the slope of the linear fitting in a plot of logarithmic strain rate vs. linear H/3. The V^* obtained was ~ $1.35b^3$ (with a $R^2 > 0.9$), where b = $2.67 \cdot 10^{-10}$ m is the Burgers vector for Zn [141].

4.4. Zn-30Mg hybrids

This section presents the microstructure and hardness results of the Zn-30Mg HPT hybrids after 1, 5, 15, and 30 turns. The microstructures were characterized using SEM and TEM, and the hardness was investigated with HV. It should be mentioned that this composition represents about the maximum Mg concentration that can be achieved in an HPT hybrid with a Zn/Mg/Zn stack configuration, since the thickness of the external Zn disks in the Zn-30Mg hybrid was only ~ 270 μm, which is significantly thinner than that of the central Mg disk (~ 960 μm).

4.4.1. HPT-processed Zn-30Mg hybrids

4.4.1.1. Microstructures of the HPT-processed Zn-30Mg hybrids

Cross-sectional SE-SEM images of the Zn-30Mg HPT hybrids after 1, 5, 15, and 30 turns are presented in Figure 76. The Zn and Mg disks did not achieve a good bonding in the central region of the sample after 1 turn, as evident from the separations between the Mg/Zn interfaces. After 5 turns, the three disks combined into a single compact sample, and the central Mg disk was still continuous along the cross-section. After 15 turns, the Mg disk fragmented into smaller phases at $r > 2$ mm, but not in the central region of the sample. After 30 turns, no significant improvement in the phase mixing between Zn and Mg was observed; both phases were still evident in relatively large regions, leading to notable macroscopic heterogeneity.

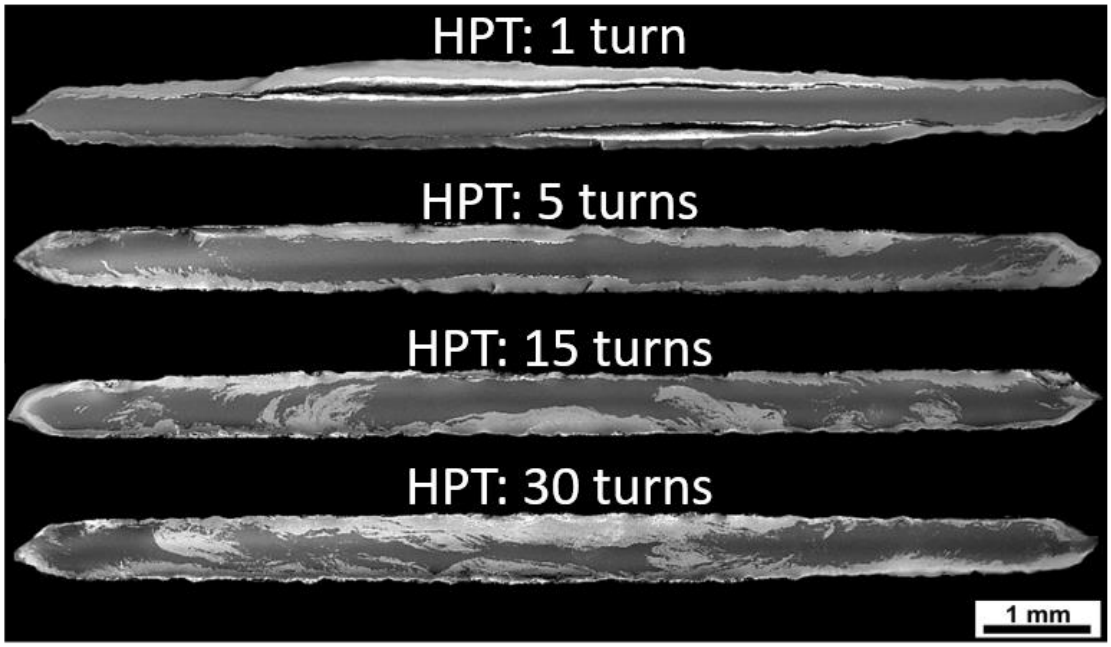

Figure 76: SE-SEM images corresponding to the cross-sections of the Zn-30Mg hybrids after HPT for 1, 5, 15, and 30 turns, processed with an applied pressure of 6 GPa and a rotational speed of 1 rpm.

Consistent with the previous investigations of the Zn-3Mg and Zn-10Mg hybrids, the regions of highest plastic deformation (i.e., disk periphery after the highest number of turns) were the focus of this study. As observed in Figure 76, these areas in the Zn-30Mg HPT hybrid after 30 turns seemed to correspond to the Mg phase (i.e., darker regions). A TEM lamella was extracted from this region to provide insight about the microstructure, which was analyzed through a series of images provided in Figure 77. Corresponding BF-STEM and HAADF images of the TEM lamella at low magnification can be observed in Figure 77 (a) and (b), respectively, where it was apparent that a single phase was present. It should be noted that the different contrast levels correspond to the significant different thicknesses of the electron transparent areas and the supports between them. An HRTEM image inside the electron transparent area is shown in Figure 77 (c), and its corresponding FFT diffractogram is presented in Figure 77 (d).

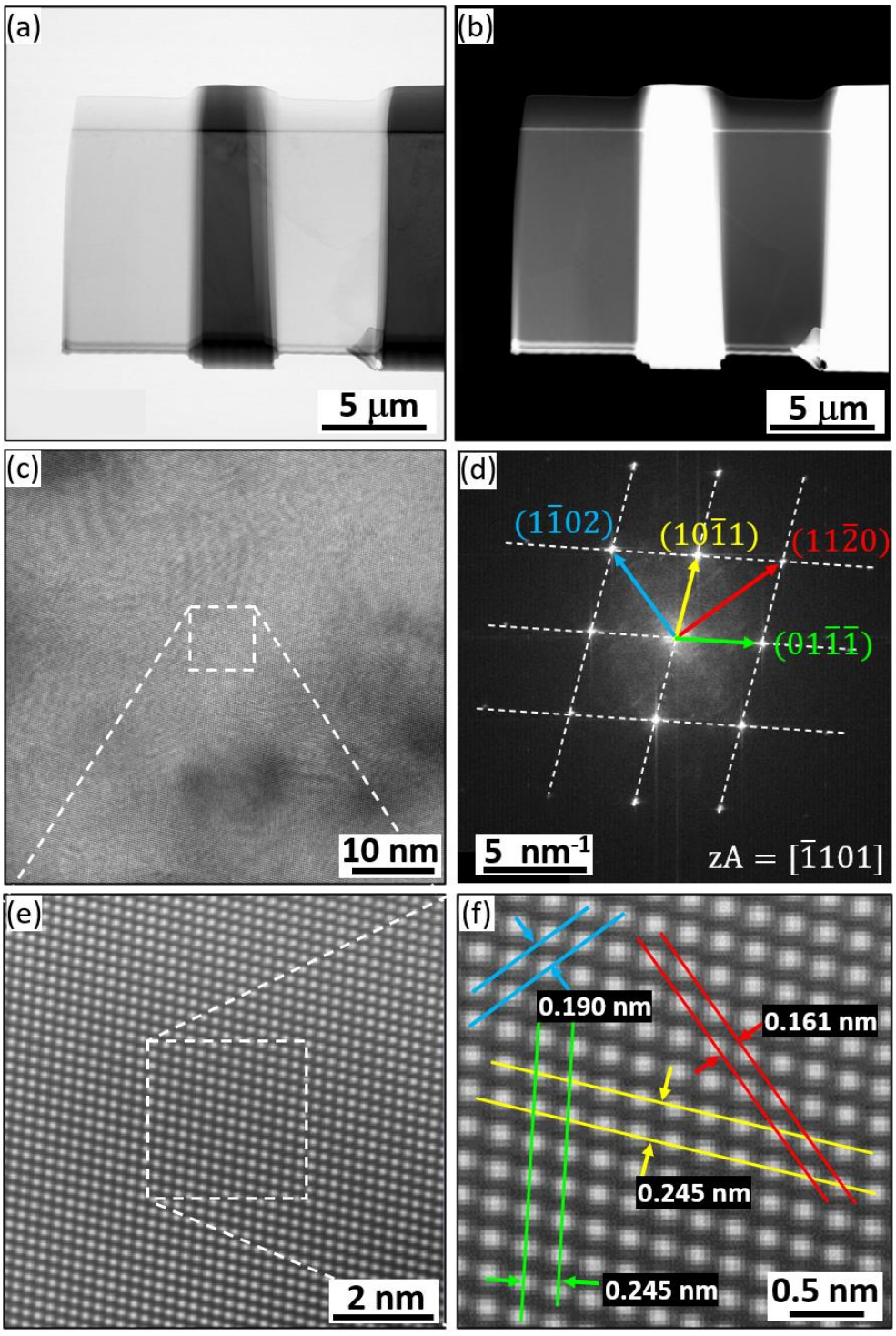

Figure 77: S/TEM analysis at the periphery of the Zn-30Mg hybrid after HPT for 30 turns: (a) BF-STEM image of the TEM lamella, (b) corresponding HAADF-STEM image, (c) HRTEM image, (d) FFT diffractogram of (c) with reflection planes corresponding to Mg and zone axis, (e) IFFT image of magnified ROI highlighted in (c), (f) magnified ROI highlighted in (e) showing the interplanar spacings corresponding to the Mg reflections identified in (d). Note that the same colors in (d) and (f) refer to the same diffraction planes.

Four different diffraction planes corresponding to Mg were identified, and their g vectors and zone axis are labeled in Figure 77 (d). An IFFT image of the magnified ROI in Figure 77 (c) is shown in (e), where the atomic structure is visible. This was further magnified in (f) in order to highlight the interplanar spacings corresponding to the reflection planes identified in (d). It should be noted that only the Mg phase was identified across the TEM lamella.

4.4.1.2. Hardness of the HPT-processed Zn-30Mg hybrids

The distribution of HV values was investigated over the cross-section of the Zn-30Mg HPT hybrids after 1, 5, 15, and 30 turns. In each sample, a rectilinear grid pattern of 4x65 HV values (i.e., a total of 260 HV values) was acquired, and they are plotted in Figure 78 in the form of color-coded maps with respect to the distance from the center and the distance from the mid-thickness at which they were measured. It should be mentioned that in the sample after 1 turn, only a 2x65 matrix of HV values near the mid-thickness of the sample, due to the cracks observed in Figure 76 between the Zn and Mg disks.

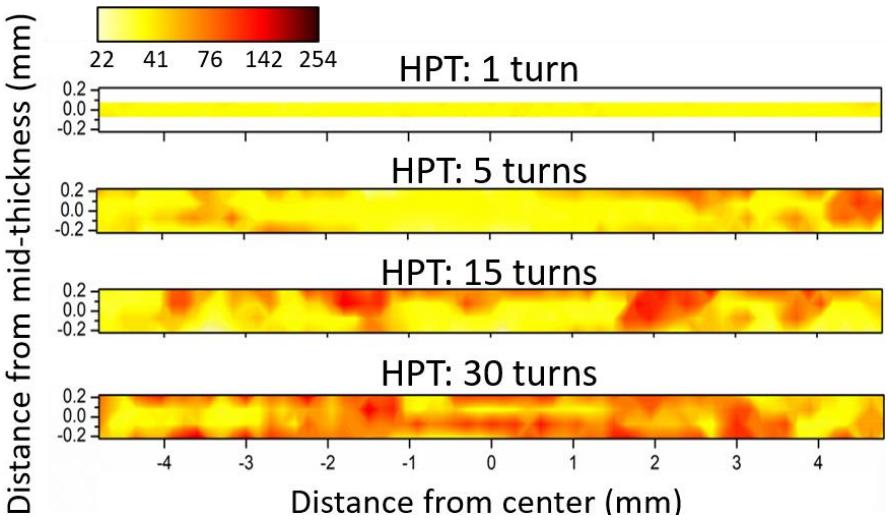

Figure 78: Color-coded HV contour maps corresponding to the cross-sections of the Zn-3Mg hybrids after HPT for 1, 5, 15, 30 turns presented in Figure 76. Each map corresponds to a 4x65 matrix of hardness indents recorded in a rectilinear grid pattern, except that for the 1 turn sample, which corresponded to a 2x65 matrix.

The mean values of each of the different HV measurements collected at the same distance from the sample center, but different distance from the mid-thickness, are provided in Figure 79. After 1 turn, a uniform hardness distribution in the central Mg disk was observed across the sample, with an average of ~ 45 HV, similar to that of pure Mg (37 HV [176]). After 5 turns, the average hardness at r < 1 mm did not change significantly, whereas average hardness values ranging between ~ 50-80 HV were found at r > 3 mm, with a maximum of ~ 100 HV at one of the edges. After 15 turns, the hardness distribution was very heterogeneous across the sample and did not follow any specific trend. Maximum hardness values of ~ 130 HV were recorded at r ~ 2 mm, whereas both edges of the sample showed an average hardness similar to that after 1 turn. After 30 turns, the hardness distribution remained very heterogeneous, like that after 15 turns. The average hardness increased in the central region up to 80-90 HV, and reached a maximum hardness of ~ 150 HV at r ~ 2-3 mm.

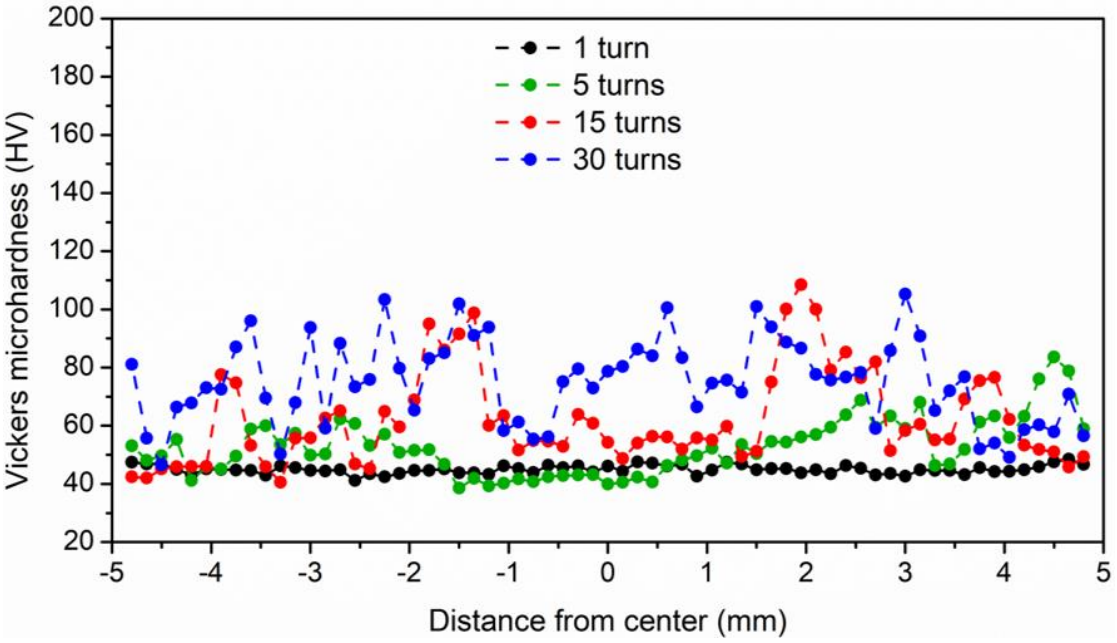

Figure 79: Evolution of the average HV values across the dimeter of the Zn-3Mg hybrids after HPT for 1, 5, 15, and 30 turns. This plot is generated with the same HV values shown in Figure 76. Each data point corresponds to the average of four different HV measurements collected at the same distance from the sample center, but different distance from the mid-thickness.

4.5. Coatings for enhanced corrosion resistance, cell viability, and antibacterial activity

4.5.1. Surface morphology and characteristics of coatings

4.5.1.1. ZnP coatings

The surface morphology of the as-homogenized Zn-3Mg alloy samples before the application of any coating, which represents the uncoated sample condition, is presented in Figure 80 (a) and (b), where the light and dark phases correspond to Zn and Mg_2Zn_{11} phases. A uniform layer of randomly oriented flake-like crystals with pores of ~ 2-3 μm diameter was formed on the sample surface after 5 min immersion in the ZnP solution, as observed in Figure 80 (c) and (d).

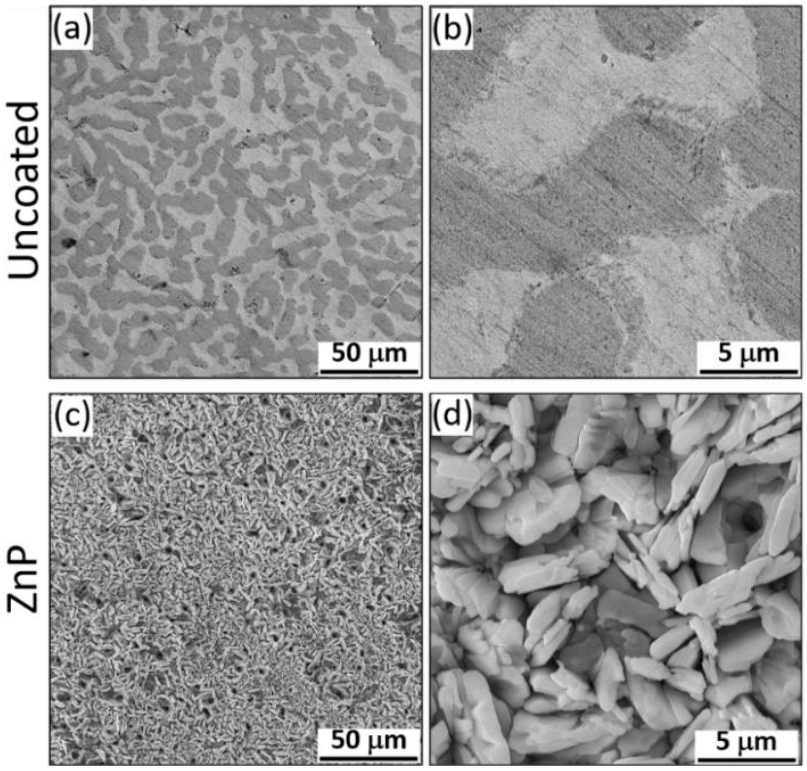

Figure 80: SE-SEM images showing the surface morphology of the Zn-3Mg alloy (a-b) uncoated, with a eutectic lamellar microstructure of Zn phases (brighter) and Mg_2Zn_{11} phases (darker), and (c-d) after the zinc phosphate (ZnP) chemical conversion coating, with a flake-like microstructure with uniformly distributed pores.

Upon immersion, it was noted that platelet crystals nucleated at multiple locations in the substrate, which grew over time, covering the entire surface of the sample after 5 min. The formation of zinc phosphate hydrate, also known as hopeite, with a chemical composition of $Zn_3(PO_4)_2 \cdot 4H_2O$ was confirmed at the surface of the ZnP sample by GIXRD.

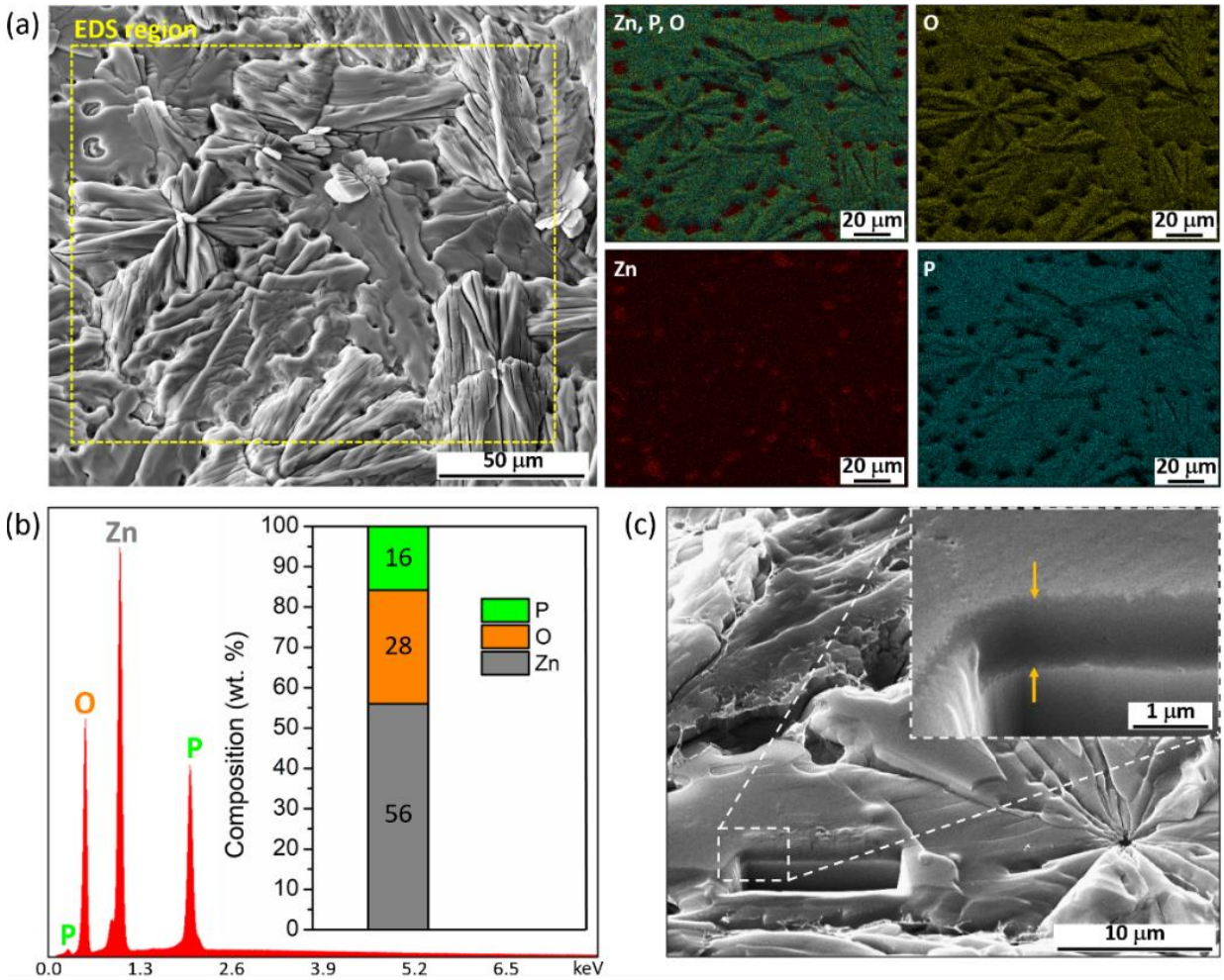

Figure 81: SE-SEM imaging and corresponding EDS elemental information of the ZnP coated sample: (a) SE-SEM image of the sample surface indicating the ROI where the EDS elemental maps of Zn, P, and O were collected, (b) EDS spectrum of the ROI highlighted in (a) and corresponding chemical composition, (c) SE-SEM image of the surface, with a stage tilt of 54 º, showing a FIB cut, from which the thickness of the ZnP coating was estimated.

Some ZnP coated samples exhibited regions with flower-like structures, like those observed in Figure 81 (a), which formed from the coalescence of neighboring nucleation sites that grew faster than others. EDS map analysis revealed a uniform elemental distribution of Zn, P, and O in the ZnP coating. Note that the higher intensity areas on the EDS Zn map correspond to the pores in the coating. The EDS spectrum and corresponding chemical composition of the area highlighted in Figure 81 (a) are provided in Figure 81 (b). The approximate thickness of the ZnP coating was measured as ~ 1 μm from a FIB cut performed in the ZnP coated surface, as shown in the inset of Figure 81 (c).

4.5.1.2. Col coatings

The surface morphologies of the different Col coatings developed by spin-coating at 3000 rpm are presented in Figure 82. A uniform distribution of Col fibrils with ~ 20-30 nm thickness, randomly oriented on the sample surface, was found after spin-coating the 2.4 mg/mL PureCol solution for 20 s, as shown in Figure 82 (a). Increasing the spin-coating time by 10 s while maintaining the same PureCol concentration resulted in less uniform coating with a lower amount of Col fibrils, which were only found at specific regions of the sample, as observed in Figure 82 (b). Col fibrils could be barely distinguished in the Col coating produced with 1.0 mg/mL PureCol solution for 30 s, as observed in Figure 82 (c). It was noted that the polishing lines were still evident in the Col coated sample surfaces, suggesting that the Col coatings had submicron thicknesses, yet they were not measured in this study.

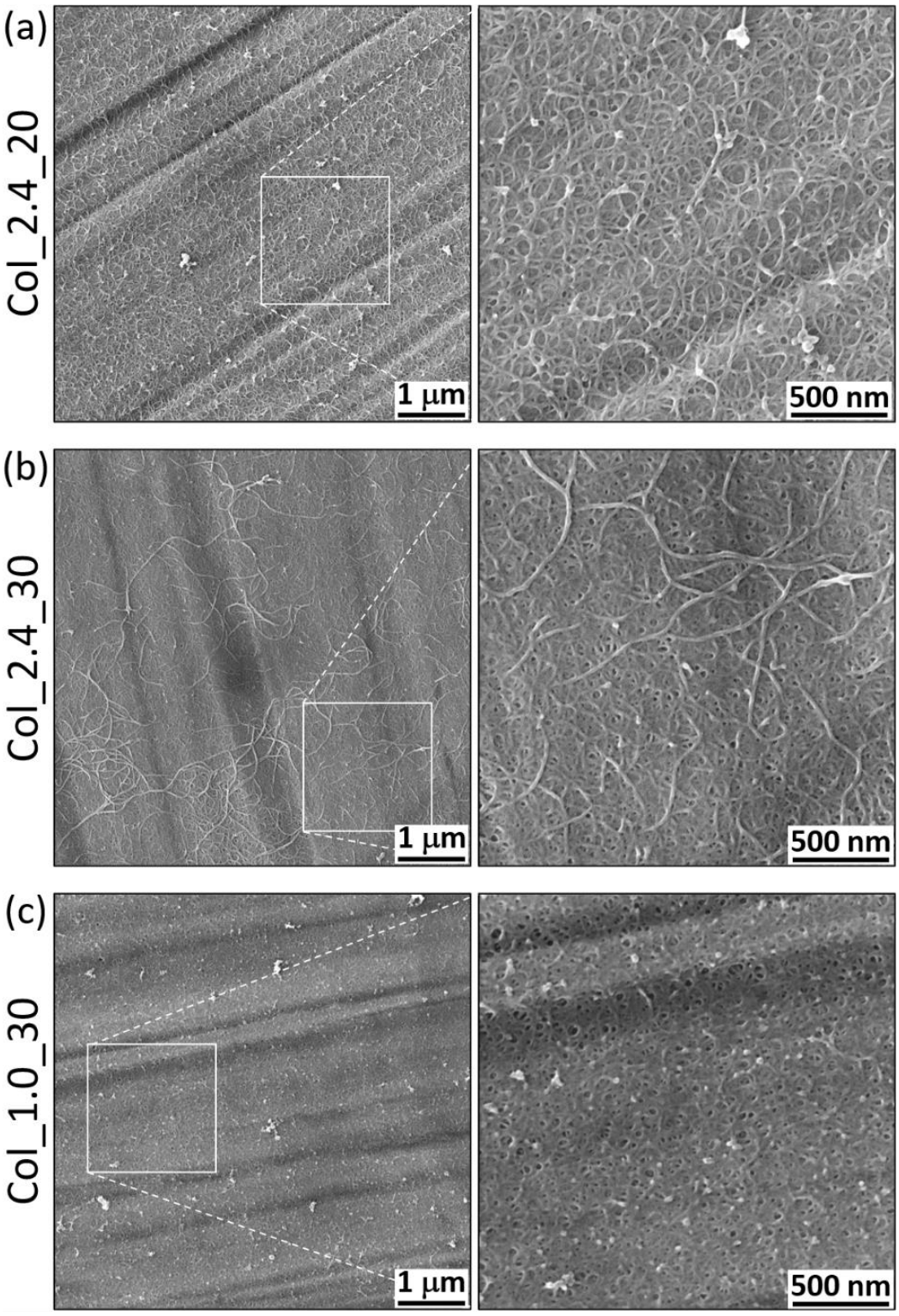

Figure 82: SE-SEM images showing the surface morphology of the Col coatings performed by spin-coating technique on the surface of the as-homogenized Zn-3Mg alloy at 3000 rpm with different PureCol concentrations and spinning times: (a) 2.4 mg/mL and 20 s, (b) 2.4 mg/mL and 30 s, and (c) 1 mg/mL and 30 s.

4.5.1.3. ZnP-Col coatings

A uniform ZnP-Col coating was obtained by spin-coating the 2.4 mg/mL PureCol solution at 3000 rpm for 20 s on the already ZnP coated sample. Figure 83 (a) shows that the Col fibrils distributed randomly and completely covered the flake-like structures of the ZnP coating, similar to those in the Zn-3Mg substrates in Figure 82 (a). In addition, the pore regions between different flake-like structures were also covered by Col fibrils, as shown in Figure 83 (b).

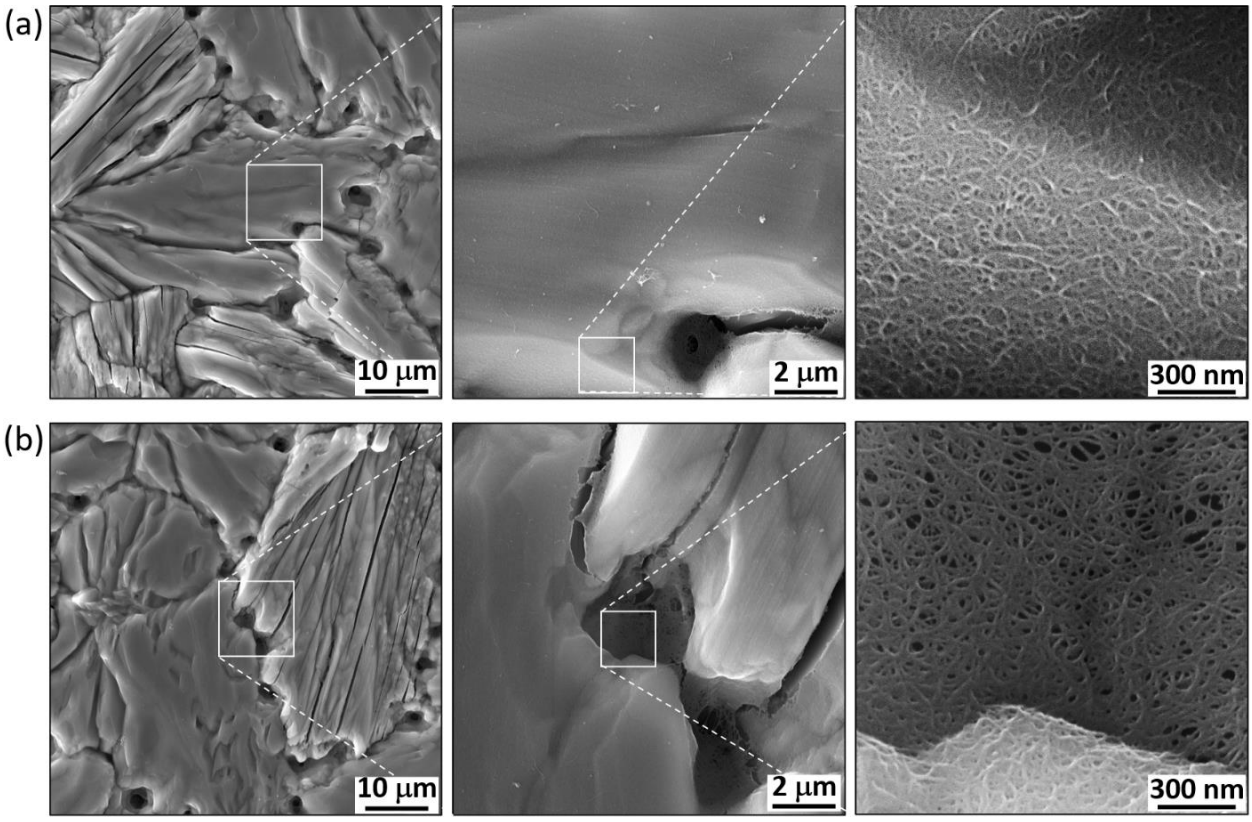

Figure 83: SE-SEM images showing the surface morphology of the ZnP-Col coating, obtained by applying the Col_2.4_20 coating on the ZnP coated surface: (a) ROI showing uniform Col coating of the flake-like ZnP microstructure, (b) ROI showing the Col coating present in pores of the ZnP microstructure.

4.5.1.4. Col-AgBGN coatings

Similar to the Col coated samples showed in Figure 82, the polishing lines of the Zn-3Mg substrate surface were still evident after spin-coating the Col-AgBGN solution at 3000 rpm for 20 s, as shown in Figure 84 (a). Spherical nanoparticles, with diameters ranging from ~ 50-200 nm, were found distributed across the sample surface, as evident in Figure 84 (b). Some examples of monodispersed nanoparticles are highlighted with orange arrows, which typically exhibited smaller sizes than those highlighted with green arrows, which tended to aggregate into clusters with neighboring nanoparticles. It should be mentioned that EDS analysis of different regions in the Col-AgBGN coated samples failed to identify any peak corresponding to Si, which is the major component of the AgBGN, and thus, the composition of the observed nanoparticles could not be estimated with this approach.

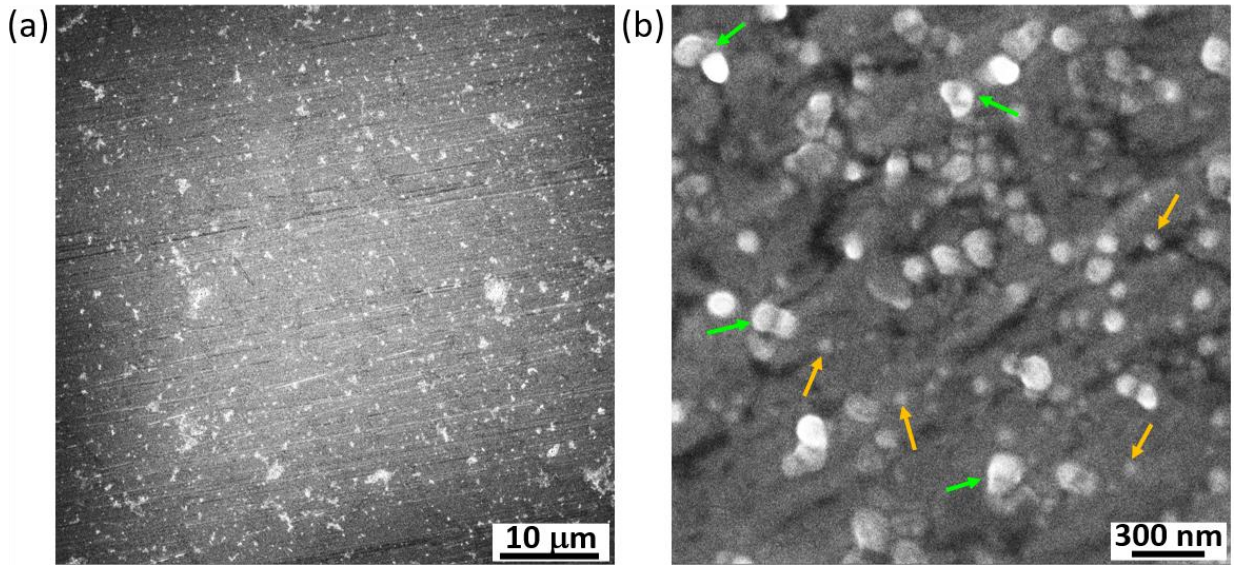

Figure 84: SE-SEM images showing the surface morphology of the Col-AgBGN coatings obtained by spin-coating on the Zn-3Mg alloy: (a) low-magnification, (b) high-magnification, showing dispersed AgBGN of < 100 nm (orange arrows) and aggregated AgBGN clusters (green arrows).

4.5.2. *In vitro* degradation and corrosion resistance

The immersion degradation behavior of uncoated and ZnP coated samples in DMEM for 6 and 21 days is shown in Figure 85. Degradation of the uncoated samples after 6 days immersion led to localized corrosion pits on the Zn phase, which corresponds to the lighter phase in Figure 85 (a). The size of these corrosion pits increased notably after 21 days immersion, as noted by the larger dark areas inside the Zn phase in Figure 85 (b). It was noted that the Mg_2Zn_{11} phase corroded more uniformly during the immersion period, showing a similar aspect after 6 and 21 days immersion. The ZnP coated samples demonstrated uniform corrosion and retained their flake-like morphology up to 21 days immersion, as shown in Figure 85 (c) and (d). In addition, the samples immersed for 21 days presented some newly-formed fine flakes, which can be distinguished in the magnified inset of Figure 85 (d).

In the uncoated samples, the amount of the Zn, both in the Zn and Mg_2Zn_{11} phases, decreased with immersion time at the expense of those elements forming the corrosion products (i.e., Na, C, O), as shown in Figure 85 (d). Whereas the amount of Mg in the Mg_2Zn_{11} phase remained practically constant during immersion, that of O increased with immersion time, suggesting the formation of additional oxide products. In the ZnP coated samples, the amount of Zn also decreased with immersion time, which was counterbalanced by a slight increase in P, O, and C, and could be associated with the formation of additional fine flake-like structures, like those observed in the magnified inset of Figure 85 (d).

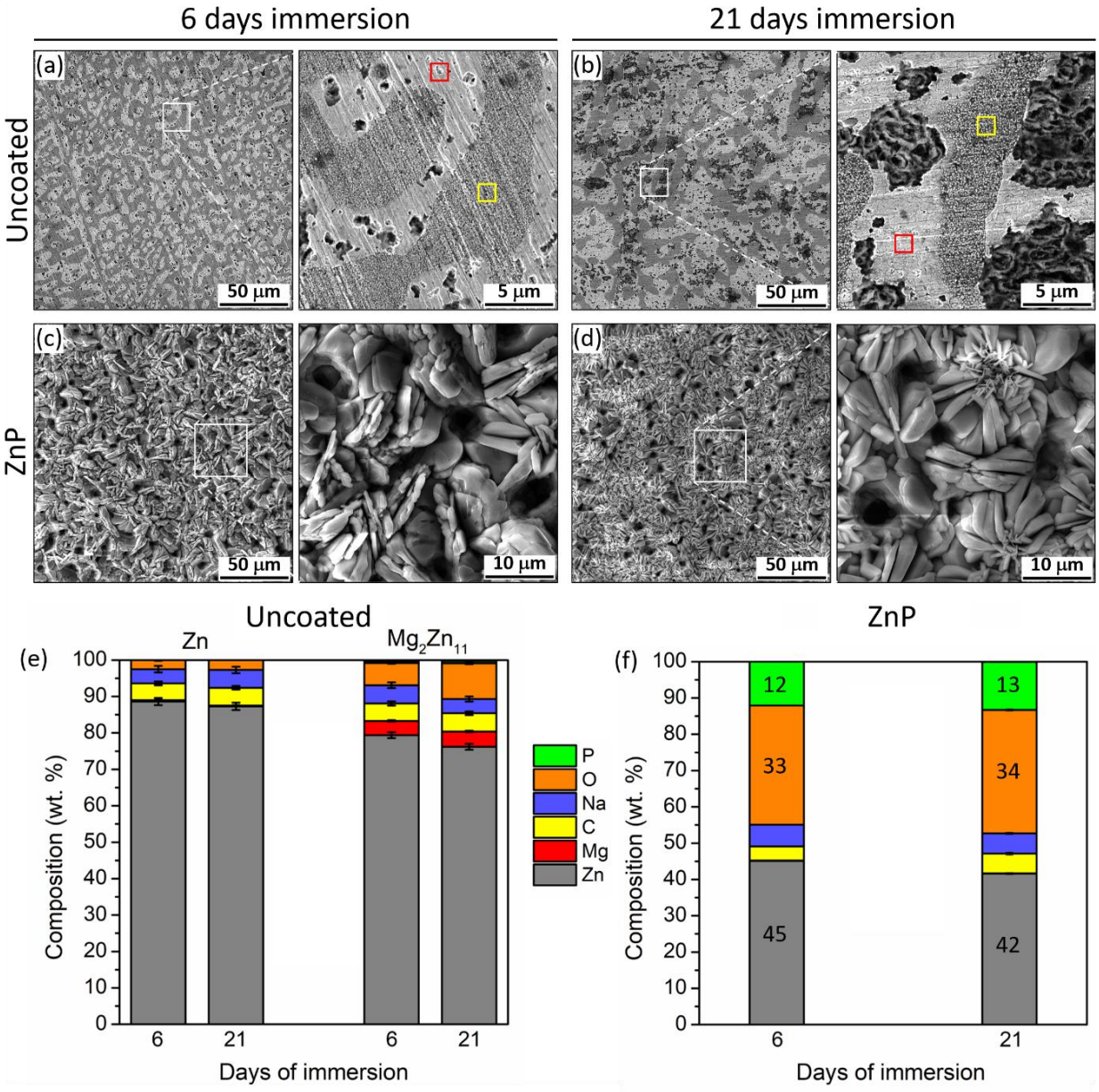

Figure 85: SE-SEM images and EDS elemental compositions showing the *in vitro* degradation in DMEM: (a-b) uncoated samples after 6 and 21 days immersion, respectively, where the red and yellow boxes indicate the regions where EDS was performed in the Zn and Mg_2Zn_{11} phases, respectively, (c-d) ZnP coated samples after 6 and 21 days immersion, respectively; EDS elemental compositions after 6 and 21 days immersion of the (e) uncoated samples at the highlighted red and yellow boxes, and (f) ZnP coated samples at the entire regions in (c) and (d).

The change in phase composition in the uncoated and ZnP coated samples at the end of the immersion test (after 21 days immersion) was evaluated by GIXRD, and the corresponding scans are presented in Figure 86. Diffraction peaks corresponding to zinc oxide (ZnO) and zinc hydroxide ($Zn(OH)_2$) phases were identified in the uncoated sample after immersion, besides those of Zn and Mg_2Zn_{11} phases, as observed in Figure 86 (a). In the ZnP coated sample, diffraction peaks corresponding to a sodium zinc phosphate hydrate ($Na_2Zn(H_2PO_4) \cdot 4H_2O$) phase were identified after immersion, in addition to $Zn_3(PO_4)_2 \cdot 4H_2O$, to which most of the peaks were assigned, as observed in Figure 86 (b). Also, Zn and Mg_2Zn_{11} phases were identified in the ZnP coated sample before and after immersion. It should be noted that the diffraction angles corresponding to different phases sometimes overlapped, such that some of the diffraction peaks were assigned to multiple phases.

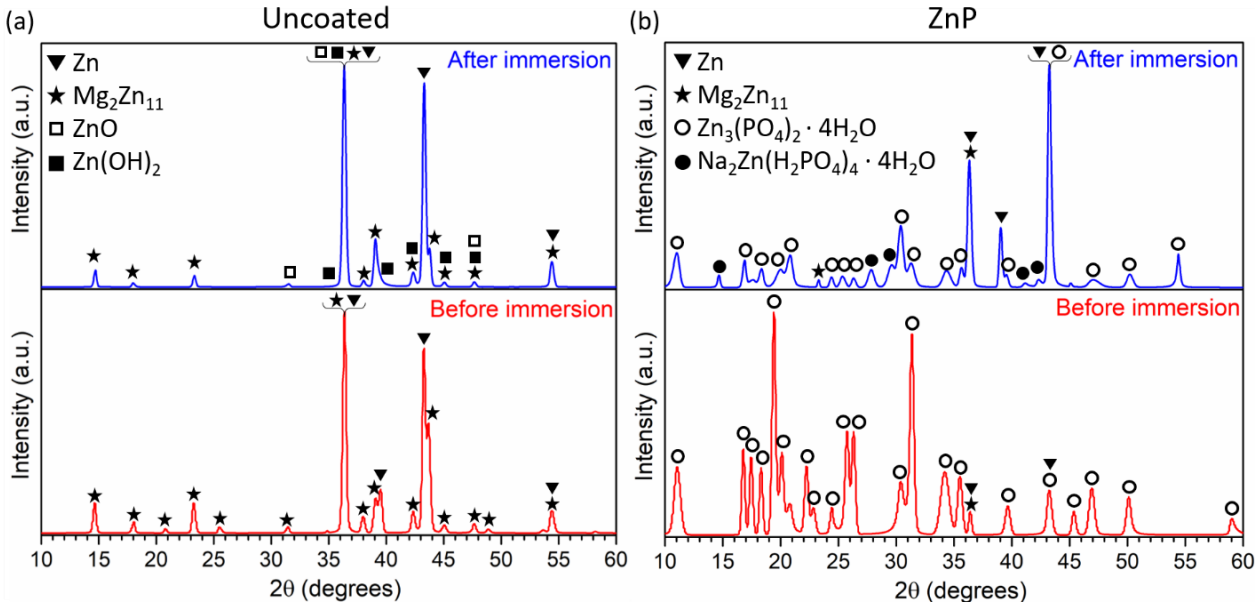

Figure 86: GIXRD scans of the (a) uncoated Zn-3Mg substrate, and (b) ZnP coated Zn-3Mg substrate, before immersion and after 21 days immersion in DMEM. Identified peaks are labeled with different symbols. Note that some peaks were attributed to several phases.

The weight loss and corrosion rate of the uncoated and ZnP sample after 6, 12, and 21 days immersion in DMEM at 37 ºC is plotted in Figure 87 (a) and (b), respectively, and the average values are presented in Table 10. The pH evolution of the immersion media, measured every other day, is represented in Figure 87 (c).

The average weight loss and corrosion rate were larger in the uncoated sample for the three time points tested. However, due to the large standard deviation error bars, no statistical significance was found between groups overall. The uncoated sample reached the maximum weight loss at day 12, which was maintained in a similar value up to day 21, whereas the corrosion rate was similar up to day 12, and then decreased approximately by half at day 21. However, the weight loss in the ZnP sample increased progressively over time, showing a more uniform degradation rate, and the corrosion rate decreased after day 12 and was maintained up to day 21. The only statistically significant difference was found between the corrosion rates of both samples at day 12, when that of the ZnP sample was about half of that of the uncoated sample.

The pH evolution of the immersion media in both samples presented similar trends, as observed in Figure 87 (c). During the first 2 days of immersion, the pH value increased from ~ 7.4 to ~ 7.65 in both samples. Then, the pH decreased slightly to ~ 7.55 at day 4, and was maintained reasonably stable between ~ 7.5-7.6 for the rest of the immersion test in both samples. In general, the pH was slightly larger, in the uncoated sample from day 4 to day 16, and practically the same between both samples from day 16 until the end of the immersion test at day 21.

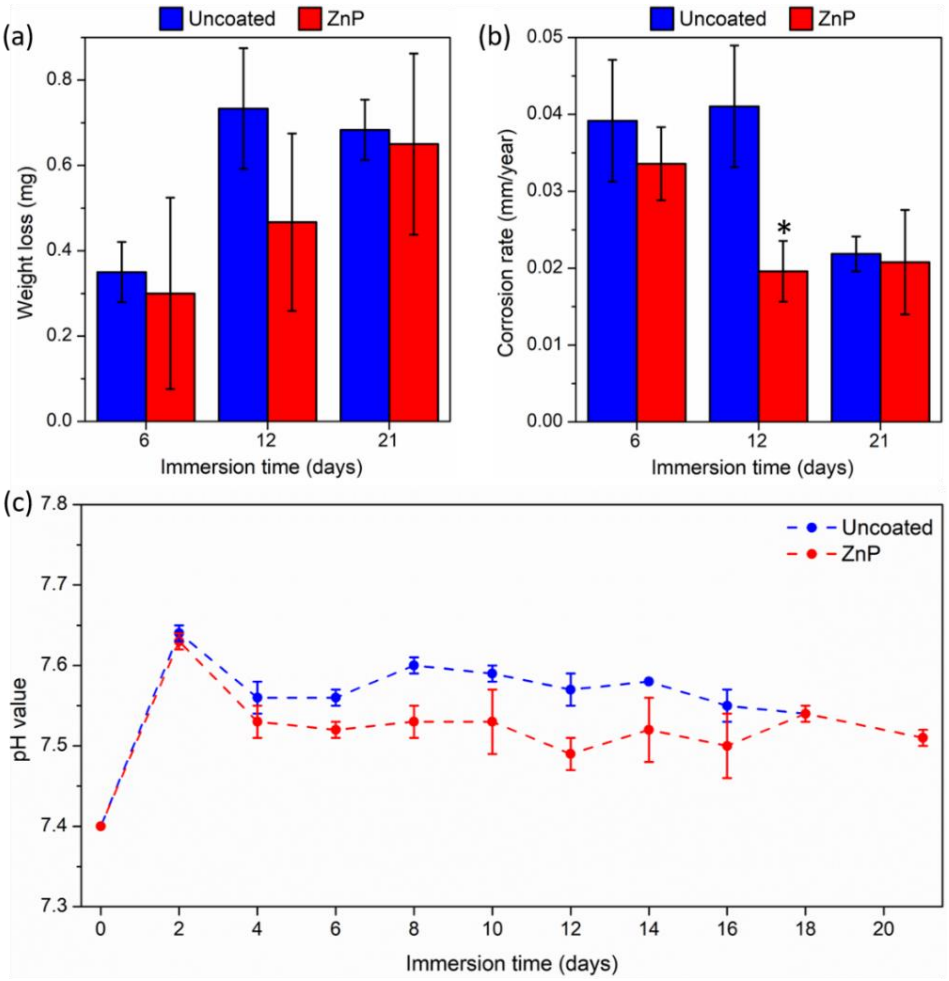

Figure 87: Evolution of the (a) weight loss, (b) corrosion rate, and (c) pH value of the uncoated and ZnP samples during the immersion test in DMEM at 37 ºC for up to 21 days. Statistical significance between groups was indicated with * for $p < 0.05$.

Table 10: Average values of the weight loss and corrosion rate of the uncoated and ZnP samples estimated from the immersion test in DMEM at 37 ºC for 21 days. These values are plotted in Figure 87.

Sample	Immersion time (days)	Weight loss (mg)	Corrosion rate (mm/year)
Uncoated	6	0.350	0.0392
	12	0.733	0.0410
	21	0.683	0.0219
ZnP	6	0.300	0.0336
	12	0.467	0.0196
	21	0.650	0.0208

4.5.3. Cytocompatibility and cell proliferation assays

4.5.3.1. Preliminary *in vitro* proliferation assay

The appearance of 7043L hMSC (passage 4) seeded at cell densities of $2.5 \cdot 10^3$, $5 \cdot 10^{3,}$ and $1 \cdot 10^4$ cell/cm^2 is shown in Figure 88 after culture for 2, 4, 7, and 9 days.

At day 2, star-like cell morphologies were observed, especially at lower cell densities, after cells attached to the bottom of the well plates. As cells proliferated, they rearranged into elongated spindle-shaped cells with parallel orientation, as observed at day 4 for the two highest cell concentrations. It was noted that the three different cell seeding densities could still be identified at day 4 from the OM images, consistent with the CCK-8 OD readings in Figure 89.

At day 7, high cell confluency led to new cells growing on top of the original cell layer, as shown at by entangled cells in the two highest cell density concentrations in Figure 88. At this stage, at least one cell layer covered the bottom of the well plate uniformly in the three groups, which resulted in similar CCK-8 OD readings in Figure 89. It was noted that despite the two highest cell densities may still contain a larger number of cells, only those cells in the most superficial layer may be able to react with the CCK-8 solution and thus, be counted. Consistent with this, cellular senescence was identified at day 9, meaning that cells stopped dividing and showed statistically similar CCK-8 OD readings from the different groups.

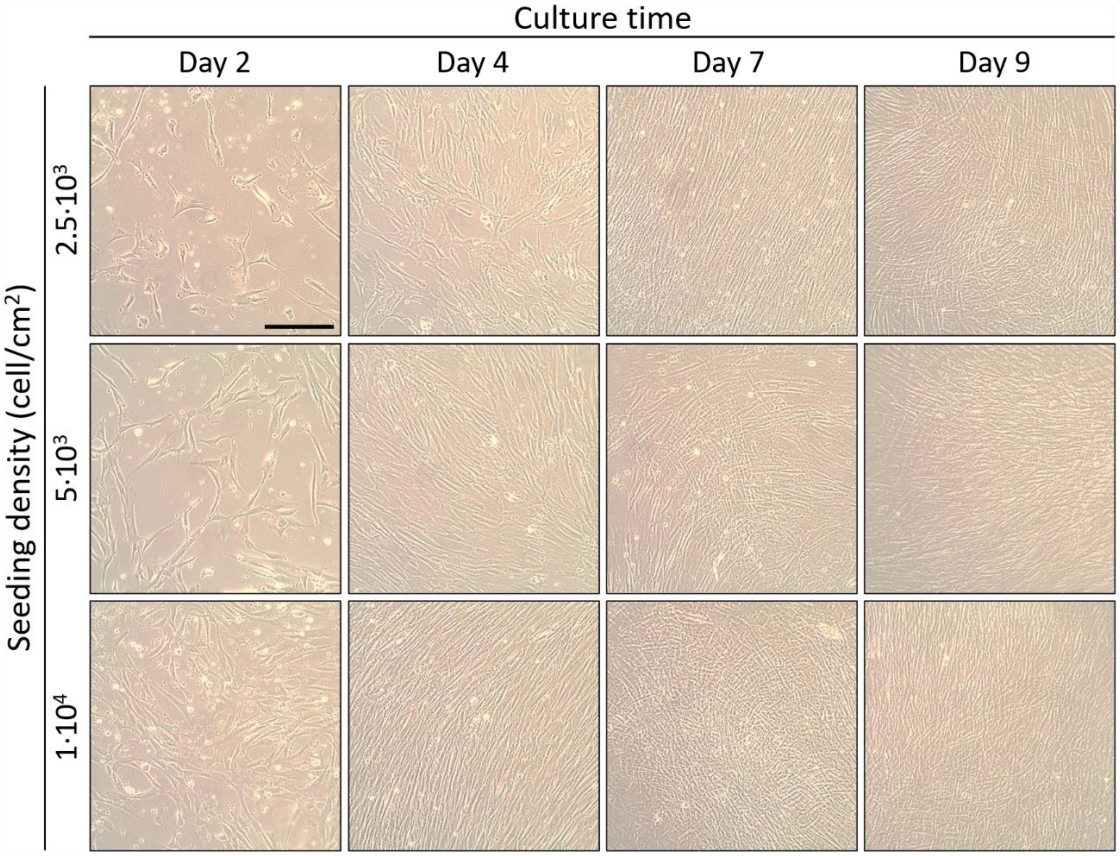

Figure 88: OM images showing the morphology of 7043L hMSC (passage 4) after 2, 4, 7, and 9 days culture in cell culture medium during the preliminary *in vitro* proliferation assay. Cells were seeded at three different densities: $2.5 \cdot 10^3$, $5 \cdot 10^{3,}$ and $1 \cdot 10^4$ cell/cm^2. The scale bar presented is common for all images and equivalent to 500 μm.

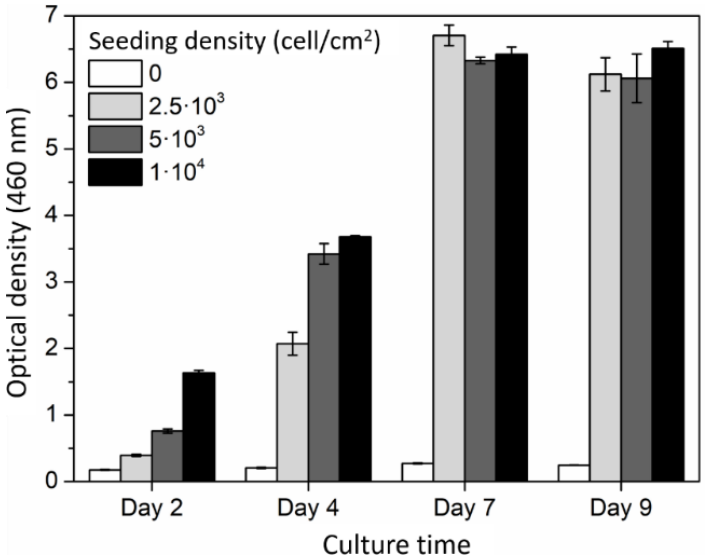

Figure 89: *In vitro* proliferation of 7043L hMSC (passage 4) measured by CCK8 assay after 2, 4, 7, and 9 days culture in cell culture medium. Error bars indicate standard deviations between triplicate samples.

4.5.3.2. Indirect contact cell proliferation assay with sample extracts

The appearance of 7043L hMSC (passage 6), seeded at a density of $2.5 \cdot 10^3$ cell/cm^2, after 4 and 6 days culture in 4-fold extract dilutions (i.e., 25 % extract concentration) of uncoated, ZnP and Col-AgBGN samples are presented in Figure 90.

A combination of star-like and spindle-like cell morphologies was observed at day 4 in the control group, consistent with those in Figure 88, and no apparent differences in cell morphology were identified in the extract groups. However, a modest increase in cell density could be observed consistently in the extract groups at day 4, as compared to the control, in agreement with the CCK-8 OD values in Figure 91.

In general, the higher cell densities observed at day 6 evolved to more elongated shapes and tended to align parallel, consistent with those shown in the first row of Figure 88. Some cell overlapping could be identified in the extract groups at day 6, where cells formed a weave-like pattern as they grew on top of each other aligned in different directions. Regardless of the effect of the sample extracts on the cells, no difference in the cellular morphological phenotypes, including shape and size, was evident as compared to the control groups.

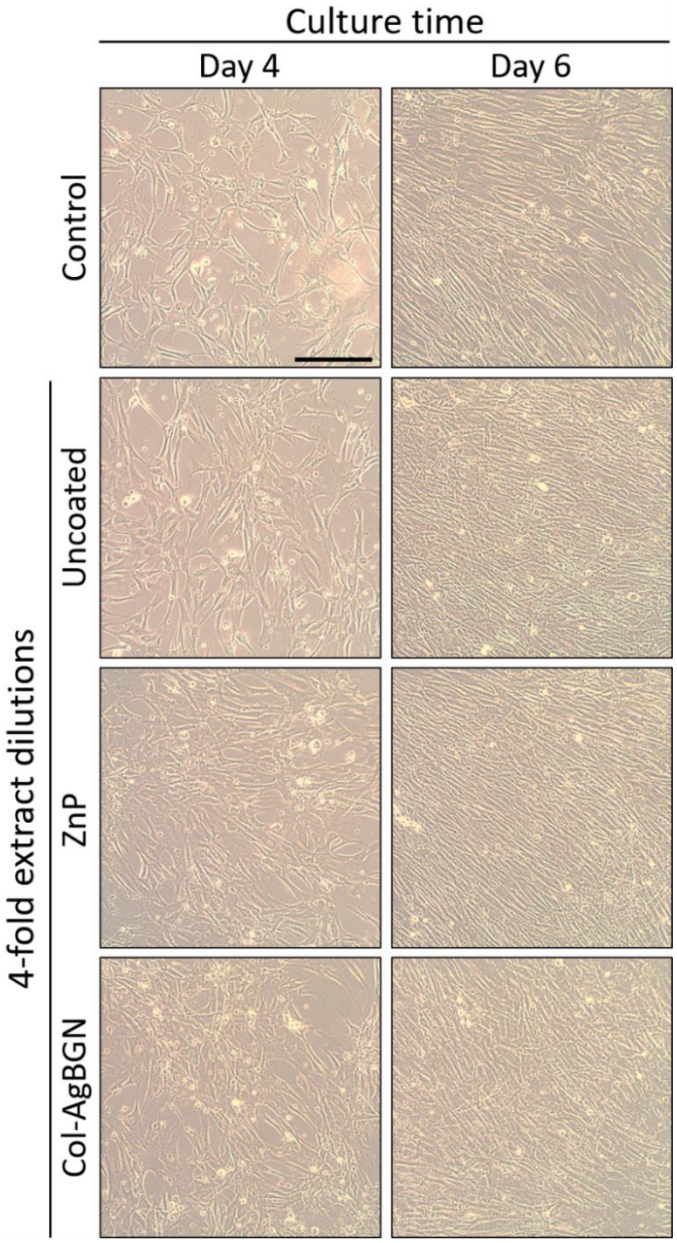

Figure 90: OM images showing the *in vitro* proliferation of 7043L hMSC (passage 6) after 4 and 6 days culture in 4-fold extract dilutions of uncoated, ZnP, and Col-AgBGN samples in cell culture medium (i.e., 25 % extract concentration). Cells were seeded at a density of $2.5 \cdot 10^3$ cell/cm^2. The extracts were obtained upon immersion the corresponding samples for 72 h at a surface area/volume ratio of 1.25 cm^2/mL in cell culture medium. The control cells were cultured in cell culture media. The scale bar presented is common for all images and equivalent to 500 μm.

The cell proliferation of 7043L hMSC (passage 6), determined from CCK-8 OD readings after 2, 4, and 6 days of culture in sample extract of different concentrations, is shown in Figure 91. Figure 91 (a) shows that at day 2, 4, and 6, the cell number was significantly greater in the 6-fold and 4-

fold uncoated extracts, as compared with the control group. In addition, the cell numbers tended to increase with the extract concentration, and there was statistical significance at day 2 and 4 between all extract concentrations, and at day 6 between the highest and lowest extract concentrations. Figure 91 (b) shows that at day 2, 4, and 6, the cell number in all ZnP extract concentrations were significantly higher than that of the control, except for the 6-fold extracts at day 6. However, no statistical difference was found between different ZnP extract concentrations. Figure 91 (c) shows that the number of cells cultured with Col-AgBGN extracts, regardless of the extract concentration, were significantly greater than the control at day 2, 4 and 6. It should be highlighted that only the Col-AgBGN extracts showed this trend, and that these extracts typically exhibited the highest CCK-8 OD values.

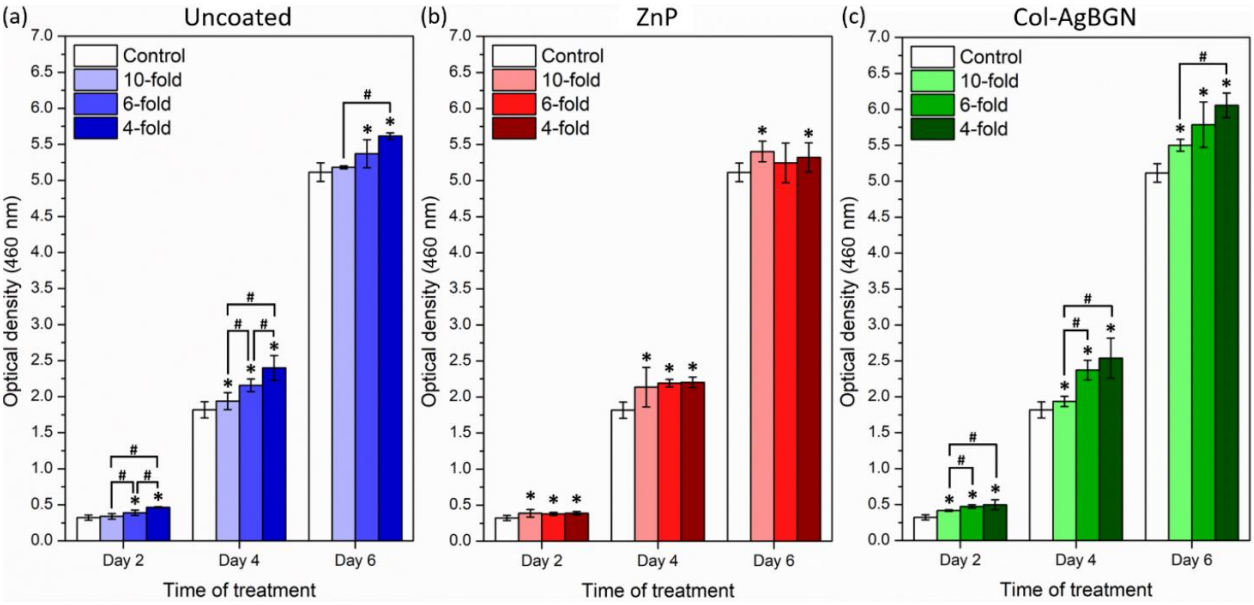

Figure 91: *In vitro* proliferation of 7043L hMSC (passage 6) measured by CCK8 assay after 2, 4 and 6 days culture in 10-fold, 6-fold, and 4-fold extract dilutions (corresponding to 10 %, 16.7 % and 25 % extract concentration in cell culture medium, respectively) of (a) Uncoated, (b) ZnP, and (c) Col-AgBGN samples. Error bars indicate standard deviations between triplicate samples. Darker colors indicate higher extract concentrations. Statistical significance codes: * $p < 0.05$ compared with control group, # $p < 0.05$ compared between groups.

4.5.4. Antibacterial adhesion and viability assessment

4.5.4.1. Bacteria adhesion to coated surfaces

The attachment and morphology of MRSA to the surface of different samples (i.e., uncoated and coated samples) after 7 days incubation in an initial bacteria suspension of 10^7 CFU/mL in TSB was evaluated through SEM, and representative images are provided in Figure 92. The uncoated sample, which showed the lowest surface roughness, presented a moderate number of bacteria, most of which exhibited smooth spherical surfaces, as highlighted in the inset of Figure 92 (a), which is a characteristic of healthy bacteria. In general, the ZnP and ZnP-Col samples showed significantly higher bacteria attachment as compared with the uncoated sample, as observed in Figure 92 (b) and (c), respectively. Careful inspection of different areas revealed that bacteria adhesion was slightly higher in the ZnP-Col surface than in the ZnP surface. It should be noted that these two samples also exhibited the largest surface area for bacteria to adhere, due to the morphology of the ZnP coating. Similar to the uncoated sample, multiple bacteria exhibited smooth spherical surfaces, as highlighted in green in Figure 92 (b) and (c). Interestingly, an example of bacteria about to divide is highlighted by the left green arrow in Figure 92 (c). Some examples of bacteria with anomalous morphologies and/or rough surfaces are highlighted by red arrows, which are typically associated with damaged and/or dead bacteria.

The Col sample exhibited a granulated surface, as observed in Figure 92 (d), also with higher bacteria attachment than the uncoated sample. Like the ZnP and uncoated samples, a good number of bacteria in the Col samples appeared to be healthy, although some bacteria fragments and bacteria with distorted shapes were also observed. Lastly, the Col-AgBGN samples presented a granulated morphology, like that in the Col sample, and significantly lower bacteria adhesion than

the other coated samples, similar to the uncoated sample. It should be highlighted that the majority of bacteria attached to the Col-AgBGN surface were either fragmented or exhibited anomalous morphologies.

It is important to emphasize that SEM imaging provided information about the morphology and amount of bacteria adhered to the samples, which can be used to interpret the health status of bacteria in relation to other characterization methods. However, SEM cannot be used alone to make an assessment of bacteria viability on the material surface. Consequently, the morphologies and approximate densities of bacteria attached to the different coated samples obtained from SEM were discussed together with the live/dead bacteria ratios calculated from fluorescent CLSM.

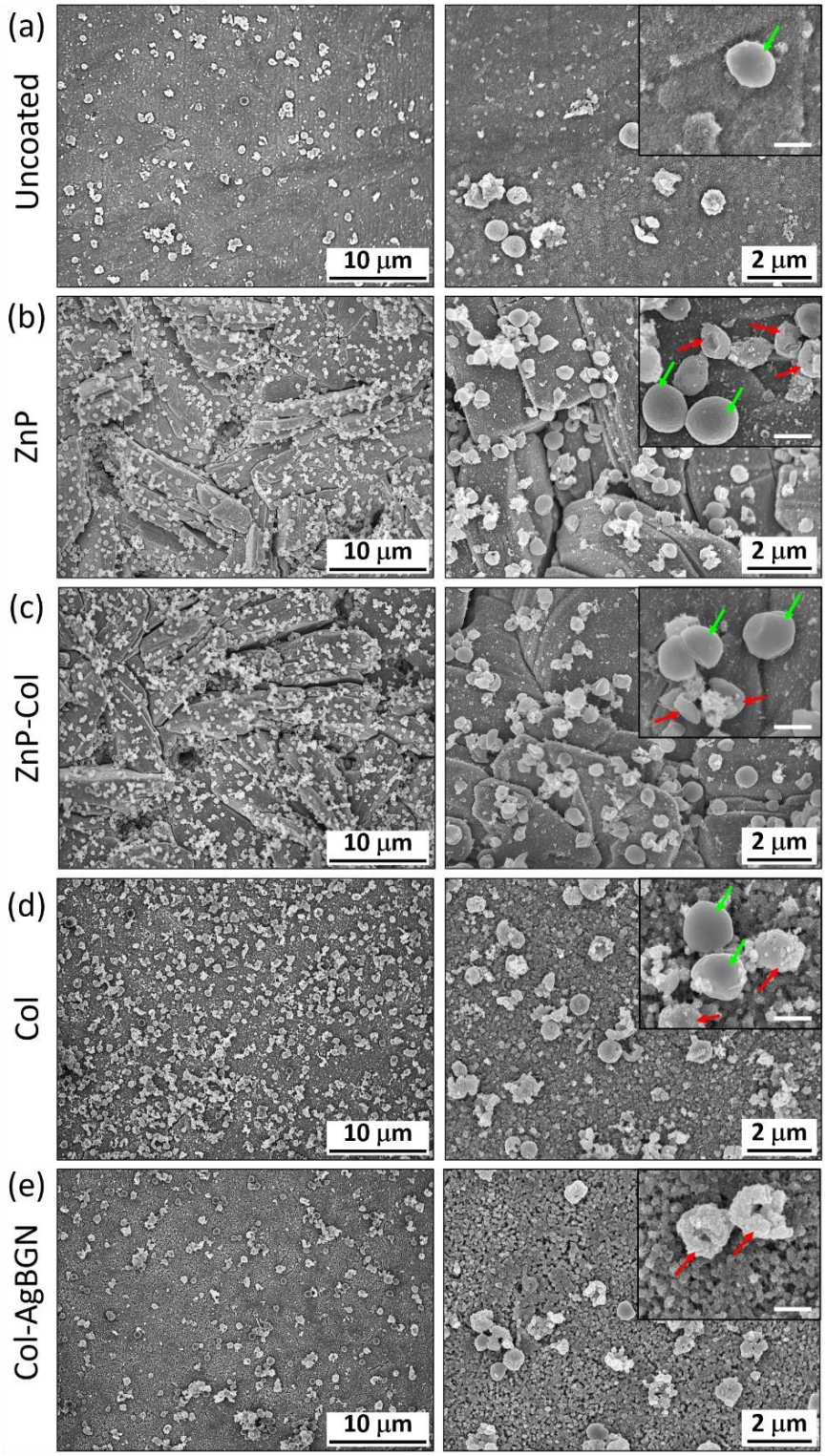

Figure 92: SE-SEM images showing MRSA adhesion to the surface of the Zn-3Mg alloy samples with different coatings, after 7 days incubation in an initial bacteria suspension of 10^7 CFU/mL in TSB: (a) Uncoated, (b) ZnP, (c) ZnP-Col, (d) Col, and (e) Col-AgBGN. The insets at the top-right corners of the higher magnification images show examples of live bacteria (green arrows) and dead bacteria (red arrows). The scale bar in the insets represents 500 nm.

4.5.4.2. Viability of bacteria adhered to coated surfaces

The viability of bacteria adhered to the sample surfaces, after 7 days incubation in an initial bacteria suspension of 10^7 CFU/mL in TSB, was assessed from the analysis of green/red pixels in fluorescence CLSM images obtained from live/dead staining, as described in section 3.8.5.3, which are indicative of live/dead bacteria. Representative CLSM images showing live and dead bacteria together, live bacteria alone, and dead bacteria alone are presented for uncoated, ZnP, ZnP-Col, Col, and Col-AgBGN samples in Figure 93. Similar ratios of green/red pixels, with a majority of green pixels, were observed in all coated samples, except in Col-AgBGN, where the number of red pixels was significantly greater than that of green pixels. Bacteria sometimes appeared as fine fluorescent points, indicating individual bacteria dispersed in the sample, like those in the uncoated and Col samples in Figure 93 (a) and (d), respectively. In other cases, larger fluorescent areas were found, either green or red, indicating bacteria colonies in the samples, like those in the ZnP and Col-AgBGN samples in Figure 93 (b) and (e), respectively.

The live/dead percentages are presented in the bar plot in Figure 94, where the error bars represent the standard deviations between triplicate samples. The percentages of live/dead bacteria were found to be similar between the uncoated, ZnP-Col, and Col samples, with 76 %, 75 %, and 71 % of live bacteria, respectively. Furthermore, no statistical difference in live/dead bacteria percentages was found between the ZnP-Col and Col samples with the uncoated sample. The percentage of live bacteria decreased to 65 % in the ZnP sample, which seemed to be statistically lower than that of the uncoated sample. Lastly, the Col-AgBGN sample exhibited a significant reduction in bacteria viability, with an average of 31 % live bacteria. Thus, the Col-AgBGN samples exhibited a notable antibacterial effect.

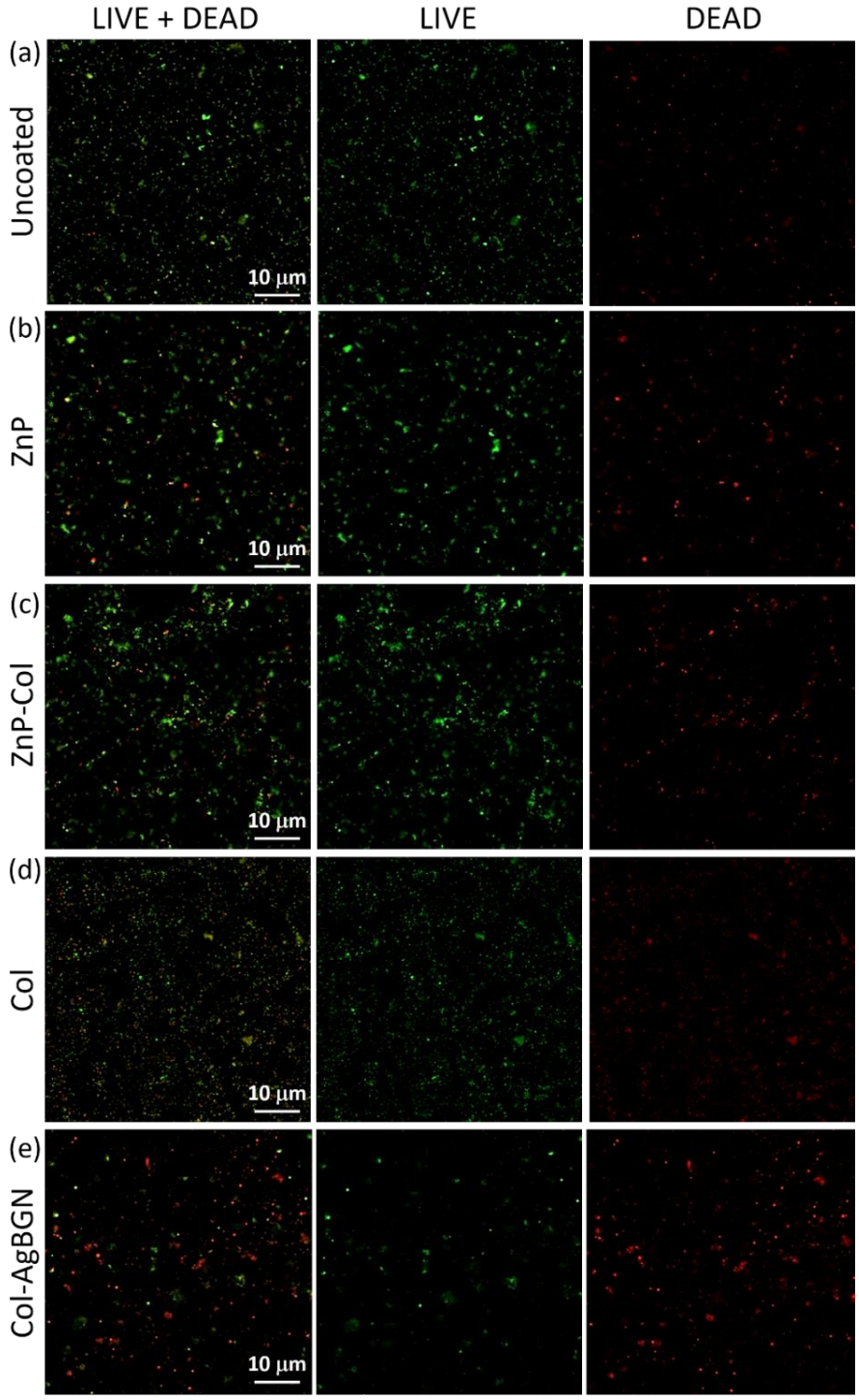

Figure 93: CLSM images showing MRSA viability on the surface of the Zn-3Mg alloy samples with different coatings, after 7 days incubation in an initial bacteria suspension of 10^7 CFU/mL in TSB: (a) Uncoated, (b) ZnP, (c) ZnP-Col, (d) Col, and (e) Col-AgBGN. SYTO 9 and propidium iodide stains were used to stain intact membranes and damaged membranes with fluorescent green and red, respectively. Images in the "LIVE + DEAD" column show green and red fluorescence, images in the "LIVE" column show only green fluorescence, and images in the "DEAD" column show only red fluorescence.

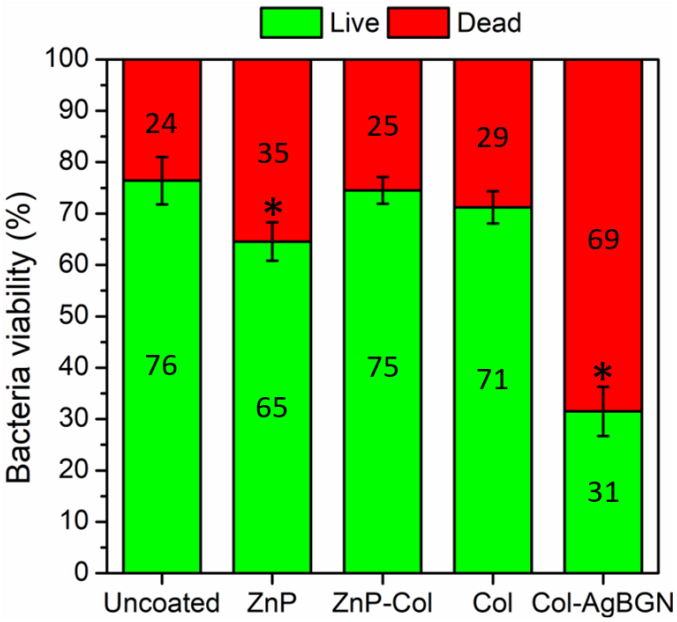

Figure 94: Quantification of live and dead MRSA on the surface of the Zn-3Mg alloy samples with different coatings, after 7 days incubation in an initial bacteria suspension of 10^7 CFU/mL in TSB. The percentages of live and dead bacteria were calculated from the number of green and red pixels in triplicate CLSM images, using a pixel color counter plugin for ImageJ. The error bars indicate the standard deviations between triplicate samples. The numbers inside the green and red bars indicate the average live and dead percentages of MRSA calculated for each sample, respectively. Statistically significance code: * $p < 0.05$ compared with uncoated group.

Table 11 presents the estimated bacteria density attached to the samples, the live/dead bacteria percentages, and the live bacteria density for the different samples. The uncoated and Col-AgBGN samples exhibited similar bacteria densities between 250-270·10^3 bacteria/mm^2, whereas the ZnP-Col and Col samples also presented similar bacteria densities between 630-650·10^3 bacteria/mm^2. The ZnP sample showed a lower bacteria density than the ZnP-Col and Col samples, but about twice as high as that of the uncoated and Col-AgBGN samples. It is worth highlighting that, despite the similar densities of bacteria in the uncoated and Col-AgBGN samples, the live bacteria density of the Col-AgBGN sample was about 60 % lower than that of the uncoated sample, since the percentage of dead bacteria was significantly greater in the Col-AgBGN sample. In general, the ZnP-Col and Col samples presented the highest live bacteria densities, followed by ZnP, uncoated, and Col-AgBGN.

Table 11: Quantification of the total bacteria density, live/dead bacteria percentages, and live bacteria density adhered to the sample surfaces, estimated from the analysis of the color pixel counts from fluorescent CLSM images.

Sample	Bacteria density (bacteria/mm^2) $\cdot 10^3$	Live bacteria (%)	Dead bacteria (%)	Live bacteria density (bacteria/mm^2) $\cdot 10^3$
Uncoated	254	76	24	193
ZnP	522	65	35	339
ZnP-Col	636	75	25	477
Col	652	71	29	463
Col-AgBGN	266	31	69	82

4.5.4.3. Viability of bacteria in suspension

The viability of an initial bacteria suspension of 10^7 CFU/mL in TSB (OD = 0.5), cultured with different samples (i.e., uncoated and coated samples) for 7 days, was evaluated from OD measurements after 1, 2, 3, 5, and 7 days. The OD values obtained from the different samples over time are presented in aggregate in Figure 95 (a). The individual evolutions of the OD value of each sample over time are shown in Figure 95 (b-g). The bacteria viability in the untreated group (i.e., no sample) was significantly higher than that of all the other groups, for all the time points, as observed in Figure 95 (a). As expected, a gradual increase in bacteria concentration over time was observed in the untreated group over time, as observed in Figure 95 (b). It should be recalled that the bacteria in this experiment could not grow attached to the bottom of the wells, such that they could either remain in suspension (i.e., planktonic bacteria) or attached to the sample surfaces.

In general, the planktonic bacteria concentration increased over time for all the groups, except for the uncoated group. As observed in Figure 95 (c), the planktonic bacteria concentration in the uncoated group remained practically constant at OD ~ 0.6 up to day 3, and then, decreased to OD ~ 0.4 at day 5, maintaining that value up to day 7. Both ZnP and ZnP-Col groups showed similar trends, as observed in Figure 95 (d) and (e), respectively, where the planktonic bacteria concentrations decreased to OD ~ 0.4-0.5 at day 3, and then, increased gradually up to OD ~ 0.8 at day 7. In the Col group, the planktonic bacteria concentration decreased to OD ~ 0.4 at day 2, and then, increased up to OD ~ 0.6 at day 5, where it remained constant up to day 7, as observed in Figure 95 (f). Lastly, the planktonic bacteria concentration in the Col-AgBGN group increased progressively up to OD ~ 1.1 at day 5, and remained statistically similar at day 7. It should be highlighted that the Col-AgBGN group was the only one to exhibit a consistent increase of planktonic bacteria concentration in solution.

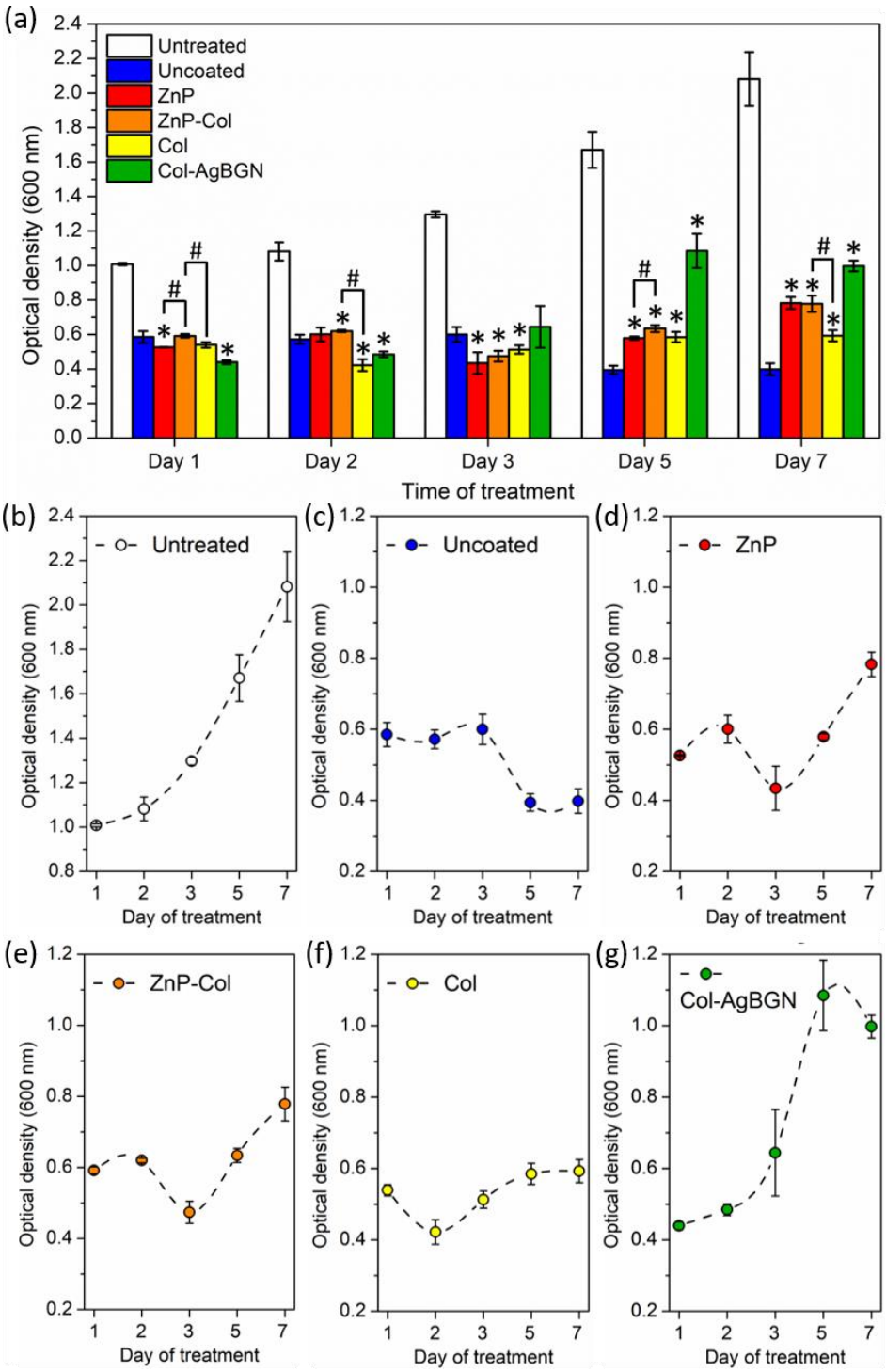

Figure 95: Assessment of MRSA suspension viability, with an initial concentration of 10^7 CFU/mL in TSB, after 1, 2, 3, 5, and 7 days incubation with Zn-3Mg alloy samples having different coatings. (a) comparative plot with the OD values for all samples and time points. (b-g) Individual plots showing the evolution of the OD values for each sample over time. Untreated refers to a MRSA suspension incubated with no sample. Error bars indicate standard deviations between triplicate samples. Statistical significance codes: * $p < 0.05$ compared with Uncoated group, # $p < 0.05$ compared between groups.

5. DISCUSSION

5.1. Zn-10Mg hybrids

This section discusses the effects of HPT processing on the evolution of the microstructure, hardness, and electrochemical properties of the Zn-10Mg hybrids. It should be noted that this hybrid composition was the first one to be studied since it consisted of Zn/Mg/Zn stacked disks of equal thickness, and thus, it served as a baseline for the other two hybrid compositions (i.e., Zn-3Mg and Zn-30Mg) discussed later.

5.1.1. Effect of HPT processing on the microstructural evolution

Mechanical bonding of the Zn-10Mg HPT hybrids was successfully achieved via HPT processing, as shown in Figure 40. The fragmentation and diffusion of the central Mg disk from the center of the sample towards the periphery became increasingly evident from 1 to 15 turns. However, after 30 turns, the Mg-rich regions, initially dominant near the sample edges, were no longer visible at lower magnifications. This suggested that a significant volume fraction of Mg atoms present in the Mg-rich areas had either dissolved as solutes in the Zn-rich matrix or combined with Zn atoms to form Mg_2Zn_{11} and $MgZn_2$ intermetallic phases. A similar rationale was proposed by Ahn et al. [95] in the Al-Mg HPT hybrid system, where Mg atoms were found to combine with Al atoms after 5 turns into $Al_{12}Mg_{17}$ intermetallic phases. The refinement of the multilayered microstructure near the disk periphery from 15 to 30 turns was identified via SEM, see Figure 41, where both a decrease of the average grain size and a narrower grain size distribution were observed. Moreover, this heterogenous microstructure consisted of nanosized layers and Mg_2Zn_{11} and $MgZn_2$ intermetallic phases, as observed by TEM, see Figure 44.

It is well established that the microstructural evolution of hexagonal closed-packed (HCP) metals during HPT is influenced by their homologous temperature (T_h) [179]. In particular, HPT processing of low melting temperature (T_m) metals like Zn (T_m = 693 K; T_h = 0.43 at RT) was found to promote continuous dynamic recrystallization (CDRX), thereby hindering extensive grain refinement and giving rise to the development of a strong basal texture with larger grain sizes than other HCP metals with higher T_m, such as Ti or Zr [180].

The latter statement is consistent with the EBSD results presented in Figure 43 from the Zn-rich region near the periphery of the Zn-10Mg HPT hybrids from 1 to 30 turns. Grain size reduction at increasing shear strain from 1 to 15 turns was due to DRX during SPD, resulting in an increase of the HAB volume fraction and the development of a strong basal texture, see Figure 43 (a-c). Moreover, basal textures are often reported in Zn and other hexagonal metals like Mg, Cd, Zr, or Ti [180–182].

Detailed inspection of the basal pole figure after 15 turns, see Figure 43 (c), revealed that the basal poles were tilted slightly away from the normal direction, which is common for Zn due to basal slip {0001}<11$\bar{2}$0> and pyramidal slip {11 $\bar{2}\bar{2}$}<11$\bar{2}$3> [182]. The grain size of the Zn-rich region after 15 turns became relatively uniform and equiaxed, with a measured GS_{ave} of ~ 4 μm, which was similar to the steady-state grain size of 5.2 μm reported by Edalati et al. [179] for pure Zn after HPT processing for 5 turns under an applied pressure of 2 GPa.

Further HPT processing to 30 turns led to a decrease in the fraction of HABs as a result of GB migration to reduce the stored energy, which was accompanied by an increase of the GS_{ave} above the steady-state grain size, see Figure 43 (d). This was suggested to occur due to the saturation of grain refinement through CDRX, where the interaction of strain hardening and dynamic recovery

led to the annihilation of dislocations in the grain interiors and HABs to achieve a more energetically favorable state [183,184].

The formation of the Mg_2Zn_{11} intermetallic phase was initially suggested from the EDS results in Table 4, which showed that the chemical composition of the light grey phase in Figure *42* was close to that of the intermetallic compound Mg_2Zn_{11} (93.7Zn – 6.3 Mg wt.%). Therefore, it was reasonable to assume that the combination of 6 GPa for 30 turns resulted in the formation of the Mg_2Zn_{11} intermetallic compound, consistent with other HPT-induced phase formations in the Al-Mg [95,185] and Al-Cu [86,87] HPT hybrid systems.

It should be noted that the areas of different contrast observed in the BSE photomicrographs in Figure *42* were due to differences in the mean atomic number (Z), such that brighter and darker BSE intensities correlate to phases with greater and lower mean Z, respectively. Therefore, the dark grey phase observed in Figure 42 (b) must have a mean Z between that of the light grey phase (Mg_2Zn_{11}; $Z_{Mg2Zn11} = 27.23$) and the black phase (Mg; $Z_{Mg} = 12$). This indicated that the Mg content of the dark grey phase is larger than that of the Mg_2Zn_{11} phase. As shown in Figure 96, the Mg-Zn binary phase diagram contains five intermetallic phases: Mg_2Zn_{11}, $MgZn_2$, Mg_2Zn_3, MgZn, and Mg_7Zn_3, arranged from lower to higher Mg content. Among these phases, the thickness of the $MgZn_2$ layer was found to be the largest between the Mg_2Zn_{11} and Mg layers in Zn-Mg diffusion couple experiments [186]. In addition, a homogenous Zn-10Mg (wt.%) alloy, with the same bulk composition as the Zn-10Mg HPT hybrids would result in a mixture of $MgZn_2$ and Mg_2Zn_{11} intermetallic phases under equilibrium conditions according to the Mg-Zn phase diagram. The latter two arguments suggested that the dark grey phase in Figure 42 (b) could be $MgZn_2$.

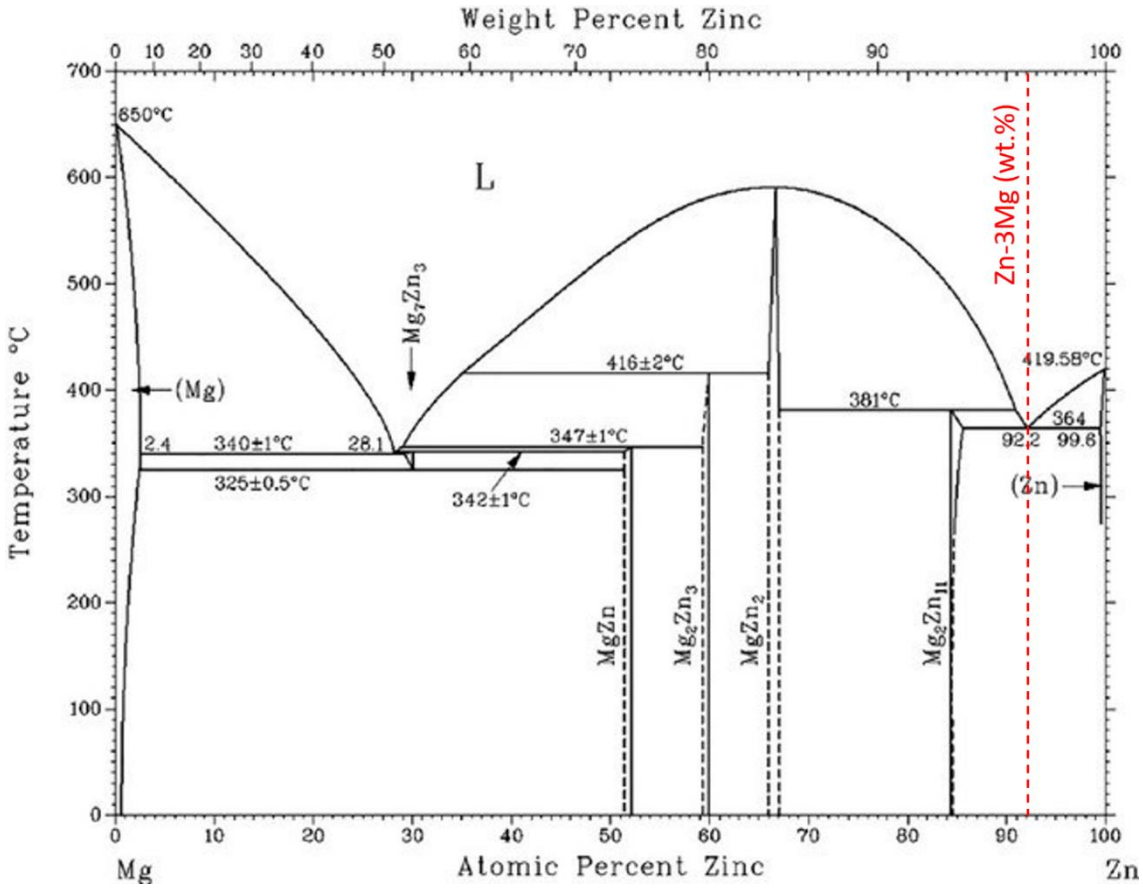

Figure 96: Binary Mg-Zn equilibrium phase diagram. The Zn-3Mg (wt.%) eutectic composition is highlighted in red. Adapted from [187].

XRD analysis confirmed the presence of $MgZn_2$ and Mg_2Zn_{11} intermetallic phases at the sample periphery after 15 and 30 turns, see Figure 45. From the quantitative phase analysis performed via Rietveld refinement, see Table 5, the amount of $MgZn_2$ (~ 13 wt. %) was considerably higher than that of Mg_2Zn_{11} (~ 2 wt. %). This was supported by the fact that the interdiffusion coefficient of $MgZn_2$ was found to be one order of magnitude larger than that of Mg_2Zn_{11} [188]. Moreover, the weight fractions of both intermetallic phases increased from 15 to 30 turns. The $MgZn_2$ content evolved from 12.8 to 16.3 (wt. %), representing a ~ 64 % increase, whereas the Mg_2Zn_{11} content evolved from 1.6 to 7.5 (wt. %), representing a ~ 234 % increase. This significant increase of the intermetallic phase fractions was correlated with a dramatic drop in the Mg content with increasing

number of turns. Note that after 1 turn, the Mg content in the disk periphery was above 80 (wt. %), which is in good agreement with the cross-sectional image in Figure 40, where the Mg phase was uniform across the mid-thickness of the sample after 1 turn. As the Mg-rich regions at the disk periphery of the cross-section became less evident with increasing number of turns, the Mg content decreased from 81, to 28, to 14 (wt. %) after 1, 15, and 30 turns, respectively. This resulted in the formation and growth of the $MgZn_2$ and Mg_2Zn_{11} phases with increasing plastic strains.

Consistent with the discussion of the XRD results above, the SAD patterns collected from the periphery of the Zn-10Mg HPT hybrids after 30 turns revealed the presence of Mg_2Zn_{11} and $MgZn_2$ intermetallic phases. The four diffraction rings labeled in Figure 44 (b) showed contributions of at least one of these intermetallic compounds. The three additional diffraction rings, of relatively lower intensity that were not labeled, corresponded to interplanar spacings of 1.040, 0.928 and 0.844 Å (from smallest to largest diameter, respectively). These unlabeled diffraction rings were likely associated with higher order reflections from large 2θ values, as was the case for $(10\bar{1}3)$ and $(20\bar{2}6)$ in the $MgZn_2$ phase, which contributed to the first and fourth ring, respectively.

In addition to the identification of Mg_2Zn_{11} and $MgZn_2$ intermetallic phases by XRD and TEM, the proximity histogram obtained from the APT analysis showed a nanosized region with a composition of 41.5Mg-58.4Zn (at. %). As observed in the Zn-Mg phase diagram in Figure 96, this composition is close to that of the Mg_2Zn_3 intermetallic phase. The other composition identified in the APT proximity histogram, 99.5Mg-0.4Zn (at.%), was associated with a Mg-Zn solid solution, as the solubility of Zn in Mg is ~ 1 (at.%) at RT.

5.1.2. Effect of HPT on the hardness evolution

The strengthening effect of Mg in Zn-Mg alloys due to the formation of hard intermetallic phases has been widely reported [15,54,189]. Mg additions of 1, 3, 5, and 7 (wt. %) to Zn resulted in Zn-Mg alloys with 82, 124, 196, and 226 HV, respectively, which was related to the increasing amounts of Mg_2Zn_{11} and $MgZn_2$ [175]. The hardness values of these two intermetallic compounds were reported elsewhere [188] from Berkovich nanoindentation experiments as ~ 3.8 GPa for Mg_2Zn_{11} and ~ 5.1 GPa for $MgZn_2$. To correlate hardness results from micro- and nano-indentation, it is important to account for the fact that, even though Vickers and Berkovich procedures determine their respective hardness values from the peak force over the contact area, their definition of the contact area is different. In Vickers indentation, the contact area refers to the surface area of the impressed surface, whereas for Berkovich nanoindentation, it is defined as the projected area of the indent [142]. The conversion equation provided elsewhere [190,191] was used to convert the nanoindentation hardness values mentioned above for Mg_2Zn_{11} and $MgZn_2$ into approximate Vickers hardness values of ~ 359 HV and ~ 482 HV, respectively, by using a correlation between the ratio of projected area to surface area.

These estimated HV values are significantly higher than those found across the Zn-Mg HPT hybrids, yet they have the same order of magnitude than those found near the periphery after 15 and 30 turns. The mixture of the fine Zn-Mg phases (i.e., finer than 20 μm) observed in Figure 41 and Figure 42, together with the fact that HV indent diagonals between 20-30 μm result in hardness values in the range of ~ 100-200 HV, made it impractical to measure the hardness of individual Mg_2Zn_{11} or $MgZn_2$ phases using Vickers hardness. Thus, the hardness heterogeneity obtained across the diameter of the Zn-10Mg HPT hybrid after 15 and 30 turns resulted from a combination

of different phases (i.e., Zn, Mg, Mg_2Zn_{11}, $MgZn_2$, and Mg_2Zn_3) as suggested from the TEM, XRD, and APT results discussed in the previous section.

The microhardness evolution of the Zn-10Mg HPT hybrids exhibited different trends compared to those of pure Zn and pure Mg alone after HPT processing. In general, for metals with moderate T_h at RT, like Zn and Mg, the hardness increases with increasing plastic deformation during HPT and, after reaching a maximum hardness value, the hardness decreases to a steady level [179]. This strain-softening behavior after hardness saturation was associated with the enhancement of DRX at severe plastic strains [180], and was reported consistently for HPT-processed Zn [179] and Mg [192], as well as for Mg-Zn alloys, namely Mg-3.4Zn (at.%) [193]. It is worth mentioning that the hardness saturation values reported in three later studies were ~ 52 HV for Zn after 5 turns [179], ~ 45 HV for Mg after 10 turns [192], and ~ 130 HV for the Mg-Zn alloy after 10 turns [193]. Unlike that of pure Zn and pure Mg, the microhardness of the Zn-10Mg HPT hybrids did not exhibit any sign of saturation after 10 turns. Overall, the HV values tended to increase gradually with increasing strain, reaching up to ~ 250 HV at ε_{eq} 600.

5.1.3. Effect of HPT processing on the electrochemical properties

Corrosion occurred in steady-state conditions after immersion of the Zn-10Mg HPT hybrid samples in SBF in the absence of any external potential, see Figure 49 (a). The more negative potentials obtained after 15 and 30 turns, as compared to after 1 turn, may be attributed to the higher reactivity of the Mg_2Zn_{11} and $MgZn_2$ intermetallic phases with SBF. It is well known that the nature and fraction of secondary phases play an important role in the corrosion behavior of absorbable alloys [3,18]. Each phase has individual electrochemical properties, and in this case, the Zn-Mg intermetallic compounds present after 15 and 30 turns may act as galvanic couples,

accelerating the corrosion rate. Moreover, the potential variations in the samples after 15 and 30 turns are indicative of compositional and microstructural differences with respect to the sample after 1 turn, which exhibited a relatively uniform potential after 2 h immersion in SBF.

From Figure 40, it was noted that the Zn and Mg layer phases did not mix after 1 turn, and therefore, it is very likely that only the Zn phase was interacting with the electrolyte. However, after 15 and 30 turns, the mixture of Zn and Mg phases, as well as the formation of Mg_2Zn_{11} and $MgZn_2$ intermetallics, contributed to the formation of corrosion products. On the one hand, corrosion of Zn leads to a series of reactions where $Zn(OH)_2$ and ZnO products are formed, without hydrogen evolution. On the other hand, corrosion of Mg leads to the formation of $Mg(OH)_2$ products and hydrogen gas. As compared to the relatively good stability of the passive layer formed in Zn, the $Mg(OH)_2$ corrosion layer is not as compact, and the chloride ions present in the SBF can easily distort the thermodynamic equilibrium leading to the formation of $MgCl_2$ [194]. Consequently, accelerated corrosion of Mg-rich regions could be the reason for the potential variations of the samples after 15 and 30 turns during OCP stabilization.

The corrosion behavior away from equilibrium conditions was analyzed after further polarization of the samples. The lower current density of the sample after 1 turn observed in Figure 49 (b), as compared to that after 15 and 30 turns, could be associated with the lower Mg content, as well as to the inherent passive nature of the ZnO layer. The higher I_{corr} values (i.e., faster corrosion rate) of the samples after 15 and 30 turns could be rationalized through two different contributions. First, the nature of the Zn-Mg intermetallic compounds could promote the formation of micro-galvanic cells, causing a faster dissolution of the protective passive layer. Second, carbonate and phosphate ionic species present in SBF, namely HCO_3^- and HPO_4^-, are known to react with the OH^- groups formed during corrosion of Mg corrosion [195], and could induce the precipitation of

insoluble products, hence, accelerating the corrosion process. The increased surface reactivity after 15 and 30 turns was also evident from less noble E_{corr} values as compared to that after 1 turn, consistent with the corrosion rates provided in Table 6.

From the PDP curves, it was found that the samples after 15 and 30 turns exhibited passive regions from their respective E_{corr} values to about -1.1 V, followed by passivity breakdown regions at increasing potentials, which are consistent with those found for Zn after immersion in PBS for 5 days [196].

Although existing literature is sometimes contradictory when reporting the effect of grain size on the corrosion properties of different metals, there is a good agreement in that a decrease in grain size in Zn [197,198] and Mg alloys [199,200] improve their corrosion resistance in NaCl electrolytes. The impedance spectra resulting from EIS analysis are used to investigate the influence of grain size on the electrochemical corrosion properties. From Table 7, it was noted that the sample after 30 turns exhibited a higher film resistance (R_f) than after 1 and 15 turns, which was associated with a more uniform protection layer with better barrier properties. However, the charge transfer resistance (R_{ct}) after 1 turn was higher than after 15 and 30 turns, which was suggested due to the lack of phase mixing after 1 turn. The polarization resistance, which can be interpreted as the corrosion resistance, is given as the sum of R_f and R_{ct} [201]. Thus, the corrosion resistance from EIS analysis would be from highest to lowest: after 1 turn ($\sim 593\ \Omega\ cm^2$), 30 turns ($\sim 444\ \Omega\ cm^2$), and 15 turns ($\sim 354\ \Omega\ cm^2$), which agreed with the corrosion rates obtained from the PDP analysis. This indicated that the sample after 30 turns exhibited overall better stability than after 15 turns, which was associated with a more extensive microstructural refinement, together with a more uniform distribution of the different phases present.

5.2. Zn-3Mg alloy

This section discusses the microstructural and hardness evolutions of the as-cast Zn-3Mg alloy after the homogenization heat treatment, HPT processing for 30 turns, and subsequent PDA. The effects of HPT and PDA on the Zn-3Mg alloy will be discussed in comparison with those of the Zn-3Mg hybrid in sections 5.4 and 5.5.

5.2.1. Effect of homogenization treatment on the microstructure

The homogenization heat treatment (360 ºC, 15 h) was performed in the as-cast Zn-3Mg alloy with the goal to dissolve the microstructural heterogeneity associated with the presence of primary globular Mg_2Zn_{11} phases in the lamellar microstructure. It should be noted that the Zn-3Mg alloy corresponds to the eutectic composition, which is highlighted in the Mg-Zn phase diagram in Figure 96. Theoretically, during the cooling of the eutectic Zn-3Mg alloy, when the temperature reaches the eutectic point (364 ºC), the liquid phase transforms into a lamellar microstructure of Mg_2Zn_{11} and Zn phases. However, the presence of the primary Mg_2Zn_{11} phases in the as-cast microstructure suggested that the Mg concentration might have been slightly larger than that of the eutectic composition. This way, the cooling path may not have crossed the eutectic point and instead crossed the liquidus line entering slightly into the L + Mg_2Zn_{11} region, forming primary proeutectic Mg_2Zn_{11} phases within the liquid matrix. Then, when the eutectic temperature is reached upon further cooling, the liquid phase transforms into lamellar Zn and Mg_2Zn_{11} phases. Therefore, the as-cast microstructure in this condition would consist of primary proeutectic Mg_2Zn_{11} phases in a eutectic matrix of lamellar Zn and Mg_2Zn_{11} phases, like that observed in Figure 97 (a-b). The homogenization heat treatment seemed effective in dissolving the primary Mg_2Zn_{11} phases, as observed in Figure 97 (f-g).

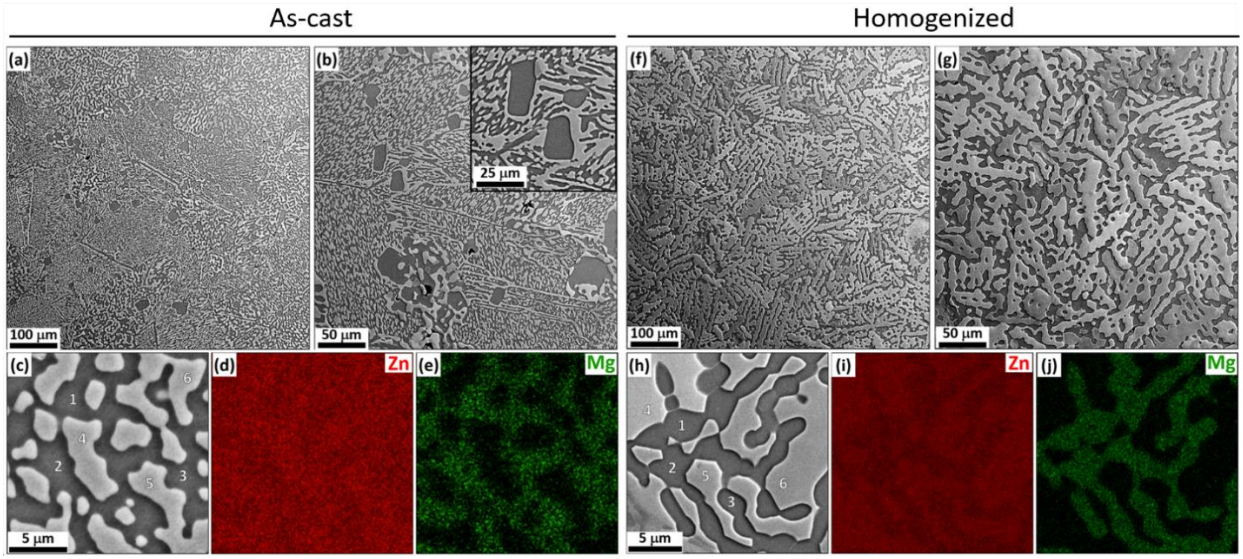

Figure 97: Representative BSE-SEM micrographs and EDS compositional maps of the Zn-3Mg alloy: (a-e) as-cast, (f-j) after homogenization heat-treatment. The points labeled from 1 to 6 in (c) and (h) indicate where EDS point analysis was performed, and their values are provided in Table 12. Adapted from [124].

In addition, the rapid cooling during the water quenching seemed effective in maintaining a uniform and interconnected lamellar microstructure after the homogenization treatment. This is in good agreement with the findings of Dambatta et al. [202], where they reported that the microstructure of the water-quenched Zn-3Mg (wt. %) became more uniform than that air-cooled or furnace-cooled after a similar homogenization heat treatment at 370 ºC for 10 h.

Table 12: Chemical compositions of the Zn-3Mg in the as-cast and as-homogenized state measured by EDS at different locations indicated in Figure 97 (c) and (h), respectively

Zn-3Mg alloy	Measurement location	Zn		Mg	
		(wt. %)	(at. %)	(wt. %)	(at. %)
As-cast	Whole area	96.7	91.7	3.3	8.3
	Points 1, 2 and 3	94.7 ± 0.3	86.9 ± 0.7	5.3 ± 0.3	13.1 ± 0.7
	Points 4, 5 and 6	100	100	0	0
As-homogenized	Whole area	97.2	92.8	2.8	7.2
	Points 1, 2 and 3	94.2 ± 0.1	85.7 ± 0.3	5.8 ± 0.1	14.3 ± 0.3
	Points 4, 5 and 6	100	100	0	0

According to the compositions in Table 12, the darker regions in the microstructure before and after homogenization were in good agreement with that of the Mg_2Zn_{11} intermetallic phase: 93.7Zn-6.3 Mg (wt. %), indicating that the investigated alloy, with an overall composition of ~ 97Zn-3Mg (wt. %), consisted of an eutectic mixture of Zn and Mg_2Zn_{11}. Moreover, the slight increase in Mg concentration in the darker regions after heat treatment may suggest that the composition of Mg_2Zn_{11} phase after heat treatment was closer to its theoretical composition under equilibrium conditions. This is consistent with the experimentally observed dissolution of Mg-rich globules that formed after casting. Thereby, the homogenization heat treatment was expected to have promoted atomic diffusion, such that Mg atoms enriched the Mg_2Zn_{11} phase, providing a composition closer to that of the equilibrium phase. The microstructural evolution from the as-cast to the homogenized condition resulted in a hardness decrease from ~139 to ~109 HV, respectively.

5.2.2. Effect of HPT processing on the microstructure and hardness evolution

The microstructure of the as-homogenized Zn-3Mg alloy after HPT consisted of a matrix of grains with sizes in the range of ~ 100-300 nm, as observed in Figure 28 (a). Analysis of the corresponding SAD pattern in Figure 28 (b-c) indicated that the microstructure consisted of a combination of Zn and Mg_2Zn_{11} phases. From the STEM images in Figure 28 (d-e), the uniform contrast level of the coarser grains suggested that they may correspond to relatively dislocation-free grains that underwent DRX during HPT processing. On the other hand, the varying contrast levels observed inside the finer grains may indicate the presence of nanoscale intermetallic phases responsible for the impingement of their grain boundaries. In particular, the contrast differences across the HAADF-STEM image in Figure 28 (e) indicated that the bright and dark areas were associated with Zn and Mg_2Zn_{11} phases, respectively. Therefore, the coarser grains with uniform contrast were identified as Zn, whereas the darker regions with non-uniform contrast were

suggested to be clusters of nanosized Mg_2Zn_{11} phases, in agreement with the nanosized domains highlighted in Figure 28 (f). In addition, the darker appearance of the grain boundaries may indicate grain boundary segregation of the Mg_2Zn_{11} phase during HPT processing. Alternatively, it may also be possible that the non-uniform contrast inside the darker areas corresponded to dislocation networks within nanosized Mg_2Zn_{11} grains, as dislocations would appear bright in HAADF mode [203], although this was not confirmed in this study. The microstructural observations of the alloy after HPT above from TEM/STEM imaging were consistent with those from a normal plane through BSE-SEM imaging in Figure 30. In support of the above discussion, nanosized Mg_2Zn_{11} phases were identified in the Zn matrix via APT, as shown in Figure 29.

The evolution from a coarse lamellar microstructure after the homogenization heat treatment to an ultrafine-grained microstructure with a GS_{ave} of 210 nm after HPT processing for 30 turns had an effect on the material hardness. The average hardness in the as-homogenized condition (~ 109 HV) increased to ~139 HV after HPT processing for 30 turns, which was mainly related to the Hall-Petch strengthening due to the severe grain size refinement. Another factor that may have played a role in the increased material hardness after HPT is the development of a strong basal texture, as observed in Figure 32, which could have led to the activation of non-basal slip systems, with higher critical resolved shear stress, according to a previous work on HPT-processed Zn [180]. Since both the as-homogenized and HPT-processed samples consisted of Zn and Mg_2Zn_{11}, the observed hardness increase could not be associated with the formation of any additional phase. Nevertheless, the fact that the Mg_2Zn_{11} intermetallic phase, which is substantially harder than Zn [15], fragmented into nanosized phases after HPT, led to a significant increase in the surface area of the Mg_2Zn_{11} phases. This phenomenon may have hindered dislocation motion during plastic deformation, increasing the material hardness. Figure 34 shows that the hardness distribution was

relatively uniform between ~ 130-150 HV across the sample after HPT, with the exception of r < 1 mm. This suggested that the shear strain accumulated after 30 turns for r > 1 mm (i.e., ~ 230) was sufficient to reach a uniform microstructure across the entire sample except in the near central region, where the plastic deformation occurs less severely, as this location is close to the rotation axis during HPT processing.

5.2.3. Effect of PDA on the microstructure and hardness evolution

After PDA, the grain size increased from ~ 100-300 nm to ~ 600-800 nm, as observed in Figure 98 (a), and the microstructure appeared to be precipitate-free, as observed in Figure 35 (b). This may indicate that in addition to the grain growth of the Zn matrix after PDA, the nanosized Mg_2Zn_{11} phases, which were suggested to be clustered between neighboring Zn grains and along the grain boundaries after HPT, diffused during PDA and coalesced into Mg_2Zn_{11} grains.

The latter hypothesis would be consistent from a thermodynamically viewpoint, since the decrease of Mg_2Zn_{11} surface area from nanosized phases to coarser grains would result in a lower energy state configuration, which would represent a more energetically favorable condition closer to the equilibrium. In support of this argument, the area fractions of Zn and Mg_2Zn_{11} phases were estimated as 0.59 and 0.41, respectively, which were reasonably close to the theoretical equilibrium volume fractions of 0.57 for Zn and 0.43 for Mg_2Zn_{11} estimated using the lever rule for the Zn-3Mg (wt. %) composition highlighted in the binary Zn-Mg equilibrium phase diagram shown in Figure 96.

As observed in Figure 98 (b), no significant difference in the distribution of misorientation angles was identified in the Zn-3Mg alloy before and after PDA, with a peak at ~ 30-35 º in both cases, which was associated with basal texture [180,204].

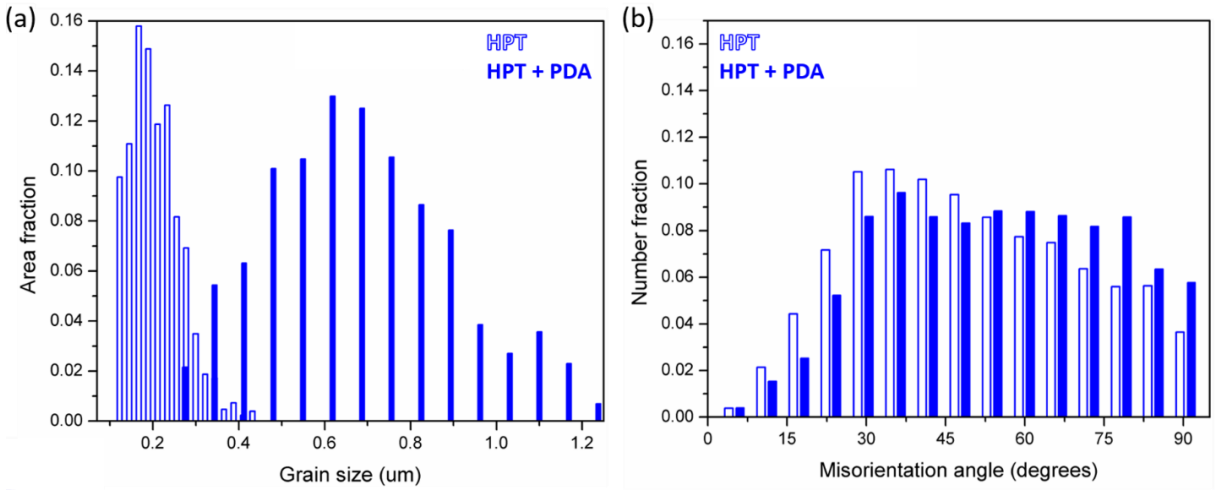

Figure 98: Comparison of the distributions of (a) grain size and (b) misorientation angle obtained from the Zn-3Mg alloy after HPT for 30 turns (i.e., HPT) and subsequent PDA (i.e., HPT + PDA). Adapted from [127].

Though phase analysis was not performed in the Zn-3Mg alloy after PDA, the formation of additional strengthening phases was not expected based on the hardness measurements provided in Figure 39, where an average hardness of ~ 136 HV was found across the disc, which was similar to that after HPT (~ 139 HV). However, unlike the relatively uniform hardness distribution across the sample radius after HPT, the average hardness after PDA increased with increasing distance from the center, as observed in Figure 39, which is consistent with the shear strain evolution during HPT provided in Equation 1 in section 2.2.1. The reason why the central region, at $r < 1$ mm, became softer with an average hardness of 110-120 HV after PDA may be associated with recrystallization and grain growth. These stages of the annealing processes may become more difficult with increasing accumulated plastic strain, where recovery may be dominant, such that the microstructure reduces the stored energy by rearrangement of dislocations. However, the presence of hard Mg_2Zn_{11} grains in the peripheral region, at $r > 4$ mm, after PDA may have also restricted grain growth to some extent, hence, leading to a slightly higher average hardness of ~ 145-150 HV.

Earlier works [205–207] have investigated the degree of strain hardening in different alloys after HPT processing through the calculation of the hardenability exponent (η), obtained from the slope of the Vickers microhardness (HV) values plotted against the equivalent strain (ε_{eq}) in natural logarithm axes. The same approach was used to evaluate the evolution of the strain hardening capability of the alloy after HPT and PDA, and they are plotted in Figure 99. The η values were estimated as 0.017 and 0.056 after HPT and HPT+PDA, respectively. The higher η value after HPT + PDA is a consequence of the lower hardness values recorded at lower equivalent strains (i.e., closer to the disk center) as compared to the sample after HPT. Overall, the η values presented were similar to those reported from HPT-processed ZK60 (η = 0.07) [207] and AZ31 (η = 0.08) [206].

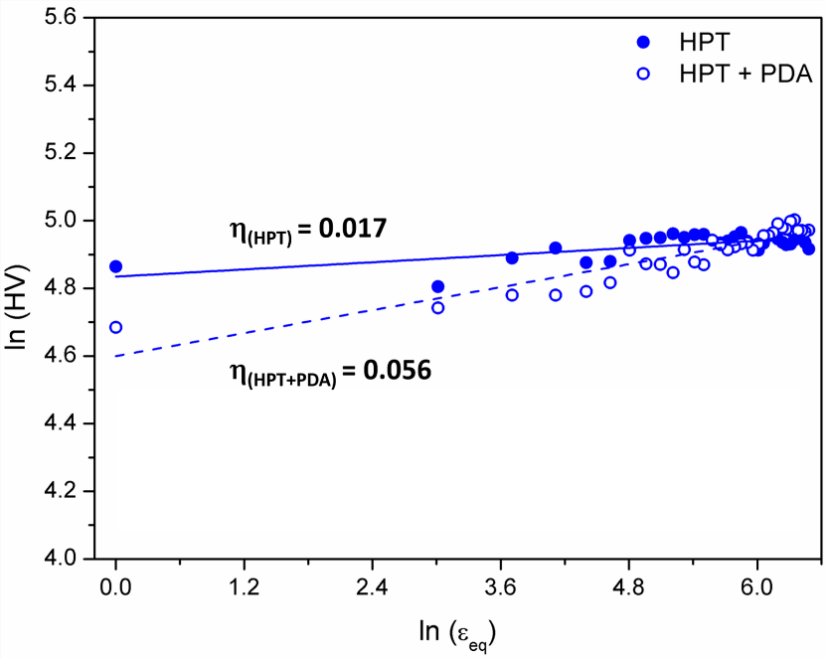

Figure 99: Natural logarithm plot of the Vickers microhardness, HV, against equivalent strain, ε_{eq}, from the as-homogenized Zn-3Mg HPT alloy after HPT for 30 turns, and after HPT for 30 turns + PDA (200 ºC, 1h). Solid and dashed blue lines indicate the linear regressions to obtain the slopes corresponding to the hardenability exponent, η, presented after HPT and HPT + PDA.

5.3. Zn-3Mg hybrids

This section discusses the microstructural and hardness evolutions of the Zn-3Mg hybrids after HPT and subsequent PDA. In addition, a plastic deformation model is proposed based on the nanoindentation results, and the evolution of the strain hardening capability during HPT is investigated. The effects of HPT and PDA on the Zn-3Mg hybrids will be compared with those on the Zn-3Mg alloy in sections 5.4 and 5.5.

5.3.1. Effect of HPT processing on the microstructure and hardness evolution

The cross-sectional SEM images presented in Figure 51, the peripheral regions, at r > 3 mm, of the Zn-3Mg hybrid after 30 turns presented a uniform contrast, which suggested a good mixing of Zn and Mg phases at the regions of highest plastic deformation. This may be associated with a relatively uniform composition in these areas. In agreement with this, the EDS map analysis performed at this disk periphery after 30 turns, see Figure 52, led to an average chemical composition of 96.9Zn-3.1Mg (wt. %), with an uniform elemental distribution of Zn and Mg. Therefore, this area of the sample became the focus of the subsequent investigations.

The microstructural features reported in section 4.3.1 from the periphery of the Zn-3Mg HPT hybrids after 30 turns were consistent between SEM and TEM/STEM analysis, from Figure 53 and Figure 54, respectively. Given that SEM and TEM imaging was performed in perpendicular planes, it was suggested that the equiaxed grains with GS_{ave} of ~ 100-200 nm truly corresponded to a uniform equiaxed microstructure that may form due to DRX during HPT. The formation of vortex-like features observed by SEM in Figure 53 has been associated in the literature [208] with turbulent flow at the interface between phases with similar levels of hardness, which is the case of Mg and Zn. The presence of nanosized precipitates observed in the STEM images, which had a

lower atomic number than the Zn-matrix according to the HAADF image, were related to the Mg_2Zn_{11} and $MgZn_2$ intermetallic phases identified by XRD in Figure 55.

Based on the relative peak intensities of the XRD scans obtained from the Zn-3Mg HPT hybrids in Figure 55, it was suggested that the intermetallic phase fractions increased, whereas that of the Mg phase decreased, from 15 to 30 turns. This is in good agreement with the larger phase fractions of intermetallics quantified from Rietveld refinement in the Zn-10Mg HPT hybrids and thus, suggested that the deformation-enhanced atomic mobility during HPT promoted the phase transformation from Mg to Mg_2Zn_{11} and $MgZn_2$ intermetallic phases.

In addition to the identification of the Mg_2Zn_{11} intermetallic phase by APT, a nanosized volume with homogeneous composition of 99.2Zn-0.3Mg (at. %) was found in the APT needle examined. It should be noted that the maximum solubility of Mg in Zn is ~ 0.3 (at. %) at 370 ºC [209], and that it is practically negligible at RT. This suggested that the region with 99.2Zn-0.3Mg (at. %) composition may be associated with the formation of a metastable supersaturated solid solution in the Zn-Mg system during HPT. This would indicate that HPT is able to extend the solid solubility between Zn and Mg, which are essentially immiscible at RT. Processing by HPT has been demonstrated to lead to the formation of supersaturated solid solutions in multiple metal systems, like Fe-Cu [210], Cu-Cr [211], Cu-Co [212], Cu-In [213], and Al-Mg [214].

The hardness along the cross-section of the Zn-3Mg hybrids increased notably from 1 to 30 turns, as observed in Figure 60. This is suggested to be due to both severe grain refinement and the formation of intermetallic compounds with increasing number of turns. The sample after 1 turn displayed a uniform average hardness of ~ 39 HV across the diameter, which was very similar to that of pure Zn and pure Mg (i.e., 36 HV and 35 HV, respectively). This suggests that, after 1 turn,

the maximum shear strain (ε_{eq} ~ 20) was insufficient to cause significant grain size refinement and phase mixing leading to the formation of hard intermetallic compounds. This argument is supported by the absence of intermetallic compounds in the XRD spectrum after 1 turn, as shown in Figure 55.

After 5 and 15 turns, the hardness increased with increasing distance from the sample center, where the hardness remained similar to that of the pure Zn and pure Mg. This trend is consistent with the shear strain relationship provided in Equation 1, which indicates that the plastic deformation of the HPT sample increases radially, and that it is theoretically zero at the sample center. Therefore, the higher plastic strains near the periphery are expected to produce finer grain sizes, leading to Hall-Petch strengthening. The gradient of shear strains across the sample is also expected to influence the hardness evolution from the sample center to the periphery, such that a larger gradient would lead to more pronounced hardness differences.

The range of equivalent strains after 15 turns ($0 < \varepsilon_{eq} < 320$) was notably larger than after 5 turns ($0 < \varepsilon_{eq} < 107$), which led to larger hardness differences across the sample. Consequently, the near central region with hardness values close to that of pure Zn and pure Mg became larger after 5 turns ($r < 2$ mm) than after 15 turns ($r < 0.5$ mm). Whereas after 5 turns the modest hardness increase is proposed to be dominated by grain size refinement, after 15 turns, both grain size refinement and intermetallic strengthening are expected to play a role in the hardening mechanism. Both Mg_2Zn_{11} and $MgZn_2$ intermetallic phases were identified after 15 turns in the Zn-3Mg hybrids, as observed in Figure 55. Although XRD analysis was not performed after 5 turns in Zn-3Mg hybrids, the formation of intermetallic compounds may not be expected, according to the XRD profile of the Zn-10Mg hybrids in Figure 45.

After 30 turns, the sample reached a more uniform average hardness distribution (~ 120-180 HV) across the sample than that after 15 turns (~ 40-160 HV), as observed in Figure 61. In general, the hardness values were larger after 30 turns than after 15 turns. As the accumulated plastic strain increased with increasing number of turns, the strain hardening propagated from the periphery to the center, as observed in the gradient-type hardness evolution in Figure 60. After 30 turns, the strain-hardening reached the center of the sample, and therefore, the hardness values at the central region were no longer similar to those of pure Zn and pure Mg.

The maximum hardness values after 30 turns were recorded at r ~ 3 mm (ε_{eq} ~ 384), at both sides of the sample, instead of at the edges of the sample (r ~ 5 mm) like after 15 turns. After 30 turns, the regions at 3 < r < 5 mm presented lower hardness values (see Figure 61), which might indicate a saturation of the grain refinement process and subsequent increase of the GS_{ave}. This hardness saturation at an intermediate region in the sample is consistent with that reported by Li et al. [215] from HPT-processed W and was related to CDRX. CDRX is a recovery dominated process that proceeds by continuous absorption of dislocations in LABs, followed by a subsequent increase of their misorientation angles and the formation of new finer grains with non-equilibrium HABs. This process continues up to a maximum equivalent strain, above which the ultrafine-grained microstructure cannot be longer refined. At this point, the newly generated dislocations within the grain interiors, as well as those forming the non-equilibrium HABs, prefer to transfer from a metastable state to a more equilibrium state with lower energy by rearranging into larger grains [216]. Thus, a grain growth may be expected when the equivalent strain in the material exceeds a critical value, which seems to be ε_{eq} ~ 384 for the Zn-3Mg hybrid system. This grain growth beyond the saturation point could then be responsible for the decrease in hardness observed after 30 turns for r > 3 mm.

5.3.2. Effect of PDA on the microstructure and hardness evolution

The cross-sectional SEM images from the Zn-3Mg hybrid before PDA (i.e., HPT: 30 turns) and after PDA (i.e., HPT: 30 turns + PDA) in Figure 100 (a) shows that the large Mg-rich phases present near the central region of the sample after HPT for 30 turns were no longer distinguishable after PDA. As observed in Figure 100 (b), the hardness distribution after PDA did not change significantly, as compared to the sample after HPT. Softening was only observed after PDA at r < 0.5 mm, where average hardness values dropped from ~ 110 HV to ~ 90 HV as compared to the sample after HPT. However, the peripheral regions of the sample after PDA, r ~ 3-5 mm, exhibited an average higher hardness than that after HPT. In addition, the hardness saturation phenomenon observed after 30 turns at r ~ 3 mm, which was described in the previous section, was not that evident after PDA.

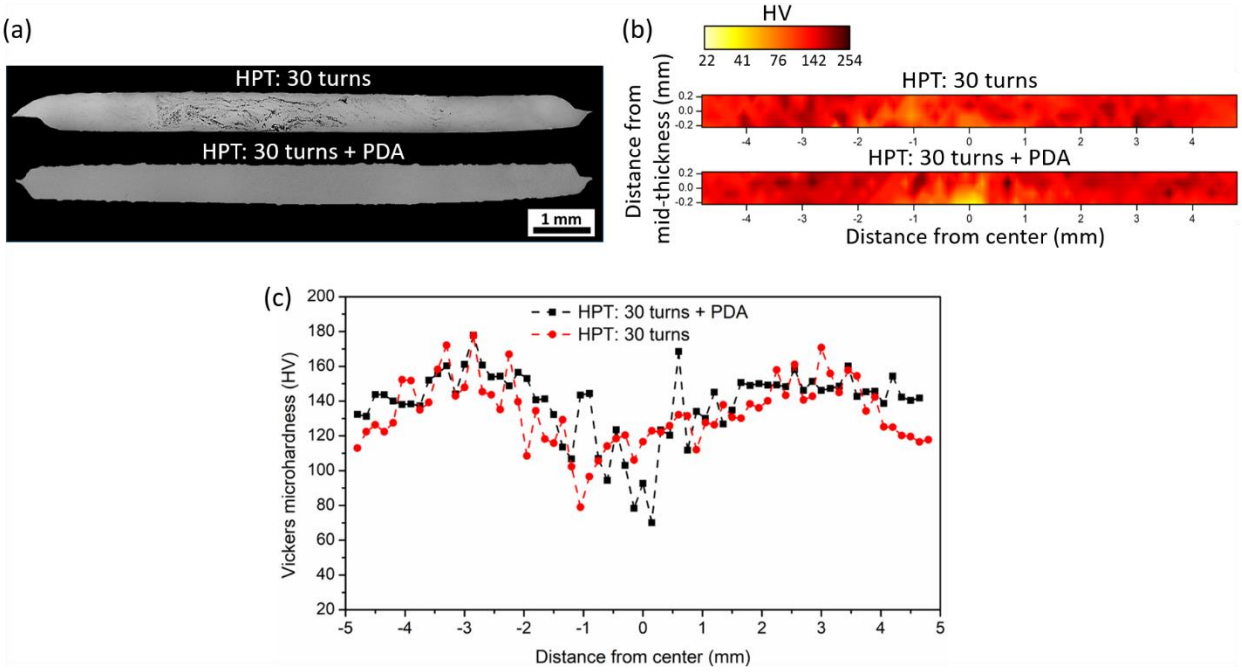

Figure 100: Comparison between Zn-3Mg hybrids after HPT for 30 turns, and HPT for 30 turns + PDA (200 ºC, 1h): (a) cross-sectional SE-SEM images, (b) corresponding color-contour HV maps, (c) evolution of the average HV along the diameter of the sample. Adapted from [127].

From Figure 100 (c), it is apparent that the right-half of the sample after PDA presented a uniform hardness of 150-160 HV for r > 1.5 mm, whereas the left-half does show a drop of the average hardness from ~160 to ~140 HV at r > 3.5 mm, although it is not as large as that of the sample after HPT (i.e., from ~180 to ~110 HV). This suggests that the microstructural evolution occurring during PDA near the sample periphery, which is detailed in the next paragraph, might be responsible for diminishing the grain growth despite the enhanced diffusion at higher temperature.

The microstructural features reported in section 4.3.2 from the periphery of the Zn-3Mg HPT hybrids after 30 turns + PDA were consistent between SEM and TEM/STEM analysis, from Figure 65 and Figure 66, respectively. These images suggested that the relatively equiaxed microstructure with uniform grain sizes of ~ 100-200 nm obtained after HPT for 30 turns, transformed after PDA into a bimodal grain size distribution of larger Zn-rich grains with a GS_{ave} of ~ 600-900 nm and smaller Mg-rich grains with a GS_{ave} of ~ 100-200 nm. This microstructural evolution can be observed by comparing the TEM microstructures in Figure 101 (a) and (c).

From the HAADF images in Figure 101 (b) and (d), it is apparent that after PDA, the finer Mg-rich grains (i.e., darker contrast) contained lighter nanoprecipitates predominantly segregated in these areas, instead of evenly distributed across the microstructure like after HPT. These nanoprecipitates present in the Mg-rich grains were identified as Mg_2Zn_{11} and $MgZn_2$ intermetallic phases from FFT analysis of HRTEM images in Figure 68. Therefore, it was suggested that the segregation of Mg_2Zn_{11} and $MgZn_2$ nanoprecipitates in the finer Mg-rich grains was assisted by enhanced diffusion during PDA, such that they acted as pinning sites preventing grain growth, hence, leading to the bimodal distribution. The complementary roles of the coarser Zn-rich grains and the finer Mg-rich grains during plastic deformation, in relation to the resulting mechanical properties, are discussed in section 5.3.4.

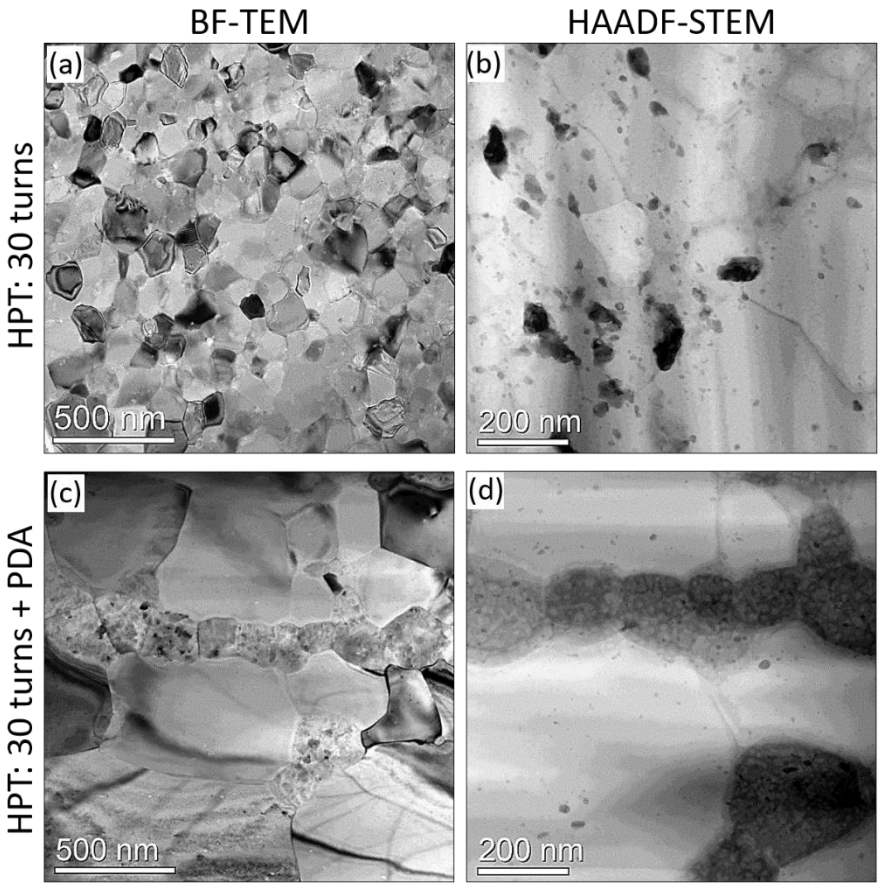

Figure 101: Comparison of TEM/STEM images acquired near the periphery at the cross-section of the Zn-3Mg hybrids after HPT for 30 turns (a, b) and HPT for 30 turns + PDA (c, d). BF-TEM and HAADF-STEM images are presented in the left and right columns, respectively. The horizontal and vertical directions in the image correspond to the shear and thickness directions in the sample, respectively, as defined in Figure 12. Adapted from [127].

The evolution of the grain size and misorientation angle distributions after PDA can be observed in Figure 102 (a) and (b), respectively. An overall increase of the GS_{ave} and the width of the GS distribution after PDA is apparent from Figure 102 (a), which is consistent with the TEM observations above. Some differences were identified in the misorientation distributions before and after PDA in Figure 102 (b). The fractions of misorientation angles at ~ 30 º, related to basal fiber texture in Zn and Mg [180,204], decreased after PDA, in agreement with the weakening of the basal pole figures shown in Figure 58 and Figure 71. Moreover, the deviation of the basal poles away from the {0001} normal, found in the Zn and Mg phases after PDA, were consistent with

the observations reported by Zeng et al. [217] in a Mg-Zn alloy after annealing. In addition, the larger I_{max} value of the Mg phase, compared to that of the Zn phase, suggested that the Mg phase may have a greater influence on the basal texture weakening after PDA. In support of the latter statement, as observed in Figure 102 (b), the PDA treatment led to a shift of misorientation angles towards higher values, exhibiting a peak at ~ 90 º, which is in good agreement with that of the Mackenzie misorientation distribution for a randomly oriented hexagonal crystal [218].

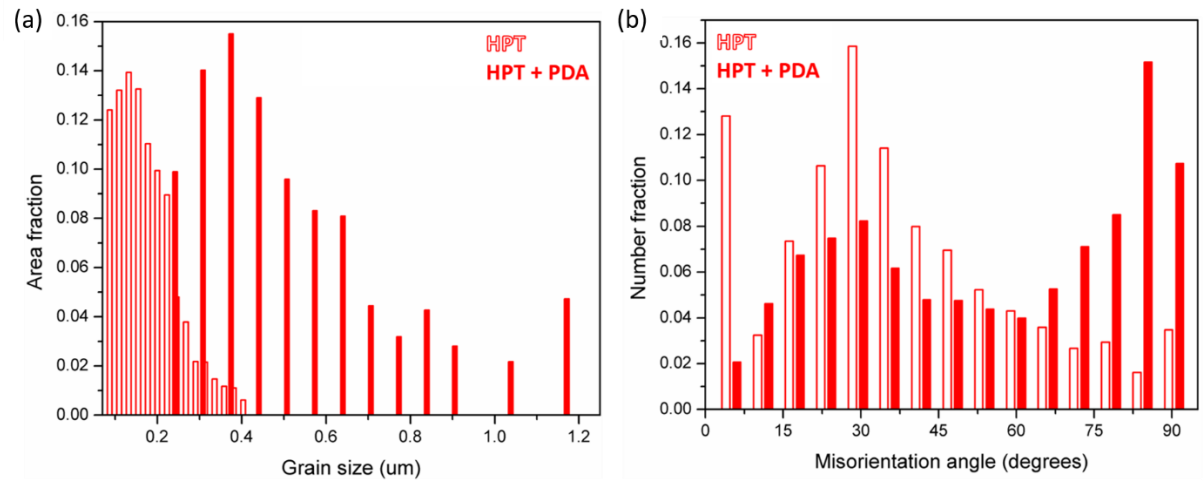

Figure 102: Comparison of the distributions of (a) grain size and (b) misorientation angle obtained from EBSD analysis of the Zn-3Mg hybrid after HPT for 30 turns (i.e., HPT) and subsequent PDA (i.e., HPT + PDA). Adapted from [127].

By comparison of the XRD profiles before and after PDA in Figure 103, a relative increase of the peaks associated with the Mg_2Zn_{11} phase and relative decrease of those related to the $MgZn_2$ phase were identified after PDA, which were rationalized from thermodynamic principles as follows. First, the composition of Mg_2Zn_{11} is 84.6Zn – 15.4Mg (at. %), whereas that of $MgZn_2$ is 67.5Zn – 32.5Mg (at. %), which implies that $MgZn_2$ requires about twice the amount of Mg atoms than Mg_2Zn_{11}. Second, the formation enthalpy of $MgZn_2$, $\Delta H^{eq}_{MgZn_2}$ ~ - 13.8 kJ/mol, is greater than that of Mg_2Zn_{11}, $\Delta H^{eq}_{Mg_2Zn_{11}}$ ~ - 8.96 kJ/mol at 298 K [37], which indicates that $MgZn_2$ contributes more energy to the overall system. Therefore, it was suggested that the thermal activation during PDA

promoted the decomposition of solute Mg atoms from $MgZn_2$ to Mg_2Zn_{11} by providing a lower energy state to the system closer to equilibrium, which is more thermodynamically favorable.

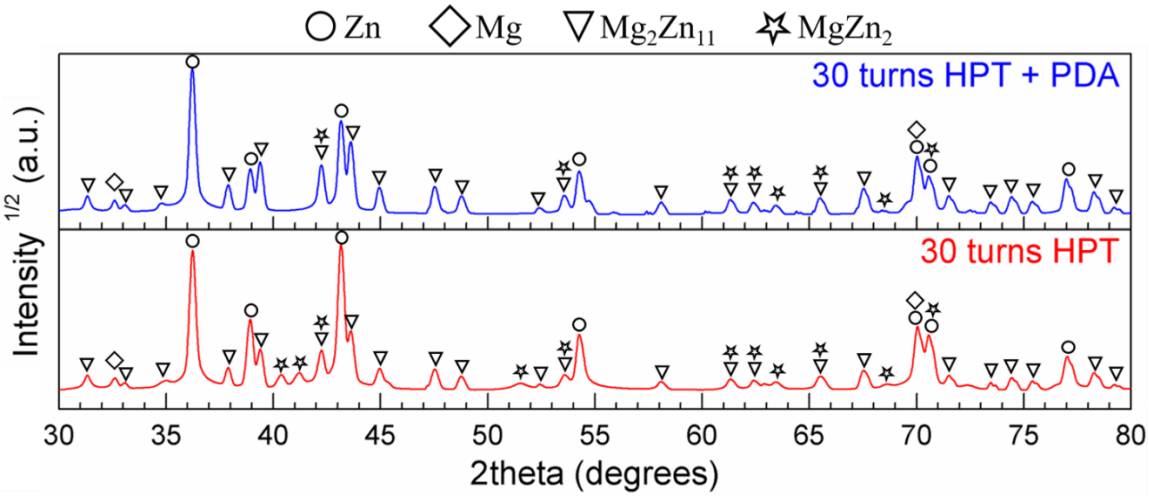

Figure 103: Comparison of the XRD patterns acquired at the mid-thickness plane of the Zn-3Mg hybrid after HPT for 30 turns, and subsequent PDA (200 ºC, 1h). Adapted from [127].

The phase transformation during PDA from $MgZn_2$ to Mg_2Zn_{11} phases proposed in the previous paragraph through the diffusion of Mg atoms may be supported by the results obtained from APT. A region with a uniform composition of 79.0Zn-20.7Mg (at. %) was measured at one side of the isoconcentration surface depicted in Figure 69. As mentioned earlier, the maximum solubility of Mg in Zn is ~ 0.3 (at. %) at 370 ºC [209], and it is practically negligible at RT. Therefore, since the measured composition is far beyond the equilibrium solubility limit of Mg in Zn, it is proposed to be related to a supersaturated solid solution (SSSS). It should be noted that the measured composition is far from the stoichiometric composition of any intermetallic compound in the Zn-Mg phase diagram (see Figure 96), and thus, cannot be attributed to any intermetallic phase. Therefore, the presence of this SSSS, together with the Mg_2Zn_{11} and $MgZn_2$ intermetallics, might be responsible for the high hardness measured near the periphery after PDA, despite the observed grain growth in the Zn-rich grains.

5.3.3. Effect of PDA on the nanoindentation behavior

The plastic instability reported from the load-displacement nanoindentation curves, both before and after PDA for all CSR values tested, was associated with the coexistence of grains and intermetallic compounds with varying compositions, sizes, and distributions. This was suggested based on the multiphase microstructures observed by SEM and TEM/STEM consistently, which may lead to large strain gradients during plastic deformation, consistent with the range of load-displacements obtained.

The formation of a bimodal microstructure at the periphery of the Zn-3Mg HPT hybrids after PDA resulted in a simultaneous increase in the H and m values, compared to after HPT for 30 turns, as observed in Figure 104. The enhancement of nanoindentation hardness after PDA for all the CSR values tested, which are presented in Table 13, was consistent with the higher hardness values measured by HV at the periphery of the sample after PDA, see Figure 100. The mean H values were always larger for the sample after PDA, and that the standard deviations did not overlap, with the exception of that at $\dot{\varepsilon} = 1.25 \cdot 10^{-4}\ s^{-1}$, indicating a significant difference between both samples in the H values.

Both samples exhibited an increase in H with increasing strain rate, which led to positive m values. This agreed with the general trend that metals tested at faster strain rates tend to exhibit smaller indentation displacements, and thus, lower plasticity since there is physically less time for dislocation motion, hence, lower plastic deformation [219].

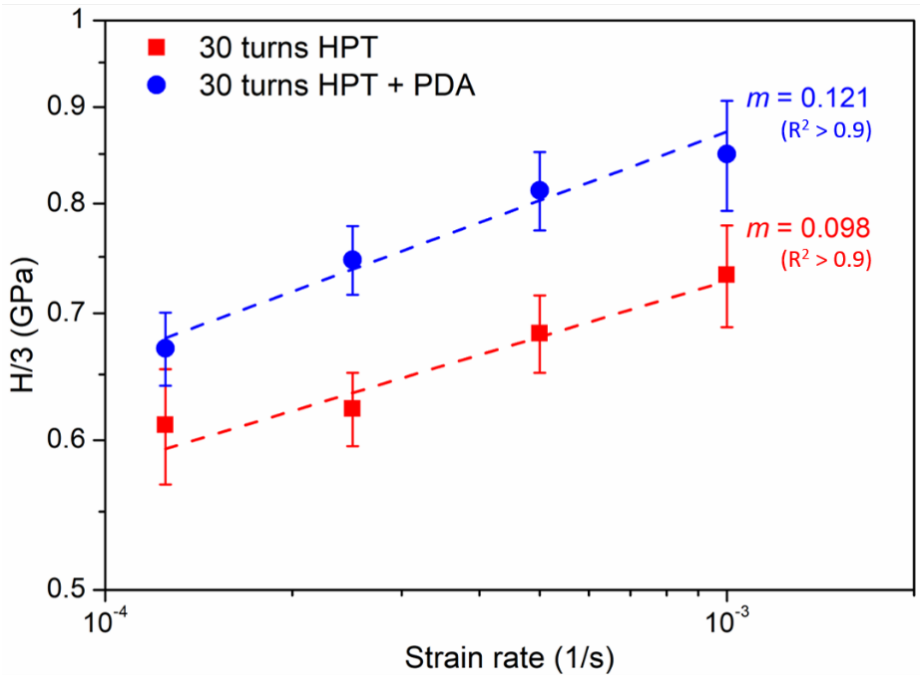

Figure 104: Comparison of the strain rate sensitivity (m) value calculated from nanoindentation in the Zn-3Mg hybrid after HPT for 30 turns, and after subsequent PDA (200 ºC, 1 h). Adapted from [127].

Table 13: Nanoindentation hardness (H) measured by nanoindentation at the periphery of the Zn-3Mg HPT hybrids after 30 turns, and after 30 turns + PDA (200 ºC, 1 h). The tabulated values correspond to those plotted in Figure 104. Adapted from [127].

$\dot{\varepsilon}$ (s^{-1})	H (GPa)	
	HPT: 30 turns	HPT: 30 turns + PDA
$1.25 \cdot 10^{-4}$	1.834 ± 0.129	2.012 ± 0.089
$2.50 \cdot 10^{-4}$	1.870 ± 0.083	2.242 ± 0.094
$5.00 \cdot 10^{-4}$	2.050 ± 0.096	2.440 ± 0.116
$1.00 \cdot 10^{-3}$	2.201 ± 0.136	2.550 ± 0.170

As observed in Figure 104, the value of m increased from 0.098 to 0.121 after PDA, which is consistent with the m increase reported in the Al-Mg HPT hybrid system after a different PDA treatment (300ºC, 1h). The significance of PDA for improving the overall ductility was demonstrated for HPT-processed Ti [119], and was attributed to an ordering of the non-equilibrium

dislocation structures leading to a more energetically favorable state without a significant grain growth. In addition, as reviewed recently [22], short-term annealing treatment was shown effective in numerous SPD-processed materials to reduce the dislocation density in the grain interiors, such that the dislocation storage capacity increases and thus, the strain hardening capability is enhanced, leading to increased ductility.

The V^* values estimated after HPT for 30 turns (~ 2.25 b^3) and subsequent PDA (~ 1.35 b^3) were in the range 1-10b^3, which was related elsewhere [220,221] to heterogeneous dislocation nucleation and grain boundary sliding, respectively. Thus, it was suggested that the slight but measurable decrease in V^* after PDA might be a consequence of the increased microstructural heterogeneity, evident from SEM/TEM imaging, where the dominant plastic deformation mechanism may be more associated with heterogeneous dislocation nucleation (i.e., since V^* is closer to 1b^3 than to 10b^3).

Based on the above discussion, the concurrent increase of H and m after PDA suggested a dual enhancement of the strength-ductility relationship, which is contrary to what was reported from HPT-processed metals having relatively uniform microstructures after PDA [222–224]. It should be noted that, although there was no direct measurement of the ε_f in the present study, there is a well-established correlation between ε_f and m, such that an increase in m would be associated with a higher ductility [225]. Indeed, multiple recent studies concerning HPT-processed materials with heterogenous microstructures after PDA have consistently reported a simultaneous increase in strength-ductility [226–228]. The concept of heterogeneous materials was recently introduced as a new class of materials with unprecedented mechanical properties, which exhibit a combination of strength and ductility that are not achievable by their homogeneous counterparts [229].

Heterostructured materials are characterized by multiscale domains, like grains or secondary phase particles [229], which were observed in the Zn-3Mg HPT hybrids after PDA. These domains may possess inherent strength differences, which will induce large strain gradients during severe plastic deformation. Therefore, the combined action of HPT and PDA in the Zn-3Mg hybrids was believed to be responsible for the dual enhancement of H and m.

The origin of the synergistic effect of PDA on the H-m relationship of the Zn-3Mg HPT hybrids was analyzed through the evolution of the unloading stiffness (S) and the displacement at peak load (h_{max}) from the load-displacement curves. Both S and hmax, defined in section 3.6.2, were calculated for the different strain rates, and their average values are plotted in Figure 105 (a) and (b), respectively, with their corresponding standard deviations indicated by the error bars. Both S and hmax decreased after PDA for all strain rates, and they also decreased with increasing strain rate. These observations were consistent with the positive m values reported, as both S and h_{max} are inversely proportional to H. Based on this, the individual effect of S and h_{max} values in the load-displacement behavior during nanoindentation are sketched in Figure 105 (c) and (d), respectively. The different theoretical mechanical responses proposed may be associated with materials with different hardness values as follows. On the one hand, as observed in Figure 105 (c), when S1 < S2, material 1 experiences larger elastic recovery during unloading, hence, exhibiting less plastic deformation, and consequently, it would be harder than material 2. On the other hand, as observed in Figure 105 (d), when $h_{max1} < h_{max2}$, material 1 requires less plastic strain to reach the peak load, and consequently, it would be harder than material 2. In these models, material 1 (i.e., blue color) represents the sample after HPT + PDA, whereas material 2 (i.e., red color) represents the sample after HPT.

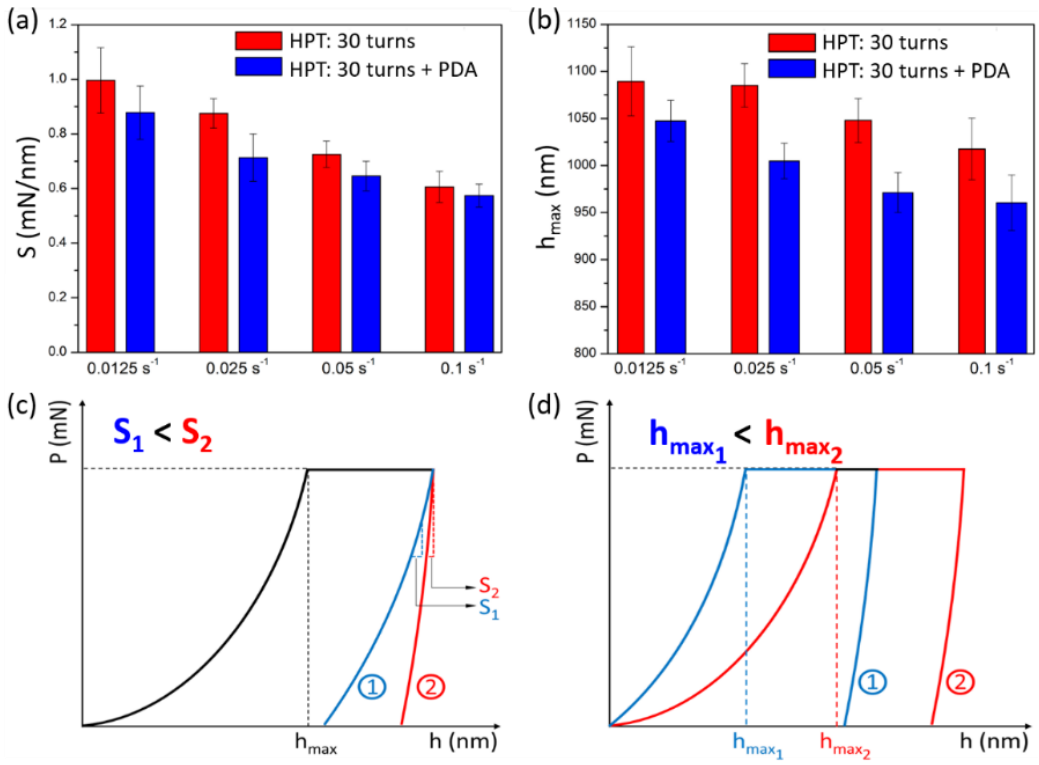

Figure 105: Evolution of (a) unloading stiffness, S, and (b) maximum displacement into surface, hmax, at increasing strain rates during nanoindentation testing of Zn–3Mg HPT hybrids after 30 turns and 30 turns + PDA (200 ºC, 1 h); Theoretical load-displacement responses of two materials having (c) different S values, and (d) different hmax values. Adapted from [127].

5.3.4. Plastic deformation model for an enhanced strength-ductility balance

Based on the earlier definition for heterostructured materials, the synergistic effect of PDA on the mechanical behavior of the Zn-3Mg HPT hybrids is proposed in Figure 106 due to the presence of hard and soft domains playing complementary roles during plastic deformation [229]. The coarser Zn-rich grains would be associated with the soft domain, while the finer Mg-rich grains containing nanoscale precipitates would correspond to the hard domain.

The proposed stress-strain curve in Figure 106 (a) for the Zn-3Mg HPT hybrid after PDA, associated with the heterogeneous material, is subdivided into three stages (i.e., stage I, II, and III), where each of the domains contribute in a different way to the deformation process. The strains

carried by the domains at stage I, II, and III are illustrated in Figure 106 (b), (c), and (d), respectively, where a darker red color indicates a higher strain.

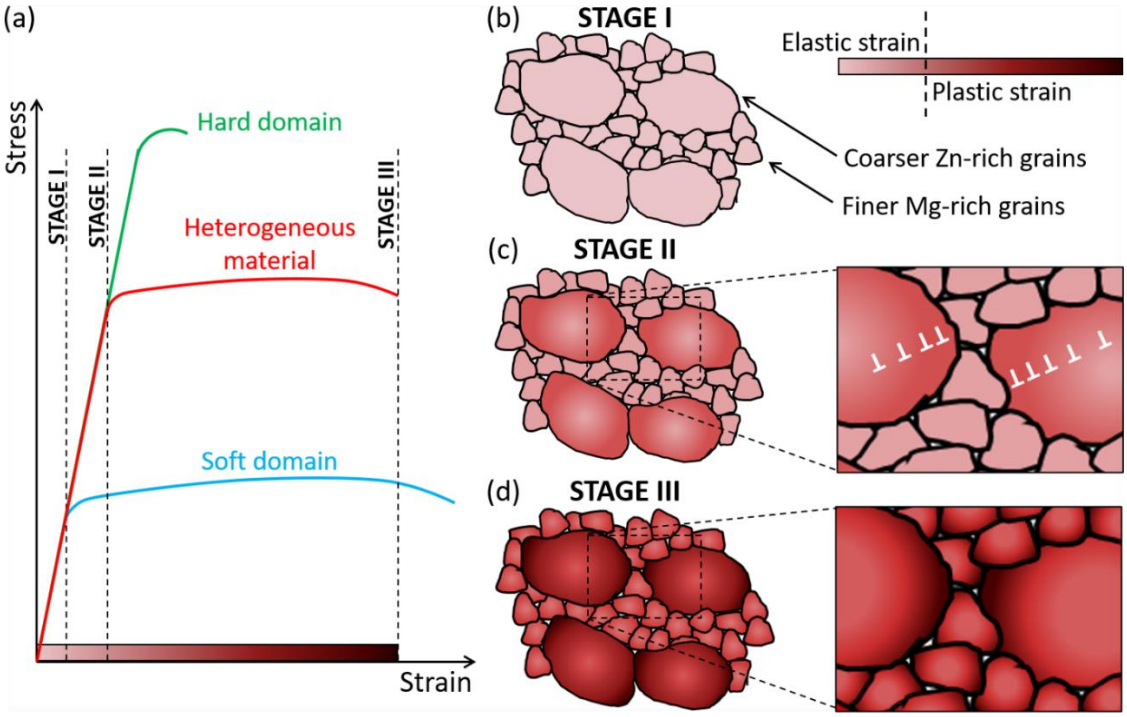

Figure 106: Proposed stress-strain behavior of the Zn-3Mg HPT hybrid after PDA (heterogeneous material) based on the complementary roles of the coarser Zn-rich grains (soft domain) and the finer Mg-rich grains (hard domain). The red stress-strain curve is subdivided into Stage I, II, and III, where the strains carried by each domain are sketched in (b), (c), and (d), respectively.

In Stage I, at low strains, both soft and hard domains will deform elastically, as indicated by the uniform light red color across the microstructure in Figure 106 (b).

In Stage II, the initial plastic deformation will be accommodated through dislocation slip on the soft domain, while the hard domains remain elastic. This will produce a mechanical incompatibility as the strain will be no longer continuous across the microstructure, resulting in a plastic strain gradient in the soft domains, as indicated by the color gradient in the coarser Zn-rich grains in Figure 106 (c). This strain gradient will be accommodated by geometrically necessary

dislocations (GNDs) that will pile-up at the soft domain, since they cannot transmit across the domain boundary, leading to a back-stress that will strengthen the originally soft phase.

In Stage III, plastic deformation will be accommodated by both hard and soft domains, and strain gradients are expected to exist near the domain boundaries, as sketched in Figure 106 (d). This will lead to neighboring domains sustaining different plastic strains and thus, producing back-stress strain hardening, which would be responsible for an enhanced ductility [230,231].

5.3.5. Analysis of the strain hardening capability

Earlier works [205–207] have investigated the degree of strain hardening in different alloys after HPT processing through the calculation of the hardenability exponent (η), obtained from the slope of the Vickers microhardness (HV) values plotted against the equivalent strain (ε_{eq}) in natural logarithm axes. The same approach was followed to evaluate the evolution of the strain hardening capability of the Zn–3Mg HPT hybrids up to 30 turns, which is shown in Figure 107 (a). Three distinct regimes were identified (i.e., Regime I, II, and III) in Figure 107 (b). Regime I, $0 < \ln(\varepsilon_{eq}) < 3.5$, equivalent to $\varepsilon_{eq} \sim$ 1-30. Regime II, $3.5 < \ln(\varepsilon_{eq}) < 6.0$, equivalent to $\varepsilon_{eq} \sim$30-400. Regime III, $6.0 < \ln(\varepsilon_{eq}) < 6.5$, equivalent to $\varepsilon_{eq} \sim$ 400-660. Linear fitting of the experimental data within each of these regimes revealed η values of 0.017, 0.535, and -0.668 for Regime I, II, and III, respectively. Regime I indicated limited strain hardening in the early stage of HPT, as compared to HPT-processed Ti–6Al–4V ($\eta = 0.031$) [205], ZK60 ($\eta = 0.07$) [207], AZ31 ($\eta = 0.08$) [206]. It was noted that the hardness of these three alloys saturated at $\ln(\varepsilon_{eq}) \sim 3$ during HPT. However, as observed in Regime II, the Zn-3Mg HPT hybrid did not reach hardness saturation in that range, but instead exhibited a significant increase in the strain-hardening capability, with a hardenability exponent of $\eta = 0.535$. It was noted that this η value was about one order of magnitude higher than

most reported values in the literature, followed by that from HPT-processed Al with η = 0.18 [206]. This notable increase in the strain hardenability was attributed to the contribution of multiple strengthening mechanisms during HPT, including severe grain refinement and precipitation of intermetallic compounds, both of which were evident from SEM/TEM imaging.

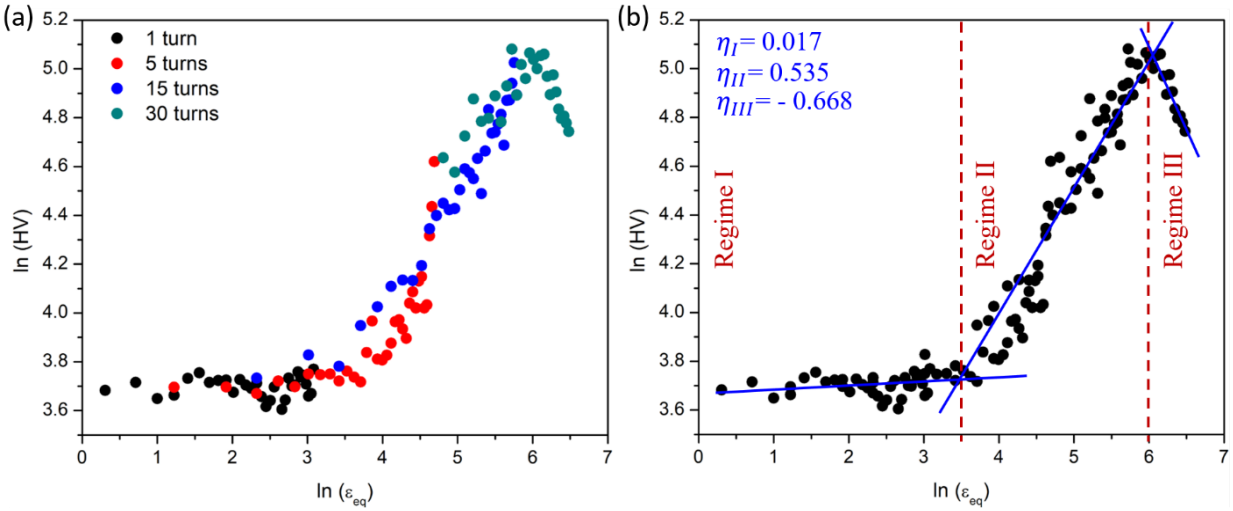

Figure 107: Natural logarithm plots of Vickers microhardness, HV, against equivalent strain, εeq, from the Zn-3Mg HPT hybrids (a) after 1, 5, 15, and 30 turns, and (b) determination of the hardenability exponent, η, in regimes I, II and III, delimited by red dash lines. Blue solid lines indicate the linear regressions to obtain the slopes corresponding to the η values presented. Adapted from [127].

The maximum hardness in the Zn-3Mg HPT hybrids was achieved at $\ln(\varepsilon_{eq}) \sim 6$, equivalent to $\varepsilon_{eq} \sim 400$, which marks the end of Regime II. Regime III shows that additional plastic strain resulted in strain softening, as indicated by a negative η value. This weakening behavior was also reported upon saturation in HPT-processed Al [206], where the ratio between the hardening and softening exponents was - 0.75, similar to that of - 0.80 found in the Zn-3Mg HPT hybrid system. This softening might be attributed to the saturation of grain size refinement after severe plastic deformation for 30 turns, where the large volume fractions of HABs present in the microstructure may promote grain boundary sliding at ambient temperature, leading to the high m value reported above, which might be in turn responsible for the proposed strength-ductility combination.

5.4. Effect of HPT + PDA on the microstructure of Zn-3Mg: hybrid vs. alloy

Both Zn and Mg_2Zn_{11} phases were found in the alloy and its hybrid counterpart after HPT and subsequent PDA. In addition, the Mg phase was also identified in the hybrid samples, as observed in the EBSD phase maps in Figure 108, where the amount of Mg in the inspected region seemed to be significantly greater than the nominal 3 (wt. %) targeted for the bulk composition. This could be rationalized by the following factors. First, there was a preferential distribution of Mg towards the regions of higher plastic deformation (i.e., sample periphery) during HPT processing, as it has been consistently reported in HPT hybrids of different compositions [25,86,87,89]. Second, the mid-thickness region of the cross-sections, where the EBSD scans were acquired, corresponded to the location where the original Mg disk was located.

Therefore, despite the extensive microstructural evolution observed during HPT, including phase mixing, grain refinement, and intermetallic formation, the mid-thickness region may still be more likely to be Mg-rich than the areas near to the sample surface. This was supported by an earlier study [232], which demonstrated that phase transformations in a HPT-processed Ti-Al-Nb alloy occurred predominantly at the near-surface regions rather than in the mid-thickness region, presumably due to a higher plastic strain at the sample surfaces.

It should be noted that the $MgZn_2$ phase found in the hybrid after HPT and PDA was not indexed in EBSD analysis, which might be due to the fact that it shares a hexagonal crystal structure with Zn and Mg, and the latter two phases were preferentially chosen by the EBSD software.

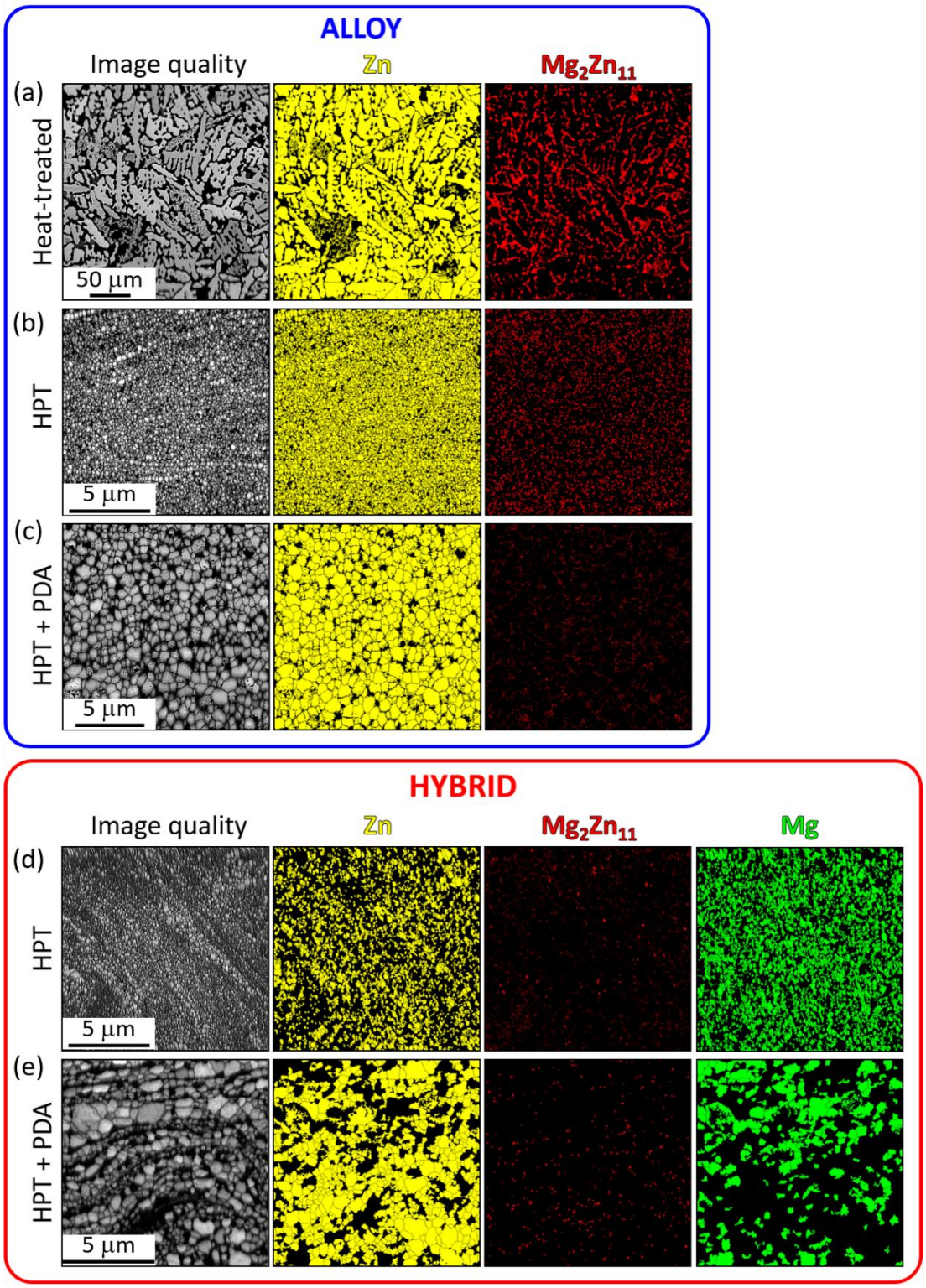

Figure 108: Image quality and phase maps acquired by EBSD near the periphery at the cross-section of the Zn-3Mg alloy after (a) homogenization heat treatment, (b) HPT for 30 turns, and (c) HPT for 30 turns + PDA; and from the Zn-3Mg hybrid after (d) HPT for 30 turns, and (e) HPT for 30 turns + PDA [124].

A comparative figure showing the distributions of GS and misorientation angles in the Zn-3Mg alloy and Zn-3Mg hybrid after HPT and PDA are presented in Figure 109. Regarding the grain refinement, HPT was similarly effective in refining the GS_{ave} of the alloy and the hybrid to ~ 200 nm, according to Figure 109 (a) and (c).

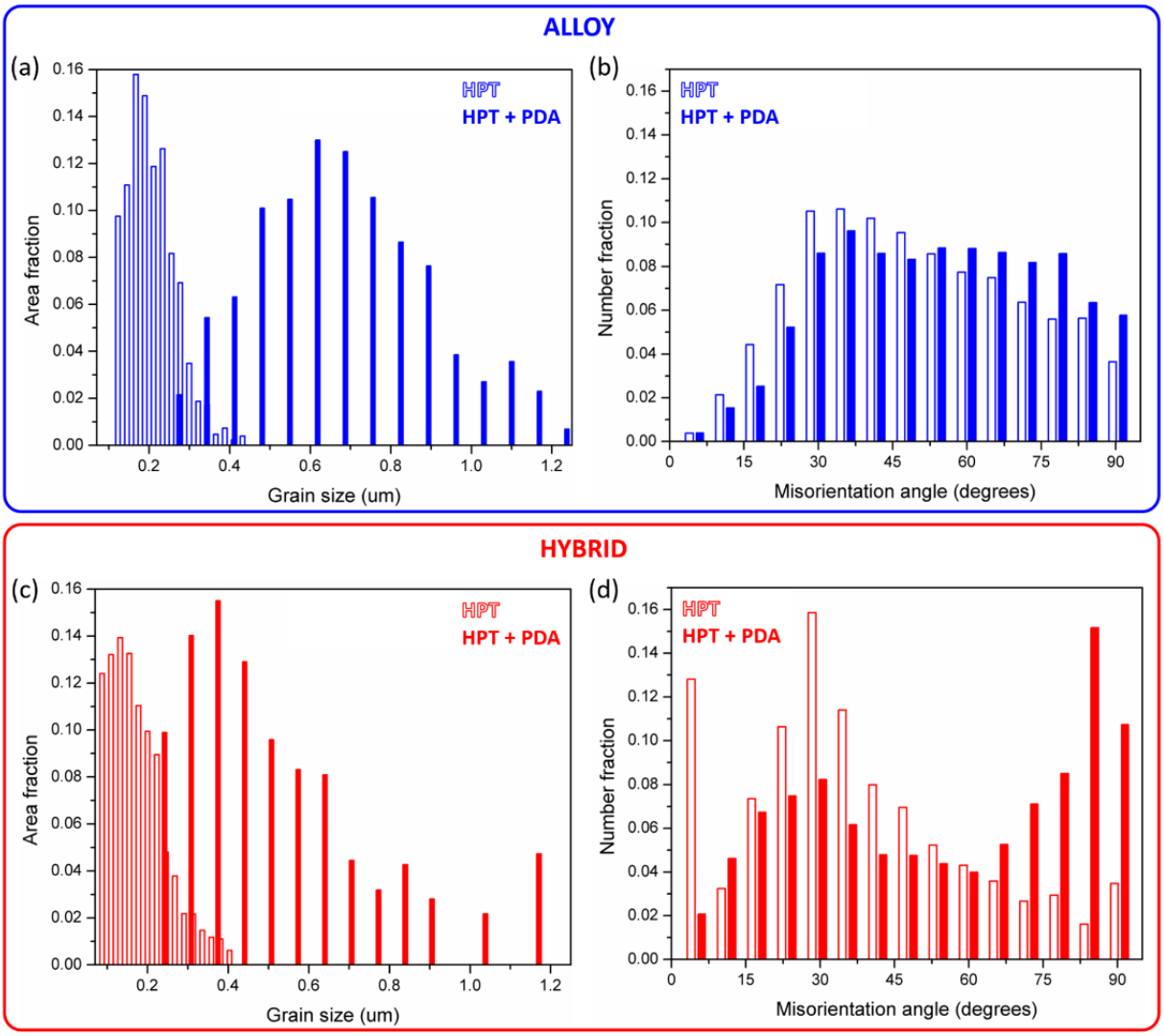

Figure 109: Grains size distributions and misorientation angle distributions obtained from EBSD analysis near the periphery at the cross-section of the Zn-3Mg (a-b) alloy and (c-d) hybrid after HPT for 30 turns, and HPT for 30 turns + PDA (200 ºC, 1 h) [124].

Despite an increase of the GS_{ave} in both material conditions after subsequent PDA, the alloy exhibited a larger GS_{ave} of ~ 700 nm, compared to that of the hybrid of ~ 400 nm. This was

correlated with the distinct microstructural features exhibited by the alloy and the hybrid after equivalent HPT + PDA as follows. The alloy exhibited relatively precipitate-free Zn and Mg_2Zn_{11} grains, with a wide range of sizes, uniformly distributed in the microstructure, which is consistent with the Gaussian distribution profile depicted in Figure 109 (a). On the other hand, the hybrid presented a microstructure containing coarser Zn grains and finer Mg-rich grains, which might be associated with a multimodal distribution of grains sizes in Figure 109 (c).

Regarding the distribution of misorientation angles, the overall large fractions of HABs found in the alloy and the hybrid after HPT were associated with DRX during HPT. The peak observed at ~ 30 º misorientation angle was attributed to the strong basal fiber texture developed in Zn and Mg after HPT observed in Figure 110 (a), (c), and (d), in agreement with other studies [180,204]. The significant decrease in the fraction of misorientation angles in the hybrid after PDA was associated with the weakening of the basal texture, as observed in Figure 110 (e) and (f). The deviation of the basal poles away from the {0001} normal, found in the Zn and Mg phases of hybrid after PDA, were consistent with the observations reported by Zeng et al. [217] in a Mg-Zn alloy after annealing. In addition, the notably larger I_{max} value of the Mg phase, compared to that of the Zn phase, suggested that the Mg phase may have a greater influence on the basal texture weakening in the hybrid after PDA. In support of the latter statement, as observed Figure 109 (d), the PDA treatment in the hybrid led to a shift of misorientation angles towards higher values, exhibiting a peak at ~ 90 º, which is in good agreement with that of the Mackenzie misorientation distribution for a randomly oriented hexagonal crystal [218].

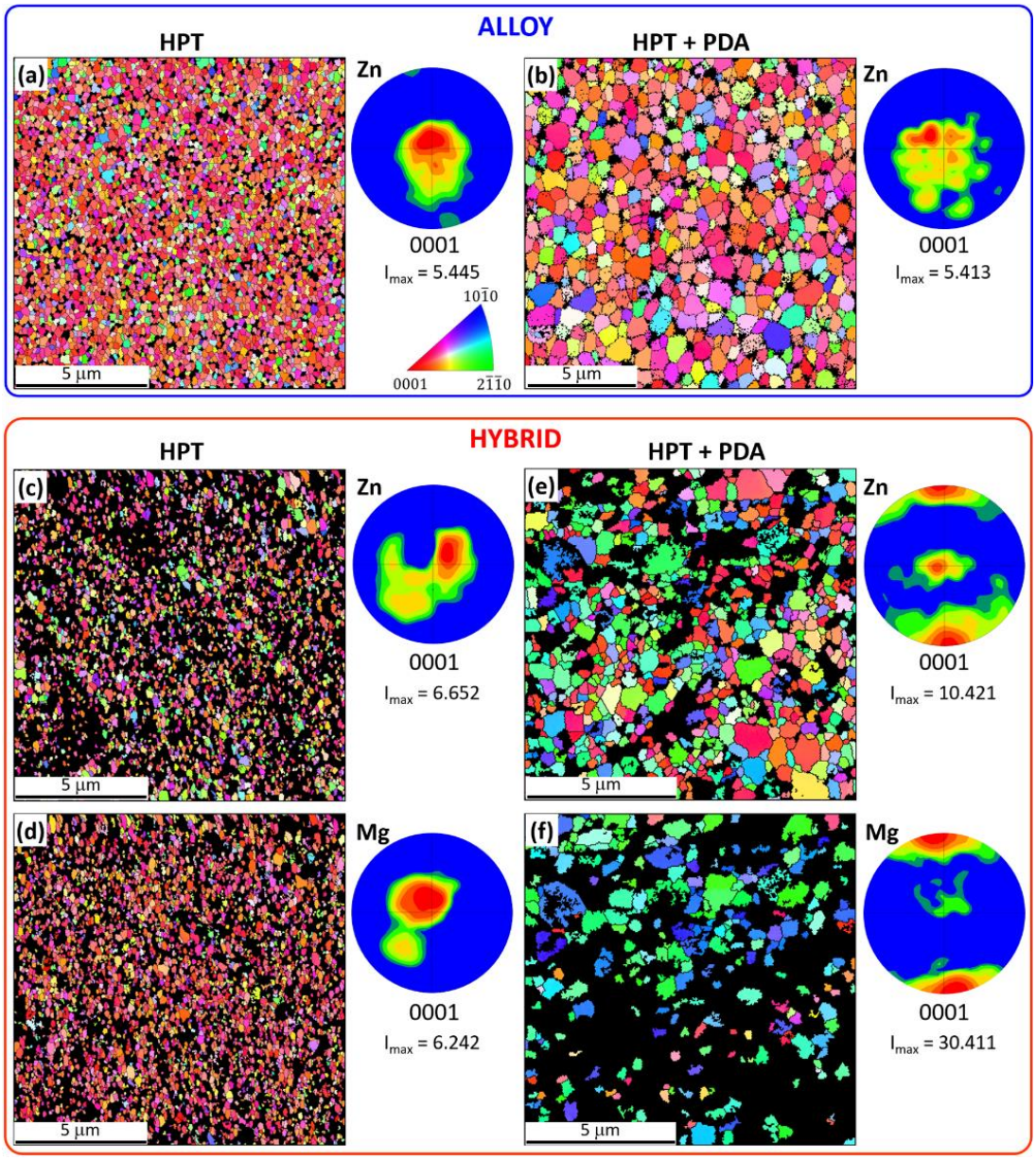

Figure 110: IPF orientation maps and corresponding basal pole figures acquired by EBSD near the periphery at the cross-section of the Zn-3Mg (a-b) alloy and (c-f) hybrid after HPT for 30 turns, and HPT for 30 turns + PDA. Imax values below the pole figures indicate the maximum texture intensity [124].

The corresponding KAM maps obtained from EBSD analysis of the Zn-3Mg alloy and hybrid are provided in Figure 111 (a-b) and (c-d), respectively, after HPT for 30 turns and subsequent PDA. It should be noted that the grains corresponding to both Zn and Mg phases were plotted together for the hybrid samples. On the one hand, the misorientation gradients in the alloy after HPT near

the grain boundaries may be related to the presence of the Mg_2Zn_{11} phases along the grain boundaries, as observed in the BF and HAADF STEM images in Figure 28 (d-e). On the other hand, the largest misorientation gradients presented in the hybrid after PDA could be a result of the increased microstructural heterogeneity. The differences in size and composition among the different domains (i.e., coarse Zn-rich grains and fine Mg-rich grains) in that heterostructure may lead to localized strain gradients, consistent with the deformation model proposed in section 5.3.4, which may be in turn responsible for the simultaneous increase of H and m.

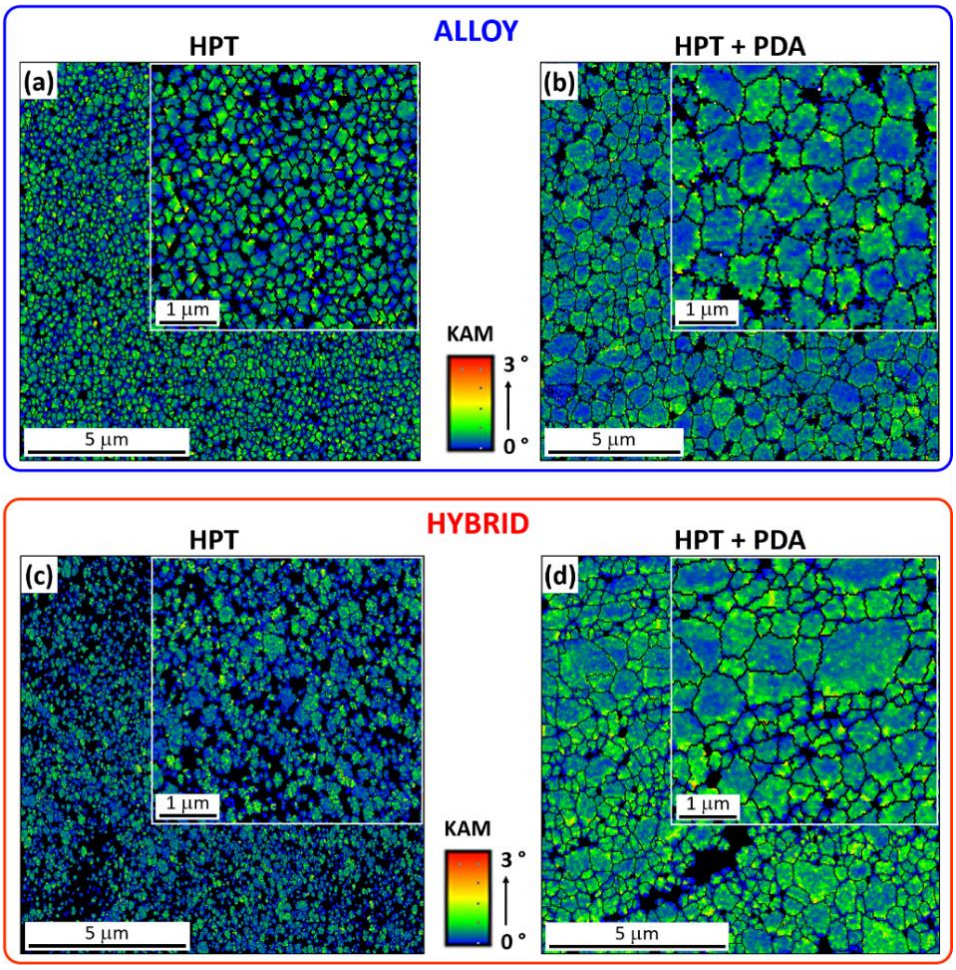

Figure 111: KAM maps acquired by EBSD near the periphery at the cross-section of the Zn-3Mg (a-b) alloy and (c-d) hybrid after HPT for 30 turns, and HPT for 30 turns + PDA [124].

5.5. Effect of HPT + PDA on the hardness of Zn-3Mg: hybrid vs. alloy

A comparison of the HV color-contour distribution maps and average HV values recorded across the radius of the Zn-3Mg alloy and Zn-3Mg hybrid after 30 turns HPT, and subsequent PDA are presented in Figure 112. It should be noted that the color scale used in the HV distribution maps, as well as the range of HV represented in the y-axis of the plots, are common for all the samples.

The hardness of the alloy after HPT remained uniform between 120-140 across the radius, with no significant hardness decrease closer to the sample center, suggesting that the microstructure may have reached a saturation point where the GS_{ave} of ~ 200 nm measured at the periphery may be constant across the sample. After PDA, the hardness was reasonably maintained along the sample, with a slight gradual decrease with decreasing distance from the center up to 100-120 HV at $r < 1$ mm. This may suggest that the GS_{ave} of ~ 600 nm measured at the periphery may be slightly larger near the sample center, which could result from the hard Mg_2Zn_{11} grains observed at the periphery preventing excessive grain growth during the annealing treatment.

Unlike the alloy, the Zn-3Mg hybrid after HPT and PDA presented highly heterogeneous hardness values across the radius. Due to the large standard deviations obtained from HV measurements collected at the same distance from the center, it is challenging to assess whether the alloy or the hybrid was harder in general terms. However, it is evident that significantly higher HV values were measured at specific regions in the hybrid sample. Since the GS_{ave} was similar in the hybrid and the alloy after HPT, the local regions associated with the highest HV values are suggested to be related to the nanosized Mg_2Zn_{11} and $MgZn_2$ intermetallic compounds identified.

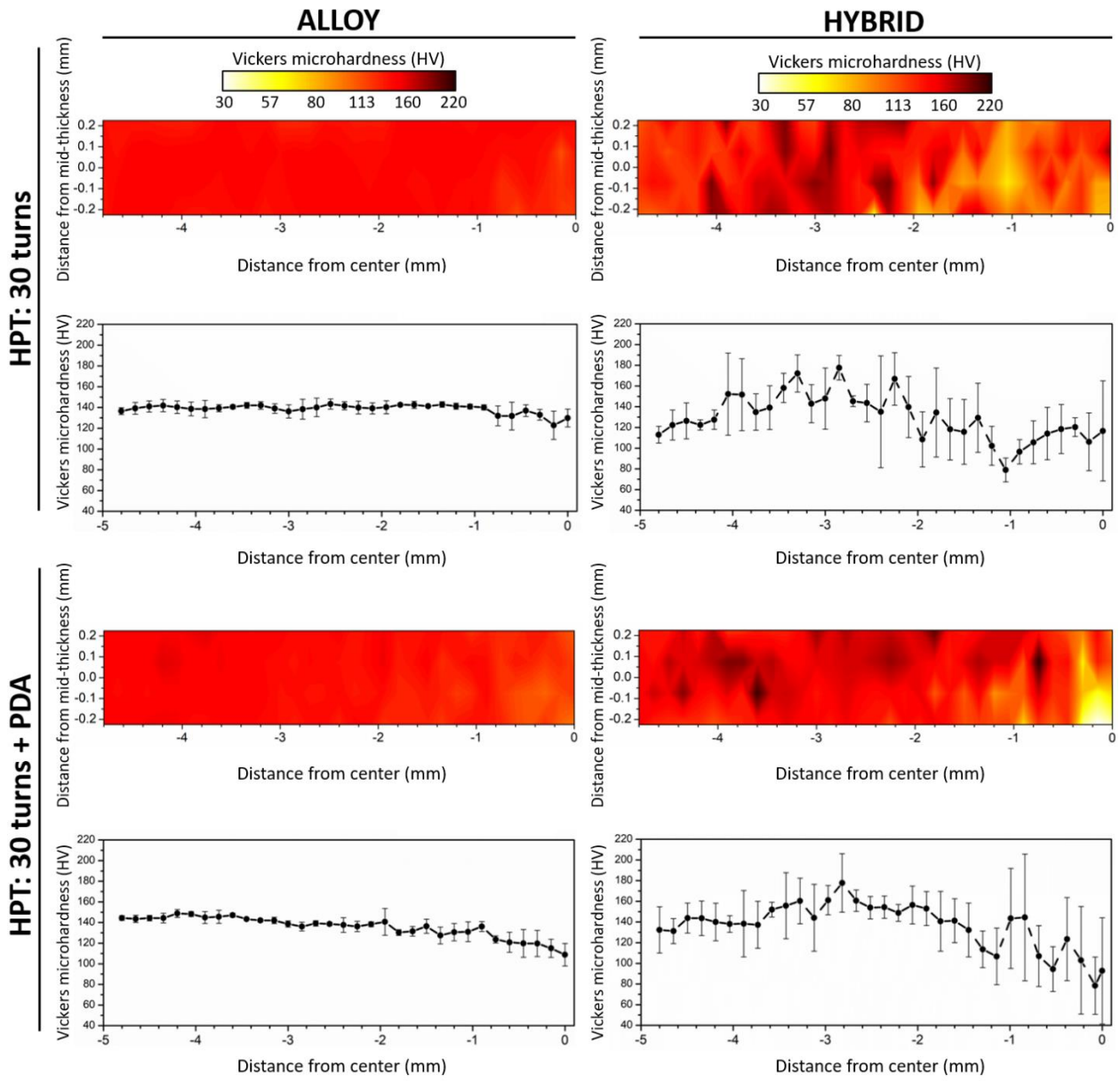

Figure 112: Comparison of HV hardness distribution maps and average hardness evolution plots across the radius of the Zn-3Mg alloy/hybrid after 30 turns, and 30 turns + PDA.

5.6. Zn-30Mg hybrids

This section discusses the microstructural and hardness evolutions of the Zn-30Mg hybrids after HPT.

5.6.1. Effect of HPT on the microstructure and hardness evolution

The cross-sectional SEM images of the Zn-30Mg HPT hybrids presented in Figure 76 showed that at least 5 turns were necessary in order to achieve a good bonding between the Zn/Mg/Zn stack of disks into a compact sample. Despite the feasibility of producing compact samples for higher number of turns, no significant mixing of the Zn and Mg phases was observed, based on the two clear contrast levels observed at the cross-sections of the samples. Even after 30 turns, the lack of a uniform contrast level anywhere in the sample, together with relatively large Zn and Mg phases present (including near the peripheral region), suggested a limited microstructural evolution. Because of this, the microstructures of the Zn-30Mg hybrids were not studied in as much detail as the other hybrid compositions. Nevertheless, in support of the latter statement regarding the lack of phase mixing, TEM analysis at the mid-thickness near the periphery of the sample after 30 turns demonstrated the presence of only Mg phase in the entire lamella, as observed in Figure 77. This is in good agreement with the darker areas observed at those locations in the cross-section of the sample after 30 turns. It should be highlighted that no other phase different than Mg was identified in the TEM lamella investigated, which only contained 4-5 grain boundaries, hence, suggesting a relatively large grain size.

Consistent with the limited microstructural evolution, including phase mixing and grain refinement, suggested from the SEM and TEM observations, the hardness distribution along the cross-sections of the samples processed for the different number of turns did not exhibit any clear

trend, as observed in Figure 79. The modest increase in the average hardness from ~ 45 HV after 1 turn to ~100 HV at some locations after 15 and 30 turns may be associated with limited grain boundary strengthening alone. Even though a phase analysis by XRD was not performed in the Zn-30Mg hybrids, the fact that no Zn-Mg phases were identified by TEM at the regions of highest plastic deformation may indicate that the observed strengthening could not be related to the formation of hard intermetallic compounds. This hypothesis would be consistent with the results obtained from Al-Fe and Al-Ti HPT hybrids processed for 20 and 50 turns, respectively, using the same A/B/A stacking approach [25]. In the latter reference, the presence of individual Al, Fe, and Ti phases without any formation of new intermetallic compounds was demonstrated after HPT processing, which resulted in a moderate hardness increase. The lack of intermetallic formation in the latter metal systems was attributed to the longer diffusion lengths required for the nucleation of such intermetallics, as compared to the significantly shorter diffusion lengths between metal powders, where the formation of intermetallic compounds was demonstrated after HPT. This may indicate that having a central Mg disk notably thicker than the external Zn disks in the Zn-30Mg hybrids may have resulted in less microstructural and hardness changes than the other hybrid compositions examined in this dissertation.

5.7. Effect of Mg content on the microstructure and hardness of Zn-Mg hybrids

Figure 113 presents a comparative summary of the SEM cross-sections and corresponding HV distribution maps of the (a) Zn-3Mg, (b) Zn-10Mg, and (c) Zn-30Mg HPT hybrids after 1, 5, 15, and 30 turns. Note also the sketches of Zn/Mg/Zn stacks for each hybrid composition, showing the approximate relative thicknesses of the Zn and Mg disks before HPT processing.

As observed in Figure 113 (a) and (b), both Zn-3Mg and Zn-10Mg hybrids achieved a good bonding between the Zn and Mg disks after 1 turn, and phase mixing increased progressively with the number of turns. After 30 turns, the SEM cross-section of the Zn-3Mg presented a relatively uniform contrast, with fine phases still distinguishable in the central region, whereas that of the Zn-10Mg was more heterogeneous, with large Mg-rich phases visible at low-magnification. These observations agree with their respective hardness values. The Zn-3Mg hybrid after 30 turns presented a more uniform hardness distribution across the sample, whereas the Zn-10Mg hybrid showed a very low hardness (~ 60 HV) at the sample center, consistent with the large Mg phase in its respective cross-sectional image. It should be noted that the maximum HV values were higher in Zn-10Mg hybrid (~ 250 HV) than in the Zn-3Mg hybrid (~ 220 HV).

From Figure 113 (c), it is evident that the Zn-30Mg hybrid did not achieve a good bonding between the Zn and Mg disks until 5 turns, and that increasing the number of turns did not result in a notable increased phase mixing, since the intermediate Mg disk was still apparent after 30 turns. Consistent with this, the hardness values did not increase significantly with the number of turns and were overall quite low as compared to the other hybrid compositions.

Therefore, this shows that increasing the Mg content in the Zn/Mg/Zn stack sequence does not result in a hybrid with an increased uniform hardness across the sample, and that only small additions of Mg (i.e., 3 wt.%) are necessary for obtaining significant strengthening in the HPT-processed Zn-Mg system. The Zn-3Mg hybrid composition, despite not having the highest HV values, would be the most interesting from an application standpoint where a uniform microstructure and mechanical behavior are typically desired. Moreover, the Zn-3Mg hybrid is the only composition that presents a symmetrical gradient-type hardness increase from the periphery to the center, consistent with the evolution of the shear strain during HPT. This is important because it allows for the identification of the saturation regime beyond which further HPT straining might not translate into more uniform microstructures or mechanical properties.

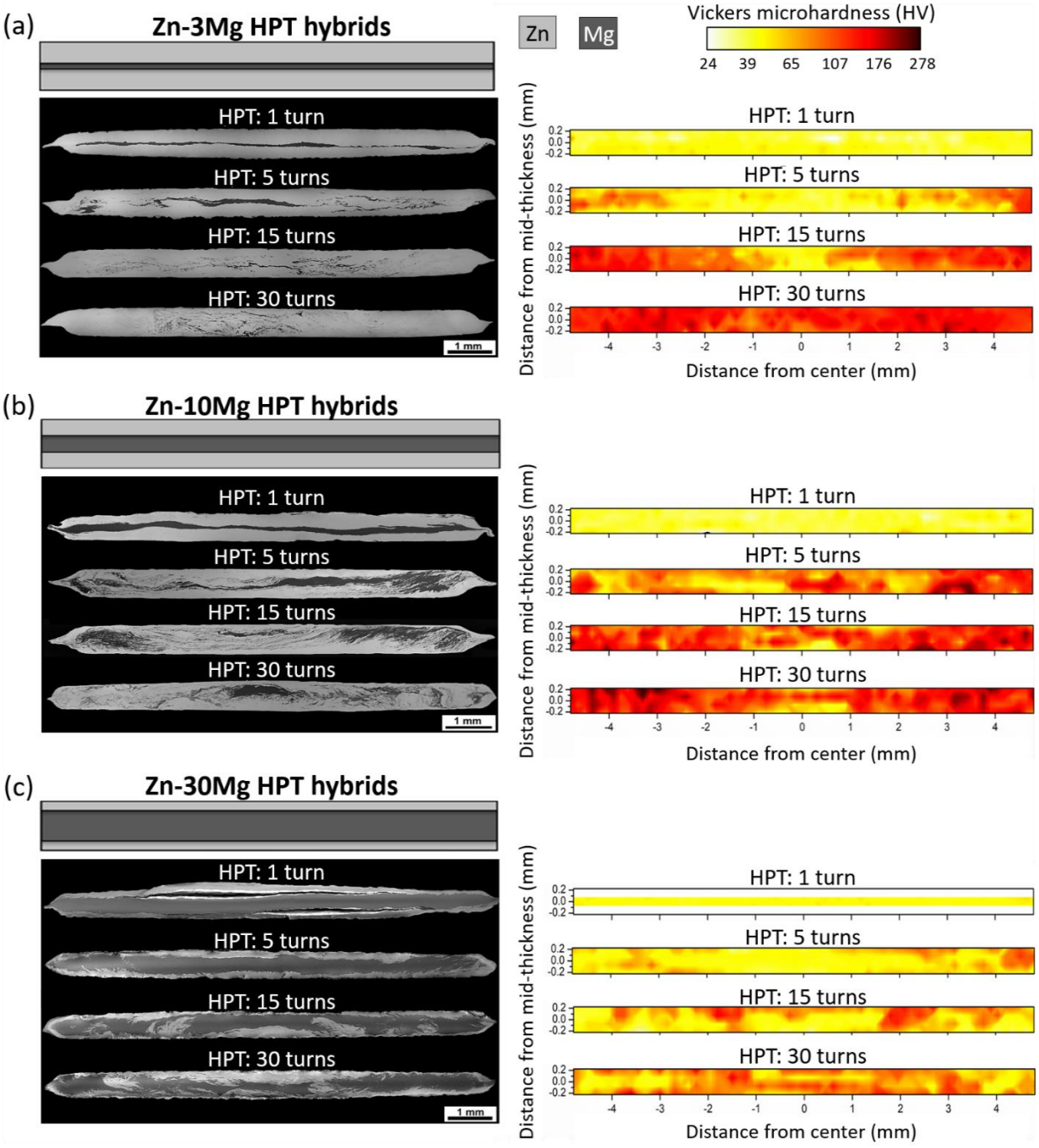

Figure 113: Comparison of the SEM cross-sections and HV distribution maps of the Zn-xMg (x = 3, 10, 30 wt.%) hybrids after HPT for 1, 5, 15 and 30 turns (a) Zn-3Mg HPT hybrids, (b) Zn-10Mg HPT hybrids, and (c) Zn-30Mg HPT hybrids.

5.8. Coatings for enhanced corrosion resistance, cell viability and antibacterial activity

5.8.1. Development of coatings

The following sections, from 5.8.1.1 to 5.8.1.4, discuss the characteristics of the different coatings obtained in a Zn-3Mg alloy substrate: ZnP, Col, ZnP-Col, and Col-AgBGN.

5.8.1.1. ZnP coatings

The flake-like appearance of the ZnP coated surfaces with a uniform pore distribution shown in Figure 80 (c) and (d) was consistent with that obtained in pure Zn [43,156], following a similar chemical conversion protocol. The chemical composition of the ZnP coating was confirmed to be hopeite, as observed in the GIXRD spectrum in Figure 86 (b). The flower-like structures observed in some coated samples, as in Figure 81, were also found in a ZnP coated AZ91D Mg alloy [233] and were related to the nucleation sites of hopeite (i.e., zinc phosphate tetrahydrate) crystals.

The growth of the ZnP coatings in the sample was suggested to consist of two stages. At the first stage (during the initial 3 min of immersion in the ZnP solution), a large number of hopeite crystals nucleated and grew homogeneously across the substrate, forming a uniform flower-like structure that eventually covers the entire sample. At the second stage, those structures interact with each other and continue growing vertically into the flake-like structure normally observed at the end of the 5 min immersion period.

5.8.1.2. Col-coatings

Among the three different Col-coatings presented in Figure 82, that obtained with 2.4 mg/mL PureCol by spin-coating for 20 s at 3000 rpm resulted in a well-defined assembly of Col fibrils, as

observed in Figure 82 (a). The estimated thickness of the Col fibrils reported was similar to that found in other Col coated samples [158,159].

An increase in the spin-coating time by 10 s decreased the number of Col fibrils attached to the surface, as observed in Figure 82 (b), since the centripetal force was active for a longer period of time pulling a higher fraction of Col fibrils away from the rotation axis. A thin porous layer of Col could be distinguished underneath the Col fibrils.

Decreasing the PureCol concentration to 1 mg/mL resulted in a coating with a porous Col coating where the Col fibrils were not evident, as observed in Figure 82 (c). It should be noted that 2.4 mg/mL PureCol was the recommended concentration for gel formation by Advanced Biomatrix, and that a lower concentration may not be sufficient for the formation of Col fibrils during incubation.

5.8.1.3. ZnP-Col coatings

The formation of ZnP-Col was achieved by spin-coating the Col solution that was deemed to be most uniform in the previous section on top of the ZnP substrate. Figure 83 showed that the Col fibrils covered the flake-like ZnP substrate completely, including both the flat and porous regions. It should be mentioned that several dual coatings based on calcium phosphate and collagen have been synthesized for enhanced biocompatibility and cell adhesion [234,235]; however, no other ZnP-Col coating was found in the literature.

5.8.1.4. Col-AgBGN coatings

A relatively uniform Col-AgBGN coating was obtained, with dispersed nanoparticles across the substrate surface. Monodispersed nanoparticles with diameters below 50 nm could be

distinguished from Figure 84, as well as nanoparticle aggregates ranging from ~ 100-200 nm. The nature of these nanoparticles could not be assessed by elemental analysis due to the low concentration of material and the strong signal from the substrates. However, the *in vitro* performance of the Col-AgBGN coatings, discussed in sections 5.8.3 and 5.8.4, strengthened the belief that the nanoparticles observed by SEM were indeed AgBGNs.

The aggregation of AgBGNs often occurs to reduce their surface energy [236,237]. PEG was used in the Col-AgBGN coating protocol to decrease the surface charge of the AgBGNs with the objective to minimize aggregation. However, the centrifugation of the AgBGN-PEG solution before replacing the resulting supernatant with 2.4 mg/mL PureCol to form the Col-AgBGN solution could have contributed to the AgBGN aggregation. Alternatively, the spin-coating technique is suggested to play a role in the aggregation process. The collagen matrix may act as a glue holding a small concentration of AgBGNs in place. During spin-coating, loosely bonded AgBGNs migrate towards the edges of the sample due to the centripetal force and may encounter sets of AgBGNs more firmly bound to the matrix, which stop their movement, causing the aggregates observed.

5.8.2. *In vitro* degradation of coatings during immersion assay

The degradation behavior of absorbable metals is responsible for the ion release and pH evolution of the media in the local environment, both of which will influence the cellular response at the implantation site. The *in vitro* degradation behavior *in vitro* was evaluated in static conditions for 21 days. The samples were immersed in DMEM at 37 ºC, and half of the media was refreshed every other day to simulate physiological conditions.

As observed by SEM in Figure 85 (a) and (b), the degradation of the uncoated sample led to dissimilar corrosion behaviors of the Zn and Mg_2Zn_{11} phases. On the one hand, corrosion pits were observed in the Zn phase after 6 days immersion, which became larger with increasing immersion time. On the other hand, the Mg_2Zn_{11} phase exhibited a similar granulated topography after 6 and 21 days immersion, suggesting a more uniform corrosion behavior. The presence of O in the EDS analysis of the uncoated sample after 6 and 21 days immersion, in Figure 85 (e), was consistent with the identification of ZnO and $Zn(OH)_2$ from GIXRD in Figure 86 (a). Moreover, whereas the O content was similar in the Zn phase after 6 and 21 days immersion (~ 2-3 (wt.%)), that in the Mg_2Zn_{11} phase increased from ~ 6 to ~ 10 (wt.%) after 6 and 21 days immersion, respectively. This could indicate that the ZnO and $Zn(OH)_2$ corrosion products mainly formed in the Mg_2Zn_{11} phase, and that their fractions increased over time. Consistent with the increased fraction of corrosion pits in the uncoated sample surface over time, the weight loss after 12 days immersion (~ 0.73 mg) was approximately double of that after 6 days immersion (~ 0.35 mg), as observed in Figure 87 (a) and Table 10. This resulted in a relatively uniform corrosion rate (~ 0.04 mm/year) from 6 to 12 days immersion, which is similar to that reported (~ 0.03 mm/year) from an immersion test of pure Zn in SBF for 10 days [238]. In addition, the pH value was reasonably stable (~ 7.55-7.6) within the physiological range during the first 12 days of immersion, which might be associated with a constant ion release in agreement with a similar trend in pure Zn and a Zn-based alloy [239].

The morphology of the ZnP sample did not change significantly during immersion, and the flake-like microstructure was still apparent after 6 and 21 days immersion. However, some relatively fine flakes were observed evenly spread across the microstructure, as shown in the inset of Figure 85 (d), which might be associated with the formation of Na-containing corrosion products

identified by GIXRD after immersion in Figure 86 (b). It should be noted that 4-5 (wt.%) C was identified in all the EDS scans of the immersed samples; however, no C-containing phase was a good match for the GIXRD spectra of either the uncoated or ZnP samples after immersion. C was also identified by EDS in pure Zn after immersion in DMEM for 3 days [43], and thus, the presence of C might be related to degradation products of DMEM.

As a result of the corrosion process, the thickness of the ZnP coating is expected to decrease, and this might be related to the increased peak intensity of the Zn and Mg_2Zn_{11} phases from the substrate in the GIXRD spectrum after 21 days immersion. Based upon the weight loss measurements of the ZnP samples after 6, 12, and 21 days immersion presented in Figure 87 (a), it is suggested that the ZnP coating degrades more uniformly and slower than the uncoated samples. The calculated corrosion rates in Figure 87 (b) were consistent with the latter statement, and in good agreement with the enhanced corrosion resistance of a similar ZnP coating compared to that of pure Zn [156]. The latter work also showed that the released Zn ion concentration measured from the immersion media of the ZnP coated sample was almost half of that from pure Zn, which could be related to the same trend observed in the corrosion rate after 12 days immersion in our study. Similar to that in Figure 87 (c), the pH value of pure Zn and ZnP samples reported in [156] ranged between 7.5-7.6 after 15 and 30 days immersion in Hanks solution, and no significant differences in pH were reported between the different samples.

5.8.3. Cytocompatibility and cell proliferation assays

The experimental conditions of the *in vitro* test were first optimized by analyzing the growth rate and confluence of the 7043L hMSC. Figure 89 shows a linear cell growth for up to 7 days of culture, and then a plateau in the three groups tested. However, the growth rate was significantly higher at a seeding density of $2.5 \cdot 10^3$ cell/cm^2, reaching a similar cell concentration than the other groups after 7 days of culture. The optical images in Figure 88 show the high cell confluency of the wells. Cells seeded at $2.5 \cdot 10^3$ cell/cm^2 were confluent and aligned parallel to each other at day 7, covering the bottom of the well. In contrast, at higher seeding densities, cell confluence was observed earlier in the experiment (i.e., day 4), and cells overlapped, leading to a cellular multilayer after 7 days.

Therefore, the indirect proliferation assay with sample extracts was performed up to 7 days since cell densities plateaued after 9 days of culture in all the groups tested. Among the three seeding densities studied, $2.5 \cdot 10^3$ cell/cm^2 was selected to ensure that the control groups in the indirect proliferation test did not reach confluence before 7 days.

Cell proliferation was assessed indirectly by exposure to sample extracts (i.e., uncoated, ZnP, and Col-AgBGN). The degradation products of the three samples had a positive effect on cell viability, showing higher cell concentration than the control at all time points, as observed in Figure 91. Furthermore, increasing extract concentrations (from 10-fold to 4-fold) led to a gradual increase in cell viability for the uncoated and Col-AgBGN extracts, whereas this trend was not observed in the ZnP extracts. The enhanced proliferation of cells cultured with extracts may be correlated to the presence of ionic species released during the degradation of the uncoated, ZnP and Col-AgBGN samples for 72 h. It should be mentioned that even though the pH values and ionic

concentrations of the extracts were not evaluated, they are both anticipated to remain within the physicological range even in the more concentrated extract (i.e., 4-fold), as cytotoxicity was not observed.

It is worth noting that the uncoated extracts showed enhanced cell proliferation as compared to the control. This is in good agreement with the trend reported by Murni et al. [35] for human osteoblast cells cultured for 3 days in 0.75 mg/mL Zn-3Mg alloy powders. However, a dramatic decrease in cell viability was reported after day 7, which is contrary to observed in our study. This was suggested to be due to the increased ion release associated with the larger surface area of the powder sample used to collect the extracts in [35], as compared to the bulk sample in our study, which might exceed the concentrations for which Zn and Mg ions are cytotoxic for cells.

The enhanced cell viability observed in the ZnP extracts, regardless of the concentration, was consistent with that reported by Su et al. [156] for endothelial and pre-osteoblast cells cultured for 5 days in 4-fold and 2-fold extract concentrations obtained from ZnP-coated pure Zn samples. The undiluted extract concentration led to cytotoxicity in pre-osteoblasts, as cell viability decreased to ~ 20 % after day 1 and kept decreasing to ~ 7 % at day 5. A decrease in extract concentration from 4-fold to 2-fold was shown to improve cytocompatibility of both cell lines [156]. Even though the highest extract concentration studied was 4-fold in our study, no correlation between the ZnP extract concentration and cell viability was observed.

The Col-AgBGN extracts were unique in that they showed significantly higher cell viability than the control samples for the three extract concentrations tested. In addition, the 4-fold extract demonstrated a statistically greater cytocompatibility than the ZnP and uncoated groups with the same extract concentration. The enhanced cell viability demonstrated by the Col-AgBGN extracts

was suggested to be mainly due to the release of ionic species (i.e., Si^{2+} and Ca^{2+}) upon degradation of the AgBGNs, as similar AgBG microparticles have demonstrated an increase in cell proliferation in another work [166]. In addition, since collagen is expected to degrade during immersion, some AgBGNs could have also been released into the immersion medium. This way, Col-AgBGN extracts may be considered as a solution containing Si^{2+}, Ca^{2+}, Ag^{+}, and AgBGN, which supplemented the cells with additional nutrients that favored their proliferation.

It should also be mentioned that the concentration of Ag^{+} ions released during AgBGN degradation, as well as their interaction with Zn^{2+}, did not result in adverse cytotoxic effects. In agreement with this, Li et al. [240] showed that fibroblasts and osteoblasts (L929 and Saos-2) cultured in 10-fold and 6-fold extract dilutions of Zn-4Ag alloy resulted in similar viabilities than the control samples, and that no statistical differences were found between pure Zn and Zn-4Ag alloy.

Lastly, the degradation of Col from the Col-AgBGN coating during immersion may have also contributed to the increased cell viability observed. The main reason why Col is used for coating biomaterials is to enhance cell adhesion and tissue integration during implantation. Thereby, cells feel more comfortable attaching to a Col-containing surface; hence, higher cell proliferation would be observed over time as opposed to not having this coating. However, cells were never in contact with the Col-AgBGN coated sample during the indirect proliferation test, and therefore, the Col degradation products present in the Col-AgBGN extracts may not have played a critical role in cell proliferation. In support of the latter argument, several works have demonstrated that, despite enhanced cell adhesion, osteoblasts do not proliferate faster in Col-coated substrates [241–243].

5.8.4. Antibacterial adhesion and viability assessment

The antibacterial behavior of the coated samples was evaluated in terms of their ability to resist MRSA colonization. Bacterial antiadhesion property is key for the implant material to prevent bacterial contamination and postoperative infection, and it was assessed by SEM. Figure 92 showed low bacteria amounts at the surface of uncoated and Col-AgBGN samples and higher bacteria numbers in ZnP, ZnP-Col, and Col samples. In agreement with this, the bacteria densities estimated from CLSM imaging also showed the same trends, as presented in Table 11.

The surface of the uncoated samples, observed by SEM, exhibited lower bacterial adhesion than those of the ZnP, ZnP-Col, and Col samples, and similar to the Col-AgBGN sample. It was suspected that this observation could be an artifact caused by a combination of two factors (i.e., the difference in surface topography and the washing steps performed before SEM imaging). All the samples containing bacteria were washed twice before fixation, and this washing process may have removed a larger amount of bacteria from the uncoated samples than from the ZnP-containing and Col-containing samples, which exhibited a significantly rougher topography where bacteria may be more firmly attached. This way, the density of bacteria attached to the uncoated sample may be indeed higher than that observed by SEM. Based on this hypothesis, the OD decrease of planktonic bacteria cultured with the uncoated sample after day 3, observed in Figure 95 (c), may be associated with an increase in the number of bacteria attached to the sample surface.

The significantly higher bacteria colonization in ZnP and ZnP-Col samples may be associated with their surface topography, which microscopic roughness may favor bacterial adhesion, in agreement with other works [244–246]. The antibacterial behavior of ZnP and Col coatings in pure Zn was investigated by Su et al. [156], who demonstrated not only lower bacterial adhesion but also a

significant decrease in bacteria viability after 1 day of culture. The results of the present study indicate that the viable bacteria after 1 day of exposure to coated samples might be able to proliferate, counteracting the antibacterial effect of the coating, and colonize the surface after 7 days, explaining the high bacteria density observed in Figure 92. The increasing ODs of planktonic bacteria cultured in ZnP and ZnP-Col samples after 3 days, observed in Figure 95 (d) and (e), respectively, suggested that the bacterial density in suspension increased up to day 7. This could be possibly due to bacteria reaching a relatively high density at the material surface after 3 days, such that new bacteria are mainly released into the suspension rather than attached to the sample surface, similar to that reported during biofilm formation [247].

Even though the Col sample presented a smoother surface topography than that of the ZnP-containing samples, the fine nanostructured roughness observed in Figure 92 (e) was suggested to be due to the Col degradation products. As mentioned in the previous section, collagen coatings are mainly applied to enhance cell adhesion, since collagen is a major component of the extracellular matrix. Therefore, due to the natural origin of collagen, as well as its fibrillar assembly in the synthesized coatings, it is reasonable to believe that collagen can also enhance bacteria attachment. In agreement with this, collagen was shown to promote both fibroblast and *S. aureus* adhesion simultaneously in a glass substrate [248]. The increasing OD of planktonic bacteria cultured with Col sample after day 2, observed in Figure 95 (f), may be rationalized with the same argument than that of ZnP-containing samples mentioned in the previous paragraph, as the three samples demonstrated high bacterial attachment by SEM.

Despite the Col sample exhibited a similar surface topography than that of the Col-AgBGN sample after 7 days culture with MRSA suspension, the bacteria viability of the latter was significantly lower than any other sample, as discussed later. Thus, the interpretation of the OD evolution of

planktonic bacteria in the Col-AgBGN sample may be different than in the other coated samples. The gradual increase in OD over time, observed in Figure 95 (g), indicated an increase of the bacterial concentration in suspension, thereby suggesting that the bacteria density attached to the sample surface decreased over time. This hypothesis may be supported by the antibacterial mechanism proposed for the Col-AgBGN coating later.

The status of the bacteria adhered to the sample surfaces was assessed by live/dead staining through CLSM imaging. Figure 93 showed that all samples presented similar ratios of green and red pixels, except that of the Col-AgBGN sample. Quantification of the bacterial viability was performed from color pixel counting in the CLSM images, and the estimated percentages of live/dead bacteria attached to the different samples are presented in Figure 94. On the one hand, ZnP-Col and Col samples showed statistically similar live/dead bacteria percentages (75 % and 71 %, respectively) than that of the uncoated sample (76 %). On the other hand, ZnP sample exhibited a statistically lower bacterial viability (65 %) than the uncoated sample, which agrees with the antibacterial effect reported by Su et al. [156] between a ZnP-coated and uncoated pure Zn.

The SEM images in Figure 92 showed that the uncoated and Col-AgBGN samples presented a similar number of bacteria attached; however, the bacteria viability on the uncoated sample (76%) was significantly higher than that in the Col-AgBGN coated sample (31%). Thereby, despite both samples showing similar bacterial densities, the density of live bacteria in the Col-AgBGN sample was less than half of that in the uncoated sample, as observed in Table 11. This evidences that the Col-AgBGN coating possesses the most effective bactericidal activity, whose antibacterial mechanism was proposed, based on the SEM observations, through a series of stages that are schematically shown in Figure 114 and described next.

Stage I, in Figure 114 (a), represents the initial stage when the Col-AgBGN sample is just immersed in the bacterial suspension. The fibrillar collagen matrix maintains the AgBGN attached to the sample surface, and bacteria remain in suspension.

At stage II, in Figure 114 (b), as the collagen matrix starts degrading over time, some AgBGN are released from the coating. Bacteria proliferation will lead to an increased number of bacteria in suspension with the AgBGNs, as well as some bacteria deposition at the coated substrate.

At stage III, in Figure 114 (c), as culture time advances, the AgBGN degrade and start releasing antibacterial Ag^{+} ionic species, similar to the effect observed in other Ag-containing BGs [249]. The released ions not only surround the AgBGN (those in suspension and those attached to the collagen matrix), creating a toxic environment around them, but also alter the composition and pH of the TSB that nurtures the bacteria. Consequently, the interaction between bacteria and Ag+ ions would lead to bacterial damage and/or lysis, which can manifest in MRSA in multiple ways, including distorted cell structures with surface deposits, the disruption of cell wall division, and cell lysis with membrane disruption [250–252].

The granulated surface of MRSA, observed in the inset of Figure 92 (e), may be associated with extracellular debris resulting from bacteria lysis, in agreement with similar observations from MRSA exposed to silver ions [251,252]. In addition, membrane disruption is suggested from the presence of cell-wall fragments, and may be correlated to the mechanical damage of cell-wall by nanosized particles puncturing nanotunnels to penetrate MRSA, as observed in [167].

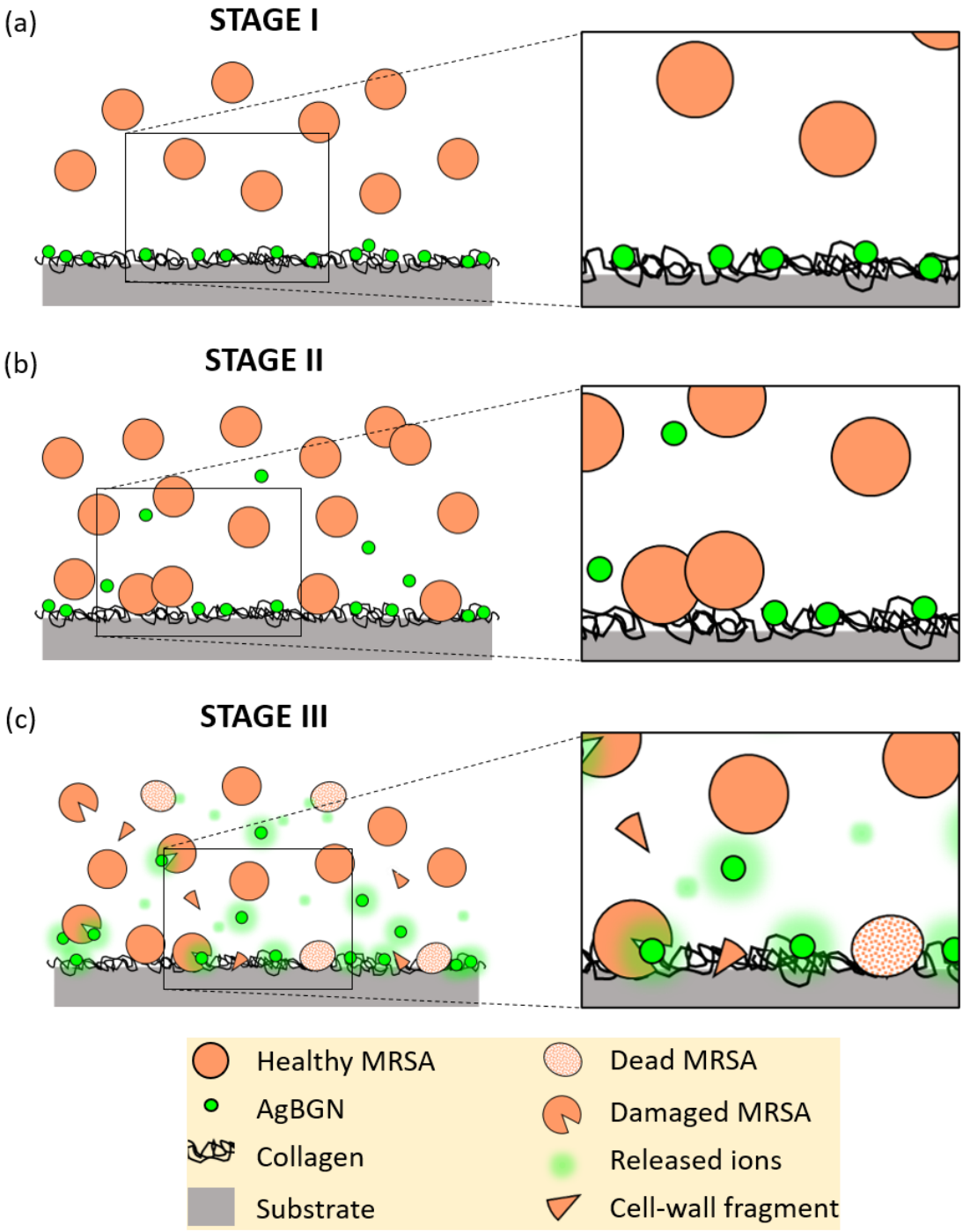

Figure 114: Scheme of the antibacterial mechanism proposed for the Col-AgBGN coatings in the Zn-3Mg alloy substrate: (a) at the initial stage of immersion, the fibrillar collagen matrix maintains the AgBGN attached to the substrate surface, and bacteria remains in suspension; (b) as the collagen matrix degrades over time, AgBGN are released from the coating to the bacteria suspension; (c) the AgBGN degrades over time releasing antibacterial Ag+ ions that create a toxic environment to bacteria. This was evident from the damaged bacteria, dead bacteria, and cell-wall fragments observed experimentally after 7 days culture of Col-AgBGN samples with MRSA.

6. SUMMARY AND CONCLUSIONS

6.1. Summary

In this dissertation, a series of Zn-xMg hybrids (x = 3, 10, 30 wt.%) were synthesized by HPT (1, 5, 15, and 30 turns; 1 rpm; 6 GPa; RT) from mechanical bonding of Zn/Mg/Zn stacked disks for the first time, and characterized to investigate their composition-processing-microstructure-property relationships. The effects of HPT on the microstructural and hardness evolution were systematically studied in the three hybrid compositions, with special emphasis on the regions of highest plastic deformation. In addition, the effects of PDA (200 ºC, 1h) on the microstructural and hardness evolution of the HPT-processed Zn-3Mg hybrid after 30 turns was also examined. The microstructural characterization involved the use of SEM, EDS, EBSD, TEM, XRD, and APT, whereas the hardness was examined by HV and Berkovich nanoindentation. Based on the H-m relationship obtained after PDA, a plastic deformation model was proposed to explain the suggested enhanced strength-ductility combination.

The microstructural and hardness evolution of a Zn-3Mg alloy after HPT and PDA was also investigated and compared to that of the hybrid counterpart with an equivalent nominal composition. In addition, the as-homogenized Zn-3Mg alloy was used as a substrate to develop different biodegradable coatings (ZnP, ZnP-Col, Col, and Col-AgBGN) for potential absorbable biomedical applications. The surface morphology and compositions of the coated samples were evaluated by SEM, EDS, and GIXRD. The *in vitro* degradation of the ZnP and uncoated sample was studied by immersion testing, and the corrosion rates were estimated from weight loss measurements. Cytocompatibility of hMSC was evaluated through indirect contact proliferation assays with extracts of the uncoated, ZnP, and Col-AgBGN samples. The antibacterial activity of

all the coated samples against MRSA was also studied by combining SEM and live/dead staining in CLSM.

6.2. Conclusions

6.2.1. Zn-10Mg hybrids

(1) The central regions of the samples after 1 and 5 turns consisted of relatively large Mg and Zn phases, without apparent phase mixing. At least 15 turns were needed to achieve the fragmentation of the Mg-rich phases, leading to a relatively uniform microstructure near the disk edges consisting of a multilayered structure with thicknesses of ~ 20-40 μm. A general tendency for decreasing the grain size and the scale of the multilayered structure was observed with increasing radial distance and number of HPT turns. After 30 turns, a sub-micron multilayered structure embedded in a Zn-rich matrix with an average grain size of ~ 600 nm at the disk periphery was observed.

(2) The grain size refinement of the Zn-rich phase, from 1 turn (GS_{ave} ~ 40 μm), to 5 turns (GS_{ave} ~ 20 μm), to 15 turns (GS_{ave} ~ 5 μm), was accompanied by a significant increase in the volume fraction of HABs from 0.52 to 0.78 to 0.83, respectively. After 30 turns, the GS_{ave} increased slightly (GS_{ave} ~ 10 ± 7 μm), and the volume fraction decreased slightly (0.73). A strong basal texture was developed after 5 turns, and the maximum value of texture intensity decreased gradually from 5 to 30 turns, which, together with the slight increase in GS_{ave} after 30 turns, suggested the saturation of the microstructure upon DRX during HPT.

(3) Both XRD and TEM confirmed that HPT was able to induce the formation of Mg_2Zn_{11} and $MgZn_2$ intermetallic compounds near the sample periphery after 15 and 30 turns, and their

volume fraction increased with the number of turns. In addition, APT revealed the presence of Mg_2Zn_3 near the sample periphery after 30 turns. The volume fraction of Mg_2Zn_3 was believed to be comparatively lower than the other two intermetallics since it was not identified by XRD or TEM.

(4) The contribution of HPT-induced nucleation of intermetallic phases, as well as severe grain refinement, resulted in an exceptional increase of the hardness with increasing number of HPT turns. Values up to ~ 200 HV and ~ 250 HV were measured after 15, and 30 turns at the disk periphery, respectively, which are about 4-5 times larger than the maximum hardness reported from HPT-processed pure Zn and pure Mg. Despite the outstanding HV values measured, the hardness distribution was far from uniform across the sample, due to the largely heterogeneous microstructure.

(5) The number of turns influenced the corrosion mechanism and the electrochemical kinetics in SBF. The HPT-processed disks after 15 and 30 turns exhibited more negative potentials than after 1 turn. The disks after 1 turn exhibited lower current density than after 30 turns and 15 turns, respectively. The same trend was observed for the corrosion resistance, as indicated by the charge transfer resistance in the EEC diagrams fitted from the EIS data, which was consistent with the OCP and PDP data.

6.2.2. Zn-3Mg alloy

(1) The homogenization heat treatment (360 ºC for 15 h + water quenching) performed in the as-cast Zn-3Mg alloy was effective in dissolving the Mg_2Zn_{11} primary phases and led to a more uniform and interconnected lamellar microstructure of eutectic Zn and Mg_2Zn_{11} phases. The small amount of porosity observed in the as-cast condition was not evident in

the as-homogenized alloy, which exhibited a slightly coarser lamellar microstructure, presumably associated with the enhanced diffusion during the heat treatment.

(2) HPT-processing of the as-homogenized Zn-3Mg alloy for 30 turns resulted in an equiaxed microstructure with a GS_{ave} of ~ 200 nm, within a unimodal GS distribution. SAD pattern analysis revealed that the microstructure consisted of Zn and Mg_2Zn_{11} phases, and that no additional phases formed during HPT processing for 30 turns. Nanocrystalline Mg_2Zn_{11} phases were resolved by HRTEM, both between neighboring precipitate-free Zn grains and at the grain boundaries. APT also revealed the presence of a nanosized Mg_2Zn_{11} phase, as well as a solid solution of Mg in the Zn matrix.

(3) The average hardness in the as-homogenized Zn-3Mg alloy (~ 109 HV) increased to ~139 HV across the sample after HPT processing for 30 turns. This was mainly related to the Hall-Petch strengthening due to the severe grain size refinement. The fragmentation of the Mg_2Zn_{11} intermetallic phase after HPT, which is substantially harder than Zn, led to a significant increase in the surface area of the Mg_2Zn_{11} phase. This may have also led to a more hindered dislocation motion during plastic deformation, hence, increasing the material hardness. In addition, the development of a strong basal texture after HPT may have also played a role in the increased hardness.

(4) After subjecting the HPT-processed Zn-3Mg alloy to PDA (200 ºC for 1h), a coarser equiaxed microstructure was observed, with a GS_{ave} of ~ 700 nm. The range of GS increased compared to after HPT, from 300 nm to 1.2 μm, but the GS distribution was still unimodal. BSE-SEM showed two clear contrast levels in the microstructure, which were related to Zn and Mg_2Zn_{11} grains. This suggested that, besides the grain growth of the Zn grains, the nanosized Mg_2Zn_{11} phases observed after HPT diffused during PDA and

coalesced into coarser Mg_2Zn_{11} grains leading to a lower energy state configuration closer to equilibrium.

(5) The average hardness of the Zn-3Mg alloy after PDA (~ 136 HV) across the sample was similar to that after HPT. However, unlike the relatively uniform hardness distribution across the sample radius after HPT, the average hardness after PDA increased slightly with increasing distance from the center. This may indicate that, despite the higher stored energy at the sample periphery, which is the main driving force for recrystallization, the presence of hard Mg_2Zn_{11} grains may difficult the occurrence of recrystallization and subsequent grain growth during PDA.

6.2.3. Zn-3Mg hybrids

(1) The central Mg disk in the Zn/Mg/Zn sequence was fragmented after 5 turns, and phase mixing increased with the number of turns, especially near the sample periphery. A microstructure consisting of ultrafine equiaxed grains, ranging between ~ 100-200 nm, and nanoscale precipitates evenly distributed was observed near the sample periphery after 30 turns. EDS analysis suggested that the bulk composition at this region was congruent with the targeted Zn-3Mg.

(2) XRD demonstrated the HPT-induced formation of Mg_2Zn_{11} and $MgZn_2$ phases after 15 and 30 turns. Their volume fraction appeared to increase at the expense of Mg phase with increasing shear straining. Besides the identification of the Mg_2Zn_{11} phase, APT showed a region with a homogenous composition of 99.2Zn-0.3Mg (at. %), presumably associated with a metastable SSSS, thereby suggesting that HPT may be capable of extending the solid solubility between Zn and Mg.

(3) The hardness evolution followed a symmetric gradient-type evolution with respect to the sample center from 1 to 30 turns. Overall, the hardness increased consistently with higher accumulated plastic strains, in agreement with the shear strain equation of the HPT procedure. A relatively uniform hardness distribution was observed across the sample after 30 turns, as compared to after 15 turns, with average values ranging between ~ 120-180 HV, and maximum values of ~ 200-230 HV near the sample periphery. The hardness increase was mainly related to the combination of grain boundary strengthening by the nanosize-grained microstructure, as well as the precipitation hardening from the Mg_2Zn_{11} and $MgZn_2$ intermetallics.

(4) The investigation of the strain hardening capability during HPT processing revealed that the Zn-3Mg hybrid followed a three-regime behavior. Regime I, up to $\varepsilon_{eq} \sim 30$, indicated a limited strain hardening in the early stage of HPT, with a hardenability exponent of $\eta \sim 0.02$, similar to other HPT-processed materials. Regime II, up to $\varepsilon_{eq} \sim 400$, showed an exceptional strain hardening, with $\eta \sim 0.54$, which is about one order of magnitude larger than most reported values. Regime III, up to $\varepsilon_{eq} \sim 660$, exhibited softening, which may be due to the saturation of the grain size refinement after severe straining, where the large fractions of HABs may promote grain boundary sliding at RT.

(5) Subjecting the HPT-processed Zn-3Mg hybrid after 30 turns to PDA (200 ºC, 1h) led to significant microstructural heterogeneity, consisting of a bimodal grain size distribution of finer Mg-rich grains (~ 100-200 nm) and coarser Zn-rich grains (~ 600-900 nm). The presence of Mg_2Zn_{11} and $MgZn_2$ intermetallics within the finer Mg-rich grains was revealed by FFT analysis of HRTEM images. This suggested that the segregation of Mg_2Zn_{11} and $MgZn_2$ nanoprecipitates in the finer Mg-rich grains was assisted by enhanced

diffusion during PDA, such that they acted as pinning sites preventing grain growth, hence, leading to the bimodal distribution.

(6) XRD results suggested that PDA led to an increased volume fraction of Mg_2Zn_{11} at the expense of $MgZn_2$, which would be associated with a decrease in the formation enthalpy, thus, providing a lower energy state to the HPT hybrid system after PDA. A region with a homogenous composition of 79.0Zn-20.7Mg (at. %) was revealed by APT, which is far beyond the equilibrium solubility limit of Mg in Zn, hence, suggesting the formation of a SSSS after PDA. The hardness increased near the sample periphery after PDA, consistently between HV and nanoindentation, despite the grain growth of the Zn-rich grains. This effect was attributed to the presence of Mg_2Zn_{11} and $MgZn_2$ intermetallics, as well as to the SSSS.

(7) Nanoindentation testing revealed that both H and m values increased after PDA. The H values increased consistently with strain rate in both material conditions, indicating lower plasticity at faster strain rates. The m values were estimated as 0.098 and 0.121, before and after PDA, respectively. This demonstrated that PDA was able to provide a dual enhancement of the hardness and plastic deformation capability, which may be associated with a simultaneous increase of the strength and ductility, contrary to the classical strength-ductility tradeoff. The proposed plastic deformation model described the complementary roles of the coarser Zn-rich grains and the finer Mg-rich grains during deformation. This model is supported by the H-m relationship observed, which suggests a strength-ductility synergy.

6.2.4. Zn-30Mg hybrids

(1) Mechanical bonding of the Zn/Mg/Zn disks required at least 5 turns, as opposed to the compact samples achieved in the Zn-3Mg and Zn-10Mg hybrids after 1 turn. Despite the feasibility of producing Zn-30Mg hybrid samples, no significant phase mixing was observed with increasing number of turns. In fact, after 30 turns, the sample consisted of relatively large Zn and Mg phases clearly distinguishable at low magnifications in the SEM. The Zn/Mg/Zn original stacking sequence was still visible, unlike in the Zn-3Mg and Zn-10Mg hybrids.

(2) The lack of phase mixing observed after 30 turns by SEM was also demonstrated by TEM and FFT analysis. The TEM lamella extracted from the mid-thickness region near the sample periphery consisted of large Mg grains, and no additional phase was identified. This suggested that HPT may not be able to form Zn-Mg phases in the Zn-30Mg hybrids, unlike that in the Zn-3Mg and Zn-10Mg hybrids.

(3) According to the limited microstructural evolution of the Zn-30Mg hybrids during HPT, including phase mixing and grain refinement, the hardness distribution did not exhibit a clear trend. The average hardness increased from a uniform ~ 45 HV after 1 turn (similar to that of pure Zn and pure Mg) to ~ 100 HV after 15 and 30 turns at some locations, which may be related to limited grain boundary strengthening. Note that the average hardness of the Zn-3Mg and Zn-10Mg hybrids was about double that measured for the Zn-30Mg hybrids.

(4) The limited microstructural evolution of the Zn-30Mg hybrids is presumably associated with the thickness of the disks in the Zn/Mg/Zn sequence. The central Mg disk was significantly thicker (i.e., 0.957 μm) than the external Zn disk (i.e., 0.272 μm), possibly

hindering phase mixing during HPT. This hypothesis is supported by the experimental observations in Zn-3Mg and Zn-10Mg hybrids, where the central Mg disk had lower or equal thickness than the Zn disks, respectively, and revealed significant phase mixing.

6.2.5. Surface functionalization of Zn-3Mg alloy substrates

(1) Four different uniform coatings, namely ZnP, Col, ZnP-Col, and Col-AgBGN, were synthesized on as-homogenized Zn-3Mg alloy substrates by using either a chemical conversion method (i.e., ZnP), a spin-coating approach (i.e., Col and Col-AgBGN), or a combination of both (i.e., ZnP-Col).

(2) *In vitro* degradation of uncoated and ZnP samples by immersion testing for 21 days showed a more uniform corrosion behavior in the ZnP sample, associated with a controlled weight loss over time. Corrosion pits formed in the Zn phase of the uncoated sample after 6 days immersion, which increased in size after 21 days immersion. Consequently, the estimated corrosion rate for the ZnP sample was comparatively lower than that of the uncoated sample. Both samples exhibited similar pH values ranging between ~ 7.5-7.6 during the 21 days immersion test, which are within the physiological range and thus, are not anticipated to cause cytotoxicity.

(3) Cell viability of the uncoated, ZnP, and Col-AgBGN samples was assessed indirectly by exposing hMSC to 3 different extract dilutions for 6 days. In general, cell viability was higher after exposure to sample extracts than in the control sample. Increasing extract concentration led to higher cell viability in the uncoated and Col-AgBGN samples. However, this trend was not observed in the ZnP extracts. Comparatively, Col-AgBGN extracts showed the greatest cytocompatibility, which was suggested to be mainly due to

the release of ionic species (i.e., Si^{2+} and Ca^{2+}) from the BG degradation, which have demonstrated increased cell proliferation consistently in other works.

(4) Antibacterial behavior was evaluated in the uncoated, ZnP, ZnP-Col, Col, and Col-AgBGN samples by their ability to resist MRSA colonization during 7 days. SEM showed higher bacterial adhesion in the ZnP, ZnP-Col, Col samples. The favorable bacterial attachment was associated with the rougher surface topography of the ZnP-containing samples and the presence of a nutrient-rich matrix like collagen in the Col-containing samples. Live/dead staining revealed significantly lower bacterial viability in Col-AgBGN (~ 31%) than in the uncoated (~ 76 %), ZnP (~ 65 %), ZnP-Col (~ 75 %), and Col (~ 71 %). This indicated that the Col-AgBGN sample exhibited the most effective antibacterial activity. Its antibacterial mechanism was proposed by a combined effect of Ag^{+} ion release and nanoparticles damaging the cell envelope.

6.3. Recommendations for future work

(1) To gain a deeper understanding of the microstructural transformation in the HPT hybrids, the central and mid-central regions of the samples could be further investigated, similar to that performed in the near peripheral regions. Particular interest might be directed to the samples processed at higher number of turns (i.e., 30 turns) where the microstructures and hardness distributions were more uniform. In addition, it would be interesting to compare the microstructures obtained from samples processed at different number of turns, but from regions with equal shear strain. For example, a shear strain of ~ 377 is present in the sample after 15 turns at r = 4 mm, and in the sample after 30 turns at r = 2 mm. These studies would contribute to the current knowledge by providing valuable information about the microstructural evolution during HPT as a function of the accumulated shear strain.

(2) The investigation of the HPT-processed hybrids in Zn-Mg system using the A/B/A multilayered approach could be expanded beyond the Zn-3Mg, Zn-10Mg, and Zn-30Mg compositions studied in this dissertation. Based on the results presented, it is recommended that the disk in the central position (i.e., B in the A/B/A sequence) is thinner than the disks in the exterior positions (i.e., A in the A/B/A sequence). This is expected to promote phase mixing and additional microstructural evolutions (i.e., severe grain size refinement, formation of intermetallic phases, and SSSS) associated with a significant hardness increase. Likewise, Mg/Zn/Mg HPT hybrids could also be explored, with higher Mg contents, which would potentially lead to faster corrosion rates, which are more suitable for short-term absorbable medical applications.

(3) The Zn-Mg HPT hybrids, either the Zn/Mg/Zn studied in this work, or the Mg/Zn/Mg suggested in the previous paragraph, could be processed for higher number of turns (i.e., above 30 turns). This way, one could find the optimum number of turns that would result in the most attractive composition-microstructure-property relationships. In addition, the effect of PDA (that performed in this work, or variations of it) is also recommended to be explored for different number of turns and compositions, as long as the microstructure is relatively uniform before the PDA treatment. These studies would provide a catalog of Zn-Mg materials enriching the current literature of HPT hybrids, which is rapidly expanding, and may also have a domino effect, thereby attracting the interest of new researchers to the field.

(4) To achieve a better mixing between the different metal disks during HPT processing, Zn-Mg hybrids could be fabricated by stacking more than three disks. For example, the stacking sequence Zn/Mg/Zn/Mg/Zn could be considered, with thinner Zn and Mg disks than those used in this study to maintain a similar diameter-to-thickness ratio in the hybrid samples. This

approach was demonstrated to favor mechanical alloying even in immiscible systems, like the Cu-Ta system [96]. In the latter work, the authors HPT-processed a stack of 19 Cu and 18 Ta disks in an alternating sequence of [Cu/Ta/Cu…Cu/Ta/Cu] for up to 150 turns [96].

(5) To be considered for any biomedical application, a full characterization of the global mechanical properties (i.e., UTS, ε_f, fatigue strength, etc.) of the HPT hybrids should be conducted. Thus, testing of miniature samples after different processing conditions is proposed to obtain a deeper understanding of the relationships between local mechanical properties (i.e., hardness, strain rate sensitivity) and global mechanical properties. Though tensile testing has been performed in multiple HPT-processed samples, a comprehensive characterization of the tensile properties of HPT hybrids in relation to their microstructure is still lacking in the literature and could be an interesting avenue to explore.

(6) The feasibility to scale up the dimensions of conventional HPT samples (i.e., 10 mm diameter and 1 mm thickness) has been demonstrated in several works (i.e., up to a maximum of 60 mm diameter and 12 mm thickness) [106]. A recent study on Al/Mg/Al HPT hybrids concluded that the microstructural and hardness evolution of samples having 25 mm diameter and 2 mm thickness were similar to those of conventional HPT samples [94]. Therefore, the feasibility of obtaining Zn-Mg HPT hybrids with larger dimensions, while maintaining similar microstructural and mechanical evolutions, would increase the number of applications that could benefit from the research conducted and knowledge gained in the laboratory-scaled hybrids.

(7) Regarding the biological characterization, the same coatings developed in this work are expected to be applicable, in general terms, to the Zn-Mg HPT hybrid samples with the goal of better controlling the corrosion rate, enhancing the cell adhesion and viability, and

providing antibacterial properties. ICP analysis of the diluted sample extracts provided to the cells would be valuable to reveal the concentration of different ionic species released during sample degradation to the DMEM, and determine how these concentrations may influence cellular functions. Additionally, the material-cell interaction could be investigated in a direct contact test (i.e., cells seeded on the material), where cell adhesion plays a significant role in the number of viable cells. This setup would also account for the *in situ* degradation of the substrate-coating platform, hence, mimicking more closely the real absorption process during clinical application. The insights gained from the direct contact tests may be interpreted in relation to those of the indirect contact assays with sample extracts evaluated in this work. Also, the cellular absorption of trace elements may trigger genotype and phenotype modifications that induce cell specialization to form tissue for specific functions. In this line, cell differentiation assays, with and without medium supplements (i.e., proteins and factors for signaling differentiation), are recommended to evaluate the effects of the degradation products alone, and their potential synergism with the supplements. Lastly, the material-tissue interaction and biocompatibility could also be evaluated *in vivo,* by implantation in small animals. For example, femoral fractures could be induced in rats to study investigate how the degradation of the implant material affects the inflammatory response, and contributes to the regeneration of bone tissue.

BIBLIOGRAPHY

BIBLIOGRAPHY

[1] D.W. Grainger, The Williams dictionary of biomaterials, Mater. Today. (1999). doi:10.1016/s1369-7021(99)80066-2.

[2] G. Katarivas Levy, J. Goldman, E. Aghion, The Prospects of Zinc as a Structural Material for Biodegradable Implants—A Review Paper, Metals (Basel). 7 (2017) 402. doi:10.3390/met7100402.

[3] E. Mostaed, M. Sikora-Jasinska, J.W. Drelich, M. Vedani, Zinc-based alloys for degradable vascular stent applications, Acta Biomater. 71 (2018) 1–23. doi:10.1016/J.ACTBIO.2018.03.005.

[4] M. Niinomi, M. Nakai, Titanium-based biomaterials for preventing stress shielding between implant devices and bone, Int. J. Biomater. (2011). doi:10.1155/2011/836587.

[5] C. Piao, D. Wu, M. Luo, H. Ma, Stress shielding effects of two prosthetic groups after total hip joint simulation replacement, J. Orthop. Surg. Res. (2014). doi:10.1186/s13018-014-0071-x.

[6] F. Witte, A. Eliezer, Biodegradable metals, in: Degrad. Implant Mater., 2012. doi:10.1007/978-1-4614-3942-4_5.

[7] H. Hermawan, Updates on the research and development of absorbable metals for biomedical applications, Prog. Biomater. (n.d.). doi:10.1007/s40204-018-0091-4.

[8] A. Francis, Y. Yang, S. Virtanen, A.R. Boccaccini, Iron and iron-based alloys for temporary cardiovascular applications, J. Mater. Sci. Mater. Med. 26 (2015) 138. doi:10.1007/s10856-015-5473-8.

[9] F. Witte, The history of biodegradable magnesium implants: A review, Acta Biomater. 23 (2015) S28–S40. doi:10.1016/j.actbio.2015.07.017.

[10] M. Peuster, C. Hesse, T. Schloo, C. Fink, P. Beerbaum, C. von Schnakenburg, Long-term biocompatibility of a corrodible peripheral iron stent in the porcine descending aorta, Biomaterials. 27 (2006) 4955–4962. doi:10.1016/J.BIOMATERIALS.2006.05.029.

[11] D. Pierson, J. Edick, A. Tauscher, E. Pokorney, P. Bowen, J. Gelbaugh, J. Stinson, H. Getty, C.H. Lee, J. Drelich, J. Goldman, A simplified in vivo approach for evaluating the bioabsorbable behavior of candidate stent materials, J. Biomed. Mater. Res. Part B Appl. Biomater. 100B (2012) 58–67. doi:10.1002/jbm.b.31922.

[12] X. Gu, Y. Zheng, Y. Cheng, S. Zhong, T. Xi, In vitro corrosion and biocompatibility of binary magnesium alloys, Biomaterials. 30 (2009) 484–498.

doi:10.1016/J.BIOMATERIALS.2008.10.021.

[13] D. Vojtěch, J. Kubásek, J. Šerák, P. Novák, Mechanical and corrosion properties of newly developed biodegradable Zn-based alloys for bone fixation, Acta Biomater. (2011). doi:10.1016/j.actbio.2011.05.008.

[14] L.M. Plum, L. Rink, H. Haase, The Essential Toxin: Impact of Zinc on Human Health, Int. J. Environ. Res. Public Health. 7 (2010) 1342–1365. doi:10.3390/ijerph7041342.

[15] J. Kubásek, D. Vojtěch, I. Pospíšilová, A. Michalcová, J. Maixner, Microstructure and mechanical properties of the micrograined hypoeutectic Zn–Mg alloy, Int. J. Miner. Metall. Mater. 23 (2016). doi:10.1007/s12613-016-1336-7.

[16] J. Niu, Z. Tang, H. Huang, J. Pei, H. Zhang, G. Yuan, W. Ding, Research on a Zn-Cu alloy as a biodegradable material for potential vascular stents application, Mater. Sci. Eng. C. 69 (2016) 407–413. doi:10.1016/j.msec.2016.06.082.

[17] H. Li, H. Yang, Y. Zheng, F. Zhou, K. Qiu, X. Wang, Design and characterizations of novel biodegradable ternary Zn-based alloys with IIA nutrient alloying elements Mg, Ca and Sr, Mater. Des. 83 (2015) 95–102. doi:10.1016/j.matdes.2015.05.089.

[18] D. Hernández-Escobar, S. Champagne, H. Yilmazer, B. Dikici, C.J. Boehlert, H. Hermawan, Current status and perspectives of zinc-based absorbable alloys for biomedical applications, Acta Biomater. 97 (2019) 1–22. doi:https://doi.org/10.1016/j.actbio.2019.07.034.

[19] J. Venezuela, M.S. Dargusch, The influence of alloying and fabrication techniques on the mechanical properties, biodegradability and biocompatibility of zinc: A comprehensive review, Acta Biomater. 87 (2019) 1–40. doi:10.1016/J.ACTBIO.2019.01.035.

[20] R.Z. Valiev, Y. Estrin, Z. Horita, T.G. Langdon, M.J. Zehetbauer, Y.T. Zhu, Fundamentals of Superior Properties in Bulk NanoSPD Materials, Mater. Res. Lett. 3831 (2015) 1–21. doi:10.1080/21663831.2015.1060543.

[21] R.Z. Valiev, I. V Alexandrov, Y.T. Zhu, T.C. Lowe, Paradox of strength and ductility in metals processed by severe plastic deformation, J. Mater. Res. 17 (2002) 5–8. doi:10.1557/JMR.2002.0002.

[22] P. Kumar, M. Kawasaki, T.G. Langdon, Review: Overcoming the paradox of strength and ductility in ultrafine-grained materials at low temperatures, J. Mater. Sci. 51 (2016) 7–18. doi:10.1007/s10853-015-9143-5.

[23] E. Bagherpour, N. Pardis, M. Reihanian, R. Ebrahimi, An overview on severe plastic deformation: research status, techniques classification, microstructure evolution, and applications, Int. J. Adv. Manuf. Technol. (2019). doi:10.1007/s00170-018-2652-z.

[24] J.K. Han, T. Herndon, J. il Jang, T.G. Langdon, M. Kawasaki, Synthesis of Hybrid Nanocrystalline Alloys by Mechanical Bonding through High-Pressure Torsion, Adv. Eng. Mater. (2020) 1901289. doi:10.1002/adem.201901289.

[25] M. Kawasaki, J.-K. Han, D.-H. Lee, J. Jang, T.G. Langdon, Fabrication of nanocomposites through diffusion bonding under high-pressure torsion, J. Mater. Res. (2018) 1–11. doi:10.1557/jmr.2018.205.

[26] K.A. McCall, C. Huang, C.A. Fierke, Function and Mechanism of Zinc Metalloenzymes, J. Nutr. 130 (2000) 1437S-1446S. doi:10.1093/jn/130.5.1437S.

[27] K.H. Brown, J.M. Peerson, J. Rivera, L.H. Allen, Effect of supplemental zinc on the growth and serum zinc concentrations of prepubertal children: a meta-analysis of randomized controlled trials, Am. J. Clin. Nutr. 75 (2002) 1062–1071. doi:10.1093/ajcn/75.6.1062.

[28] International Zinc Nutrition Consultative Group (IZiNCG), K.H. Brown, J.A. Rivera, Z. Bhutta, R.S. Gibson, J.C. King, B. Lönnerdal, M.T. Ruel, B. Sandtröm, E. Wasantwisut, C. Hotz, International Zinc Nutrition Consultative Group (IZiNCG) technical document #1. Assessment of the risk of zinc deficiency in populations and options for its control., Food Nutr. Bull. 25 (2004) S99-203. http://www.ncbi.nlm.nih.gov/pubmed/18046856.

[29] P. Trumbo, S. Schlicker, A.A. Yates, M. Poos, Dietary Reference Intakes for Energy, Carbohydrate, Fiber, Fat, Fatty Acids, Cholesterol, Protein and Amino Acids, J. Am. Diet. Assoc. 102 (2002) 1621–1630. doi:10.1016/S0002-8223(02)90346-9.

[30] S. Fairweather-Tait, R.F. Hurrell, Bioavailability of Minerals and Trace Elements, Nutr. Res. Rev. 9 (1996) 295. doi:10.1079/NRR19960016.

[31] J. Nriagu, Zinc Toxicity in Humans Introduction Functions of Zinc in Humans Epidemiology Acute Health Effects Chronic and Subchronic Toxicity Potential for Zinc Accumulation Further Reading, in: Encycl. Environ. Heal., 2011: pp. 801–807. doi:https://doi.org/10.1016/b978-0-444-52272-6.00675-9.

[32] P.J. Little, R. Bhattacharya, A.E. Moreyra, I.L. Korichneva, Zinc and cardiovascular disease., Nutrition. 26 (2010) 1050–7. doi:10.1016/j.nut.2010.03.007.

[33] W. Maret, H.H. Sandstead, Zinc requirements and the risks and benefits of zinc supplementation, J. Trace Elem. Med. Biol. 20 (2006) 3–18. doi:10.1016/J.JTEMB.2006.01.006.

[34] J. Ma, N. Zhao, D. Zhu, Endothelial Cellular Responses to Biodegradable Metal Zinc, ACS Biomater. Sci. Eng. 1 (2015). doi:10.1021/acsbiomaterials.5b00319.

[35] N.S. Murni, M.S. Dambatta, S.K. Yeap, G.R.A. Froemming, H. Hermawan, Cytotoxicity evaluation of biodegradable Zn-3Mg alloy toward normal human osteoblast cells, Mater. Sci. Eng. C. (2015). doi:10.1016/j.msec.2015.01.056.

[36] E.R. Shearier, P.K. Bowen, W. He, A. Drelich, J. Drelich, J. Goldman, F. Zhao, In Vitro Cytotoxicity, Adhesion, and Proliferation of Human Vascular Cells Exposed to Zinc, ACS Biomater. Sci. Eng. 2 (2016) 634–642. doi:10.1021/acsbiomaterials.6b00035.

[37] C.J. Krones, B. Klosterhalfen, N. Butz, F. Hoelzl, K. Junge, M. Stumpf, C. Peiper, U. Klinge, V. Schumpelick, Effect of zinc pretreatment on pulmonary endothelial cells in vitro and pulmonary function in a porcine model of endotoxemia, J. Surg. Res. 123 (2005) 251–256. doi:10.1016/J.JSS.2004.08.024.

[38] J. Ma, N. Zhao, D. Zhu, Bioabsorbable zinc ion induced biphasic cellular responses in vascular smooth muscle cells, Sci. Rep. 6 (2016) 26661. doi:10.1038/srep26661.

[39] D. Zhu, Y. Su, M.L. Young, J. Ma, Y. Zheng, L. Tang, Biological Responses and Mechanisms of Human Bone Marrow Mesenchymal Stem Cells to Zn and Mg Biomaterials, ACS Appl. Mater. Interfaces. 9 (2017) 27453–27461. doi:10.1021/acsami.7b06654.

[40] H.R. Bakhsheshi-Rad, E. Hamzah, H.T. Low, M. Kasiri-Asgarani, S. Farahany, E. Akbari, M.H. Cho, Fabrication of biodegradable Zn-Al-Mg alloy: Mechanical properties, corrosion behavior, cytotoxicity and antibacterial activities, Mater. Sci. Eng. C. 73 (2017) 215–219. doi:10.1016/j.msec.2016.11.138.

[41] C. Zhao, H. Wu, P. Hou, J. Ni, P. Han, X. Zhang, Enhanced corrosion resistance and antibacterial property of Zn doped DCPD coating on biodegradable Mg, Mater. Lett. 180 (2016) 42–46. doi:10.1016/J.MATLET.2016.04.035.

[42] C. Xiao, L. Wang, Y. Ren, S. Sun, E. Zhang, C. Yan, Q. Liu, X. Sun, F. Shou, J. Duan, H. Wang, G. Qin, Indirectly extruded biodegradable Zn-0.05wt%Mg alloy with improved strength and ductility: In vitro and in vivo studies, J. Mater. Sci. Technol. 34 (2018) 1618–1627. doi:10.1016/j.jmst.2018.01.006.

[43] Y. Su, H. Yang, J. Gao, Y. Qin, Y. Zheng, D. Zhu, Interfacial Zinc Phosphate is the Key to Controlling Biocompatibility of Metallic Zinc Implants, Adv. Sci. (2019) 1900112. doi:10.1002/advs.201900112.

[44] H.F. Li, X.H. Xie, Y.F. Zheng, Y. Cong, F.Y. Zhou, K.J. Qiu, X. Wang, S.H. Chen, L. Huang, L. Tian, L. Qin, Development of biodegradable Zn-1X binary alloys with nutrient alloying elements Mg, Ca and Sr, Sci. Rep. 5 (2015) 1–14. doi:https://doi.org/10.1038/srep10719.

[45] P.K. Bowen, J. Drelich, J. Goldman, Zinc exhibits ideal physiological corrosion behavior for bioabsorbable stents, Adv. Mater. (2013). doi:10.1002/adma.201300226.

[46] H. Yang, C. Wang, C. Liu, H. Chen, Y. Wu, J. Han, Z. Jia, W. Lin, D. Zhang, W. Li, W. Yuan, H. Guo, H. Li, G. Yang, D. Kong, D. Zhu, K. Takashima, L. Ruan, J. Nie, X. Li, Y. Zheng, Evolution of the degradation mechanism of pure zinc stent in the one-year study of rabbit abdominal aorta model, Biomaterials. 145 (2017) 92–105.

doi:10.1016/J.BIOMATERIALS.2017.08.022.

[47] R.F. Lynch, Zinc: Alloying, Thermomechanical Processing, Properties, and Applications, in: Encycl. Mater. Sci. Technol., 2004. doi:10.1016/b0-08-043152-6/01786-1.

[48] R.A. Yokel, P.J. McNamara, Aluminium Toxicokinetics: An Updated MiniReview, Pharmacol. Toxicol. 88 (2001) 159–167. doi:10.1034/j.1600-0773.2001.d01-98.x.

[49] G. Hercz, D.L. Andress, H.G. Nebeker, J.H. Shinaberger, D.J. Sherrard, J.W. Coburn, Reversal of Aluminum-Related Bone Disease After Substituting Calcium Carbonate for Aluminum Hydroxide, Am. J. Kidney Dis. 11 (1988) 70–75. doi:10.1016/S0272-6386(88)80179-3.

[50] G. Dunea, S.D. Mahurkar, B. Mamdani, E.C. Smith, Role of aluminum in dialysis dementia, Ann. Intern. Med. 88 (1978) 502–4. doi:10.7326/0003-4819-88-4-502.

[51] A. Mirza, A. King, C. Troakes, C. Exley, Aluminium in brain tissue in familial Alzheimer's disease, J. Trace Elem. Med. Biol. 40 (2017) 30–36. doi:10.1016/j.jtemb.2016.12.001.

[52] C.J. (Colin J. Smithells, E.A. (Eric A. Brandes, G.B. Brook, Smithells light metals handbook, Butterworth-Heinemann, 1998.

[53] E. Mostaed, M. Sikora-Jasinska, A. Mostaed, S. Loffredo, A.G. Demir, B. Previtali, D. Mantovani, R. Beanland, M. Vedani, Novel Zn-based alloys for biodegradable stent applications: Design, development and in vitro degradation, J. Mech. Behav. Biomed. Mater. (2016). doi:10.1016/j.jmbbm.2016.03.018.

[54] H. Jin, S. Zhao, R. Guillory, P.K. Bowen, Z. Yin, A. Griebel, J. Schaffer, E.J. Earley, J. Goldman, J.W. Drelich, Novel high-strength, low-alloys Zn-Mg (< 0.1 wt% Mg) and their arterial biodegradation, Mater. Sci. Eng. C. 84 (2018) 67–79. doi:10.1016/j.msec.2017.11.021.

[55] X. Liu, J. Sun, K. Qiu, Y. Yang, Z. Pu, L. Li, Y. Zheng, Effects of alloying elements (Ca and Sr) on microstructure, mechanical property and in vitro corrosion behavior of biodegradable Zn-1.5Mg alloy, J. Alloys Compd. 664 (2016) 444–452. doi:10.1016/j.jallcom.2015.10.116.

[56] Z. Tang, J. Niu, H. Huang, H. Zhang, J. Pei, J. Ou, G. Yuan, Potential biodegradable Zn-Cu binary alloys developed for cardiovascular implant applications, J. Mech. Behav. Biomed. Mater. 72 (2017) 182–191. doi:10.1016/j.jmbbm.2017.05.013.

[57] Z. Tang, H. Huang, J. Niu, L. Zhang, H. Zhang, J. Pei, J. Tan, G. Yuan, Design and characterizations of novel biodegradable Zn-Cu-Mg alloys for potential biodegradable implants, Mater. Des. 117 (2017) 84–94. doi:10.1016/j.matdes.2016.12.075.

[58] S. Sun, Y. Ren, L. Wang, B. Yang, H. Li, G. Qin, Abnormal effect of Mn addition on the

mechanical properties of as-extruded Zn alloys, Mater. Sci. Eng. A. 701 (2017) 129–133. doi:10.1016/J.MSEA.2017.06.037.

[59] P. Sotoudeh Bagha, S. Khaleghpanah, S. Sheibani, M. Khakbiz, A. Zakeri, Characterization of nanostructured biodegradable Zn-Mn alloy synthesized by mechanical alloying, J. Alloys Compd. 735 (2018) 1319–1327. doi:10.1016/j.jallcom.2017.11.155.

[60] R.Z. Valiev, A.P. Zhilyaev, T.G. Langdon, Bulk Nanostructured Materials, 2009. doi:10.1002/9783527626892.

[61] R. Valiev, Nanostructuring of metals by severe plastic deformation for advanced properties., Nat. Mater. 3 (2004) 511–516. doi:10.1038/nmat1180.

[62] R.Z. Valiev, Y. Estrin, Z. Horita, T.G. Langdon, M.J. Zehetbauer, Y. Zhu, Producing Bulk Ultrafine-Grained Materials by Severe Plastic Deformation: Ten Years Later, Jom. 68 (2016) 1216–1226. doi:10.1007/s11837-016-1820-6.

[63] R.Z. Valiev, R.K. Islamgaliev, I. V. Alexandrov, Bulk nanostructured materials from severe plastic deformation, Prog. Mater. Sci. 45 (2000) 103–189. doi:10.1016/S0079-6425(99)00007-9.

[64] L. Wang, Y. Shi, Y. Zhang, M. Li, High tensile ductility and strength in a gradient structured Zr, Mater. Lett. 228 (2018) 500–503. doi:10.1016/j.matlet.2018.06.084.

[65] K.M. Youssef, R.O. Scattergood, K.L. Murty, J.A. Horton, C.C. Koch, Ultrahigh strength and high ductility of bulk nanocrystalline copper, Appl. Phys. Lett. 87 (2005) 091904. doi:10.1063/1.2034122.

[66] A. Vinogradov, D. Orlov, Y. Estrin, Improvement of fatigue strength of a Mg-Zn-Zr alloy by integrated extrusion and equal-channel angular pressing, Scr. Mater. 67 (2012) 209–212. doi:10.1016/j.scriptamat.2012.04.021.

[67] M. Kawasaki, T.G. Langdon, Developing superplasticity and a deformation mechanism map for the Zn-Al eutectoid alloy processed by high-pressure torsion, Mater. Sci. Eng. A. 528 (2011) 6140–6145. doi:10.1016/j.msea.2011.04.053.

[68] D. V. Shangina, J. Gubicza, E. Dodony, N.R. Bochvar, P.B. Straumal, N.Y. Tabachkova, S. V. Dobatkin, Improvement of strength and conductivity in Cu-alloys with the application of high pressure torsion and subsequent heat-treatments, in: J. Mater. Sci., Kluwer Academic Publishers, 2014: pp. 6674–6681. doi:10.1007/s10853-014-8339-4.

[69] J.M. Cubero-Sesin, M. Arita, Z. Horita, High Strength and Electrical Conductivity of Al-Fe Alloys Produced by Synergistic Combination of High-Pressure Torsion and Aging, Adv. Eng. Mater. 17 (2015) 1792–1803. doi:10.1002/adem.201500103.

[70] K. Suehiro, S. Nishimura, Z. Horita, S. Mitani, K. Takanashi, H. Fujimori, High-pressure

torsion for production of magnetoresistance in Cu-Co alloy, J. Mater. Sci. 43 (2008) 7349–7353. doi:10.1007/s10853-008-2813-9.

[71] M. Krystian, M.J. Zehetbauer, H. Kropik, B. Mingler, G. Krexner, Hydrogen storage properties of bulk nanostructured ZK60 Mg alloy processed by Equal Channel Angular Pressing, in: J. Alloys Compd., Elsevier Ltd, 2011: pp. S449–S455. doi:10.1016/j.jallcom.2011.01.029.

[72] T. Nishizaki, S. Lee, Z. Horita, T. Sasaki, N. Kobayashi, Superconducting properties in bulk nanostructured niobium prepared by high-pressure torsion, Phys. C Supercond. Its Appl. 493 (2013) 132–135. doi:10.1016/j.physc.2013.03.046.

[73] P.W. Bridgman, On torsion combined with compression, J. Appl. Phys. 14 (1943) 273–283. doi:10.1063/1.1714987.

[74] V.M. Segal, Materials processing by simple shear, Mater. Sci. Eng. A. 197 (1995) 157–164. doi:10.1016/0921-5093(95)09705-8.

[75] Y. Saito, N. Tsuji, H. Utsunomiya, T. Sakai, R.G. Hong, Ultra-fine grained bulk aluminum produced by accumulative roll-bonding (ARB) process, Scr. Mater. 39 (1998) 1221–1227. doi:10.1016/S1359-6462(98)00302-9.

[76] A. Hohenwarter, A. Bachmaier, B. Gludovatz, S. Scheriau, R. Pippan, Technical parameters affecting grain refinement by high pressure torsion, in: Int. J. Mater. Res., 2009: pp. 1653–1661. doi:10.3139/146.110224.

[77] R. Pippan, S. Scheriau, A. Hohenwarter, M. Hafok, Advantages and Limitations of HPT: A Review, Mater. Sci. Forum. 584–586 (2008) 16–21. doi:10.4028/www.scientific.net/MSF.584-586.16.

[78] J.-K. Han, J. Jang, T.G. Langdon, M. Kawasaki, Bulk-State Reactions and Improving the Mechanical Properties of Metals through High-Pressure Torsion, Mater. Trans. 60 (2019) 1131–1138. doi:https://doi.org/10.2320/matertrans.MF201908.

[79] R.Z. Valiev, Y.V. Ivanisenko, E.F. Rauch, B. Baudelet, Structure and deformaton behaviour of Armco iron subjected to severe plastic deformation, Acta Mater. 44 (1996) 4705–4712. doi:10.1016/S1359-6454(96)00156-5.

[80] N. Polakowski, E. Ripling, Strength and Structure of Engineering Materials, Prentice-Hall, Englewood Cliffs. (1966). doi:10.13182/nse66-a28179.

[81] A.P. Zhilyaev, T.G. Langdon, Using high-pressure torsion for metal processing: Fundamentals and applications, Prog. Mater. Sci. 53 (2008) 893–979. doi:10.1016/j.pmatsci.2008.03.002.

[82] R. Kapoor, Severe Plastic Deformation of Materials, in: Mater. Under Extrem. Cond.,

Elsevier, 2017: pp. 717–754. doi:10.1016/B978-0-12-801300-7.00020-6.

[83] M. Kawasaki, H.J. Lee, B. Ahn, A.P. Zhilyaev, T.G. Langdon, Evolution of hardness in ultrafine-grained metals processed by high-pressure torsion, J. Mater. Res. Technol. 3 (2014) 311–318. doi:10.1016/j.jmrt.2014.06.002.

[84] M. Kawasaki, Different models of hardness evolution in ultrafine-grained materials processed by high-pressure torsion, J. Mater. Sci. 49 (2014) 18–34. doi:10.1007/s10853-013-7687-9.

[85] K. Edalati, Z. Horita, High-pressure torsion of pure metals: Influence of atomic bond parameters and stacking fault energy on grain size and correlation with hardness, Acta Mater. 59 (2011) 6831–6836. doi:10.1016/j.actamat.2011.07.046.

[86] K. Oh-ishi, K. Edalati, H.S. Kim, K. Hono, Z. Horita, High-pressure torsion for enhanced atomic diffusion and promoting solid-state reactions in the aluminum–copper system, Acta Mater. 61 (2013) 3482–3489. doi:10.1016/J.ACTAMAT.2013.02.042.

[87] J.-K. Han, D.K. Han, G.Y. Liang, J.-I. Jang, T.G. Langdon, M. Kawasaki, Direct Bonding of Aluminum-Copper Metals through High-Pressure Torsion Processing, Adv. Eng. Mater. 20 (2018) 1800642. doi:10.1002/adem.201800642.

[88] V.N. Danilenko, S.N. Sergeev, J.A. Baimova, G.F. Korznikova, K.S. Nazarov, R.K. Khisamov, A.M. Glezer, R.R. Mulyukov, An approach for fabrication of Al-Cu composite by high pressure torsion, Mater. Lett. 236 (2019) 51–55. doi:10.1016/j.matlet.2018.09.158.

[89] M. Kawasaki, B. Ahn, H.-J. Lee, A.P. Zhilyaev, T.G. Langdon, Using high-pressure torsion to process an aluminum-magnesium nanocomposite through diffusion bonding, Acta Mater. 59 (2015) 1974–1985. doi:10.1016/j.actamat.2010.11.063.

[90] J.K. Han, H.J. Lee, J. il Jang, M. Kawasaki, T.G. Langdon, Micro-mechanical and tribological properties of aluminum-magnesium nanocomposites processed by high-pressure torsion, Mater. Sci. Eng. A. 684 (2017) 318–327. doi:10.1016/j.msea.2016.12.067.

[91] M. Kawasaki, S.H. Jung, J.M. Park, J. Lee, J. il Jang, J.K. Han, Mechanical Bonding of Aluminum Hybrid Alloy Systems through High-Pressure Torsion, Adv. Eng. Mater. 22 (2020) adem.201900483. doi:10.1002/adem.201900483.

[92] M. Kawasaki, J. Jang, Micro-Mechanical Response of an Al-Mg Hybrid System Synthesized by High-Pressure Torsion, Materials (Basel). 10 (2017) 596. doi:10.3390/ma10060596.

[93] B. Ahn, H.J. Lee, I.C. Choi, M. Kawasaki, J. Il Jang, T.G. Langdon, Micro-Mechanical Behavior of an Exceptionally Strong Metal Matrix Nanocomposite Processed by High-Pressure Torsion, Adv. Eng. Mater. 18 (2016) 1001–1008. doi:10.1002/adem.201500520.

[94] J.-K. Han, J.-M. Park, W. Ruan, K.T. Carpenter, A. Tabei, J. Jang, M. Kawasaki, Size Effect on Microstructural Evolution and Micromechanical Responses of Mechanically Bonded Aluminum and Magnesium by High-Pressure Torsion, Adv. Eng. Mater. (2019) 1900971. doi:10.1002/adem.201900971.

[95] B. Ahn, A.P. Zhilyaev, H.-J. Lee, M. Kawasaki, T.G. Langdon, Rapid synthesis of an extra hard metal matrix nanocomposite at ambient temperature, Mater. Sci. Eng. A. 635 (2015) 109–117. doi:10.1016/j.msea.2015.03.042.

[96] N. Ibrahim, M. Peterlechner, F. Emeis, M. Wegner, S. V. Divinski, G. Wilde, Mechanical alloying via high-pressure torsion of the immiscible Cu50Ta50 system, Mater. Sci. Eng. A. 685 (2017) 19–30. doi:https://doi.org/10.1016/j.msea.2016.12.106.

[97] S.O. Rogachev, R. V. Sundeev, V.M. Khatkevich, Evolution of the structure and strength of steel/vanadium alloy/steel hybrid material during severe plastic deformation, Mater. Lett. 173 (2016) 123–126. doi:10.1016/j.matlet.2016.03.044.

[98] S.O. Rogachev, S.A. Nikulin, A.B. Rozhnov, V.M. Khatkevich, T.A. Nechaykina, M. V. Gorshenkov, R. V. Sundeev, Multilayer "Steel/Vanadium Alloy/Steel" Hybrid Material Obtained by High-Pressure Torsion at Different Temperatures, Metall. Mater. Trans. A. 48 (2017) 6091–6101. doi:10.1007/s11661-017-4342-0.

[99] S.O. Rogachev, S.A. Nikulin, V.M. Khatkevich, N.Y. Tabachkova, R. V. Sundeev, Structure Formation and Hardening of the Hybrid Material Based on Vanadium and Zirconium Alloys during High-Pressure Torsion, Russ. Metall. 2018 (2018) 372–376. doi:10.1134/S0036029518040110.

[100] B. Beausir, J. Scharnweber, J. Jaschinski, H.G. Brokmeier, C.G. Oertel, W. Skrotzki, Plastic anisotropy of ultrafine grained aluminium alloys produced by accumulative roll bonding, Mater. Sci. Eng. A. 527 (2010) 3271–3278. doi:10.1016/j.msea.2010.02.006.

[101] A. Azushima, R. Kopp, A. Korhonen, D.Y. Yang, F. Micari, G.D. Lahoti, P. Groche, J. Yanagimoto, N. Tsuji, A. Rosochowski, A. Yanagida, Severe plastic deformation (SPD) processes for metals, CIRP Ann. - Manuf. Technol. 57 (2008) 716–735. doi:10.1016/j.cirp.2008.09.005.

[102] Y.F. Sun, H. Fujii, T. Nakamura, N. Tsuji, D. Todaka, M. Umemoto, Critical strain for mechanical alloying of Cu-Ag, Cu-Ni and Cu-Zr by high-pressure torsion, Scr. Mater. 65 (2011) 489–492. doi:10.1016/j.scriptamat.2011.06.005.

[103] T. Miyazaki, D. Terada, Y. Miyajima, C. Suryanarayana, R. Murao, Y. Yokoyama, K. Sugiyama, M. Umemoto, Y. Todaka, N. Tsuji, Synthesis of non-equilibrium phases in immiscible metals mechanically mixed by high pressure torsion, in: J. Mater. Sci., Springer, 2011: pp. 4296–4301. doi:10.1007/s10853-010-5240-7.

[104] O. Bouaziz, H.S. Kim, Y. Estrin, Architecturing of Metal-Based Composites with

Concurrent Nanostructuring: A New Paradigm of Materials Design, Adv. Eng. Mater. 15 (2013) 336–340. doi:10.1002/adem.201200261.

[105] A.P. Zhilyaev, G. V. Nurislamova, B.K. Kim, M.D. Baró, J.A. Szpunar, T.G. Langdon, Experimental parameters influencing grain refinement and microstructural evolution during high-pressure torsion, Acta Mater. 51 (2003) 753–765. doi:10.1016/S1359-6454(02)00466-4.

[106] A. Hohenwarter, R. Pippan, Sample Size and Strain-Rate-Sensitivity Effects on the Homogeneity of High-Pressure Torsion Deformed Disks, Metall. Mater. Trans. A Phys. Metall. Mater. Sci. 50 (2019) 601–608. doi:10.1007/s11661-018-4989-1.

[107] T. Fujioka, Z. Horita, Development of high-pressure sliding process for microstructural refinement of rectangular metallic sheets, Mater. Trans. 50 (2009) 930–933. doi:10.2320/matertrans.MRP2008445.

[108] L.S. Toth, V.Q. Vu, S.S. Dhinwal, Y. Zhao, R. Massion, C. Chen, C.F. Davis, T.C. Lowe, The mechanics of High Pressure Compressive Shearing with application to ARMCO® steel, Mater. Charact. 154 (2019) 127–137. doi:10.1016/j.matchar.2019.05.039.

[109] K. Edalati, Z. Horita, Continuous high-pressure torsion, in: J. Mater. Sci., Springer, 2010: pp. 4578–4582. doi:10.1007/s10853-010-4381-z.

[110] Z. Lee, F. Zhou, R.Z. Valiev, E.J. Lavernia, S.R. Nutt, Microstructure and microhardness of cryomilled bulk nanocrystalline Al-7.5%Mg alloy consolidated by high pressure torsion, Scr. Mater. 51 (2004) 209–214. doi:10.1016/j.scriptamat.2004.04.016.

[111] M.I. Abd El Aal, E. Yoo Yoon, H. Seop Kim, Recycling of AlSi8Cu3 alloy chips via high pressure torsion, Mater. Sci. Eng. A. 560 (2013) 121–128. doi:10.1016/j.msea.2012.09.045.

[112] K. Edalati, Z. Horita, Universal Plot for Hardness Variation in Pure Metals Processed by High-Pressure Torsion, Mater. Trans. 51 (2010) 1051–1054. doi:10.2320/matertrans.M2009431.

[113] D.A. Rigney, S. Karthikeyan, The evolution of tribomaterial during sliding: A brief introduction, in: Tribol. Lett., Springer, 2010: pp. 3–7. doi:10.1007/s11249-009-9498-3.

[114] N.Q. Vo, J. Zhou, Y. Ashkenazy, D. Schwen, R.S. Averback, P. Bellon, Atomic mixing in metals under shear deformation, JOM. 65 (2013) 382–389. doi:10.1007/s11837-012-0542-7.

[115] Y. Ashkenazy, N.Q. Vo, D. Schwen, R.S. Averback, P. Bellon, Shear induced chemical mixing in heterogeneous systems, Acta Mater. 60 (2012) 984–993. doi:10.1016/j.actamat.2011.11.014.

[116] S.N. Arshad, T.G. Lach, M. Pouryazdan, H. Hahn, P. Bellon, S.J. Dillon, R.S. Averback,

Dependence of shear-induced mixing on length scale, Scr. Mater. 68 (2013) 215–218. doi:10.1016/j.scriptamat.2012.10.027.

[117] S. V. Divinski, J. Ribbe, D. Baither, G. Schmitz, G. Reglitz, H. Rösner, K. Sato, Y. Estrin, G. Wilde, Nano- and micro-scale free volume in ultrafine grained Cu-1 wt.%Pb alloy deformed by equal channel angular pressing, Acta Mater. 57 (2009) 5706–5717. doi:10.1016/j.actamat.2009.07.066.

[118] K.S. Kormout, R. Pippan, A. Bachmaier, Deformation-Induced Supersaturation in Immiscible Material Systems during High-Pressure Torsion, Adv. Eng. Mater. 19 (2017) 1–19. doi:10.1002/adem.201600675.

[119] R.Z. Valiev, A. V. Sergueeva, A.K. Mukherjee, The effect of annealing on tensile deformation behavior of nanostructured SPD titanium, Scr. Mater. 49 (2003) 669–674. doi:10.1016/S1359-6462(03)00395-6.

[120] M. Kawasaki, S.H. Jung, J.-M. Park, J. Lee, J. Jang, J.-K. Han, Mechanical Bonding of Aluminum Hybrid Alloy Systems through High-Pressure Torsion, Adv. Eng. Mater. 22 (2020) 1900483. doi:10.1002/adem.201900483.

[121] M. Kawasaki, S.N. Alhajeri, C. Xu, T.G. Langdon, The development of hardness homogeneity in pure aluminum and aluminum alloy disks processed by high-pressure torsion, Mater. Sci. Eng. A. 529 (2011) 345–351. doi:10.1016/j.msea.2011.09.039.

[122] H.-J. Lee, B. Ahn, M. Kawasaki, T.G. Langdon, Evolution in hardness and microstructure of ZK60A magnesium alloy processed by high-pressure torsion, J. Mater. Res. Technol. 4 (2015) 18–25. doi:10.1016/J.JMRT.2014.10.015.

[123] K. Edalati, Y. Hashiguchi, P.H.R. Pereira, Z. Horita, T.G. Langdon, Effect of temperature rise on microstructural evolution during high-pressure torsion, Mater. Sci. Eng. A. 714 (2018) 167–171. doi:10.1016/j.msea.2017.12.095.

[124] D. Hernández-Escobar, R.R. Unocic, M. Kawasaki, C.J. Boehlert, High-pressure torsion processing of Zn–3Mg alloy and its hybrid counterpart: A comparative study, J. Alloys Compd. 831 (2020) 154891. doi:10.1016/j.jallcom.2020.154891.

[125] S.L. Flegler, J.W. Heckman, K.L. Klomparens, Scanning and transmission electron microscopy: an introduction, Oxford University Press, 1994. doi:10.5860/CHOICE.31-4353.

[126] Astm Standard, E112-12:Standard Test Methods for Determining Average Grain Size, ASTM Int. E112-12 (2012) 1–27. doi:10.1520/E0112-12.1.4.

[127] D. Hernández-Escobar, J. Marcus, J.-K. Han, R.R. Unocic, M. Kawasaki, C.J. Boehlert, Effect of post-deformation annealing on the microstructure and micro-mechanical behavior of Zn–Mg hybrids processed by High-Pressure Torsion, Mater. Sci. Eng. A. 771 (2020)

138578. doi:10.1016/j.msea.2019.138578.

[128] H.G.J. Moseley, The high-frequency spectra of the elements, London, Edinburgh, Dublin Philos. Mag. J. Sci. 26 (1913) 1024–1034. doi:10.1080/14786441308635052.

[129] J.I. Goldstein, D.E. Newbury, J.R. Michael, N.W.M. Ritchie, J.H.J. Scott, D.C. Joy, Scanning Electron Microscopy and X-Ray Microanalysis, Springer New York, New York, NY, 2018. doi:10.1007/978-1-4939-6676-9.

[130] R. Castaing, Electron Probe Microanalysis, Adv. Electron. Electron Phys. 13 (1960) 317–386. doi:10.1016/S0065-2539(08)60212-7.

[131] D.B. Williams, C.B. Carter, Transmission electron microscopy: A textbook for materials science, Springer, 2009. doi:10.1007/978-0-387-76501-3.

[132] L.A. Giannuzzi, B.W. Kempshall, S.M. Schwarz, J.K. Lomness, B.I. Prenitzer, F.A. Stevie, FIB lift-out specimen preparation techniques ex-situ and in-situ methods, in: Introd. to Focus. Ion Beams Instrumentation, Theory, Tech. Pract., Springer US, 2005: pp. 201–228. doi:10.1007/0-387-23313-X_10.

[133] M. Klinger, A. Jäger, Crystallographic Tool Box (CrysTBox): Automated tools for transmission electron microscopists and crystallographers, J. Appl. Crystallogr. 48 (2015) 2012–2018. doi:10.1107/S1600576715017252.

[134] B.D. Cullity, S.R. Stock, Elements of X-ray diffraction, 3rd edition, 2001.

[135] D.F. Swinehart, The Beer-Lambert Law, J. Chem. Educ. 39 (1962) 333. doi:10.1021/ed039p333.

[136] D.J. Larson, T.J. Prosa, R.M. Ulfig, B.P. Geiser, T.F. Kelly, Local Electrode Atom Probe Tomography, Springer New York, New York, NY, 2013. doi:10.1007/978-1-4614-8721-0.

[137] ASTM, ASTM E384: Standard Test Method for Microindentation Hardness of Materials, Annu. B. ASTM Stand. (2016) 1–42. https://www.astm.org/Standards/E384.

[138] B.N. Lucas, W.C. Oliver, Indentation Power-Law Creep of High-Purity Indium, n.d. https://link.springer.com/content/pdf/10.1007%2Fs11661-999-0051-7.pdf.

[139] C.L. Wang, Y.H. Lai, J.C. Huang, T.G. Nieh, Creep of nanocrystalline nickel: A direct comparison between uniaxial and nanoindentation creep, Scr. Mater. 62 (2010) 175–178. doi:10.1016/j.scriptamat.2009.10.021.

[140] I.-C. Choi, B.-G. Yoo, Y.-J. Kim, M.-Y. Seok, Y. Wang, J. Jang, Estimating the stress exponent of nanocrystalline nickel: Sharp vs. spherical indentation, Scr. Mater. 65 (2011) 300–303. doi:10.1016/J.SCRIPTAMAT.2011.04.031.

[141] E.A. Brandes, G.B. Brook, Smithells Metals Reference Book, 7th ed., Oxford: Butterworth-Heinemann, 1992. doi:10.1016/B978-075067509-3/50014-2.

[142] E. Broitman, Indentation Hardness Measurements at Macro-, Micro-, and Nanoscale: A Critical Overview, Tribol. Lett. 65 (n.d.). doi:10.1007/s11249-016-0805-5.

[143] W.C. Oliver, G.M. Pharr, An improved technique for determining hardness and elastic modulus using load and displacement sensing indentation experiments, (2018). doi:10.1557/JMR.1992.1564.

[144] C. Charitidis, Nanomechanical properties and nanoscale deformation of engineering metals and alloys, in: Mater. Surf. Eng., Elsevier, 2012: pp. 23–59. doi:10.1533/9780857096036.23.

[145] D. Chicot, M. Yetna N'Jock, E.S. Puchi-Cabrera, A. Iost, M.H. Staia, G. Louis, G. Bouscarrat, R. Aumaitre, A contact area function for Berkovich nanoindentation: Application to hardness determination of a TiHfCN thin film, Thin Solid Films. 558 (2014) 259–266. doi:10.1016/J.TSF.2014.02.044.

[146] J.R. Taylor, An Introduction to Error Analysis: The Study of Uncertainties in Physical Measurements, 1997. doi:10.1063/1.882103.

[147] S. Shim, J. Jang, G.M. Pharr, Extraction of flow properties of single-crystal silicon carbide by nanoindentation and finite-element simulation, Acta Mater. 56 (2008) 3824–3832. doi:10.1016/J.ACTAMAT.2008.04.013.

[148] Q. Wei, Strain rate effects in the ultrafine grain and nanocrystalline regimes—influence on some constitutive responses, J. Mater. Sci. 42 (2007) 1709–1727. doi:10.1007/s10853-006-0700-9.

[149] G102-89, Standard Practice for Calculation of Corrosion Rates and Related Information from Electrochemical Measurements, ASTM Int. 89 (2015) 1–7. doi:10.1520/G0102-89R15E01.2.

[150] Z. D., W. C.S., W. C., L. Y., Cellular responses of osteoblast-like cells to 17 elemental metals, J. Biomed. Mater. Res. - Part A. (2017).

[151] X. Tong, D. Zhang, X. Zhang, Y. Su, Z. Shi, K. Wang, J. Lin, Y. Li, J. Lin, C. Wen, Microstructure, mechanical properties, biocompatibility, and in vitro corrosion and degradation behavior of a new Zn–5Ge alloy for biodegradable implant materials, Acta Biomater. 82 (2018) 197–204. doi:10.1016/j.actbio.2018.10.015.

[152] H. Yang, X. Qu, W. Lin, C. Wang, D. Zhu, K. Dai, Y. Zheng, In vitro and in vivo studies on zinc-hydroxyapatite composites as novel biodegradable metal matrix composite for orthopedic applications, Acta Biomater. 71 (2018) 200–214. doi:10.1016/J.ACTBIO.2018.03.007.

[153] R.A. Surmenev, M.A. Surmeneva, A.A. Ivanova, Significance of calcium phosphate coatings for the enhancement of new bone osteogenesis – A review, Acta Biomater. 10 (2014) 557–579. doi:10.1016/j.actbio.2013.10.036.

[154] M. Cozzolino, A.S. Dusso, E. Slatopolsky, Role of calcium-phosphate product and bone-associated proteins on vascular calcification in renal failure., J. Am. Soc. Nephrol. 12 (2001) 2511–6. http://www.ncbi.nlm.nih.gov/pubmed/11675430.

[155] B. Liu, X. Zhang, G.Y. Xiao, Y.P. Lu, Phosphate chemical conversion coatings on metallic substrates for biomedical application: A review, Mater. Sci. Eng. C. 47 (2015) 97–104. doi:10.1016/j.msec.2014.11.038.

[156] Y. Su, K. Wang, J. Gao, Y. Yang, Y.X. Qin, Y. Zheng, D. Zhu, Enhanced cytocompatibility and antibacterial property of zinc phosphate coating on biodegradable zinc materials, Acta Biomater. (2019). doi:10.1016/j.actbio.2019.03.055.

[157] J.M. Ross, Cell-Extracellular Matrix Interactions, in: Front. Tissue Eng., Elsevier, 1998: pp. 15–27. doi:10.1016/b978-008042689-1/50004-2.

[158] U. Geißler, U. Hempel, C. Wolf, D. Scharnweber, H. Worch, K.W. Wenzel, Collagen type I-coating of Ti6A14V promotes adhesion of osteoblasts, J. Biomed. Mater. Res. 51 (2000) 752–760. doi:10.1002/1097-4636(20000915)51:4<752::AID-JBM25>3.0.CO;2-7.

[159] N. Zhao, D. Zhu, Collagen self-assembly on orthopedic magnesium biomaterials surface and subsequent bone cell attachment, PLoS One. 9 (2014) e110420. doi:10.1371/journal.pone.0110420.

[160] M.D. Tyona, A theoritical study on spin coating technique, Adv. Mater. Res. 2 (2013) 195–208. doi:10.12989/amr.2013.2.4.195.

[161] J. anne N. Oliver, Y. Su, X. Lu, P.H. Kuo, J. Du, D. Zhu, Bioactive glass coatings on metallic implants for biomedical applications, Bioact. Mater. 4 (2019) 261–270. doi:10.1016/j.bioactmat.2019.09.002.

[162] A. El-Fiqi, T.H. Kim, M. Kim, M. Eltohamy, J.E. Won, E.J. Lee, H.W. Kim, Capacity of mesoporous bioactive glass nanoparticles to deliver therapeutic molecules, Nanoscale. (2012). doi:10.1039/c2nr31775c.

[163] N. Pajares-Chamorro, X. Chatzistavrou, Bioactive Glass Nanoparticles for Tissue Regeneration, ACS Omega. (2020). doi:10.1021/acsomega.0c00180.

[164] M. Tian, F. Chen, W. Song, Y. Song, Y. Chen, C. Wan, X. Yu, X. Zhang, In vivo study of porous strontium-doped calcium polyphosphate scaffolds for bone substitute applications, J. Mater. Sci. Mater. Med. (2009). doi:10.1007/s10856-009-3713-5.

[165] C. Stähli, M. James-Bhasin, A. Hoppe, A.R. Boccaccini, S.N. Nazhat, Effect of ion release

from Cu-doped 45S5 Bioglass® on 3D endothelial cell morphogenesis, Acta Biomater. (2015). doi:10.1016/j.actbio.2015.03.009.

[166] N. Pajares-Chamorro, Y. Wagley, C. V. Maduka, D.W. Youngstrom, A. Yeger, S.F. Badylak, N.D. Hammer, K. Hankenson, X. Chatzistavrou, Silver-doped bioactive glass particles for in vivo bone tissue regeneration and enhanced methicillin-resistant Staphylococcus aureus (MRSA) inhibition, Mater. Sci. Eng. C. (2020). doi:10.1016/j.msec.2020.111693.

[167] N. Pajares-Chamorro, J. Shook, N.D. Hammer, X. Chatzistavrou, Resurrection of antibiotics that methicillin-resistant Staphylococcus aureus resists by silver-doped bioactive glass-ceramic microparticles, Acta Biomater. (2019). doi:10.1016/j.actbio.2019.07.012.

[168] O. Sakata, M. Nakamura, Grazing Incidence X-Ray Diffraction, in: Springer Ser. Surf. Sci., 2013: pp. 165–190. doi:10.1007/978-3-642-34243-1_6.

[169] ASTM G31-12a - Standard Guide for Laboratory Immersion Corrosion Testing of Metals, (n.d.). doi:10.1520/G0031-12A.

[170] ASTM, ASTM G1-03: Standard Practice for Preparing, Cleaning, and Evaluating Corrosion Test Specimens., ASTM Spec. Tech. Publ. i (2017) 505–510. doi:10.1520/G0001-03R17E01.2.

[171] ISO 10993-5: Biological evaluation of medical devices - Tests for in vitro cytotoxicity, ISO Stand. (2009).

[172] J. Wang, F. Witte, T. Xi, Y. Zheng, K. Yang, Y. Yang, D. Zhao, J. Meng, Y. Li, W. Li, K. Chan, L. Qin, Recommendation for modifying current cytotoxicity testing standards for biodegradable magnesium-based materials, Acta Biomater. 21 (2015) 237–249. doi:10.1016/j.actbio.2015.04.011.

[173] P.D. Fey, J.L. Endres, V.K. Yajjala, T.J. Widhelm, R.J. Boissy, J.L. Bose, K.W. Bayles, A genetic resource for rapid and comprehensive phenotype screening of nonessential Staphylococcus aureus genes, MBio. (2013). doi:10.1128/mBio.00537-12.

[174] D. Hernández-Escobar, Z.U. Rahman, H. Yilmazer, M. Kawasaki, C.J. Boehlert, Microstructural evolution and intermetallic formation in Zn-Mg hybrids processed by High-Pressure Torsion, Philos. Mag. 99 (2019) 557–584. doi:10.1080/14786435.2018.1546962.

[175] I. Pospíšilová, D. Vojtěch, Mechanical properties of Zn-Mg alloys, Metal. 5 (2013) 15–17.

[176] S.-Y. Chang, S.-W. Lee, K.M. Kang, S. Kamado, Y. Kojima, Improvement of Mechanical Characteristics in Severely Plastic-deformed Mg Alloys, Mater. Trans. 45 (2005) 488–492. doi:10.2320/matertrans.45.488.

[177] Y. Cao, M. Kawasaki, Y.B. Wang, S.N. Alhajeri, X.Z. Liao, W.L. Zheng, S.P. Ringer, Y.T.

Zhu, T.G. Langdon, Unusual macroscopic shearing patterns observed in metals processed by high-pressure torsion, J. Mater. Sci. 45 (2010) 4545–4553. doi:10.1007/s10853-010-4485-5.

[178] Y. Cao, Y.B. Wang, R.B. Figueiredo, L. Chang, X.Z. Liao, M. Kawasaki, W.L. Zheng, S.P. Ringer, T.G. Langdon, Y.T. Zhu, Three-dimensional shear-strain patterns induced by high-pressure torsion and their impact on hardness evolution, Acta Mater. 59 (2011) 3903–3914. doi:10.1016/J.ACTAMAT.2011.03.015.

[179] K. Edalati, Z. Horita, Significance of homologous temperature in softening behavior and grain size of pure metals processed by high-pressure torsion, Mater. Sci. Eng. A. 528 (2011) 7514–7523. doi:10.1016/j.msea.2011.06.080.

[180] B. Srinivasarao, A.P. Zhilyaev, T.G. Langdon, M.T. Pérez-Prado, On the relation between the microstructure and the mechanical behavior of pure Zn processed by high pressure torsion, Mater. Sci. Eng. A. 562 (2013) 196–202. doi:10.1016/j.msea.2012.11.027.

[181] B.J. Bonarski, E. Schafler, B. Mingler, W. Skrotzki, B. Mikulowski, M.J. Zehetbauer, Texture evolution of Mg during high-pressure torsion, J. Mater. Sci. 43 (2008) 7513–7518. doi:10.1007/s10853-008-2794-8.

[182] Y.. Wang, J.. Huang, Texture analysis in hexagonal materials, Mater. Chem. Phys. 81 (2003) 11–26. doi:10.1016/S0254-0584(03)00168-8.

[183] L.S. Toth, C. Gu, Ultrafine-grain metals by severe plastic deformation, Mater. Charact. 92 (2014) 1–14. doi:10.1016/j.matchar.2014.02.003.

[184] S. Gourdet, F. Montheillet, A model of continuous dynamic recrystallization, Acta Mater. 51 (2003) 2685–2699. doi:10.1016/S1359-6454(03)00078-8.

[185] M. Kawasaki, B. Ahn, H. Lee, A.P. Zhilyaev, T.G. Langdon, Using high-pressure torsion to process an aluminum–magnesium nanocomposite through diffusion bonding, J. Mater. Res. 31 (2016) 88–99. doi:10.1557/jmr.2015.257.

[186] S.K. Das, Y.-M. Kim, T.K. Ha, I.-H. Jung, Investigation of anisotropic diffusion behavior of Zn in hcp Mg and interdiffusion coefficients of intermediate phases in the Mg–Zn system, Calphad. 42 (2013) 51–58. doi:10.1016/J.CALPHAD.2013.07.002.

[187] S.-S. Hiroaki Okamoto, Supplemental Literature Review of Binary Phase Diagrams: Cs-In, Cs-K, Cs-Rb, Eu-In, (n.d.). doi:10.1007/s11669-013-0233-2.

[188] C.C. Kammerer, S. Behdad, L. Zhou, F. Betancor, M. Gonzalez, B. Boesl, Y.H. Sohn, Diffusion kinetics, mechanical properties, and crystallographic characterization of intermetallic compounds in the Mg–Zn binary system, Intermetallics. 67 (2015) 145–155. doi:10.1016/J.INTERMET.2015.08.001.

[189] C. Yao, Z. Wang, S.L. Tay, T. Zhu, W. Gao, Effects of Mg on microstructure and corrosion properties of Zn-Mg alloy, J. Alloys Compd. 602 (2014) 101–107. doi:10.1016/j.jallcom.2014.03.025.

[190] Y. Takayama, R. Kasada, Y. Sakamoto, K. Yabuuchi, A. Kimura, M. Ando, D. Hamaguchi, H. Tanigawa, Nanoindentation hardness and its extrapolation to bulk-equivalent hardness of F82H steels after single- and dual-ion beam irradiation, J. Nucl. Mater. (2013). doi:10.1016/j.jnucmat.2012.12.033.

[191] I. Standard, ISO14577-1: 2002 Metallic Materials-Instrumented Indentation Test for Hardness and Materials Parameters – Part 1: Test method., (2002).

[192] K. Edalati, A. Yamamoto, Z. Horita, T. Ishihara, High-pressure torsion of pure magnesium: Evolution of mechanical properties, microstructures and hydrogen storage capacity with equivalent strain, Scr. Mater. 64 (2011) 880–883. doi:10.1016/j.scriptamat.2011.01.023.

[193] F. Meng, J.M. Rosalie, A. Singh, H. Somekawa, K. Tsuchiya, Ultrafine grain formation in Mg-Zn alloy by in situ precipitation during high-pressure torsion, Scr. Mater. 78–79 (2014) 57–60. doi:10.1016/j.scriptamat.2014.01.036.

[194] L. Li, M. Zhang, Y. Li, J. Zhao, L. Qin, Y. Lai, Corrosion and biocompatibility improvement of magnesium-based alloys as bone implant materials: a review, Regen. Biomater. 4 (2017) 129–137. doi:10.1093/rb/rbx004.

[195] Y. Xin, T. Hu, P.K. Chu, Degradation behaviour of pure magnesium in simulated body fluids with different concentrations of HCO, (2011). doi:10.1016/j.corsci.2011.01.015.

[196] Y. Chen, W. Zhang, M.F. Maitz, M. Chen, H. Zhang, J. Mao, Y. Zhao, N. Huang, G. Wan, Comparative corrosion behavior of Zn with Fe and Mg in the course of immersion degradation in phosphate buffered saline, Corros. Sci. 111 (2016) 541–555. doi:10.1016/J.CORSCI.2016.05.039.

[197] K.M.S. Youssef, C.C. Koch, P.S. Fedkiw, Improved corrosion behavior of nanocrystalline zinc produced by pulse-current electrodeposition, Corros. Sci. 46 (2004) 51–64. doi:10.1016/S0010-938X(03)00142-2.

[198] M. Cheng Li, L. Li Jiang, W. Qi Zhang, Y. Hai Qian, S. Zhen Luo, J. Nian Shen, Electrochemical corrosion behavior of nanocrystalline zinc coatings in 3.5% NaCl solutions, (n.d.). doi:10.1007/s10008-007-0293-5.

[199] R. Ambat, N.N. Aung, W. Zhou, Evaluation of microstructural effects on corrosion behaviour of AZ91D magnesium alloy, Corros. Sci. 42 (2000) 1433–1455. doi:10.1016/S0010-938X(99)00143-2.

[200] N. Birbilis, K.D. Ralston, S. Virtanen, H.L. Fraser, C.H.J. Davies, Grain character influences on corrosion of ECAPed pure magnesium, Corros. Eng. Sci. Technol. 45 (2010)

224–230. doi:10.1179/147842209X12559428167805.

[201] B. Shize Jin, S. Amira, E. Ghali, S. Jin, S. Amira, E. Ghali, Electrochemical Impedance Spectroscopy Evaluation of the Corrosion Behavior of Die Cast and Thixocast AXJ530 Magnesium Alloy in Chloride Solution**, (2007). doi:10.1002/adem.200600199.

[202] M.S. Dambatta, S. Izman, H. Hermawan, D. Kurniawan, Influence of Heat Treatment Cooling Mediums on the Degradation Property of Biodegradable Zn-3Mg Alloy, (n.d.). doi:10.4028/www.scientific.net/AMR.845.7.

[203] L.A. Jácome, C. Somsen, G. Eggeler, Systematic dislocation analysis assessment by HAADF STEM imaging, MC 2009, Vol 3 Mater. Sci. 3 (2009) 201–202. doi:10.3217/978-3-85125-062-6-473.

[204] J.A. Del Valle, M.T. Pérez-Prado, O.A. Ruano, Deformation mechanisms responsible for the high ductility in a Mg AZ31 alloy analyzed by electron backscattered diffraction, Metall. Mater. Trans. A Phys. Metall. Mater. Sci. 36 (2005) 1427–1438. doi:10.1007/s11661-005-0235-8.

[205] Y.C. Wang, T.G. Langdon, Effect of heat treatment on microstructure and microhardness evolution in a Ti–6Al–4V alloy processed by high-pressure torsion, J. Mater. Sci. 48 (2013) 4646–4652. doi:10.1007/s10853-012-7071-1.

[206] M. Kawasaki, R.B. Figueiredo, Y. Huang, T.G. Langdon, Interpretation of hardness evolution in metals processed by high-pressure torsion, J. Mater. Sci. 49 (2014) 6586–6596. doi:10.1007/s10853-014-8262-8.

[207] S.A. Torbati-Sarraf, S. Sabbaghianrad, R.B. Figueiredo, T.G. Langdon, Orientation imaging microscopy and microhardness in a ZK60 magnesium alloy processed by high-pressure torsion, J. Alloys Compd. 712 (2017) 185–193. doi:10.1016/J.JALLCOM.2017.04.054.

[208] S.O. Rogachev, S.A. Nikulin, V.M. Khatkevich, R. V. Sundeev, A.A. Komissarov, Features of Structure Formation in Layered Metallic Materials Processed by High Pressure Torsion, Metall. Mater. Trans. A Phys. Metall. Mater. Sci. 51 (2020) 1781–1788. doi:10.1007/s11661-020-05654-y.

[209] W. Hume-Rothery, E. Rounsefell, The system magnesium-zinc, J. Inst. Met. 41 (1929) 119–138.

[210] A. Bachmaier, M. Kerber, D. Setman, R. Pippan, The formation of supersaturated solid solutions in Fe-Cu alloys deformed by high-pressure torsion, Acta Mater. 60 (2012) 860–871. doi:10.1016/j.actamat.2011.10.044.

[211] A. Bachmaier, G.B. Rathmayr, M. Bartosik, D. Apel, Z. Zhang, R. Pippan, New insights on the formation of supersaturated solid solutions in the Cu-Cr system deformed by high-pressure torsion, Acta Mater. 69 (2014) 301–313. doi:10.1016/j.actamat.2014.02.003.

[212] A. Bachmaier, M. Pfaff, M. Stolpe, H. Aboulfadl, C. Motz, Phase separation of a supersaturated nanocrystalline Cu-Co alloy and its influence on thermal stability, Acta Mater. 96 (2015) 269–283. doi:10.1016/j.actamat.2015.05.053.

[213] B.B. Straumal, A.R. Kilmametov, A.A. Mazilkin, L. Kurmanaeva, Y. Ivanisenko, A. Korneva, P. Zięba, B. Baretzky, Transformations of Cu-In supersaturated solid solutions under high-pressure torsion, Mater. Lett. 138 (2015) 255–258. doi:10.1016/j.matlet.2014.10.009.

[214] J.-K. Han, K.-D. Liss, T.G. Langdon, M. Kawasaki, Synthesis of a bulk nanostructured metastable Al alloy with extreme supersaturation of Mg, Sci. Rep. 9 (2019) 17186. doi:10.1038/s41598-019-53614-3.

[215] P. Li, X. Wang, K.M. Xue, Y. Tian, Y.C. Wu, Microstructure and recrystallization behavior of pure W powder processed by high-pressure torsion, Int. J. Refract. Met. Hard Mater. 54 (2016) 439–444. doi:10.1016/j.ijrmhm.2015.10.004.

[216] K. Huang, R.E. Logé, A review of dynamic recrystallization phenomena in metallic materials, Mater. Des. 111 (2016) 548–574. doi:10.1016/j.matdes.2016.09.012.

[217] Z.R. Zeng, M.Z. Bian, S.W. Xu, C.H.J. Davies, N. Birbilis, J.F. Nie, Effects of dilute additions of Zn and Ca on ductility of magnesium alloy sheet, Mater. Sci. Eng. A. 674 (2016) 459–471. doi:10.1016/j.msea.2016.07.049.

[218] V.I. Skrytnyy, M. V Gavrilov, T.P. Khramtsova, A.S. Kolyanova, A.S. Krasnov, S. V Porechniy, V.N. Yaltsev, Misorientation Distribution Function of Crystals, KnE Mater. Sci. 4 (2018) 342. doi:10.18502/kms.v4i1.2185.

[219] M. Kawasaki, J.K. Han, D.H. Lee, J. Il Jang, T.G. Langdon, Micro-Scale Mechanical Behavior of Ultrafine-Grained Materials Processed by High-Pressure Torsion, Mater. Sci. Forum. 941 (2018) 1495–1500. doi:10.4028/www.scientific.net/MSF.941.1495.

[220] I.-C. Choi, D.-H. Lee, B. Ahn, K. Durst, M. Kawasaki, T.G. Langdon, J. Jang, Enhancement of strain-rate sensitivity and shear yield strength of a magnesium alloy processed by high-pressure torsion, Scr. Mater. 94 (2015) 44–47. doi:10.1016/J.SCRIPTAMAT.2014.09.014.

[221] S. Mridha, M. Sadeghilaridjani, S. Mukherjee, Activation volume and energy for dislocation nucleation in multi-principal element alloys, Metals (Basel). (2019). doi:10.3390/met9020263.

[222] Y. Huang, M. Lemang, N.X. Zhang, P.H.R. Pereira, T.G. Langdon, Achieving superior grain refinement and mechanical properties in vanadium through high-pressure torsion and subsequent short-term annealing, Mater. Sci. Eng. A. 655 (2016) 60–69. doi:10.1016/J.MSEA.2015.12.086.

[223] O. Andreau, J. Gubicza, N. Xian Zhang, Y. Huang, P. Jenei, T.G. Langdon, Effect of short-

term annealing on the microstructures and flow properties of an Al-1% Mg alloy processed by high-pressure torsion, Mater. Sci. Eng. A. 615 (2014) 231–239. doi:10.1016/j.msea.2014.07.018.

[224] H. Shahmir, J. He, Z. Lu, M. Kawasaki, T.G. Langdon, Effect of annealing on mechanical properties of a nanocrystalline CoCrFeNiMn high-entropy alloy processed by high-pressure torsion, Mater. Sci. Eng. A. 676 (2016) 294–303. doi:10.1016/J.MSEA.2016.08.118.

[225] D. Woodford, Strain-rate sensitivity as a measure of ductility, ASM Trans. Quart. 62 (1969).

[226] P. Asghari-Rad, P. Sathiyamoorthi, N. Thi-Cam Nguyen, J.W. Bae, H. Shahmir, H.S. Kim, Fine-tuning of mechanical properties in V10Cr15Mn5Fe35Co10Ni25 high-entropy alloy through high-pressure torsion and annealing, Mater. Sci. Eng. A. 771 (2020) 138604. doi:10.1016/j.msea.2019.138604.

[227] P. Asghari-Rad, P. Sathiyamoorthi, N.T.C. Nguyen, A. Zargaran, T.S. Kim, H.S. Kim, A powder-metallurgy-based fabrication route towards achieving high tensile strength with ultra-high ductility in high-entropy alloy, Scr. Mater. 190 (2021) 69–74. doi:10.1016/j.scriptamat.2020.08.038.

[228] Z.Q. Ren, A.A. Churakova, X. Wang, S. Goel, S.N. Liu, Z.S. You, Y. Liu, S. Lan, D. V. Gunderov, J.T. Wang, R.Z. Valiev, Enhanced tensile strength and ductility of bulk metallic glasses Zr52.5Cu17.9Al10Ni14.6Ti5 via high-pressure torsion, Mater. Sci. Eng. A. 803 (2020) 140485. doi:10.1016/j.msea.2020.140485.

[229] X. Wu, Y. Zhu, Heterogeneous materials: a new class of materials with unprecedented mechanical properties, 5 (2017) 527–532. doi:10.1080/21663831.2017.1343208.

[230] C. Wang, H.T. Yang, X. Li, Y.F. Zheng, In Vitro Evaluation of the Feasibility of Commercial Zn Alloys as Biodegradable Metals, J. Mater. Sci. Technol. 32 (2016) 909–918. doi:https://doi.org/10.1016/j.jmst.2016.06.003.

[231] E. Ma, T. Zhu, Towards strength–ductility synergy through the design of heterogeneous nanostructures in metals, Mater. Today. 20 (2017) 323–331. doi:10.1016/J.MATTOD.2017.02.003.

[232] X. Li, R.J. Dippenaar, J.K. Han, M. Kawasaki, K.D. Liss, Phase transformation and structure evolution of a Ti-45Al-7.5Nb alloy processed by high-pressure torsion, J. Alloys Compd. 787 (2019) 1149–1157. doi:10.1016/j.jallcom.2019.02.174.

[233] G.Y. Li, J.S. Lian, L.Y. Niu, Z.H. Jiang, Q. Jiang, Growth of zinc phosphate coatings on AZ91D magnesium alloy, Surf. Coatings Technol. 201 (2006) 1814–1820. doi:10.1016/j.surfcoat.2006.03.006.

[234] J.C. Brodie, E. Goldie, G. Connel, J. Merry, M.H. Grant, Osteoblast interactions with calcium phosphate ceramics modified by coating with type I collagen, J. Biomed. Mater.

Res. - Part A. (2005). doi:10.1002/jbm.a.30279.

[235] Y. Guo, Y. Su, R. Gu, Z. Zhang, G. Li, J. Lian, L. Ren, Enhanced corrosion resistance and biocompatibility of biodegradable magnesium alloy modified by calcium phosphate/collagen coating, Surf. Coatings Technol. (2020). doi:10.1016/j.surfcoat.2020.126318.

[236] W. Xia, J. Chang, Preparation and characterization of nano-bioactive-glasses (NBG) by a quick alkali-mediated sol-gel method, Mater. Lett. (2007). doi:10.1016/j.matlet.2006.11.048.

[237] G.M. Luz, J.F. Mano, Nanoengineering of bioactive glasses: Hollow and dense nanospheres, J. Nanoparticle Res. (2013). doi:10.1007/s11051-013-1457-0.

[238] L. Liu, Y. Meng, C. Dong, Y. Yan, A.A. Volinsky, L.-N. Wang, Initial formation of corrosion products on pure zinc in simulated body fluid, J. Mater. Sci. Technol. (2018). doi:10.1016/J.JMST.2018.05.005.

[239] P. Li, J. Dai, E. Schweizer, F. Rupp, A. Heiss, A. Richter, U.E. Klotz, J. Geis-Gerstorfer, L. Scheideler, D. Alexander, Response of human periosteal cells to degradation products of zinc and its alloy, Mater. Sci. Eng. C. 108 (2020). doi:10.1016/j.msec.2019.110208.

[240] P. Li, C. Schille, E. Schweizer, F. Rupp, A. Heiss, C. Legner, U.E. Klotz, J.G. Gerstorfer, L. Scheideler, Mechanical characteristics, in vitro degradation, cytotoxicity, and antibacterial evaluation of Zn-4.0Ag alloy as a biodegradable material, Int. J. Mol. Sci. (2018). doi:10.3390/ijms19030755.

[241] D. Becker, U. Geissler, U. Hempel, S. Bierbaum, D. Scharnweber, H. Worch, K.-W. Wenzel, Proliferation and differentiation of rat calvarial osteoblasts on type I collagen-coated titanium alloy., J. Biomed. Mater. Res. (2002).

[242] A.G. Andrianarivo, J.A. Robinson, K.G. Mann, R.P. Tracy, Growth on type I collagen promotes expression of the osteoblastic phenotype in human osteosarcoma MG-63 cells, J. Cell. Physiol. (1992). doi:10.1002/jcp.1041530205.

[243] L. Masi, A. Franchi, M. Santucci, D. Danielli, L. Arganini, V. Giannone, L. Formigli, S. Benvenuti, A. Tanini, F. Beghe, M. Mian, M.L. Brandi, Adhesion, growth, and matrix production by osteoblasts on collagen substrata, Calcif. Tissue Int. (1992). doi:10.1007/BF00334548.

[244] M. Lorenzetti, I. Dogša, T. Stošicki, D. Stopar, M. Kalin, S. Kobe, S. Novak, The influence of surface modification on bacterial adhesion to titanium-based substrates, ACS Appl. Mater. Interfaces. (2015). doi:10.1021/am507148n.

[245] S. Wu, B. Zhang, Y. Liu, X. Suo, H. Li, Influence of surface topography on bacterial adhesion: A review (Review), Biointerphases. (2018). doi:10.1116/1.5054057.

[246] W. Teughels, N. Van Assche, I. Sliepen, M. Quirynen, Effect of material characteristics and/or surface topography on biofilm development, Clin. Oral Implants Res. (2006). doi:10.1111/j.1600-0501.2006.01353.x.

[247] Z. Song, L. Borgwardt, N. Høiby, H. Wu, T.S. Sørensen, A. Borgwardt, Prosthesis infections after orthopedic joint replacement: the possible role of bacterial biofilms, Orthop. Rev. (Pavia). 5 (2013) 14. doi:10.4081/or.2013.e14.

[248] T. He, Z.L. Shi, N. Fang, K.G. Neoh, E.T. Kang, V. Chan, The effect of adhesive ligands on bacterial and fibroblast adhesions to surfaces, Biomaterials. (2009). doi:10.1016/j.biomaterials.2008.09.049.

[249] X. Chatzistavrou, J.C. Fenno, D. Faulk, S. Badylak, T. Kasuga, A.R. Boccaccini, P. Papagerakis, Fabrication and characterization of bioactive and antibacterial composites for dental applications, Acta Biomater. (2014). doi:10.1016/j.actbio.2014.04.030.

[250] S.A. Johari, M. Mohtar, S.A. Syed Mohamad, M.F. Mohammat, R. Sahdan, A. Mohamed, M.J. Mohamad Ridhwan, In Vitro Evaluations and in Vivo Toxicity and Efficacy Studies of MFM501 against MRSA, Biomed Res. Int. (2017). doi:10.1155/2017/8032865.

[251] C.C. Otto, T.M. Cunningham, M.R. Hansen, S.E. Haydel, Effects of antibacterial mineral leachates on the cellular ultrastructure, morphology, and membrane integrity of Escherichia coli and methicillin-resistant Staphylococcus aureus, Ann. Clin. Microbiol. Antimicrob. (2010). doi:10.1186/1476-0711-9-26.

[252] Q.L. Feng, J. Wu, G.Q. Chen, F.Z. Cui, T.N. Kim, J.O. Kim, A mechanistic study of the antibacterial effect of silver ions on Escherichia coli and Staphylococcus aureus, J. Biomed. Mater. Res. (2000). doi:10.1002/1097-4636(20001215)52:4<662::AID-JBM10>3.0.CO;2-3.